Gravity and Laboratory Suspension Effects on the Dynamics of Controlled Flexible Spacecraft

by

Daniel A. Rey

B.A.Sc., Systems Design Engineering, University of Waterloo
Waterloo, Ontario, Canada (1989)

SUBMITTED TO THE DEPARTMENT OF
AERONAUTICS AND ASTRONAUTICS
IN PARTIAL FULFILLMENT OF THE REQUIREMENTS
FOR THE DEGREE OF

Master of Science in Aeronautics and Astronautics

at the

Massachusetts Institute of Technology

February 1993

Signature of Author _____
Department of Aeronautics and Astronautics
January 16, 1993

Certified by _____
Professor Harold L. Alexander
Department of Aeronautics and Astronautics
Thesis Advisor

Accepted by _____
Professor Harold Y. Wachman
Chairman, Department Graduate Committee

Gravity and Laboratory Suspension Effects on the Dynamics of Controlled Flexible Spacecraft

by

Daniel A. Rey

SUBMITTED TO THE DEPARTMENT OF AERONAUTICS AND ASTRONAUTICS
ON JANUARY 12, 1993, IN PARTIAL FULFILLMENT OF THE
REQUIREMENTS FOR THE DEGREE OF
MASTER OF SCIENCE IN AERONAUTICS AND ASTRONAUTICS

A comprehensive description is given of the effects of gravitational loading and of a laboratory suspension system on the dynamics of controlled space structures which are tested on the ground pre-flight. Initial stress effects, initial deformation effects, and suspension system effects are examined in turn, in a general manner. This work focuses on how these effects perturb the modal structure of a suspended beam or beam-type structure.

The fundamentals of initial stress modeling theory are presented to convey an understanding of the origin of the geometric stiffness effect and how the latter differs from the initial deformation type of effect. The role played by non-linear strain and element rotation is described to link the direct effects of gravity on the structure with those on the sensors and actuators. A general finite element geometric stiffening framework is presented and verified for a twelve-degree-of-freedom beam element subject to concentrated nodal loads. The same framework is subsequently used to derive the geometric stiffness matrix for a beam element subject to both concentrated nodal loads and distributed loads. Non-dimensional parameters are derived describing the sensitivity of the eigensystem of clamped-free, pinned-pinned and free-free beams, or beam-like structures, to geometric stiffening effects and static suspension stiffening effects.

The direct effects of gravity on the control and output matrices of the controlled structure model due to perturbations to the dynamic performance of accelerometers and proof-mass actuators are thoroughly described. A single non-dimensional measure is derived describing the sensitivity of either device to the effect of gravity. The modeling technique is applied to the MACE testbed and found to improve the accuracy of accelerometer output transfer functions.

A parametric variation analysis of gravity effects on a simplified model of the MACE testbed is performed and a higher order model of the MACE testbed is developed for comparison with experimental data. Suspension, gravity stiffening, and initial deformation effects are all included in the MACE model. A flexible appendage experiment is designed to sensitize the MACE testbed to initial deformation effects and experiments are performed to verify the predictions.

Information is provided in the appendices on the details of using existing finite element codes to capture gravity and suspension effects, as well as on the optimal design of simple extensional spring suspension systems.

Thesis Supervisor: Dr. Harold L. Alexander, Ph.D.
Assistant Professor of Aeronautics and Astronautics

Acknowledgements

I would sincerely like to thank my thesis advisor, Prof. H. Alexander for the trust, patience and encouragement which always accompanied his judicious counsel. I hope my career path will provide me with the opportunity to work with Sandy again someday. I would also like to thank Prof. E. F. Crawley, my co-supervisor and Director of the Space Engineering Research Center for his guidance and for taking me on as part of the SERC team since my arrival at M.I.T. It has been a tremendously rewarding and enriching experience working with Ed and everyone else at SERC. I am certain that I will miss working with such a dynamic and knowledgeable group of fine people.

While everyone at SERC has contributed in some way to my experience at M.I.T. over the past 3 years, I am particularly grateful to my colleague and friend Etienne Balmès for his insightful and truly invaluable technical assistance, to my office-mate Roger Glaese for conspiring with me on the modeling of the MACE testbed, to Marc Andersson for his tireless and excellent work supporting SERC's computer facilities while having his own research work to perform, to Gary Blackwood for sharing the results of his work on the Interferometer, and to Doug MacMartin for sharing his latex expertise over the years and for sharing the gas expenses on the Ottawa trips! Special thanks also to Taehyoun Kim for his assistance in providing me with Dr. Minguet's composite beams and model data. Thanks to SERC UROPer Attila Lengyel for the scanning of the MACE flexible appendage experiment photographs.

I was also very fortunate to have had the opportunity to benefit from the technical expertise of Dr. Paolo Gaudenzi who was on sabbatical at M.I.T. from the Università di Roma, Aerospace Department – Grazie Paolo!

Also deserving of thanks are a number of individuals from the Lockheed Missiles and Space Company who contributed to this thesis by enriching my work experience with their Structural Dynamics Group over the summer of 1990. Thank-you to Dr. Laurence Loh, Mr. Marc Gronet, Dr. John Sesak and Mr. Warren Hoskins.

Last but not least I would like to thank all of my dear family and all of my friends, some close and some far, for their precious love and support. God bless them all.

This work was supported by the M.I.T. Space Engineering Research Center under NASA grant NAGW-1335, and by the NASA Langley Research Center under NASA contract NAS1-18690.

Contents

List of Figures

List of Tables

Chapter 1

Introduction

As the projected size of future large spacecraft grows, the tendency is for their resonant frequencies to drop. As performance requirements similarly continue to grow the trend is for the spacecraft control system bandwidth to increase. When the flexible dynamics of the spacecraft structure approach or enter the controller bandwidth it is necessary to take into account the interactions of the control system and the structure. This is the principle motivation for control structure technology development – a current area of widespread and intensive research [1,2].

The solution to the control structure interaction problem requires that the structure be designed for control or that the control system be designed for the structure, i.e. taking into account the structural flexibility. Both of these solutions, or a combination thereof, require an accurate model or set of models of the spacecraft structural dynamics. The accuracy required of the model is proportional to the control authority one wishes to exercise. Even very small errors in the model can lead to closed-loop instabilities as control authority is increased [1, 3]. An alternative technique is to use more than one model and to attempt to describe a space of feasible plant behaviors [4, 5]. While less sensitive to modeling errors, this and other robust control strategies would benefit nonetheless from obtaining better models at the outset [3].

To verify the model of the spacecraft dynamics and to verify the stability and performance of the controlled payloads (or controlled elements of the structure) actual

physical tests are essential [6–10]. These tests may be performed on components of the spacecraft, on models of the spacecraft, or on the spacecraft itself. Given the costs associated with performing routine tests in orbit, and the risks of delaying tests until orbital operation, these tests are typically performed on the ground. Special test environments, procedures, or suspension devices can be used to simulate the free-free boundary conditions of space but these methods only approximate the spacecraft's operational environment.

Given the need to test controlled space structures on the ground, coupled with the need for high fidelity models of the in-orbit dynamics of spacecraft, three important questions arise which are addressed by this thesis. First, what are the perturbing effects of gravity and of a suspension system on the dynamics of a controlled flexible structure? Second, how may these effects be captured in a model of the system dynamics? And third, when is such modeling required? Including the effects of gravity and the laboratory suspension system in the ground-based model results in an improved 1–g model for model-based control, and an improved 0–g model which is obtained by removing the gravity and suspension effects from the 1–g model after it is tuned using ground-based data.

Currently the most popular and practical approach to modeling the dynamics of a structure (and developing the associated model of the controlled structure) is to use the displacement-based finite element method. This thesis examines therefore how the effects of gravity and of a suspension system may be captured in a displacement-based finite element model. To obtain useful non-dimensional parameters and to study the fundamental coupling mechanisms on a simple three dimensional structure this thesis focuses on beam-type structures and how their eigenstructure (vibration modes and resonant frequencies) is affected by gravity and the presence of a suspension system. Furthermore, to comprehensively address the question of how gravity affects the ground testing of a controlled flexible structure, this thesis also examines the effects of gravity on structural sensors and actuators.

1.1 Background

This section provides additional background on the motivation for this thesis and on the controlled structure technology problem.

Spacecraft Design

The typical design procedure used in the past to prevent control-structure interactions aboard spacecraft has been to stiffen the spacecraft structure so that structural resonances lay outside the control bandwidth. When one refers to a *flexible* spacecraft the implication is usually that the structural flexibility is an important concern and cannot be so easily eliminated. An excellent present-day example of a spacecraft whose performance was adversely affected by structural dynamic interactions is the Hubble Space Telescope where solar array flexibility degraded the pointing performance [11,12]. This was corrected by modifying the pointing control algorithm using in-flight identification data, but the flexible appendage excitation problem could have been anticipated and prevented through the use of ground-based model and test data. Other examples of space platforms which will most likely be susceptible to control structure interaction problems are the Space Station Freedom (particularly during assembly with the Remote Manipulator System), the Large Synthetic Aperture Radar Satellite, the Earth Observation System and the Large Space-Based Interferometer mission.

Other than stiffening the structure, approaches for solving the control structure interaction problem are: to passively increase the damping in the structure with a judicious placement of dissipative material, to isolate the structure from the disturbance sources, to isolate the output devices (i.e. the performance metric) from the structure, to use low authority control for local damping at critical locations in the structure, and to use high authority control to modify or avoid the excitation of the global modal behavior of the structure. Figure 1-1 illustrates the principal elements of the structural control problem [1]. All of the aforementioned techniques

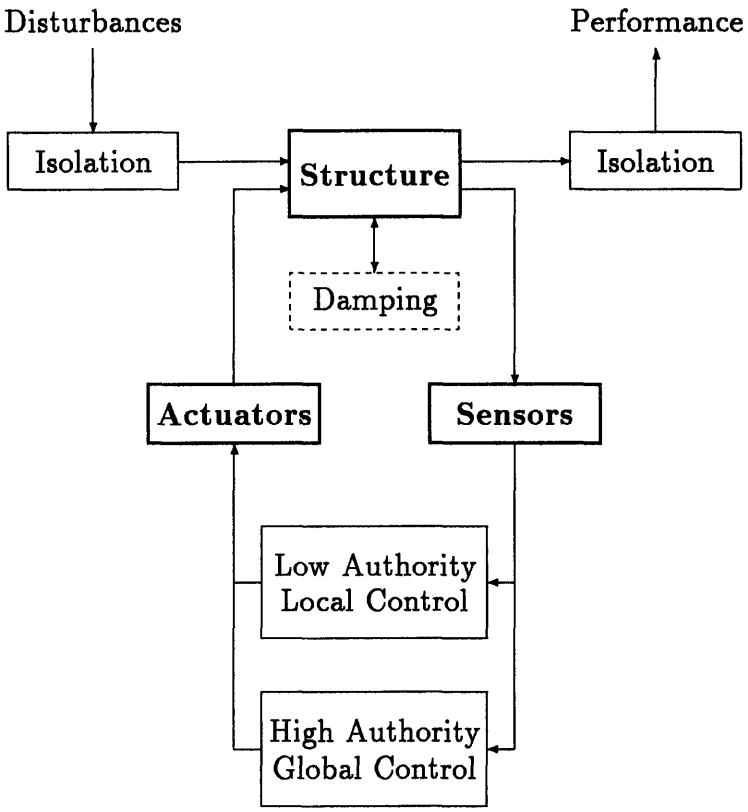

Figure 1-1: Controlled Structures Technology Problem

have one thing in common and that is their requirement for a model of the plant, i.e. the structure, the sensors and the actuators. The effectiveness or success of the structural control technique is directly related to the accuracy of this model.

Spacecraft Modeling

There are two fundamental models pertinent to this discussion: the structural dynamics mass and stiffness model, and the controlled structure state space model. The structural dynamics model essentially consists of a discretized mass and stiffness (M and K) representation of the structure while the controlled structure model consists of the state-space A, B, C and D matrices, i.e. the system, control, output and feed-through matrices (see Chapter 4). Information provided by the structural dynamics model is used to construct the controlled structure state space model. The fundamen-

tal system properties provided by the structural dynamics model to derive the state space model are the structural eigenfrequencies and eigenmodes, collectively referred to as the eigensystem. Thus, in this study of the effects of gravity and of a suspension system on the dynamics of controlled flexible spacecraft we are principally concerned with the perturbations to the eigensystem of the suspended structure. Direct effects on the control and output sensitivities (and hence on the state space model) are also possible for certain structural sensors and actuators. These effects are examined in Chapter 4 for the accelerometer and the proof-mass actuator. Note that the study of gravity and suspension effects on the damping in the structure is not considered here due to the established difficulties of *a-priori* damping modeling and the common practice of measurement-based damping identification.

Spacecraft Testing

To develop an accurate and meaningful model of the structural dynamics it is necessary to tune the system model based on experimental data, particularly in the case of controlled structures [1, 3]. This requires that pre-flight models of the system, or its fundamental components, be built and tested [6–10]. For safety, cost and practicality reasons the structural dynamics tests and closed-loop system performance tests are most often performed on the ground (rather than in the operational orbital environment) with the structure suspended from above using long cables and soft springs to simulate the free-free boundary conditions of space [10]. This ground-based testing unfortunately introduces a number of discrepancies as compared to the orbital environment, e.g. aero/acoustic effects, suspension effects, gravity effects and thermal/radiation effects [13]. It is felt that the most significant of these are the family of gravity and suspension effects. Ashley [10] and Wada [14] for example state that gravity effects represent a major obstacle to the testing of large space structures rather than a minor inconvenience. Hanks and Pinson [6] compare the differences between ground-based test results and orbital results to "noise" on the ground-based test data which must either be removed or accounted for. They identify the following three approaches for removing, reducing, or accounting for the effects of gravity and a suspension system:

1. Special Test Environments
   (e.g. 0–g parabolic aircraft flights and vacuum chamber drop tests)

2. Special Test Procedures
   (e.g. subassembly testing, component testing, test article size reduction via scaling and test article suspension using sophisticated low-frequency suspension devices)

3. Analytical Modeling
   (i.e. analytically removing the gravity and suspension effects incorporated in the ground-based model to yield the orbital model)

For practical reasons the use of 0–g parabolic aircraft flights and vacuum chamber drop tests is not well suited to the testing of controlled structures. This thesis and the M.I.T. Space Engineering Research Center therefore adopt a combination of the remaining two options in an effort to address the real problems encountered in the ground-based verification of controlled flexible spacecraft: i.e. analytically accounting for gravity and suspension system effects in the model of a structure which has been suspended using state-of-the-art low-frequency suspension devices. This approach is also the one which has widely been adopted by industry. While most of the elements of the work presented in this thesis have been used for some time by the aerospace industry, the industry's interest was not on the nature and prediction of gravity and suspension effects but on the final answer (i.e. what is the final structural dynamics model?). The result is that gravity effect modeling methods vary from project to project and corporation to corporation and no comprehensive treatment of the topic of gravity and suspension effects has ever been produced. This thesis attempts to fill this void by addressing the three questions of what are the effects of gravity and of a suspension system on a controlled flexible spacecraft, how are they are modeled, and when are they important.

Using the analytical gravity and suspension effect modeling technique one derives two structural dynamics models: a ground-based or 1–g model and an orbital or

0–g model derived from the 1–g model. The 0–g model is simply obtained by removing the effects of gravity and of the suspension system from the 1–g model. To obtain the best possible 0–g model it is important to include the effects of gravity and of the suspension system in the ground-based model *prior* to the tuning of the model in order to avoid tuning the wrong parameters in an effort to compensate for gravity and suspension effects.

The principal M.I.T. Space Engineering Research Center testbed used in this work is a multiple payload platform model known as the Middeck Active Control Experiment (MACE) testbed [13, 15]. The MACE testbed is geared precisely towards the study of gravity and suspension effects present even with state-of-the-art pneumatic-electric suspension devices [16, 17]. In the future this testbed will serve to verify the range of validity of the analytical techniques described in this work with an actual orbital test aboard the Space Shuttle.

1.2 Overview of Gravity and Suspension Effects

The effects of gravity and of a suspension system on a controlled flexible structure can be grouped into the following categories:

1. Suspension Effects
2. Gravity Effects on Structure
    - 2.1 Geometric Stiffening
    - 2.2 Initial Deformation Effects
3. Gravity Effects on Sensors and Actuators
4. Non-linear Gravity and Suspension Effects

In general terms, the effect of attaching a suspension system to the test article is to change the system boundary conditions. By augmenting the system description

to include the suspension system the overall system mass and stiffness description is perturbed thus affecting the system eigenstructure.

The two gravity effects on the structure similarly result in changes to the system eigenstructure. Geometric stiffening is a change in the system stiffness due to initial internal stresses which occur due to gravitational loading. Initial deformation effects are perturbations to both the system mass and stiffness properties due to initial deformations which occur when the otherwise unloaded structure is suspended and deforms in the gravity field.

The direct effects of gravity on the performance of certain sensors and actuators are a result of harmonic rotation of the devices when attached to a vibrating structure. Presently, only accelerometers and proof-mass actuators have been identified as structural control devices susceptible to this effect.

All of the above linear effect categories are examined in this work. The non-linear effects are not studied herein. The non-linear effects of gravity and of the suspension system are typically linear effects on non-linear components, e.g. gravity loading of joints or mechanisms with backlash or deadband. Occasionally a suspension system may introduce minor non-linear dynamic effects such as stiction or Coulomb friction but these are typically negligible.

1.3 Survey of Previous Work

This section briefly highlights the past work performed in the area of modeling gravity and suspension effects.

1.3.1 Suspension Effects on Structures

In 1974 R. Herr of the NASA Langley Research Center performed seminal research on cable suspension system perturbations to the lateral flexural eigenfrequencies of slender aerospace structures [18]. Herr identifies the non-dimensional parameter $\frac{g}{\omega_n^2 l}$ as a

preliminary measure of the magnitude of the error in the flexural frequency, where l is the vehicle length. Herr also found, for his vertically suspended rocket-like structures, that axial stiffening effects were the dominant source of error.

Hanks and Pinson, also of the NASA Langley Research Center, discussed the trade-off between lowering suspension pendular frequencies and lowering cable violin mode frequencies with increasing cable length [6].

M. Gronet and R. Brewster of Lockheed Missiles and Space Co. and E. F. Crawley of M.I.T. identified potential suspension cable interactions with the space station hybrid scale model, specifically: added mass, added stiffness and coupling of cable dynamics with the structure [19]. The dislocation method is mentioned as a method of tuning the cable tension in the model to mimic the experimental tuning which is performed to obtain a level suspended structure. In their discussion of cable location selection they describe the optimal suspension stiffness distribution to be proportional to the attachment point mass and or stiffness so that the eigenmodes of the test article remain unperturbed and the eigenfrequencies shift uniformly.

Experimental results obtained from the Middeck Open-Loop Dynamics Experiment (MODE), a space flight experiment (STS 48, Sept. 1992), indicated that the effect of a four point suspension system attached to the four corners of the top surface of a the square truss test article was to introduce a significant yet predictable linear change on the test article's torsional resonant frequencies and damping ratios [20]. Resonant frequencies increased linearly with an increase in vertical suspension bounce frequency, while damping ratios decreased linearly with increasing suspension frequency.

The experimental work of V. Cooley [21] in comparing zero spring rate mechanisms (ZSRMs) to pneumatic-electric suspension devices found that mass coupling effects dominated stiffness effects for his test article. Damping effects were found to be substantial.

1.3.2 Gravity Effects on Structures

Ben Wada of the Jet Propulsion Laboratory refined a Special Test Procedure for suspended structures he named the Multiple Boundary Condition Test (MBCT) [14, 22, 23]. The approach of his MBCT work consists of using multiple pin joints or clamps to support the structure and reducing the support spacing to the point where gravity effects can be considered negligible. No description of the circumstances under which the gravity effects can be considered negligible is presented although Wada does identify gravity sag and gravity stiffening as two important effects of gravity on the structure. By performing a large number of tests with a variety of boundary conditions he identifies different sub-matrices of the system mass and stiffness matrices with every test. Therefore the approach is in essence a form of sub-assembly testing where gravity effects are ignored. The method attempts to predict the system 0–g dynamics and cannot be used for the derivation of a 1–g model.

C. F. Shih's work [24, 25] derives the closed-form expressions for the 2D eigen-behavior of a vertical and horizontal pinned-pinned beam subject to its own weight. While the scope of this work is very limited it is a practical reference for the development of simple rules of thumb for simple structures. Shih's colleagues at the Jet Propulsion Laboratory, J. Chen and J. Garba [26], also examined the special case of 2D horizontal pinned-pinned beam behavior. They identified a very small effect on the shapes of the bending modes but a substantial effect on the resonant frequencies. This effect was found to decrease with increasing wave number.

M. Gronet, R. Brewster and E. F. Crawley [19] describe some of the system issues in ground-based testing of flexible structures. While the focus of their review was on suspension effects, the use of geometric stiffness modeling techniques is mentioned as a means to capture gravity stiffening effects.

No explicit work was found which dealt with the incorporation of gravity and suspension effects in a finite element model.

1.3.3 Gravity Effects on Sensors and Actuators

Norris, Thompson and Das [27] recently examined the attenuating effect of gravity on the dynamic performance of accelerometers subject to bending-induced rotation in the vertical plane. Their work is extended here to include amplification effects, sign changes, torsionally induced rotation, arbitrary accelerometer and rotation orientations and the dual effect on the proof-mass actuator.

1.4 Methodology and Outline

Methodology

The approach adopted in this thesis is to keep the analysis, the results, and the observations concerning gravity and suspension effects as general as possible. Since the method of choice for modeling the dynamics of complex structures is the finite element method, this thesis is largely concerned with the incorporation of gravity and suspension effects into the finite element framework. Unfortunately, to illustrate the derivation of a geometric stiffness matrix, to examine the nature of the modal couplings induced by gravity or the suspension system, and to derive useful non-dimensional parameters for predicting the magnitude of the gravity and suspension effects, it is necessary to focus on a particular type of element or structure. This thesis focuses thus on beam-like structures and beam-type finite elements due to their widespread applicability in finite element models and their susceptibility to gravity effects.

Since the suspension system itself is susceptible to gravity effects, the theory of initial stress stiffening and the effect of initial deformations are examined first. A general framework is presented to allow for the derivation of a geometric stiffness matrix or initial stress stiffness matrix for an arbitrary element and to present the initial deformation effect on a finite element model in a general context. A geometric stiffness matrix is derived for a homogeneous 12 degree-of-freedom Bernoulli-Euler

beam element subjected to concentrated nodal loads, and is compared to the results of Yang and McGuire [28, 29] to verify the methodology. A second geometric stiffness matrix which incorporates gravity-like distributed forces is then derived for a Bernoulli-Euler beam element and its performance is compared to that of the previously derived concentrated-load geometric stiffness matrix. The enhanced geometric stiffness matrix was found to be unnecessary if one uses the proper consistent nodal loads.

The sensitivity of the eigenstructure of clamped-free, pinned-pinned and free-free beam elements to the effects of initial stress stiffening are examined in a general analytical fashion by identifying the symbolic eigenvectors of the unperturbed system and using them to project the symbolic representation of the perturbed eigensystem onto the original eigenspace. This technique results in a "sensitivity matrix" which readily exposes the resulting eigenfrequency shifts and modal couplings. The relationship between this eigenprojection technique and the definitions of the eigenvector and eigenvalue derivatives is also presented. An important advantage of using this analytical technique to describe the impact of the perturbations on the beam eigenstructure is the ease with which key non-dimensional parameters can subsequently be identified.

The initial stress effects examined are initial bending, torsion, and extensional stresses. The effects of shear loads are ignored since the focus is on long slender flexible structures. A general analytical treatment of the effects of initial deformation on the eigenstructure of a beam element was also attempted but exceeded available computational resources. A verification analysis is performed where the eigensystem of a drooping beam is identified and compared to the published analytical results of Minguet [30]. The Minguet reference case is one of the only references available where the effects of small initial deformations and stress stiffening on a full three dimensional beam eigenstructure is detailed. Unfortunately the Minguet beam was a composite beam rather than a homogeneous beam which limited the extent to which

his results could be reproduced. Eigenfrequencies were shifted for both the loaded and unloaded case but the eigenmodes were accurately predicted.

The static effects of a suspension system on the eigenstructure of a horizontally suspended free-free beam are then examined in a similar analytical fashion. Non-dimensional parameters are derived to describe the sensitivity of a beam-like structure to the suspension stiffness effects. The dynamic effects of the suspension system are not examined in this thesis as it is shown rather how these effects can be captured by including the suspension system in the finite element model before the computation of geometric stiffening effects.

To study the effects of gravity on structural sensors and actuators an effort is made to identify fundamental perturbation mechanisms which affect even the ideally performing sensor or actuator. It was found that only those devices whose operation is based on a translating internal mass are susceptible to a gravity induced perturbations. The focus is therefore on the accelerometer and the proof-mass actuator. To identify the corresponding perturbations to the controlled structure input and output matrices the approach was to identify the fundamental gravity effect on the dynamic performance equations and then to examine the modal modeling of the performance equations. Non-dimensional parameters describing the sensitivity of the devices to the additive gravity perturbation effect were then derived, and found to be identical for both these devices.

The MACE testbed is used as a case study for all three of gravity stiffening, initial deformation and sensor/actuator effects. A parametric variation analysis is performed using the ADINA finite element modeling software [31] to capture gravity and suspension effects in a simplified version of the MACE model. The effectiveness of the non-dimensional parameters presented in Chapters 2 and 3 is investigated. A high fidelity model of the MACE testbed is developed and used to generate the important system transfer functions for comparison with experimental transfer function data.

Outline

Chapter 2 of this thesis examines the direct effects of gravity on the property matrices of a structure, i.e. the effects of initial stress stiffening and the effects of initial deformations on the mass and stiffness matrices of a structure. The most theoretical of all chapters, Chapter 2 presents a formal derivation of the geometric stiffening and initial deformation effects. Highlighted is the relationship between infinitesimal rotations and the non-linear strain contribution to the geometric stiffness matrix. The final result of the first section of Chapter 2 is a set of equations describing how the mass and stiffness matrices should be formed to capture initial stress and initial deformation effects. The subsequent sections of Chapter 2 focus on beam-like structures and the finite element beam element. A new geometric stiffness matrix is derived which allows for gravity-like distributed loads. The nature of the effect of initial stresses or initial deformations on the eigenstructure of a clamped-clamped, pinned-pinned, or free-free beam element are derived, observations are made, and non-dimensional parameters identified. Chapter 2 closes with a verification of the gravity effect modeling techniques and the analysis of a few sample problems.

Chapter 3 investigates the effects of a suspension system on the eigenstructure of a horizontally suspended beam or beam-type structure. The focus is principally on static effects although it is shown how dynamic effects are captured by including the suspension system in the structural model and incorporating the geometric stiffening effects. Non-dimensional parameters are again identified to help predict the magnitude of the suspension stiffening effects on the structure dynamics. The different types of dynamic effects that one should be aware of are also described.

Having studied the direct effects of gravity and the suspension system on the controlled structure dynamics, Chapter 4 examines the effects on the structure's sensors and actuators. The effect of gravity on the accelerometer and proof-mass actuator is identified along with another non-dimensional sensitivity parameter. The modeling techniques derived in this chapter are applied to the MACE testbed and shown to

improve the transfer function of a horizontally oriented accelerometer.

Chapter 5 then comprehensively applies the gravity and suspension modeling techniques described in Chapters 2 and 3 to the MACE testbed. The ADINA finite element program is used to perform a parametric variation analysis and a high-fidelity analysis of the MACE testbed. Five different configurations are studied in the parametric variation analysis to study the applicability of the non-dimensional parameters and the variation in the nature of the gravity and suspension effects with variations in the test article properties. The incorporation of gravity and suspension effects in the high fidelity MACE model is shown to improve the low frequency description of the test article, largely due to suspension effects and the application of geometric stiffness effects to the latter. To sensitize the MACE test article to initial deformation effects a flexible appendage experiment was designed and performed. Two graphite-epoxy composite beams (identical to those used by Minguet in his study of small droop effects) were attached to the node above the performance payload in the horizontal plane forming a T with the bus. The appendages selected were not straight but slightly bowed by just the amount needed to cancel the droop effect of gravity. This made it possible to perform two experiments: a full droop experiment with the slight curvature facing down and a no-droop experiment with the slight curvature mounted upwards and straightened by the distributed gravity load. Transfer function data is presented for the two cases and the predicted higher frequency modal coupling effects due to the initial deformations are witnessed.

The final chapter summarizes the conclusions presented in this thesis and arrived at over the course of this research. Recommendations for future work are listed after the conclusions.

Appendix A presents the information required to implement the gravity and suspension modeling techniques of Chapters 2 and 3 in a finite element program. The general information provided is applicable to most finite element packages but additional detail is presented for the use of the ADINA finite element modeling package.

The multi-step, non-linear ADINA analysis procedure is described and a sample set of run-streams is provided.

Appendix B offers a set of procedures for selecting extensional springs for a simple vertical spring suspension system. This approach is only valid for test articles whose first resonant frequency is near or above 2 Hz. Lower-frequency test articles require cable and spring lengths which are typically not possible due to ceiling height limitations, dictating therefore the use of more sophisticated suspension devices.

1.5 Contributions

Identified in this work are the different mechanisms by which gravity and a laboratory suspension system affect the dynamics of suspended flexible structures. A coherent step-by-step derivation of the geometric stiffness effect and the initial deformation effect on the system mass and stiffness matrices is presented to highlight the difference between the two effects, to identify the assumptions and limitations of the theory, and to allow for original applications of the theory. The role of rotation in stress stiffening and initial deformation is presented and proposed as a unifying link to the sensor/actuator family of effects where rotation in a gravity field is the underlying origin of the perturbation.

An original contribution of this work is the derivation of a geometric stiffness matrix, K_{gd}, for a Bernoulli-Euler beam element which allows for linearly distributed axial loads and uniformly distributed transverse loads. However, by comparing the performance of the K_{gd} matrix to the geometric stiffness matrix K_g, which only allowed for concentrated nodal loads, it was found that the enhancement of using K_{gd} over K_g is negligible if one uses consistent nodal loads and a sufficient number of elements. An exception to this is is the case of pure distributed axial loading for which use of the K_{gd} matrix is recommended.

A second, more practical original contribution is a set of non-dimensional param-

eters for quickly evaluating the approximate magnitude of gravity load and static suspension effects on the eigensystem of suspended beam-type structures or beam-type components of a structure. The beam configurations studied were the clamped-free, pinned-pinned, and free-free beam which together cover most of the boundary conditions one would typically encounter for a beam-like component or element of a spacecraft structure. The non-dimensional parameters associated with initial deformation effects and with dynamic suspension effects are left for future work. The thesis describes how the latter parameters can be derived.

Another valuable contribution of this work is the thorough description of gravity effects on sensors and actuators and the modeling thereof. The work is an extension of the accelerometer work of Norris, Thompson and Das [27] and describes amplification effects in addition to attenuation effects, is generalized to describe arbitrary device and rotation orientations, and identifies the fundamental non-dimensional gravity effect sensitivity ratio common to both the accelerometer and the proof-mass actuator.

The application of the modeling techniques developed herein to a realistic controlled flexible spacecraft testbed also allowed for the identification of realistic gravity and suspension system effect types and magnitudes. For the structural dynamicist who, for the first time, is faced with the problem of incorporating gravity and suspension effects in a finite element model, the summary of Appendix A is a valuable tool.

Chapter 2

Gravitational Load Effects on Structures

The objectives of this chapter are to:

- identify the origin of gravity effects on suspended flexible structures,
- derive general modeling techniques for the effects of gravity on the eigensystems of flexible structures,
- examine general effects on the eigensystem of a beam or beam-like structure,
- derive non-dimensional parameters which describe the sensitivity of a beam or beam-like structure to gravity effects,
- verify modeling techniques and evaluate performance of non-dimensional parameters by performing a numerical study of the dynamics of beam-like structures in a gravity field.

To ensure clarity of purpose it is stressed here that the gravity effects we are interested in are the effects on the eigenfrequencies and eigenmodes of the suspended structure as these are the building blocks of the controlled structure model. We seek therefore to identify the perturbation to the homogeneous system equations of motion, i.e. the

unforced equations of motion which yield the infinitesimal displacement eigenproblem. Since damping is generally incorporated into the system model a posteriori (based on conservative damping estimates or measurements), we are strictly interested in the effects of gravity on the mass and stiffness matrices which define the structure's eigensystem. The two direct effects of gravity on the dynamics of a suspended flexible structure will be shown to be *initial stress effects* and *initial deformation effects.* Initial stress effects are perturbations to the system stiffness matrix which are due to the presence of stresses in the deformed reference structure. Initial deformation effects are perturbations to both the mass and stiffness matrices which result from changes in the reference structure geometry when gravity loading is applied to the undeformed suspended reference structure.

Chapter Outline

The chapter essentially addresses the different objectives in sequence:

Section 1 contains a general derivation of the modeling of the two direct gravity effects on the structural dynamics.

Section 2 derives a standard initial stress stiffness matrix for a beam element, as well as a new initial stress stiffness matrix which also captures distributed load effects.

Section 3 analyses the impact of initial stress effects on the eigensystems of clamped-free, pinned-pinned, and free-free beam-like structures, and derives associated non-dimensional sensitivity parameters.

Section 4 analyses the impact of initial deformation effects on eigensystem of free-free beam-like structure and derivation of non-dimensional parameters.

Section 5 combines initial deformation and initial stress modeling techniques in the numerical study of sample problems with known solutions.

For the reader who is only interested in the key equations and the final results it is recommended to refer directly to the fundamental intermediate results of Equations 2.34, 2.37, and 2.51 (on pages 52, 53, and 56) and to Equations 2.59, 2.61 and 2.62 (on pages 58, 58 and 58) for the key final results.

Chapter Overview

This chapter examines the modeling of gravity effects on the continuous structure starting from an exact, non-linear statement of the principle of virtual work which captures initial stress effects on the system stiffness properties. The effect of initial stresses is to stiffen or destiffen static or dynamic infinitesimal element rotations of a magnitude comparable to the strains. In this case, the initial stresses are due to the presence of the constant gravitational load field. An incremental decomposition of the stress and strain terms, followed by a finite element discretization, yields a matrix form of the incremental principle of virtual work which makes clear the origin and form of the different stiffness matrix components. One of these stiffness matrix components captures the stress stiffening effect, another is the classic stiffness matrix, and the two others are eliminated in the linearization required to form the eigenproblem. By incorporating inertial load effects, the system mass matrix is obtained and shown to be invariant to the stress stiffening effect. In the discussion of the solution of the non-linear equilibrium statement, the second gravity effect is introduced, i.e. the effect of initial deformations which affects both the mass and stiffness properties of the system. Assumptions and limitations are highlighted throughout the derivation.

After deriving and presenting the general form of the stress stiffening and initial deformation effects on the equations of motion of a discretized structure, this chapter focuses on the particular case of a three-dimensional Bernoulli-Euler beam element, and structures composed of such elements. Two geometric stiffness matrices which capture initial stress stiffening effects for a beam element are derived–one which is limited to lumped nodal loads and another which allows for certain gravity-like dis-

tributed loads along the length of the beam element. These perturbations to the original elemental stiffness matrix depend only the internal stress state which can be determined based on the resolved nodal loads. The initial deformation transformation matrices, on the other hand, are only a function of the rigid-body reorientation of the individual beam element neutral axes.

Given general analytical descriptions of the two gravity effects on the system property matrices of a beam element, an eigensystem sensitivity analysis is performed to examine the impact of the gravitational loading on those flexible spacecraft dynamic properties of interest, i.e. the resonant frequencies and eigenmodes. Non-dimensional parameters which describe the sensitivity of a beam element or beam-like structure to the gravity perturbations are then derived.

A verification analysis is then performed, making use of both the geometric stiffness and initial deformation refinement procedures to study special cases of gravitational loading for which well established results exist.

2.1 Initial Stress Modeling Theory

This section describes the theory behind incorporating gravity effects into a structural dynamics model. In brief, the solution is to augment the regular stiffness matrix with an initial stiffness matrix and to redefine the reference structure after computing initial deformations. If necessary, the stiffness reformations should be included in the solution for the static deformation state which is an incremental procedure in the case of large deflections.

The initial stiffness matrix is obtained, as will be shown, by including the non-linear strain terms in the equilibrium statement for the deformed configuration. These non-linear strain terms are made important by the gravitational loading as they describe rotation of the element. The initial stiffness method or geometric stiffness method is derived here in order to understand how it captures the effects of gravity

loading in addition to understanding its limitations and implied assumptions. It is worthwhile to present here a rather detailed derivation in order to understand the role of dynamic elemental rotations in the geometric stiffness matrix, as well as the difference between the stress stiffening effect and the initial deformation effect. The point of identifying the role of the dynamic elemental rotations is to establish a link with the source of the gravity effect on the sensors and actuators as described by Rey et al. in [32] and in Chapter 4, where harmonic rotation of the device in the gravity field leads to an additive perturbation to the device input or output.

2.1.1 Background

It is somewhat surprising to find that the key to capturing the effects of gravity on the linear structural dynamics model is to be found in the non-linear or large displacement modeling literature, especially since our goal is to identify gravity effects on the small displacement eigenproblem. This can be explained by recognizing that the large displacement theory captures the effects of element rotations which are made important by internal stresses. As pointed out by Martin [33], the large displacement theory distinguishes itself from the small displacement theory not necessarily because large displacements occur in a literal sense but because stresses exist which influence the structural stiffness in the presence of certain displacements (i.e. rotations of a magnitude comparable to the strains). Large displacement theory, or geometrical non-linear theory, is thus a fundamental component of stability analysis which is a special case of the generalized eigenproblem we are interested in. Note that it is not necessary that the structure be stressed close to the point of structural collapse for the perturbation to the eigensystem to be significant given the controlled structure context where even small errors can lead to instabilities.

The first attempt to take into account a uniform initial stress is attributed to Southwell in 1913 [34,35]. In 1928 Biezeno and Hencky introduced incremental stress-strain relations in their work on elastic stability theory [36, 37]. In terms of the

discrete structural property matrices, the seminal paper which proposed an updating of the stiffness matrix for the large deflections of a structure subject to heating and external loads was written by Turner et al. in 1959 [38]. The geometric arguments used by these and other initial researchers [33, 39–41] to incorporate the effect of membrane forces in the direct stiffness method led to the name geometric stiffness matrix. Simple bar elements and beam elements were considered first [33, 42] and then similar geometric arguments were used for various plate elements [43, 44].

2.1.2 Derivation

Approach

Several different approaches exist to derive the initial stress stiffness matrix, much in the same manner as different approaches exist for deriving the regular stiffness matrix. It is possible to use a virtual work approach using virtual displacements or virtual stresses, or one can use a potential energy approach. The next step would be to apply one of a number of different discretization techniques such as Galerkin's method, Assumed Modes/Ritz-Method or the Finite Element Method.

The approach adopted here is to use the principle of virtual work and to discretize using a displacement-based, finite element representation. The displacement-based finite element method is by far the most common and successful method of deriving complex finite-order structural models for static and dynamic analysis. The method essentially consists of discretizing a structure into elements such as beams, rods, plates, shells, etc. where each element has a finite number of discrete translation or rotation degrees-of-freedom at a limited number of nodal points. These elements have associated mass and stiffness matrices which are obtained by assuming displacement interpolation shapes between their nodal points and integrating the appropriate terms of the discretized principle of virtual work. The mass and stiffness matrices are assembled into global mass and stiffness matrices by superposition.

The steps in this derivation are first to survey the classic **small displacement**

analysis relations used in the regular stiffness matrix derivation before proceeding to describe the **large displacement analysis** strain tensor which captures the all-important element rotation information using non-linear strain measures. To yield the system property matrices for an Updated Lagrangian formulation, the concepts and notation of an **incremental formulation of the static equilibrium** are described. An **incremental decomposition of the stresses and strains** is then performed to yield a general incremental principle of virtual work which captures the effects of initial stress through the use of non-linear strain measures. A **finite element discretization** of this variational statement of equilibrium is then performed to yield a discrete incremental static equilibrium expression which in turn yields an expression for the **stiffness matrices**. A **linearization** of the stiffness matrices is then performed and various **iterative solution** techniques are described to solve for the initial static displacements. Finally, the **mass matrix** is derived to describe the dynamic system behavior and the small displacement **eigenproblem** is formulated about the statically deformed equilibrium.

It is assumed in the developments which follow that the material properties are constant, the constitutive relations are linear, the deformations are elastic and the strains are small with respect to 1.

Small Displacement Analysis

In a small displacement analysis it is possible to derive the system mass and stiffness properties by applying finite element modeling techniques to the following statement of equilibrium between the internal virtual work and the external virtual work for a general body at time t, [45]

$$\int_{{}^tV} {}^t\mathcal{T}_{ij}\, {}^t\overline{e}_{ij}\, {}^t dV = \int_{{}^tV} f_i^B\, {}^t\overline{u}_i\, {}^t dV + \int_{{}^tS} f_i^S\, {}^t\overline{u}_i^S\, {}^t dS + \sum_k {}^t F_k\, {}^t\overline{u}_k^P \qquad (2.1)$$

or,

$$\int_V \mathcal{T}_{ij}\, \overline{e}_{ij}\, dV = \mathcal{R} \tag{2.2}$$

where ${}^t\mathcal{T}_{ij}$ is the instantaneous Cauchy stress tensor evaluated at time t, ${}^t\overline{e}_{ij}$ are the linear (small displacement or classical) virtual strains, and ${}^t f_i^B$, ${}^t f_i^S$ and ${}^t F_k$ are respectively the body forces, surface tractions and concentrated forces at time t. The virtual displacements are denoted by $\overline{u}$, where the S superscript denotes surface displacements and the P denotes the displacements of those points where the concentrated forces are applied.

The strain-displacement relation for the classical, small displacement, strain tensor is given by

$$e_{ij} \triangleq \tfrac{1}{2}\left(\frac{\delta u_i}{\delta x_j} + \frac{\delta u_j}{\delta x_i}\right) \triangleq \tfrac{1}{2}\left(u_{i,j} + u_{j,i}\right) \tag{2.3}$$

where u_i $(i = 1, 2, 3)$ is a Cartesian displacement measure, x_i $(i = 1, 2, 3)$ is a Cartesian position measure, and $u_{i,j}$ is the derivative of the i^{th} displacement measure with respect to the j^{th} direction $(j = 1, 2, 3)$. The classic small displacement stress-strain relation is given by

$$\mathcal{T}_{ij} \triangleq C_{ijkl}\, e_{kl} \tag{2.4}$$

where C_{ijkl} is constant in this treatment limited to linear elastic materials. Such measures of stress and strain, while very practical for small displacement analysis, are not plausible for large displacement analysis as they are not invariant to rigid-body rotations and translations. It is necessary to use more general stress and strain measures to make apparent the effect of gravitational loading. Note that the word "displacement" is used here as it is in the literature to describe both translational and rotational displacements.

Large Displacement Analysis Strain Tensor

The general strain measure used in this analysis is the Green-Lagrange strain tensor which is invariant under rigid body motion and is valid for both small and large

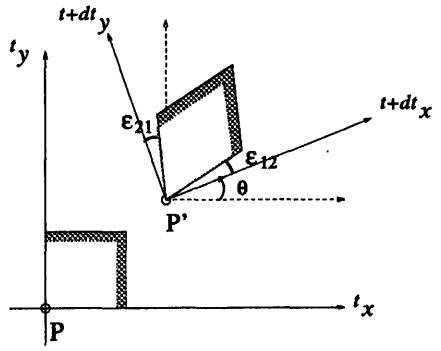

Figure 2-1: Simultaneous Deformation, Rotation and Translation of an Infinitesimal Element in Two Dimensions

displacements, [46]

$$\epsilon_{ij} \triangleq \frac{1}{2}\left(u_{i,j} + u_{j,i} + u_{k,i}\,u_{k,j}\right) \triangleq e_{ij} + \eta_{ij} \tag{2.5}$$

Note that the Green-Lagrange strain tensor is composed of the classical linear strain-displacement quantity, e_{ij}, and an additional non-linear quantity, η_{ij}.

Rotation Representation in Strain Tensor

The Green-Lagrange strain-displacement relation is occasionally referred to as the large displacement strain definition as it makes the strain tensor invariant to rigid-body motion. The reason for this, it will be shown, is that the Green-Lagrange strain tensor captures first order rotation information. It will also be shown that small displacements and small strains are not a sufficient condition to justify the use of the classical strain-displacement relation. Rather, it will be found necessary to evaluate the relative magnitudes of the strains and rotations.

For an infinitesimal element subject to an elastic deformation and a rigid-body displacement there is a unique rotation, θ, of the coordinate frame which maintains symmetry of the strain tensor. This is readily appreciated in two dimensions as portrayed in Figure 2-1. For the two dimensional planar case, the rotation angle is

given by, [45]

$$\theta = \tan^{-1} \frac{\frac{\delta u_2}{\delta x_1} - \frac{\delta u_1}{\delta x_2}}{2 + \frac{\delta u_1}{\delta x_1} + \frac{\delta u_2}{\delta x_2}} \tag{2.6}$$

but for small strains $\frac{\delta u_1}{\delta x_1}$ and $\frac{\delta u_2}{\delta x_2}$ are much less than 1 so that the rotation is described by

$$\theta \doteq \omega_{21} \triangleq \frac{1}{2}\left(\frac{\delta u_2}{\delta x_1} - \frac{\delta u_1}{\delta x_2}\right) \tag{2.7}$$

Similarly, for the three dimensional case we can define a rotation tensor ω_{ij},

$$\omega_{ij} \triangleq \frac{1}{2}\left(\frac{\delta u_i}{\delta x_j} - \frac{\delta u_j}{\delta x_i}\right) \tag{2.8}$$

Note that there are only three rotations as $\omega_{ij} \equiv 0$ for $i = j$.

Based on the work of Novohilov [47], it is possible to write the Green-Lagrange strain tensor of Equation (2.5) exactly in terms of the classical strain tensor e_{ij} of Equation (2.3), and the rotation tensor ω_{ij} of Equation (2.8),

$$\begin{aligned}
\epsilon_{11} &= e_{11} + \tfrac{1}{2}\left[e_{11}^2 + \left(\tfrac{1}{2}e_{12} + \omega_{21}\right)^2 + \left(\tfrac{1}{2}e_{13} - \omega_{13}\right)^2\right] \\
\epsilon_{22} &= e_{22} + \tfrac{1}{2}\left[e_{22}^2 + \left(\tfrac{1}{2}e_{12} - \omega_{21}\right)^2 + \left(\tfrac{1}{2}e_{23} + \omega_{32}\right)^2\right] \\
\epsilon_{33} &= e_{33} + \tfrac{1}{2}\left[e_{33}^2 + \left(\tfrac{1}{2}e_{13} + \omega_{13}\right)^2 + \left(\tfrac{1}{2}e_{23} - \omega_{32}\right)^2\right] \\
\epsilon_{12} &= e_{12} + e_{11}\left(\tfrac{1}{2}e_{12} - \omega_{21}\right) + e_{22}\left(\tfrac{1}{2}e_{12} + \omega_{21}\right) + \left(\tfrac{1}{2}e_{13} - \omega_{13}\right)\left(\tfrac{1}{2}e_{23} + \omega_{32}\right) \\
\epsilon_{13} &= e_{13} + e_{11}\left(\tfrac{1}{2}e_{13} + \omega_{13}\right) + e_{33}\left(\tfrac{1}{2}e_{13} - \omega_{13}\right) + \left(\tfrac{1}{2}e_{12} + \omega_{21}\right)\left(\tfrac{1}{2}e_{23} - \omega_{32}\right) \\
\epsilon_{23} &= e_{23} + e_{22}\left(\tfrac{1}{2}e_{23} - \omega_{32}\right) + e_{33}\left(\tfrac{1}{2}e_{23} + \omega_{32}\right) + \left(\tfrac{1}{2}e_{12} - \omega_{21}\right)\left(\tfrac{1}{2}e_{13} + \omega_{13}\right)
\end{aligned} \tag{2.9}$$

Since the rotation tensor is anti-symmetric, i.e. $\omega_{ij} = -\omega_{ji}$, and the linear strain term is symmetric, i.e. $e_{ij} = e_{ji}$, we are able to write Equation (2.10) in the following more general tensor notation,

$$\begin{aligned}
\epsilon_{ii} &= e_{ii} + \tfrac{1}{2}\left[e_{ii}^2 + \left(\tfrac{1}{2}e_{ij} + \omega_{ji}\right)^2\right] \; ; \;\; i \neq j \\
\epsilon_{ij} &= e_{ij} + e_{ii}\left(\tfrac{1}{2}e_{ij} - \omega_{ji}\right) + e_{jj}\left(\tfrac{1}{2}e_{ij} + \omega_{ji}\right)
\end{aligned} \tag{2.10}$$

$$+\left(\tfrac{1}{2}e_{ik}+\omega_{ki}\right)\left(\tfrac{1}{2}e_{jk}+\omega_{kj}\right)\ ;\ \ i\neq j;\, i\neq k;\, j\neq k$$

Neglecting the squares of the strains yields the more compact form,

$$\begin{aligned}\epsilon_{ii} &= e_{ii}+\tfrac{1}{2}\left[e_{ij}\omega_{ji}+\omega_{ji}^2\right]\ ;\ \ i\neq j\\ \epsilon_{ij} &= e_{ij}-e_{ii}\omega_{ji}+e_{jj}\omega_{ji}+\tfrac{1}{2}\left(e_{ik}\omega_{ki}+e_{jk}\omega_{kj}\right)\\ &\quad +\omega_{ki}\omega_{kj}\ ;\ \ i\neq j;\, i\neq k;\, j\neq k\end{aligned} \tag{2.11}$$

Clearly, the Green-Lagrange strain tensor captures not only the classical, pure deformation, small displacement strain but also the strain–rotation terms and second order rotation terms. These terms cannot necessarily be neglected by the sole condition of small displacements, i.e. rotations $\omega_{ij} \ll 1$, as the rotations must also be small compared to the linear strain terms, i.e. $\omega_{ij} \ll e_{ij}$. For massive bodies the first condition implies the second [47]. The need to include the non-linear terms is thus most important for slender flexible bodies, where the extension in directions 1 or 2 is small compared to the remaining direction(s), e.g. rods, beams, plates and shells.

Having found that the Green-Lagrange strain tensor captures element rotation information and that the non-linearity is not only a concern in the case of large displacements (as suggested by the often-used name for the tensor) but also in the case of small rotations of magnitude comparable to the small strains, we now examine how the non-linear strain terms lead to a stiffness perturbation in the presence of initial stress.

It is interesting to note that the non-linear strain description described here is essentially a description of elemental rotations superimposed on the linear strains and that by incorporating this strain description in the derivation of the system property matrices the effect of gravitational loading will be captured. There is thus a strong parallel with the work of Rey et al. [32] on the effects of gravity on the dynamic performance of structural sensors or actuators where dynamic rotation of the device in

a gravity field was the fundamental mechanism by which gravity perturbed the system dynamics (this work is detailed in Chapter 4). Due to the discrete nature of the sensor or actuator rotation a discrete non-dimensional ratio describing the magnitude of the gravity effect was easily derived [32], but since stress stiffening of the structure is a distributed effect it is not possible to similarly identify a unique non-dimensional ratio without integration. Since such an integration is already incorporated in the stiffness matrix computation it is possible to identify meaningful non-dimensional gravity effect sensitivity ratios for discrete finite elements. This topic is addressed in Sections 2.3.4 and 2.4.4 in the context of a beam element.

Incremental Formulation of Static Equilibrium

Introducing the non-linear strain definition will lead to stiffnesses K which are a function of the displacements U and the initial stresses $\mathcal{T}$ which in turn are both functions of the loading R. We are thus faced with a static problem of the form,

$$K\,(\,U(R),\mathcal{T}(R)\,)\;U = R \tag{2.12}$$

To solve this non-linear problem it is best to proceed by small load increments which will ensure that in the case of multiple solutions the solution converged to is the correct equilibrium [35].

It is therefore useful at this point to introduce the concept of an incremental analysis which will allow us to solve the non-linear principle of virtual work equilibrium statement in terms of known initial conditions and an unknown increment. This approach will make clear the need to redefine the reference structure in the event of finite deflections.

In the incremental formulation, it is necessary to identify the time at which a quantity or tensor is evaluated (denoted herein with a left *superscript*) and the equilibrium configuration co-ordinate frame used as a reference (denoted herein with a left *subscript* if different from the left superscript). Given that the gravitational load is

constant or static its application in increments makes the problem artificially dynamic. The time variable t is thus a dummy variable. In a Total Lagrangian (T.L.) formulation the reference configuration is the initial configuration so that Equation (2.5) is written as

$$ {}^{t+\Delta t}_{t}\epsilon_{ij} = \frac{1}{2}\left({}^{t+\Delta t}_{0}u_{i,j} + {}^{t+\Delta t}_{0}u_{j,i} + {}^{t+\Delta t}_{0}u_{k,i}\,{}^{t+\Delta t}_{0}u_{k,j}\right) = {}^{t+\Delta t}_{0}e_{ij} + {}^{t+\Delta t}_{0}\eta_{ij} \tag{2.13} $$

In an Updated Lagrangian (U.L.) formulation the reference configuration is the equilibrium configuration at the previous increment so that Equation (2.5) now takes the form

$$ {}^{t+\Delta t}_{t}\epsilon_{ij} = \frac{1}{2}\left({}^{t+\Delta t}_{t}u_{i,j} + {}^{t+\Delta t}_{t}u_{j,i} + {}^{t+\Delta t}_{t}u_{k,i}\,{}^{t+\Delta t}_{t}u_{k,j}\right) = {}^{t+\Delta t}_{t}e_{ij} + {}^{t+\Delta t}_{t}\eta_{ij} \tag{2.14} $$

Both of these approaches yield the same result in theory [45]. For conciseness a single Δt subscript will be used to indicate the evaluation of an incremental quantity about t at $t + \Delta t$. The U.L. strain-displacement relation is thus written as

$$ {}^{t+\Delta t}_{t}\epsilon_{ij} = \frac{1}{2}\left({}_{\Delta t}u_{i,j} + {}_{\Delta t}u_{j,i} + {}_{\Delta t}u_{k,i}\,{}_{\Delta t}u_{k,j}\right) = {}_{\Delta t}e_{ij} + {}_{\Delta t}\eta_{ij} \tag{2.15} $$

The Updated Lagrangian formulation will be used in this development as it more clearly separates the stress stiffening effect from the initial deformation effect. In the U.L. formulation, the strains are obtained by differentiation with respect to the configuration at time t, and the system property matrices are obtained by integration over the configuration volume at time t, which simplifies the strain-displacement relationship. To transform the K matrix of the deformed structure to global coordinates a projection is required but in the case of the Total Lagrangian formulation this effect is captured in a more complex strain-displacement relation (B_L) obscuring the difference between the stress stiffening effect and the initial deformation effect. This will be further described in section 2.1.3.

To formulate the expression for the internal virtual work we require the stress measure which is the energy conjugate of the Green-Lagrange strain measure. This stress tensor is the 2nd Piola-Kirchhoff stress tensor, [45],

$$ {}^{t}_{0}S_{ij} \triangleq \frac{{}^{o}\rho}{{}^{t}\rho}\left(\frac{\delta^0 x_i}{\delta^t x_m}\,{}^{t}\mathcal{T}_{mn}\,\frac{\delta^0 x_j}{\delta^t x_n}\right) \triangleq \frac{{}^{o}\rho}{{}^{t}\rho}\left({}^{0}_{t}x_{i,m}\,{}^{t}\mathcal{T}_{mn}\,{}^{0}_{t}x_{j,n}\right) \tag{2.16} $$

where the change in material density due to volumetric changes is captured by the density ratio ${}^{o}\rho/{}^{t}\rho$. That the Green-Lagrange strain tensor and 2nd Piola-Kirchhoff stress tensor are energetically conjugate implies, [45]

$$ \int_{{}^{t}V} {}^{t+\Delta t}_{t}S_{ij}\,{}^{t+\Delta t}_{t}\bar{\epsilon}_{ij}\,{}^{t}dV = \int_{{}^{t+\Delta t}V} {}^{t+\Delta t}\mathcal{T}_{mn}\,{}^{t+\Delta t}\bar{e}_{mn}\,{}^{t+\Delta t}dV \tag{2.17} $$

i.e. the internal virtual work of the configuration at $t+\Delta t$ defined about the configuration at time t with the Piola-Kirchhoff stress measure and the Green-Lagrange strain measure is equal to the internal virtual work per unit current volume at time $t+\Delta t$ using the small displacement stress and strain measures.

To capture the effects of the gravitational loading it is necessary to consider the equilibrium of the initially stressed body in a deformed configuration which may include non-negligible rotations. The principle of virtual work must therefore be applied at time $t+\Delta t$ with the body in an unknown configuration. From Equation (2.2) the equilibrium equation we are therefore trying to reduce to matrix form is

$$ \int_{{}^{t+\Delta t}V} {}^{t+\Delta t}\mathcal{T}_{ij}\,{}^{t+\Delta t}\bar{e}_{ij}\,{}^{t+\Delta t}dV = {}^{t+\Delta t}\mathcal{R} \tag{2.18} $$

The above expression cannot be evaluated since the volume is unknown at time $t+\Delta t$. To capture the effects of small rotations in the presence of initial stresses we rewrite Equation (2.18) using the Green-Lagrange strain tensor and the Piola-Kirchhoff stress tensor. From Equations (2.17) and (2.18) the equilibrium of the deformed body at

time $t + \Delta t$ can be written in terms of the known configuration at time t as,

$$\int_{{}^tV} {}^{t+\Delta t}_{t}S_{ij}\, {}^{t+\Delta t}_{t}\overline{\epsilon}_{ij}\, {}^{t}dV = {}^{t+\Delta t}\mathcal{R} \tag{2.19}$$

Incremental Decomposition of Stresses and Strains

To solve the general non-linear large displacement problem described by Equation (2.19) the stress and strain components can be decomposed into *known* initial quantities at time t and *unknown* increments denoted by a left subscript Δt. The 2nd Piola-Kirchhoff stress tensor becomes

$${}^{t+\Delta t}_{t}S_{ij} = {}^{t}_{t}S_{ij} + {}_{\Delta t}S_{ij} = {}^{t}\mathcal{T}_{ij} + {}_{\Delta t}S_{ij} \tag{2.20}$$

and the Green-Lagrange strain tensor is given by

$${}^{t+\Delta t}_{t}\epsilon_{ij} \;=\; {}_{\Delta t}e_{ij} + {}_{\Delta t}\eta_{ij} \tag{2.21}$$

It is important to note here that the stress tensor has both an initial value component and an incremental component, whereas the strain is by its very definition uniquely described by an increment about a known reference, (i.e. ${}^{t}_{t}\epsilon_{ij} \equiv 0$). It is also of note that the known initial Piola-Kirchhoff stress tensor at time t is equivalent to the Cauchy stress tensor, (i.e. ${}^{t}_{t}S_{ij} \equiv {}^{t}\mathcal{T}_{ij}$), based on Equation (2.16).

Making use of the incremental relations we can rewrite Equation (2.19) as

$$\int_{{}^tV} \left({}_{\Delta t}\overline{e}_{ij} + {}_{\Delta t}\overline{\eta}_{ij}\right) \left({}^{t}\mathcal{T}_{ij} + {}_{\Delta t}S_{ij}\right) {}^{t}dV = {}^{t+\Delta t}\mathcal{R} \tag{2.22}$$

Rearranging, we have

$$\int_{{}^tV} {}_{\Delta t}S_{ij} \left({}_{\Delta t}\overline{e}_{ij} + {}_{\Delta t}\overline{\eta}_{ij}\right) {}^{t}dV + \int_{{}^tV} {}^{t}\mathcal{T}_{ij}\, {}_{\Delta t}\overline{\eta}_{ij}\, {}^{t}dV = {}^{t+\Delta t}\mathcal{R} - \int_{{}^tV} {}^{t}\mathcal{T}_{ij}\, {}_{\Delta t}\overline{e}_{ij}\, {}^{t}dV \tag{2.23}$$

Making use of the constitutive relation

$$ {}_{\Delta t}S_{ij} = C_{ijrs}\,{}^{t+\Delta t}_{t}\epsilon_{ij} \tag{2.24} $$

we are able to substitute incremental strains for the incremental stresses to obtain

$$ \int_{tV} C_{ijrs}\left({}_{\Delta t}e_{ij} + {}_{\Delta t}\eta_{ij}\right)\left({}_{\Delta t}\overline{e}_{ij} + {}_{\Delta t}\overline{\eta}_{ij}\right)\,{}^{t}dV + \int_{tV} {}^{t}\mathcal{T}_{ij}\,{}_{\Delta t}\overline{\eta}_{ij}\,{}^{t}dV = {}^{t+\Delta t}\mathcal{R} - \int_{tV} {}^{t}\mathcal{T}_{ij}\,{}_{\Delta t}\overline{e}_{ij}\,{}^{t}dV \tag{2.25} $$

Expanding Equation (2.25) yields the sought-after general incremental principle of virtual work equilibrium expression,

$$ \begin{aligned} \int_{tV} {}_{\Delta t}e_{ij}\,C_{ijrs}\,{}_{\Delta t}\overline{e}_{ij}\,{}^{t}dV \;+\; & \\ \int_{tV} {}_{\Delta t}\eta_{ij}\,C_{ijrs}\,{}_{\Delta t}\overline{e}_{ij}\,{}^{t}dV + \int_{tV} {}_{\Delta t}e_{ij}\,C_{ijrs}\,{}_{\Delta t}\overline{\eta}_{ij}\,{}^{t}dV \;+\; & \\ \int_{tV} {}_{\Delta t}\eta_{ij}\,C_{ijrs}\,{}_{\Delta t}\overline{\eta}_{ij}\,{}^{t}dV \;+\; & \\ \int_{tV} {}^{t}\mathcal{T}_{ij}\,{}_{\Delta t}\overline{\eta}_{ij}\,{}^{t}dV \;=\; & {}^{t+\Delta t}\mathcal{R} - \int_{tV} {}^{t}\mathcal{T}_{ij}\,{}_{\Delta t}\overline{e}_{ij}\,{}^{t}dV \end{aligned} \tag{2.26} $$

By appropriately applying finite element modeling principles, this general incremental form of the principle of virtual work will lead to the desired system property matrices which include the effects of gravity. Notice the increasing order of the displacement derivative powers in the first four terms as the first integral contains a product of two linear strain terms, the second and third integrals contains a product of a linear strain term and a non-linear strain term, and the fourth integral contains the product of two non-linear strain terms.

Finite Element Discretization

Using interpolation functions to describe the behavior of the continuous variables x_i and u_i between the nodal points x_i^k with nodal displacements u_i^k [46,45,48], we let

$$ {}^t x_i(r) = \sum_{k=1}^{N} h_k(r)\, {}^t x^k \tag{2.27} $$

$$ {}^t u_i(r) = \sum_{k=1}^{N} h_k(r)\, {}^t u^k \tag{2.28} $$

where r identifies the point of interest in the body and the order of r depends on the type of element being derived. By appropriately assembling the displacement interpolation functions for a given element into a matrix $H^{(m)}$, their derivatives into a strain-displacement matrix $B^{(m)}$ and the incremental nodal point displacements into a vector ${}_{\Delta t}U^{(m)}$, we can describe the m^{th} element incremental displacement tensor ${}_{\Delta t}u^{(m)}$, the m^{th} element linear incremental strain tensor ${}_{\Delta t}e_{ij}^{(m)}$, and the m^{th} element non-linear incremental strain tensor ${}_{\Delta t}\eta_{ij}^{(m)}$ in matrix notation as follows

$$ {}_{\Delta t}u^{(m)} \Rightarrow \left[{}_t^t H \; {}_{\Delta t}U \right]^{(m)} \tag{2.29} $$

$$ {}_{\Delta t}e_{ij}^{(m)} \Rightarrow \left[{}_t^t B_L \; {}_{\Delta t}U \right]^{(m)} \tag{2.30} $$

$$ \begin{aligned} {}^t\mathcal{T}_{ij\,\Delta t}\eta_{ij}^{(m)} &\Rightarrow \tfrac{1}{2}\left[\left({}_t^t B_{NL} \; {}_{\Delta t}U \right)^T \mathcal{T} \left({}_t^t B_{NL} \; {}_{\Delta t}U \right) \right]^{(m)} \\ &\Rightarrow \tfrac{1}{2}\left[{}_{\Delta t}U^T \, {}_t^t B_{NL}^T \, \mathcal{T} \, {}_t^t B_{NL} \; {}_{\Delta t}U \right]^{(m)} \end{aligned} \tag{2.31} $$

where $\mathcal{T}$ is an appropriate arrangement of the stress terms. The form of the H, B_L, B_{NL} and $\mathcal{T}$ matrices are dependent on the specific type of finite element being modeled. In section 2.2 a beam element is studied in greater detail and the specific forms of H, B and $\mathcal{T}$ are made apparent.

Taking the first variation of Equation (2.30) and Equation (2.31) yields

$$ {}_{\Delta t}\overline{e}_{ij}^{(m)} \Rightarrow \left[{}^{t}_{t}B_{L}\, {}_{\Delta t}\overline{U} \right]^{(m)} \tag{2.32} $$

$$ {}^{t}\mathcal{T}_{ij\,\Delta t}\overline{\eta}_{ij}^{(m)} \Rightarrow \left[{}_{\Delta t}\overline{U}^{T}\, {}^{t}_{t}B^{T}_{NL}\, \mathcal{T}\, {}^{t}_{t}B_{NL}\, {}_{\Delta t}U \right]^{(m)} \tag{2.33} $$

Note that applying the chain rule to Equation (2.31) results in a matrix product of both the variation in U and the actual U. Substituting Equations (2.30), (2.31), (2.32) and (2.33) into the general incremental principle of virtual work equilibrium statement Equation (2.27), yields

$$ \begin{aligned} {}_{\Delta t}\overline{U}^{T\,(m)} \left[\int_{{}_{t}V} B^{T}_{L}\, {}^{t}C\, B_{L}\, {}^{t}dV \right]^{(m)} {}_{\Delta t}U^{(m)} \; + \\ {}_{\Delta t}\overline{U}^{T\,(m)} \left[\int_{{}_{t}V} \left(B^{T}_{L}\, {}^{t}C\, \left({}_{\Delta t}U^{T}\, B^{T}_{NL}\, B_{NL} \right) + \left(B^{T}_{NL}\, B_{NL}\, {}_{\Delta t}U \right)\, {}^{t}C\, B_{L} \right) {}^{t}dV \right]^{(m)} {}_{\Delta t}U^{(m)} \; + \\ {}_{\Delta t}\overline{U}^{T\,(m)} \left[\int_{{}_{t}V} B^{T}_{NL}\, B_{NL}\, {}_{\Delta t}U\, {}^{t}C\, {}_{\Delta t}U^{T}\, B^{T}_{NL}\, B_{NL}\, {}^{t}dV \right]^{(m)} {}_{\Delta t}U^{(m)} \; + \\ {}_{\Delta t}\overline{U}^{T\,(m)} \left[\int_{{}_{t}V} B^{T}_{NL}\, \mathcal{T}\, B_{NL}\, {}^{t}dV \right]^{(m)} {}_{\Delta t}U^{(m)} \; = \\ {}_{\Delta t}\overline{U}^{T\,(m)}\, {}^{t+\Delta t}R^{(m)} - {}_{\Delta t}\overline{U}\, {}^{t}F^{(m)} \end{aligned} \tag{2.34} $$

where

$$ {}^{t}F^{(m)} = \left[\int_{{}_{t}V} B_{L}\, \mathcal{T}\, {}^{t}dV \right]^{(m)} \tag{2.35} $$

and

$$ \begin{aligned} {}^{t+\Delta t}R^{(m)} &= \left[\int_{{}_{0}V} H^{T}\, {}^{t+\Delta t}_{0}f^{B}\, {}^{0}dV + \int_{{}_{0}V} H^{S\,T}\, {}^{t+\Delta t}_{0}f^{S}\, {}^{0}dS \right]^{(m)} \\ &= {}^{t+\Delta t}R_{B}^{(m)} + {}^{t+\Delta t}R_{S}^{(m)} \end{aligned} \tag{2.36} $$

For deformation-independent loading such as gravitational loading we are able to reference the loading to the initial configuration as was done in Equation (2.36). Note that this is not admissible in the case of "follower" forces (i.e. non-conservative

forces where the direction of application of the force "follows" or is dependent on the instantaneous orientation of the body at the point of application).

The transition from an elemental equilibrium to an equilibrium of the finite element assemblage is straightforward. The virtual displacement theorem is repeatedly invoked by imposing unit virtual displacements at each of the displacement components in turn. This is equivalent to letting ${}_{\Delta t}\overline{U} = I$ where I is the identity matrix. The m superscript is thus dropped from the H and B matrices and the local element nodal displacement vector $U^{(m)}$ becomes the global nodal displacement vector U.

We are now in a position to identify the different global stiffness matrices. In Equation (2.34), each left-hand-side term corresponds to a stiffness term as it weights a displacement to balance a force. The left-hand-side terms in square brackets therefore correspond to stiffness matrices and we can write the static equilibrium as follows,

$$ {}^{t}\left[K_o + K_1(\Delta U) + K_2(\Delta U^2) + K_g(\mathcal{T})\right] \Delta U = {}^{t+\Delta t}R - {}^{t}F \tag{2.37} $$

The matrix K_o is the classical stiffness matrix, K_1 and K_2 are first order and second order functions of the displacement increments (sometimes referred to as the initial displacement matrices [49]) and K_g is the sought after geometric stiffness matrix which is uniquely a function of the initial stress state.

Linearization of Discrete Incremental Equilibrium Expression

As the stiffness matrices of Equation (2.37) weight an incremental displacement they clearly combine to represent a tangential stiffness, denoted hereafter by K_T, at a given equilibrium point or configuration. A numerically efficient method of solving the non-linear equation is to linearize and iterate at each increment until the error due to linearization is negligible. Assuming a constant stress state over the increment, a constant tangent stiffness matrix K_T is obtained by dropping the K_1 and K_2, i.e.

$$ {}^{t}K_T = K_o + K_g({}^{t}\mathcal{T}_{ij}) \tag{2.38} $$

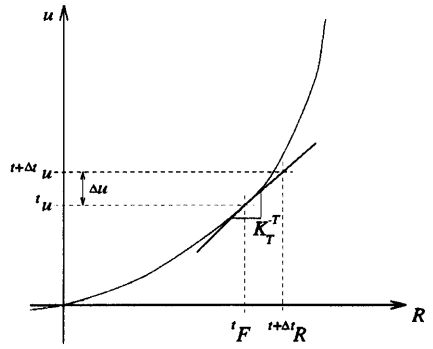

Figure 2-2: Geometric Interpretation of Incremental Solution Equation

$$^{t}[K_T(\mathcal{T})]\,\Delta U \;=\; ^{t+\Delta t}R - {}^{t}F \tag{2.39}$$

To recognize the trivial structure of Equation (2.39) it is helpful to use a geometric interpretation of the force-stiffness curve in two dimensions, i.e. for a single degree of freedom system. The latter is portrayed in Figure 2-2. Note the error in the linear predicted displacement $^{t+\Delta t}u$ under loading $^{t+\Delta t}\mathcal{R}$.

Iterative Solution of Discrete Incremental Equilibrium Expression

To eliminate the error incurred by linearization one typically solves for the zeroes, i.e. the incremental displacement, in the following system of equations where the right hand side approximates the error in the predicted response. The error expression is formed by taking the difference between the applied external loads and the resulting internal nodal loads both at time $t + \Delta t$. Iterations are performed on the system of equations until $\Delta U^{(i)} \Rightarrow 0$, i.e.

$$\begin{aligned} ^{t}K_T\Delta U^{(i)} &= {}^{t+\Delta t}R - {}^{t+\Delta t}F^{(i-1)} \\ {}^{t+\Delta t}U^{(i)} &= {}^{t+\Delta t}U^{(i-1)} + \Delta U^{(i)} \end{aligned} \tag{2.40}$$

where

$$^{t+\Delta t}F^{(i-1)} = \int_{^{t+\Delta t}V} B_L\, {}^{t+\Delta t}\mathcal{T}^{(i-1)}\, {}^{t+\Delta t}dV \tag{2.41}$$

Note that the nodal loads at time $t + \Delta t$ are approximated by using the result of a previous iteration where ${}^{t+\Delta t}\mathcal{T}^{(i-1)}$ is a function of ${}^{t+\Delta t}U^{(i-1)}$. This corresponds to a Newton-Raphson root-finding approach. More efficient methods such as the modified Newton-Raphson approach only update the system stiffness matrix with each load increment rather than for each iteration. The choice of solution method will not be further discussed as it is not particular to the modeling of gravity effects. Reference [50] can be consulted for a thorough comparison of the computational effectiveness of a variety of solution procedures for geometrical nonlinear structural analysis.

Mass Matrix Derivation

As with any static equilibrium analysis, extending the results to a dynamic equilibrium requires "only" including inertia effects. Thus, we now seek to identify the mass matrix description. Using d'Alembert's principle we augment the body force vector with the inertial load terms in nodal coordinates

$$ {}^{t+\Delta t}R_B = {}^{t+\Delta t}R_b - \int_{t+\Delta t V} \left({}^{t+\Delta t}\rho H \, {}^{t+\Delta t}\ddot{U} \right) \, {}^{t+\Delta t}dV \tag{2.42} $$

Given a fixed mass per unit volume we can express the inertial loading in terms of the original volume and density [45], i.e.

$$ \int_{t+\Delta t V} \left({}^{t+\Delta t}\rho H \, {}^{t+\Delta t}\ddot{U} \right) \, {}^{t+\Delta t}dV = \int_{{}^0V} {}^{0}\rho H \, {}^{t+\Delta t}\ddot{U} \, {}^{0}dV \tag{2.43} $$

The practical consequence of this is that by using isoparametric finite elements where the displacement interpolation functions are the same as the position interpolation functions the mass matrix need not be updated in an incremental analysis. Discretizing the acceleration by taking the second derivative of Equation (2.29) and assembling as was done for the incremental displacement yields the following linearized equilib-

rium statement,

$$\left[{}^{t}K_o + {}^{t}K_g({}^{t}\mathcal{T})\right]\Delta U = \int_{{}^{0}V} H^T \left({}^{t+\Delta t}_{0}f^B - {}^{o}\rho\, {}^{t+\Delta t}\ddot{U}\right) {}^{0}dV + {}^{t+\Delta t}R_s + {}^{t}F \qquad (2.44)$$

or

$$M\, {}^{t+\Delta t}\ddot{U} + \left[{}^{t}K_o + {}^{t}K_g({}^{t}\mathcal{T})\right]\Delta U = {}^{t+\Delta t}R_b + {}^{t+\Delta t}R_s + {}^{t}F \qquad (2.45)$$

where

$$M = {}^{o}\rho \int_{{}^{0}V} H^T H\, {}^{0}dV \qquad (2.46)$$

and R_b does not include inertial body forces.

Eigenproblem Formulation

Recall that the objective of this entire development is to formulate the small displacement eigenproblem $M\ddot{U} + KU = 0$ which captures the effects of gravitational loading. Since

$${}^{t+\Delta t}\ddot{U} = ({}^{t}\ddot{U} + \Delta\ddot{U}) \qquad (2.47)$$

we can rewrite Equation (2.45) as follows,

$$M\Delta\ddot{U} + \left[{}^{t}K_o + {}^{t}K_g\right]\Delta U = {}^{t+\Delta t}R_b + {}^{t+\Delta t}R_s + {}^{t}F + M\, {}^{t}\ddot{U} \qquad (2.48)$$

For a static configuration at time t we have the following eigensystem equation

$$M\Delta\ddot{U} + \left[{}^{t}K_o + {}^{t}K_g\right]\Delta U = 0 \qquad (2.49)$$

To yield the desired eigensystem form where the displacements represent small displacements about the deformed configuration we redefine the reference structure by letting $\Delta U \equiv U$ to obtain

$$M\ddot{U} + \left[{}^{t}K_o + {}^{t}K_g\right]U = 0 \qquad (2.50)$$

where, from Equation (2.34) and Equation (2.37)

$$\begin{aligned} {}^{t}K_o &= \int_{{}^{t}V} {}^{t}B_L^T \, {}^{t}C \, {}^{t}B_L \, {}^{t}dV \\ {}^{t}K_g &= \int_{{}^{t}V} {}^{t}B_{NL}^T \, T \, {}^{t}B_{NL} \, {}^{t}dV \end{aligned} \tag{2.51}$$

The solution for the explicit terms in these matrices is described in section 2.2.

2.1.3 Stress Stiffening and Initial Deformation Effect

We now identify the separate stress stiffening and initial deformation effects. Recall that an isoparametric element based mass matrix M is invariant to the choice of reference configuration when using an Updated Lagrangian formulation [45]. The displacements and the stiffness matrices on the other hand are given with respect to the deformed equilibrium configuration so that Equation (2.50) may be written as

$$M\ddot{U} + \left[{}_{t}^{t}K_o + {}_{t}^{t}K_g\right] U = 0 \tag{2.52}$$

More generally, if isoparametric elements are not used we have

$${}_{t}^{t}M\ddot{U} + \left[{}_{t}^{t}K_o + {}_{t}^{t}K_g\right] U = 0 \tag{2.53}$$

or

$${}_{t}^{t}M\,{}^{t}\ddot{U} + {}_{t}^{t}K_T U = 0 \tag{2.54}$$

Taking the Laplace transform yields

$$\left(s^2 \, {}_{t}^{t}M + {}_{t}^{t}K_T\right) U = 0 \tag{2.55}$$

To compare the eigenvectors and the system property matrices of the stressed and deformed structure with those of the unstressed and undeformed configuration it is necessary to express ${}_{t}^{t}M$ and ${}_{t}^{t}K_o$ in the global co-ordinates used for the original ${}_{o}^{o}M$

and ${}^{o}_{o}K_T$. This is achieved using a standard orthogonal rotation matrix for each element denoted here by $T^{(m)}$. Thus, given

$$T^{(m)}\,{}^{t}x^{(m)} = {}^{0}x^{(m)} \quad \text{or} \quad {}^{t}x^{(m)} = T^{(m)^{-1}}\left({}^{0}x^{(m)}\right) \tag{2.56}$$

we have

$${}^{t}U^{(m)} = T^{(m)^{-1}}\left({}^{o}U^{(m)}\right) \quad \text{and} \quad {}^{t}\ddot{U}^{(m)} = T^{(m)^{-1}}\left({}^{o}\ddot{U}^{(m)}\right) \tag{2.57}$$

so that for a single element

$$\left(s^2\,T^{(m)^T}\left[{}^{t}_{t}M^{(m)}\right]T^{(m)} + T^{(m)^T}\left[{}^{t}_{t}K^{(m)}_{o} + {}^{t}_{t}K^{(m)}_{g}\right]T^{(m)}\right)T^{(m)^{-1}}\left({}^{o}U\right) = 0 \tag{2.58}$$

will yield an eigensystem which is projected onto the global coordinate reference frame. Alternatively, we can write for the assemblage

$$\left(s^2\widetilde{M} - \widetilde{K}_T\right)\widetilde{U} = 0 \tag{2.59}$$

where

$$\begin{aligned}\widetilde{M}^{(m)} &= T^{(m)^T}\left[{}^{t}_{t}M^{(m)}\right]T^{(m)} \\ &= T^{(m)^T}\left[{}^{o}\rho\int_{{}^{o}V} H^T H\,{}^{0}dV\right]^{(m)} T^{(m)}\end{aligned} \tag{2.60}$$

and

$$\begin{aligned}\widetilde{K}^{(m)}_{T} &= T^{(m)^T}\left[{}^{t}_{t}K^{(m)}_{o} + {}^{t}_{t}K^{(m)}_{g}\right]T^{(m)} \\ &= T^{(m)^T}\left[\int_{{}^{t}V} {}^{t}B^{T}_{L}\,{}^{t}C\,{}^{t}B_{L}\,{}^{t}dV + \int_{{}^{t}V} {}^{t}B^{T}_{NL}\,\mathcal{T}\,{}^{t}B_{NL}\,{}^{t}dV\right]^{(m)} T^{(m)}\end{aligned} \tag{2.61}$$

Highlighted thus by Equation (2.58) or by Equations (2.59), (2.61) and (2.62) are the two separate effects of gravitational loading: the stress stiffening effect, K_g, and the initial deformation effect captured by the T transformation and projection. Note

that only in an Updated Lagrangian formulation can the transformation effect of the initial deformations on the structure be identified separately from the stress stiffening effect, K_g. In the Total Lagrangian formulation the transformation T is embedded in the formulation of the system property matrices since the displacements and strains are always referred to the original configuration.

Having described the *general formulation* and *origin* of the stress stiffening and initial deformation effects, the next section focuses on the more explicit formulation for a beam element. This in turn makes it possible to examine the *effects* of stress stiffening and initial deformation on the eigensystem of beam or beam-type structures in Sections 2.3 and 2.4.

2.2 Beam Element Formulation

In this section we examine more closely the derivation of the system matrices for a beam element and focus in particular on deriving expressions for the constituent matrices of Equation (2.51) which describes the formulation of the regular and geometric stiffness matrices. Our first objective is to compare the geometric stiffness matrix K_g, which captures the stress stiffening effects of gravity, with the original stiffness matrix K_o for a beam element.

This work will focus on the beam element, as it is the most appropriate element for describing the constituent elements of those types of slender flexible spacecraft structures which are most susceptible to gravity effects. The beam element describes axial or rod behavior, bending in two planes, and torsion. Shear is not considered herein as it is almost always negligible for the slender type of structural elements we are interested in. To simplify the identification of gravity effects, this analysis will focus on beams of rectangular cross-section which are straight and have a constant cross-sectional area.

In this section we briefly repeat the well-known formulation of the traditional

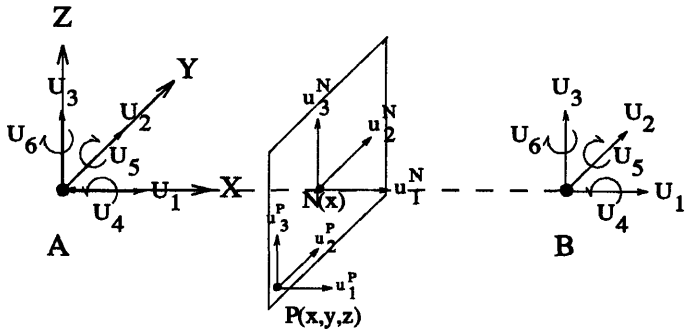

Figure 2-3: Beam Element Reference Axes and Co-ordinate Notation

stiffness matrix before deriving a closed-form expression for an incremental geometric stiffness matrix making use of the generalized notation of Cook [48]. A comparison is made with Yang's closed form expression for K_g and weaknesses of Cook's generalized notation are highlighted before extending his work and the work of Yang and McGuire [28, 29] to allow for distributed forces between the concentrated nodal loads. The approach adopted here, unlike Bathe's numerical integration approach (which is well suited to computational implementation) is to derive the general expression for the incremental geometric stiffness matrix in symbolic terms for analytical purposes.

2.2.1 Beam Element Fundamentals

The beam element derived here is a 2 node beam with 3 nodal translations (U_1, U_2, U_3) and 3 nodal rotations (U_4, U_5, U_6) at each node A and B. As can be seen in figure 2-3 the neutral axis coincides with the X axis of the local XYZ reference frame. The position of any point P throughout the beam is given by (x, y, z). The displacements of a point N on the neutral axis are denoted by $u_i^N(x)$ and rotation of the normal plane about the neutral axis at N is denoted by $\theta_x^N(x)$. The translational displacements of all points P are denoted by $u_i^P(x, y, z)$.

The displacements of any point along the neutral axis and the rotation of any cross-section about the neutral axis can be interpolated from the description of the

nodal displacements, i.e.

$$\begin{bmatrix} u_1^N(x) \\ u_2^N(x) \\ u_3^N(x) \\ \theta_x^N(x) \end{bmatrix} = \left[\begin{array}{cccccc|cccccc} H_1 & 0 & 0 & 0 & 0 & 0 & H_2 & 0 & 0 & 0 & 0 & 0 \\ 0 & H_3 & 0 & 0 & 0 & H_4 & 0 & H_5 & 0 & 0 & 0 & H_6 \\ 0 & 0 & H_3 & 0 & -H_4 & 0 & 0 & 0 & H_5 & 0 & -H_6 & 0 \\ 0 & 0 & 0 & H_1 & 0 & 0 & 0 & 0 & 0 & H_2 & 0 & 0 \end{array}\right] \mathrm{U} \tag{2.62}$$

where

$$\mathrm{U} = \left[\mathrm{U}_1^A \cdots \mathrm{U}_6^A \,\middle|\, \mathrm{U}_1^B \cdots \mathrm{U}_6^B \right]^T \tag{2.63}$$

The linear interpolation functions for the axial and torsional displacement are given by H_1 and H_2 whereas H_3, H_4, H_5 and H_6 are Hermitian functions for the interpolation of bending displacement-based on nodal displacement and slope, i.e. for a beam element of length h

$$\begin{aligned} H_1 &= 1 - (x/h) \\ H_2 &= x/h \\ H_3 &= 1 - 3(x/h)^2 + 2(x/h)^3 \\ H_4 &= \left(x/h - 2(x/h)^2 + (x/h)^3\right) h \\ H_5 &= 3(x/h)^2 - 2(x/h)^3 \\ H_6 &= \left((x/h)^3 - (x/h)^2\right) h \end{aligned} \tag{2.64}$$

Having identified the displacement interpolation matrix it is convenient at this point to present the classic Bernoulli-Euler beam element mass matrix. Performing the integration of Equation (2.46) and making use of the displacement interpolation

relations of Equation (2.64) yields [51]

$$M_o = \rho A l \left[\begin{array}{cccccc|cccccc} \frac{1}{3} & 0 & 0 & 0 & 0 & 0 & \frac{1}{6} & 0 & 0 & 0 & 0 & 0 \\ & \frac{13}{35} & 0 & 0 & 0 & \frac{11l}{210} & 0 & \frac{9}{70} & 0 & 0 & 0 & \frac{-13l}{420} \\ & & \frac{13}{35} & 0 & \frac{-11l}{210} & 0 & 0 & 0 & \frac{9}{70} & 0 & \frac{13l}{420} & 0 \\ & & & \frac{I_x}{3A} & 0 & 0 & 0 & 0 & 0 & \frac{I_x}{6A} & 0 & 0 \\ & & & & \frac{l^2}{105} & 0 & 0 & 0 & \frac{-13l}{420} & 0 & \frac{-l^2}{140} & 0 \\ & & & & & \frac{l^2}{105} & 0 & \frac{13l}{420} & 0 & 0 & 0 & \frac{-l^2}{140} \\ \hline & & & & & & m_{1\cdot1} & 0 & 0 & 0 & 0 & 0 \\ & & & & & & & m_{2\cdot2} & 0 & 0 & 0 & -m_{2\cdot6} \\ & & & & & & & & m_{3\cdot3} & 0 & -m_{3\cdot5} & 0 \\ & & \text{sym.} & & & & & & & m_{4\cdot4} & 0 & 0 \\ & & & & & & & & & & m_{5\cdot5} & 0 \\ & & & & & & & & & & & m_{6\cdot6} \end{array}\right] \tag{2.65}$$

where ρ is volumetric mass density, A is cross-sectional area, l is element length and I_x is polar moment of inertia.

Cross-section Deformation Description

In classical beam mechanics the transverse shear stress and transverse normal stresses are zero so that $\mathcal{T}_{23} = \mathcal{T}_{32} = \mathcal{T}_{22} = \mathcal{T}_{33} = 0$. Since planar sections normal to the neutral axis remain planar and normal when the element is deformed, it is possible to describe the position of any point in the beam as a function of the behavior of the neutral axis point which lies in its normal plane, i.e. for small displacements

$$\begin{aligned} u_1^P(x,y,z) &= u_1^N(x) - z\,u_{3,x}^N(x) - y\,u_{2,x}^N(x) \\ u_2^P(x,y,z) &= u_2^N(x) - z\,\theta_x^N(x) \\ u_3^P(x,y,z) &= u_3^N(x) + y\,\theta_x^N(x) \end{aligned} \tag{2.66}$$

From Equations (2.64) and (2.66) we can write the following three-dimensional displacement interpolation matrix for any point in the beam element, where a prime ($'$) indicates differentiation with respect to x,

$$u^P = \left[\begin{array}{cccccc|cccccc} H_1 & -yH_3' & -zH_3' & 0 & zH_4' & -yH_4' & H_2 & -yH_5' & -zH_6' & 0 & zH_5' & -yH_6' \\ 0 & H_3 & 0 & -zH_1 & 0 & H_4 & 0 & H_5 & 0 & -zH_2 & 0 & H_6 \\ 0 & 0 & H_3 & yH_1 & -H_4 & 0 & 0 & 0 & H_5 & yH_2 & -H_6 & 0 \end{array}\right] \mathrm{U} \tag{2.67}$$

or

$$u^P = H\,\mathrm{U} \tag{2.68}$$

where

$$u^P = \left[u_1^P(x,y,z)\ u_2^P(x,y,z)\ u_3^P(x,y,z)\right]^T \tag{2.69}$$

The matrix H can be referred to as the displacement interpolation matrix.

2.2.2 Linear and Non-linear Strain-Displacement Relations

Given the displacement field description of Equation (2.67) for any point in the beam volume we are now in a position to derive both the linear and non-linear strain-displacement matrices, B_L and B_{NL}.

Linear Strain-Displacement Relations

From the linear strain definition Equation (2.3) and the interpolation matrix definition Equation (2.67), we can write the following strain-displacement relation for the three independent strain components e_{11}^P, e_{12}^P and e_{13}^P,

$$e^P = B_L\,\mathrm{U} \tag{2.70}$$

where

$$B_L = \left[\begin{array}{cccccc|cccccc} H_1' & -yH_3'' & -zH_3'' & 0 & zH_4'' & -yH_4'' & H_2' & -yH_5'' & -zH_5'' & 0 & zH_6'' & -yH_6'' \\ 0 & 0 & 0 & \frac{-zH_1'}{2} & 0 & 0 & 0 & 0 & 0 & \frac{-zH_2'}{2} & 0 & 0 \\ 0 & 0 & 0 & \frac{yH_1'}{2} & 0 & 0 & 0 & 0 & 0 & \frac{yH_2'}{2} & 0 & 0 \end{array}\right] \tag{2.71}$$

and

$$e^P = \left[e_{11}^P(x,y,z)\ e_{12}^P(x,y,z)\ e_{13}^P(x,y,z) \right]^T \tag{2.72}$$

Non-Linear Strain-Displacement Relations

Deriving the non-linear strain-displacement matrix, B_{NL}, is not as straightforward as for the linear strain-displacement matrix, B_L, because of the non-linearity and the need to obtain the proper stress term weighting. Recall the fundamental form of the geometric stiffness virtual work integral,

$$\int_{tV} {}^t\mathcal{T}_{ij}\, {}_{\Delta t}\overline{\eta}_{ij}\, {}^t dV \tag{2.73}$$

For clarity, letting u, v, and w represent the u_1, u_2, and u_3 co-ordinates in a local XYZ frame and letting σ_x, $\mathcal{T}_{xy}$, $\mathcal{T}_{xz}$, σ_y, $\mathcal{T}_{yz}$ and σ_z represent the stresses $\mathcal{T}_{11}$, $\mathcal{T}_{12}$, $\mathcal{T}_{13}$, $\mathcal{T}_{22}$, $\mathcal{T}_{23}$ and $\mathcal{T}_{33}$ we expand the above and write

$$\begin{aligned} \tfrac{1}{2}\int_{tV} \Big(& \left(u_{,x}^2 + u_{,y}^2 + u_{,z}^2\right)\sigma_x + \left(v_{,x}^2 + v_{,y}^2 + v_{,z}^2\right)\sigma_y + \left(w_{,x}^2 + w_{,y}^2 + w_{,z}^2\right)\sigma_z + \\ & \left(u_{,x}u_{,y} + v_{,x}v_{,y} + w_{,x}w_{,y}\right)\mathcal{T}_{xy} + \left(u_{,x}u_{,z} + v_{,x}v_{,z} + w_{,x}w_{,z}\right)\mathcal{T}_{xz} + \\ & \left(u_{,y}u_{,z} + v_{,y}v_{,z} + w_{,y}w_{,z}\right)\mathcal{T}_{yz} \Big)\, {}^t dV \end{aligned} \tag{2.74}$$

We can now write a general expression in matrix form for the geometric stiffness

contribution to the virtual work using a matrix parsing based on the work of Cook [48],

$$\frac{1}{2}\int_{{}^tV} \overline{W}^T \left[\begin{array}{c|c|c} S & 0 & 0 \\ \hline 0 & S & 0 \\ \hline 0 & 0 & S \end{array}\right] W\, {}^tdV = \frac{1}{2}\int_{{}^tV} \overline{W}^T \mathcal{T} W\, {}^tdV \tag{2.75}$$

where

$$W = \left[\begin{array}{ccc|ccc|ccc} u_{,x} & u_{,y} & u_{,z} & v_{,x} & v_{,y} & v_{,z} & w_{,x} & w_{,y} & w_{,z} \end{array}\right]^T \tag{2.76}$$

and

$$S = \begin{bmatrix} \sigma_x & \mathcal{T}_{xy} & \mathcal{T}_{xz} \\ \mathcal{T}_{xy} & \sigma_y & \mathcal{T}_{yz} \\ \mathcal{T}_{xz} & \mathcal{T}_{yz} & \sigma_z \end{bmatrix} \tag{2.77}$$

The only problem with this formulation is the difficulty in dropping higher order terms embedded in the interpolation function derivatives which make up W. This will now be examined more closely in the context of a beam element formulation.

For a Bernoulli-Euler beam $\sigma_y = \sigma_z = \mathcal{T}_{yz} = 0$ so that S becomes

$$S = \begin{bmatrix} \sigma_x & \mathcal{T}_{xy} & \mathcal{T}_{xz} \\ \mathcal{T}_{xy} & 0 & 0 \\ \mathcal{T}_{xz} & 0 & 0 \end{bmatrix} \tag{2.78}$$

but for small strains $u_{,x}^2$ is negligible with respect to $u_{,x}$ so that the $(1,1)$ term of S should be made to be zero.

To separate the virtual and actual nodal displacements from the work expression we rewrite the vector of displacement partial derivatives as a function of the nodal

co-ordinates

$$W(x,y,z) = \left[\begin{array}{c|c|c} \frac{\delta}{\delta x} & 0 & 0 \\ \frac{\delta}{\delta y} & 0 & 0 \\ \frac{\delta}{\delta z} & 0 & 0 \\ \hline 0 & \frac{\delta}{\delta x} & 0 \\ 0 & \frac{\delta}{\delta y} & 0 \\ 0 & \frac{\delta}{\delta z} & 0 \\ \hline 0 & 0 & \frac{\delta}{\delta x} \\ 0 & 0 & \frac{\delta}{\delta y} \\ 0 & 0 & \frac{\delta}{\delta z} \end{array}\right] \left[\begin{array}{c} u(x,y,z) \\ v(x,y,z) \\ w(x,y,z) \end{array}\right] = (D)\,(H\,\mathrm{U}) \tag{2.79}$$

Therefore, since the work expression has the required quadratic form in U, i.e.

$$\tfrac{1}{2}\int_{tV} \overline{\mathrm{U}}^T H^T D^T \mathcal{T}\, DH\, \mathrm{U}\; {}^t dV \tag{2.80}$$

we can identify the sought after non-linear strain-displacement interpolation matrix B_{NL},

$$B_{NL} = DH \tag{2.81}$$

which is key in the definition of K_g, Equation (2.51). Thus, for the beam element,

$$B_{NL} = \left[\begin{array}{cccccc|cccccc} H_1' & -yH_3'' & -zH_3'' & 0 & zH_4'' & -yH_4'' & H_2' & -yH_5'' & -zH_5'' & 0 & zH_6'' & -yH_6'' \\ 0 & -H_3' & 0 & 0 & 0 & -H_4' & 0 & -H_5' & 0 & 0 & 0 & -H_6' \\ 0 & 0 & -H_3' & 0 & H_4' & 0 & 0 & 0 & -H_5' & 0 & H_6' & 0 \\ \hline 0 & H_3' & 0 & \frac{-zH_1'}{2} & 0 & H_4' & 0 & H_5' & 0 & \frac{-zH_2'}{2} & 0 & H_6' \\ 0 & 0 & 0 & 0 & 0 & 0 & 0 & 0 & 0 & 0 & 0 & 0 \\ 0 & 0 & 0 & -H_1 & 0 & 0 & 0 & 0 & 0 & -H_2 & 0 & 0 \\ \hline 0 & 0 & H_3' & \frac{yH_1'}{2} & -H_4' & 0 & 0 & 0 & H_5' & \frac{yH_2'}{2} & -H_6' & 0 \\ 0 & 0 & 0 & H_1 & 0 & 0 & 0 & 0 & 0 & H_2 & 0 & 0 \\ 0 & 0 & 0 & 0 & 0 & 0 & 0 & 0 & 0 & 0 & 0 & 0 \end{array}\right] \tag{2.82}$$

Note that for small strains $v_{,y}$ and $w_{,z}$ (rows 5 and 9) are identically zero.

From Equation (2.78) and Equation (2.82) we can now write the following closed-form expression for K_g in terms of the internal stress state,

$$K_g = \int_{tV} B_{NL}^T \mathcal{T} B_{NL}\, {}^tdV = \int_{tV} B_{NL}^T \left[\begin{array}{c|c|c} S & 0 & 0 \\ \hline 0 & S & 0 \\ \hline 0 & 0 & S \end{array}\right] B_{NL}\, {}^tdV \tag{2.83}$$

2.2.3 Stiffness Matrix Evaluations

Recall from Equation (2.51) the expression derived for the classic stiffness matrix,

$${}^tK_o = \int_{tV} {}^tB_L^T\, {}^tC\, {}^tB_L\, {}^tdV \tag{2.84}$$

For a uniform beam the constitutive properties are constant and the C matrix is

given by

$$C = \begin{bmatrix} E & 0 & 0 \\ 0 & G & 0 \\ 0 & 0 & G \end{bmatrix} \tag{2.85}$$

where E is Young's modulus and G is the shear modulus given by

$$G = \frac{E}{2(1+\nu)} \tag{2.86}$$

Evaluating Equation (2.84) is straightforward and yields the conventional Hermitian beam element stiffness matrix, [48, 52, 51], reproduced in Equation (2.87) for future reference.

$$K_o = \left[\begin{array}{cccccc|cccccc} \frac{EA}{l} & 0 & 0 & 0 & 0 & 0 & -k_{1\cdot1} & 0 & 0 & 0 & 0 & 0 \\ & \frac{12EI_z}{l^3} & 0 & 0 & 0 & \frac{6EI_z}{l^2} & 0 & -k_{2\cdot2} & 0 & 0 & 0 & k_{2\cdot6} \\ & & \frac{12EI_y}{l^3} & 0 & \frac{-6EI_y}{l^2} & 0 & 0 & 0 & -k_{3\cdot3} & 0 & k_{3\cdot5} & 0 \\ & & & \frac{6GJ}{5l} & 0 & 0 & 0 & 0 & 0 & -k_{4\cdot4} & 0 & 0 \\ & & & & \frac{4EI_y}{l} & 0 & 0 & 0 & -k_{3\cdot5} & 0 & \frac{2EI_y}{l} & 0 \\ & & & & & \frac{4EI_z}{l} & 0 & -k_{2\cdot6} & 0 & 0 & 0 & \frac{2EI_z}{l} \\ \hline & & & & & & k_{1\cdot1} & 0 & 0 & 0 & 0 & 0 \\ & & & & & & & k_{2\cdot2} & 0 & 0 & 0 & -k_{2\cdot6} \\ & & & & & & & & k_{3\cdot3} & 0 & -k_{3\cdot5} & 0 \\ & & \text{sym.} & & & & & & & k_{4\cdot4} & 0 & 0 \\ & & & & & & & & & & k_{5\cdot5} & 0 \\ & & & & & & & & & & & k_{6\cdot6} \end{array}\right] \tag{2.87}$$

Note that the result of Equation (2.87) is based on the assumptions of the classic Bernoulli-Euler beam and does not include shear effects or other refinements (see [53] for examples) in order to simplify the focus on gravity effects. The moment of inertia

about y and about z is denoted by I_y and I_z respectively. The St. Venant torsional constant, J, is equal to the polar moment of inertia I_x for a circular cross-section and is smaller otherwise, e.g.

$$J \approx \frac{a^3 b^3}{3(a^2 + b^2)} \tag{2.88}$$

for a narrow rectangular cross-section where a and b are width and thickness. (Consult Table 8-18 of Reference [54] for information regarding other cross-section shapes.) To interpret Equation (2.87) recall the ordering of the degrees of freedom given by Equation (2.63) and portrayed in Figure 2-3.

Evaluating Equation (2.83) to obtain the geometric stiffness matrix is significantly more complex than for the regular stiffness matrix as it requires a description of the internal stress state of the element over the entire beam length and cross-section. In modeling a space structure ground test-bed, this stress evaluation and integration computation is typically automated and forms part of the incremental analysis. In the case of the ADINA finite element modeling software, numerical integration is used with discrete stress evaluations typically at Gauss points [31].

For the purposes of studying the impact of the geometric stiffness matrix, K_g, on the tangential stiffness matrix, $K_T = K_o + K_g$, it is desirable to obtain an explicit K_g in terms of the applied loads. This requires that one either make certain assumptions concerning the applied loading or consider special loading cases. Both approaches are considered here. First we derive K_g given the assumption of concentrated loads only and applied strictly at the element nodes. This case was studied by Yang and McGuire [28] and is used to validate the different approach used here. Secondly we derive K_g for the more pertinent case of a beam element subject to concentrated nodal loads and both transverse and axial distributed loads of the same nature as gravitational loading. A similar case which included distributed loading was studied by Barsoum and Gallagher [55] but axial deformations were not considered given their focus on torsional buckling behavior.

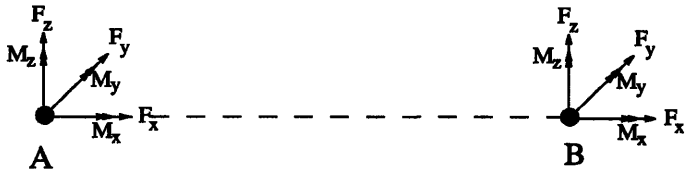

Figure 2-4: Beam Element Nodal Load Sign Convention

Concentrated Nodal Load Case

The result of the assumption of strictly concentrated nodal loads applied only at the nodal points is that the axial force, shear force and torsional moment are constant throughout the beam element while the bending moment is either constant or varies linearly in the presence of shear. Since the nodal forces of a given element must be in static equilibrium, we have,

$$\begin{aligned} F_x^B &= -F_x^A \\ F_y^B &= -F_y^A \\ F_z^B &= -F_z^A \\ M_x^B &= -M_x^A \\ M_y^B &= -M_y^A - F_z^A h \\ M_z^B &= -M_z^A + F_y^A h \end{aligned} \tag{2.89}$$

where a standard finite element static sign convention is used for the forces and moments at the element nodes, as shown in Figure 2-4, (rather than a standard mechanics deformation sign convention). Given the above nodal force relations, the continuous force and moment descriptions through-out the beam element can be written as,

$$\begin{aligned} F_x(x) &= F_x^B \\ F_y(x) &= F_y^B = -\frac{M_z^A + M_z^B}{h} \end{aligned}$$

$$
\begin{aligned}
F_z(x) &= F_z^B = \frac{M_y^A + M_y^B}{h} \\
M_x(x) &= M_x^B \qquad (2.90) \\
M_y(x) &= -M_y^A(1 - x/h) + M_y^B(x/h) \\
M_z(x) &= -M_z^A(1 - x/h) + M_z^B(x/h) \qquad (2.91)
\end{aligned}
$$

The axial stress in a Bernoulli-Euler beam element, given by

$$\sigma_x = \frac{F_x}{A} + \frac{M_y z}{I_y} + \frac{M_z y}{I_z} \qquad (2.92)$$

can thus be written in terms of nodal loads as follows

$$\sigma_x = \frac{F_x^B}{A} + \left(\frac{-M_y^A(1 - x/h) + M_y^B(x/h)}{I_y}\right) z + \left(\frac{-M_z^A(1 - x/h) + M_z^B(x/h)}{I_z}\right) y \qquad (2.93)$$

To identify the shear stress description it is necessary to make certain limiting assumptions concerning the type of beam cross-section. Assuming a narrow rectangular cross-section or a circular cross-section and assuming that there is no resistance to warping, i.e. simple St. Venant torsion, the contribution of torsion to the shear stress can be added to the stress due to shear forces to yield

$$
\begin{aligned}
\mathcal{T}_{xy} &= \frac{F_y}{A} - \frac{M_x z}{2I_y} \\
\mathcal{T}_{xz} &= \frac{F_z}{A} - \frac{M_x y}{2I_z} \qquad (2.94)
\end{aligned}
$$

In terms of nodal loads we have thus

$$
\begin{aligned}
\mathcal{T}_{xy} &= -\left(\frac{M_z^A + M_z^B}{Ah}\right) - \frac{M_x^B z}{2I_y} \\
\mathcal{T}_{xz} &= \left(\frac{M_y^A + M_y^B}{Ah}\right) + \frac{M_x^B y}{2I_z} \qquad (2.95)
\end{aligned}
$$

(recall that in the absence of shear and distributed loads $M_y^A = -M_y^B$ and $M_z^A = -M_z^B$).

Given $\sigma_x(x)$, $\mathcal{T}_{xy}(z)$ and $\mathcal{T}_{yz}(x)$ we can now compute K_g in terms of the applied nodal loads. Substituting the above stress definitions in Equation (2.78) and substituting both the result and Equation (2.82) into the K_g equation (Equation (2.83)) before performing a triple integration over the element volume yields the closed-form expression for Kg in terms of the applied nodal loads shown in Equation (2.96). By identifying those stiffness terms which are identical it is possible to write Equation (2.96) in the more compact form shown in Equation (2.97).

A comparison with the result of Yang and McGuire's special case analysis, [28], verifies that this general approach, based on Cook's general notation [48], is correct. Two minor differences are present however. The terms of the form of the $k_{2,4}$ and $k_{3,4}$ terms, i.e. M^A/l, are given by [28] as $1.1M^A/l - M^B/(10l)$, and the terms of the form of $k_{4,5}$ and $k_{4,6}$, i.e. $(M^A + M^B)/6$, are given as $M^A/10 + M^B/5$. All other terms being identical. It is concluded thus that the general approach described herein for deriving the geometric stiffness matrix of an element is sound. General observations concerning the stress stiffening effect for a loaded beam element are made in section 2.3.1 following the derivation of the distributed load case geometric stiffness matrix.

Distributed Load Case Derivation

A more appropriate set of assumptions in the study of gravity effects would be to consider a beam element subject to a stress distribution which allows for distributed forces over the length of the element in addition to concentrated nodal forces and moments. One could include uniform, linear, quadratic or other higher order distributed load distributions but to directly obtain the gravitational loading case which we are interested in, we shall apply here a uniformly distributed transverse loading in one plane only and a linearly distributed load in the axial direction, (the latter are in addition to the standard concentrated loads). The transverse distributed load

$$
K_g = \left[\begin{array}{cccccc|cccccc}
0 & \frac{M_z^A+M_z^B}{l^2} & \frac{-\left(M_y^A+M_y^B\right)}{l^2} & 0 & 0 & 0 & 0 & \frac{-\left(M_z^A+M_z^B\right)}{l^2} & \frac{M_y^A+M_y^B}{l^2} & 0 & 0 & 0 \\
 & \frac{6F_x^B}{5l} & 0 & \frac{M_y^A}{l} & \frac{C_T M_x^B}{6l} & \frac{F_x^B}{10} & \frac{-\left(M_z^A+M_z^B\right)}{l^2} & \frac{-6F_x^B}{5l} & 0 & \frac{M_y^B}{l} & \frac{-\left(C_T M_x^B\right)}{6l} & \frac{F_x^B}{10} \\
 & & \frac{6F_x^B}{5l} & \frac{M_z^A}{l} & \frac{-F_x^B}{10} & \frac{C_T M_x^B}{6l} & \frac{M_y^A+M_y^B}{l^2} & 0 & \frac{-6F_x^B}{5l} & \frac{M_z^A}{l} & \frac{-F_x^B}{10} & \frac{-\left(C_T M_x^B\right)}{6l} \\
 & & & \frac{F_x^B(I_y+I_z)}{Al} & \frac{M_z^A+M_z^B}{6} & \frac{-\left(M_y^A+M_y^B\right)}{6} & 0 & \frac{-M_y^A}{l} & \frac{-M_z^B}{l} & \frac{-F_x^B(I_y+I_z)}{Al} & \frac{-\left(M_z^A+M_z^B\right)}{6} & \frac{M_y^A+M_y^B}{6} \\
 & & & & \frac{2F_x^B l}{15} & 0 & 0 & \frac{-\left(C_T M_x^B\right)}{6l} & \frac{F_x^B}{10} & \frac{-\left(M_z^A+M_z^B\right)}{6} & \frac{-\left(F_x^B l\right)}{30} & \frac{C_T M_x^B}{12} \\
 & & & & & \frac{2F_x^B l}{15} & 0 & \frac{-F_x^B}{10} & \frac{-\left(C_T M_x^B\right)}{6l} & \frac{M_y^A+M_y^B}{6} & \frac{-\left(C_T M_x^B\right)}{12} & \frac{-\left(F_x^B l\right)}{30} \\
\hline
 & & & & & & 0 & \frac{M_z^A+M_z^B}{l^2} & \frac{-\left(M_y^A+M_y^B\right)}{l^2} & 0 & 0 & 0 \\
 & & & & & & & \frac{6F_x^B}{5l} & 0 & \frac{-M_y^B}{l} & \frac{C_T M_x^B}{6l} & \frac{-F_x^B}{10} \\
 & & & & & & & & \frac{6F_x^B}{5l} & \frac{-M_z^B}{l} & \frac{F_x^B}{10} & \frac{C_T M_x^B}{6l} \\
 & & & & & & & & & \frac{F_x^B(I_y+I_z)}{Al} & \frac{M_z^A+M_z^B}{6} & \frac{-\left(M_y^A+M_y^B\right)}{6} \\
 & & & & & & & & & & \frac{2F_x^B l}{15} & 0 \\
 & & & & & & & & & & & \frac{2F_x^B l}{15}
\end{array}\right]
\qquad (2.96)
$$

sym.

$$K_g = \left[\begin{array}{cccccc|cccccc}
0 & \frac{M_z^A+M_z^B}{l^2} & \frac{-\left(M_y^A+M_y^B\right)}{l^2} & 0 & 0 & 0 & 0 & -k_{1\cdot2} & -k_{1\cdot3} & 0 & 0 & 0 \\
 & \frac{6F_x^B}{5l} & 0 & \frac{M_y^A}{l} & \frac{C_T M_x^B}{6l} & \frac{F_x^B}{10} & -k_{1\cdot2} & -k_{2\cdot2} & 0 & -k_{8\cdot10} & -k_{2\cdot5} & k_{2\cdot6} \\
 & & k_{2\cdot2} & \frac{M_z^A}{l} & -k_{2\cdot6} & k_{2\cdot5} & -k_{1\cdot3} & 0 & -k_{2\cdot2} & -k_{9\cdot10} & -k_{2\cdot6} & -k_{2\cdot5} \\
 & & & \frac{F_x^B(I_y+I_z)}{Al} & \frac{\left(M_z^A+M_z^B\right)}{6} & \frac{-\left(M_y^A+M_y^B\right)}{6} & 0 & -k_{2\cdot4} & -k_{3\cdot4} & -k_{4\cdot4} & -k_{4\cdot5} & -k_{4\cdot6} \\
 & & & & \frac{2F_x^B l}{15} & 0 & 0 & -k_{2\cdot5} & k_{2\cdot6} & -k_{4\cdot5} & \frac{-k_{5\cdot5}}{4} & \frac{k_{2\cdot5}\,l}{2} \\
 & & & & & k_{5\cdot5} & 0 & -k_{2\cdot6} & -k_{2\cdot5} & -k_{4\cdot6} & \frac{-k_{2\cdot5}\,l}{2} & \frac{-k_{5\cdot5}}{4} \\
\hline
 & & & & & & 0 & k_{1\cdot2} & k_{1\cdot3} & 0 & 0 & 0 \\
 & & & & & & & k_{2\cdot2} & 0 & \frac{-M_y^B}{l} & k_{2\cdot5} & -k_{2\cdot6} \\
 & & & & & & & & k_{2\cdot2} & \frac{-M_z^B}{l} & k_{2\cdot6} & k_{2\cdot5} \\
 & & & \text{sym.} & & & & & & k_{4\cdot4} & k_{4\cdot5} & k_{4\cdot6} \\
 & & & & & & & & & & k_{5\cdot5} & 0 \\
 & & & & & & & & & & & k_{5\cdot5}
\end{array}\right] \tag{2.97}$$

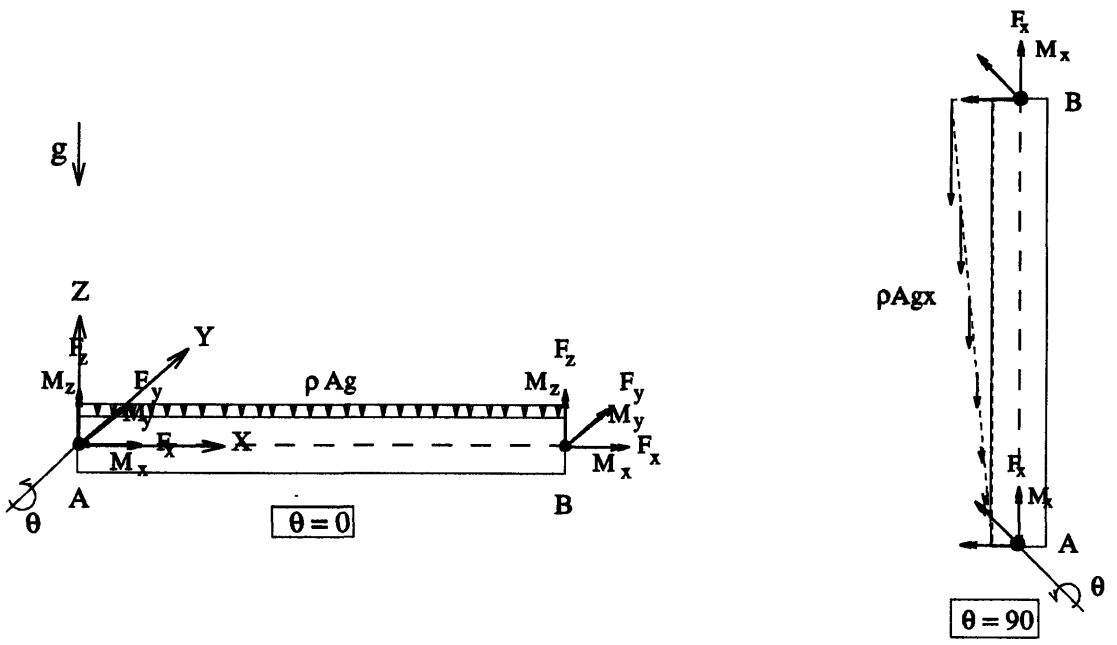

Figure 2-5: Beam Element subject to Concentrated Nodal Loads and Mass-Proportional Distributed Loading

and bending moments are weighted here by a $\cos(\theta)$ term and the distributed and concentrated axial load terms are weighted by a $\sin(\theta)$ term so as to describe the gravitational loading of a beam element at an angle θ with the horizontal plane (see Figure 2-5 for the $\theta = 0$ and $\theta = 90$ cases). Note that all loadings are through the shear axis to avoid eccentricity complications and the sign convention adopted for the distributed loading is positive downwards in the XZ plane. By allowing for these loading effects of the distributed mass of the beam element we now have the following nodal force relations

$$\begin{aligned} F_x^B &= -F_x^A + \rho A g_s h \\ F_y^B &= -F_y^A \\ F_z^B &= -F_z^A + \rho A g_c h \\ M_x^B &= -M_x^A \\ M_y^B &= -M_y^A - F_z^A h + \frac{\rho A g_c h^2}{2} \end{aligned} \tag{2.98}$$

$$M_z^B = -M_z^A + F_y^A h \tag{2.99}$$

The continuous force and moment descriptions are now given by,

$$\begin{aligned}
F_x(x) &= F_x^B - \rho A g_s (h - x) \\
F_y(x) &= F_y^B = -\frac{M_z^A + M_z^B}{h} \\
F_z(x) &= F_z^B - \rho A g_c (h - x) = \frac{M_y^A + M_y^B}{h} - \frac{\rho A g_c h}{2} + \rho A g_c x \\
M_x(x) &= M_x^B \qquad (2.100) \\
M_y(x) &= -M_y^A(1 - x/h) + M_y^B(x/h) - \frac{\rho A g_c h}{2} x + \frac{\rho A g_c}{2} x^2 \\
M_z(x) &= -M_z^A(1 - x/h) + M_z^B(x/h) \qquad (2.101)
\end{aligned}$$

The stress expressions of Equations (2.92) and (2.94) are now augmented with the distributed load effects to yield,

$$\begin{aligned}
\sigma_x = &\left(\frac{F_x^B}{A} - \rho g (h - x)\right) \sin(\theta) + \\
&\left(-M_y^A(1 - x/h) + M_y^B(x/h) - \frac{\rho A g h x}{2} + \frac{\rho A g x^2}{2}\right) \frac{z}{I_y} \cos(\theta) + \\
&\left(-M_z^A(1 - x/h) + M_z^B(x/h)\right) \frac{y}{I_z} \cos(\theta)
\end{aligned} \tag{2.102}$$

and

$$\mathcal{T}_{xy} = -\left(\frac{M_z^A + M_z^B}{Ah}\right) \cos(\theta) - \frac{M_x^B z}{2I_y} \tag{2.103}$$

$$\mathcal{T}_{xz} = \left(\frac{M_y^A + M_y^B}{Ah} - \frac{\rho g h}{2} + \rho g x\right) \cos(\theta) + \frac{M_x^B y}{2I_z} \tag{2.104}$$

for a uniform beam element of density ρ, length h and cross-sectional area A.

Solving for the new K_g, as was done before for the concentrated load K_g, yields the geometric stiffness matrix with distributed load effects, K_{gd}, shown in Equa-

tion (2.105).

$$K_{gd} = \left[\begin{array}{c|c} K_{gd11} & K_{gd12} \\ \hline \text{sym.} & K_{gd22} \end{array}\right] \tag{2.105}$$

where

$$K_{gd11} = \begin{bmatrix} 0 & \frac{\left(M_z^A+M_z^B\right)c\theta}{l^2} & \frac{-\left(M_y^A+M_y^B\right)c\theta}{l^2} & 0 & \frac{-(\rho Alg)c\theta}{12} & 0 \\ & \frac{3\left(2F_x^B-\rho Alg\right)s\theta}{5l} & 0 & \frac{\left(10M_y^A-\rho Al^2g\right)c\theta}{10l} & \frac{C_TM_x^B}{6l} & \frac{F_x^Bs\theta}{10} \\ & & k_{2\cdot2} & \frac{M_z^Ac\theta}{l} & -k_{2\cdot6} & k_{2\cdot5} \\ & & & \frac{I_x\left(2F_x^B-\rho Alg\right)s\theta}{2Al} & \frac{\left(M_z^A+M_z^B\right)c\theta}{6} & \frac{-\left(10M_y^A+10M_y^B-7\rho Al^2g\right)c\theta}{60} \\ & \text{sym.} & & & \frac{l\left(4F_x^B-3\rho Alg\right)s\theta}{30} & 0 \\ & & & & & k_{5\cdot5} \end{bmatrix}$$

$$K_{gd12} = \begin{bmatrix} 0 & -k_{1\cdot2} & -k_{1\cdot3} & 0 & -k_{1\cdot5} & 0 \\ -k_{1\cdot2} & -k_{2\cdot2} & 0 & -k_{8\cdot10} & -k_{2\cdot5} & k_{9\cdot11} \\ -k_{1\cdot3} & 0 & -k_{2\cdot2} & -k_{9\cdot10} & -k_{9\cdot11} & -k_{2\cdot5} \\ 0 & -k_{2\cdot4} & -k_{3\cdot4} & -k_{4\cdot4} & -k_{4\cdot5} & \frac{\left(10M_y^A+10M_y^B-3\rho Al^2g\right)c\theta}{60} \\ -k_{1\cdot5} & -k_{2\cdot5} & k_{2\cdot6} & -k_{4\cdot5} & \frac{-\left(l\left(2F_x^B-\rho Alg\right)s\theta\right)}{60} & k_{2\cdot5}l/2 \\ 0 & -k_{2\cdot6} & -k_{2\cdot5} & \frac{\left(10M_y^A+10M_y^B+3\rho Al^2g\right)c\theta}{60} & -k_{2\cdot5}l/2 & k_{5\cdot11} \end{bmatrix}$$

and

$$K_{gd22} = \begin{bmatrix} 0 & k_{1\cdot2} & k_{1\cdot3} & 0 & k_{1\cdot5} & 0 \\ & k_{2\cdot2} & 0 & \frac{-\left(10M_y^B-\rho Al^2g\right)c\theta}{10l} & k_{2\cdot5} & -k_{9\cdot11} \\ & & k_{3\cdot3} & \frac{-M_z^Bc\theta}{l} & \frac{\left(F_x^B-\rho Alg\right)s\theta}{10} & k_{2\cdot5} \\ & & & k_{4\cdot4} & k_{4\cdot5} & \frac{-\left(10M_y^A+10M_y^B+7\rho Al^2g\right)c\theta}{60} \\ & & \text{sym.} & & \frac{l\left(4F_x^B-\rho Alg\right)s\theta}{30} & 0 \\ & & & & & k_{11\cdot11} \end{bmatrix}$$

Table 2.1: General Nature of Stress Stiffening Effects on Beam

Load Type	Nature of Stress Stiffening Effect
Axial load	stiffens/destiffens all bending and torsion modes. couples bending and axial modes.
Bending moment	couples axial and torsional modes with bending modes.
Torsional moment	couples bending modes.

2.3 Beam Element Stress Stiffening Effects

2.3.1 General Observations

Having derived general expressions for the geometric stiffness matrices of a beam element, a number of general observations can be made concerning the nature of the initial stress effect on the tangential stiffness matrix by directly inspecting K_g (Equation (2.97)) and K_{gd} (Equation (2.105)), and by comparing them with K_o (Equation (2.87)).

The most important load type is clearly the axial load, (F_x^B), which appears in every K_g and K_{gd} element which corresponds to a non-zero element of K_o (except for the axial degree of freedom). The result is a stiffening of all bending and torsion modes for a tensile load, and a destiffening of the same modes for a compressive load.

The effect of bending moment (M_y,M_z) induced stresses is to couple axial deformations and torsional deformations with bending deformations.

The effect of torsional moment (M_x) induced stresses is strictly to couple the out-of-plane bending modes. These observations are summarized in Table 2.1.

Comparing Equation (2.97) with Equation (2.105) it is also possible to observe the particular effects of the distributed loading. The distributed axial loading $\rho Alg\sin(\theta)$ only appears where the concentrated axial nodal load terms F_x^B previously appeared as one would expect. It is of note however that the relative weighting of the distributed axial loading term $\rho Alg\sin(\theta)$ compared to the $F_x^B\sin(\theta)$ term varies. Similarly, not

all transverse bending moment terms $M_y \cos(\theta)$, $M_z \cos(\theta)$ have an added distributed transverse loading term $\rho Alg \cos(\theta)$ and for those which do, the relative magnitude of the distributed loading term varies as compared to the concentrated load terms. The most interesting effect of incorporating distributed load effects in the stress description is the introduction of a set of new identical coupling terms due to distributed transverse loading, namely $k_{1,5}$, $k_{1,11}$, $k_{5,7}$, $k_{7,11}$, and their symmetric counter-parts. The effect of these terms is to strengthen the coupling between bending in the plane of the transverse loading and axial deformations.

Note that if the distributed transverse loading was also applied in the XY plane in addition to the XZ plane (with appropriate weighting terms) the M_z terms of elements $k_{3,4}$ and $k_{4,5}$ would also be subject to the same form of additive distributed loading as $k_{2,4}$ and $k_{4,6}$ by symmetry arguments. Similarly, the new $k_{1,5}$ family of terms would also appear with appropriate weighting at $k_{1,6}$, $k_{1,12}$, $k_{6,7}$ and $k_{7,12}$ by symmetry arguments.

2.3.2 Eigensystem Sensitivity Analysis Technique

A simple yet powerful method of identifying the effects of perturbations to the system property matrices of a discretized (e.g. finite element) structure on the latter's eigensystem is described in this section. The technique consists of projecting the *perturbed* $M^{-1}K$ system matrix product onto the original eigenspace using the original unperturbed eigenvectors ${}^{o}\Phi$. By examining the resulting matrix one can readily identify the perturbing effects on the original eigenvalues and eigenmodes. Details of the projection technique, and its relation to the eigenpair derivatives and the first order eigenpair perturbations are described in this section. In the following section the eigenprojection technique is used in a general symbolic analysis of a single beam element subject to three different sets of boundary conditions. This low order analytical approach was used rather than a high order numerical approach to provide greater insight and to more readily yield general non-dimensional parameters (as computed

in Section 2.3.4).

Sensitivity Matrix Analysis Technique

The general eigenvalue problem equation for the unperturbed system is written as

$$ {}^{o}K\Phi - {}^{o}M\Phi\Lambda = 0 \tag{2.106} $$

and the simple eigenvalue problem equation (i.e. the first order form) is written as

$$ \left({}^{o}M^{-1}\,{}^{o}K\right)\,{}^{o}\Phi = {}^{o}\Phi\,\Lambda \tag{2.107} $$

where ${}^{o}\Phi$ is the column matrix of unperturbed right eigenvectors, ${}^{o}M$ and ${}^{o}K$ are the unperturbed mass and stiffness system matrices, and Λ is the diagonal matrix of unperturbed eigenvalues. Regardless of the normalization of Φ the ${}^{o}\Phi^{-1}\,\left({}^{o}M^{-1}\,{}^{o}K\right)\,{}^{o}\Phi$ projection will always yield the uncoupled diagonal matrix Λ, i.e.

$$ \Lambda = {}^{o}\Phi^{-1}\,\left({}^{o}M^{-1}\,{}^{o}K\right)\,{}^{o}\Phi \tag{2.108} $$

This trivial projection of the unperturbed system matrix product onto the unperturbed eigenspace yields a diagonal matrix of original eigenvalues where every column corresponds to an uncoupled fundamental mode.

Performing the same projection with a perturbed mass and stiffness system, i.e. ${}^{t}M, {}^{t}K$ (where the dummy variable t indicates a system state other than the original), will result in a matrix, say Ψ, which will be referred to as the *sensitivity matrix*:

$$ \Psi = {}^{o}\Phi^{-1}\,\left({}^{t}M^{-1}\,{}^{t}K\right)\,{}^{o}\Phi \tag{2.109} $$

For the $(i,j)^{\text{th}}$ element of Ψ

$$ \Psi_{ij} = {}^{o}\phi_{i}^{-1}\,\left({}^{t}M^{-1}\,{}^{t}K\right)\,{}^{o}\phi_{j} \tag{2.110} $$

where ${}^o\phi_i^{-1}$ is the i^{th} row of ${}^o\Phi^{-1}$ and ${}^o\phi_j$ is the j^{th} column of ${}^o\Phi$.

The difference between the elements of Ψ and Λ represent perturbations to the eigensystem of $({}^oM^{-1}\,{}^oK)$. Perturbations to the eigenfrequencies result in changes to the diagonal terms of the original projection, while perturbations to the eigenmodes result in non-zero off-diagonal terms in Ψ. The positions of the off-diagonal terms describe which modes are coupled and the magnitude of the terms describes to what degree.

Further information can be extracted from Ψ by recognizing that the matrix inherently captures all the information required for the computation of the perturbed eigenvalues and eigenvectors and their derivatives. The advantage of computing Ψ as opposed to individual eigenvalues, eigenvectors and derivatives is that Ψ captures the latter information in a single matrix calculation and the computation is not limited to the effect of a perturbation of a single parameter.

Eigenvalue and Eigenvector Derivatives

The easily derived expression for the partial derivative of an eigenvalue of an undamped mass and stiffness system with respect to some parameter β is [56–59]

$$\frac{\delta\lambda_i}{\delta\beta} = \frac{{}^o\phi_{L_i}^T \left(\frac{\delta\,{}^tK}{\delta\beta} - {}^o\lambda_i \frac{\delta\,{}^tM}{\delta\beta}\right) {}^o\phi_{R_i}}{{}^o\phi_{L_i}^T\,{}^oM\,{}^o\phi_{R_i}} \tag{2.111}$$

where ϕ_L and ϕ_R are the left and right eigenvectors respectively (for M and K symmetric the system is self-adjoint so that $\phi_L = \phi_R$).

For the first order eigenvalue problem formulation we can simplify Equation (2.111) to the following

$$\frac{\delta\lambda_i}{\delta\beta} = {}^o\phi_{L_i}^T \frac{\delta\left({}^tM^{-1}\,{}^tK\right)}{\delta\beta} {}^o\phi_{R_i} \tag{2.112}$$

or,

$$\frac{\delta\lambda_i}{\delta\beta} = {}^o\phi_{R_i}^{-1} \frac{\left(\left({}^tM^{-1}\,{}^tK\right)\right)}{\delta\beta} {}^o\phi_{R_i} \tag{2.113}$$

and, as is the case in this analysis, if the original eigenvectors are not functions of the parameter β we can write the following

$$\frac{\delta \lambda_i}{\delta \beta} = \frac{\delta}{\delta \beta} \left({}^{o}\phi_{R_i}^{-1} \left({}^{t}M^{-1}\, {}^{t}K \right) {}^{o}\phi_{R_i} \right) \tag{2.114}$$

Comparing Equation (2.114) with Equation (2.110) we have

$$\frac{\delta \lambda_i}{\delta \beta} = \frac{\delta \Psi_{ii}}{\delta \beta} \tag{2.115}$$

and therefore, taking the partial derivatives of the diagonal terms of Ψ, directly yields the eigenvalue partial derivatives.

The eigenvector derivatives are given by [56–59]

$$\frac{\delta \phi_i}{\delta \beta} = \sum_{j \neq i} \frac{\left({}^{o}\phi_{L_j}^{T} \left(\frac{\delta {}^{t}K}{\delta \beta} - {}^{o}\lambda_i \frac{\delta {}^{t}M}{\delta \beta} \right) {}^{o}\phi_{R_i} \right)}{{}^{o}\lambda_i - {}^{o}\lambda_j} {}^{o}\phi_j \tag{2.116}$$

or

$$\frac{\delta \phi_i}{\delta \beta} = \sum_{j \neq i} \frac{\frac{\delta}{\delta \beta} \left({}^{o}\phi_{R_j}^{-1} \left({}^{t}M^{-1}\, {}^{t}K \right) {}^{o}\phi_{R_i} \right)}{{}^{o}\lambda_i - {}^{o}\lambda_j} {}^{o}\phi_j \tag{2.117}$$

From Equation (2.110) we can simplify further to obtain

$$\frac{\delta \phi_i}{\delta \beta} = \sum_{j \neq i} \frac{\frac{\delta}{\delta \beta} \Psi_{ij}}{{}^{o}\lambda_i - {}^{o}\lambda_j} {}^{o}\phi_j \tag{2.118}$$

Thus, normalizing the off-diagonal elements of the i^{th} column of Ψ by the $(\lambda_i - \lambda_j)$ difference in the original diagonal elements of Ψ (i.e. Λ of Equation (2.107)) yields the weighting coefficients for the eigenvalue derivative expression.

First Order Eigenvalue and Eigenvector Perturbation

Having identified the relation between the sensitivity matrix and the eigenpair derivatives we now proceed to identify the relation between the sensitivity matrix, the orig-

inal eigenpairs and the perturbed eigenpairs. Based on the perturbation method we can express the eigenvalues of the $({}^{t}M^{-1}\,{}^{t}K)$ system as the following series [59]

$$ {}^{t}\lambda_i = {}^{(0)}\lambda_i + {}^{(1)}\lambda_i \Delta\beta + {}^{(2)}\lambda_i \Delta\beta^2 + {}^{(3)}\lambda_i \Delta\beta^3 + \ldots \tag{2.119} $$

where the ${}^{(n)}\lambda_i$ are weighting coefficients and the $\Delta\beta$ are perturbations of increasing order. The first order perturbation to λ_i, in the case of distinct eigenvalues, is given by

$$ {}^{t}\lambda_i = {}^{(0)}\lambda_i + \frac{\delta\lambda_i}{\delta\beta}\Delta\beta \tag{2.120} $$

Substituting Equation (2.115) into Equation (2.120) yields

$$ {}^{t}\lambda_i = {}^{(0)}\lambda_i + \frac{\delta\Psi_{ii}}{\delta\beta}\Delta\beta \tag{2.121} $$

Writing the sensitivity matrix as the sum of the unperturbed projection matrix and a matrix of weighted first order perturbations $c_{ij}\,\beta_{ij}$ we have

$$ \Psi_{ij} = \Lambda_{ij} + c_{ij}\,\beta_{ij} \tag{2.122} $$

where the c_{ij} are the weighting coefficients and the β_{ij} are the first order perturbations, (i.e. for the stress stiffening case the perturbations are the nodal loading terms such as F_x, M_x, and M_y). Substituting Equation (2.122) in Equation (2.121) for the case i=j and taking the partial derivative of Ψ_{ii} with respect to β_{ii} yields

$$ {}^{t}\lambda_i = \Lambda_{ii} + c_{ii}\Delta\beta_{ii} \tag{2.123} $$

Since the resonant frequency (or eigenfrequency) is the square root of the eigenvalue [60–62] we have the following for the first order perturbation to the resonant frequency

$$ {}^{t}\omega_i = \sqrt{\Lambda_{ii} + c_{ii}\Delta\beta_{ii}} = \sqrt{{}^{o}\omega_i^2 + c_{ii}\Delta\beta_{ii}} \tag{2.124} $$

and, in non-dimensional form

$$\frac{{}^{t}f_i}{{}^{o}f_i} = \frac{{}^{t}\omega_i}{{}^{o}\omega_i} = \sqrt{1 + \frac{c_{ii}\Delta\beta_{ii}}{\Lambda_{ii}}} \tag{2.125}$$

For the perturbed eigenvector we can make the appropriate substitutions to similarly show that

$${}^{t}\phi_i = {}^{o}\phi + \sum_{j \neq i} \frac{c_{ji}\Delta\beta_{ji}}{{}^{o}\lambda_i - {}^{o}\lambda_j} {}^{o}\phi_j \tag{2.126}$$

Equations (2.123) and (2.126) could also be derived by directly integrating Equations (2.115) and (2.118), and making use of the fact that the perturbations are zero for the unperturbed system. In summary, by subtracting the original projection matrix Λ from the sensitivity matrix Ψ we can identify the first order perturbations to the eigenvalues, and the first-order modal coupling perturbations $c_{ji}\Delta\beta_{ji}$ can directly be identified by inspecting the off-diagonal of Ψ. However, it should be pointed out here that the eigenfrequency shift predicted by Equation (2.123) only captures the effect of a pure frequency perturbation and does not include the effects on the eigenfrequencies which result from the modal coupling predicted by Equation (2.126). Establishing the exact relation which describes the effect of modal coupling on the eigenfrequencies is recommended for future work.

2.3.3 Eigensystem Sensitivity Analysis Results

Rather than perform the eigensensitivity analysis numerically on a large accurate discrete model with many modes under certain very specific conditions, a general exact analytical (i.e. symbolic) eigensystem sensitivity analysis was performed using only the fundamental modes of a single beam element subject to pre-load effects. This approach was selected in order to identify valuable, general non-dimensional parameters and to allow the study of multiple simultaneous perturbing loads. The approach was also selected based on the knowledge that the fundamental modes typically have the greatest impact on the system performance metric and are more

susceptible to gravity and suspension effects.

Three different sets of boundary conditions were used in order to study the most common configurations of beam-type elements of a structure. The boundary conditions examined here are

1. clamped-free, (e.g. a flexible appendage clamped to a stiff structure),
2. pinned-pinned, (e.g. a strut which spans a bay of a truss type structure) and
3. free-free, (e.g. a beam supported by a soft suspension system).

While the boundary conditions listed above are only approximations to the real boundary conditions, it is felt that approximation is a good one. Insight is also gained as to the effects on the global behavior of the structure itself in the case of a long slender structure (such as the M.I.T.–SERC MACE test article [13, 15]) or on major beam-type elements of the structure itself (such as the truss legs of the M.I.T.–SERC Interferometer testbed [63]).

Clamped-Free Beam Unperturbed Eigensystem Characteristics

Constraining all degrees of freedom at one end of the beam element results in a clamped-free beam with no rigid-body modes. The system property matrices for this boundary condition case are denoted by M_c and K_c. The unnormalized eigenvectors of the unperturbed $\mathcal{T}(M_c^{-1}K_c)$ system are the columns of the eigenvector matrix ${}^o\Phi_c$

$$
{}^o\Phi_c = \begin{bmatrix}
0 & 0 & 0 & 0 & 1 & 0 \\
0 & 0 & \frac{-2l}{-9+\sqrt{39}} & \frac{-2l}{-9-\sqrt{39}} & 0 & 0 \\
\frac{2l}{-9+\sqrt{39}} & \frac{2l}{-9-\sqrt{39}} & 0 & 0 & 0 & 0 \\
0 & 0 & 0 & 0 & 0 & 1 \\
1 & 1 & 0 & 0 & 0 & 0 \\
0 & 0 & 1 & 1 & 0 & 0
\end{bmatrix} \tag{2.127}
$$

where, recall, the order of the degrees of freedom for the unconstrained node are

$$U_c = \left[\begin{array}{cccccc} U_B^1 & U_B^2 & U_B^3 & U_B^4 & U_B^5 & U_B^6 \end{array} \right] \tag{2.128}$$

as illustrated in Figure 2-3 or equivalently,

$$U_c = \left[\begin{array}{cccccc} x_B & y_B & z_B & \theta x_B & \theta y_B & \theta z_B \end{array} \right] \tag{2.129}$$

The projection of the original system, i.e. ${}^o\Phi^{-1}\,{}^o(M_c^{-1}K_c){}^o\Phi$, yields the diagonal matrix of eigenvalues Λ as expected.

$$ {}^o\Psi^c = \begin{array}{c} \begin{array}{cccccc} \text{bending}_{z_1} & \text{bending}_{z_2} & \text{bending}_{y_1} & \text{bending}_{y_2} & \text{axial} & \text{torsion} \end{array} \\ \left[\begin{array}{cccccc} \frac{12.4802\,EI_y}{\rho Al^4} & 0 & 0 & 0 & 0 & 0 \\ 0 & \frac{1211.52\,EI_y}{\rho Al^4} & 0 & 0 & 0 & 0 \\ 0 & 0 & \frac{12.4802\,EI_z}{\rho Al^4} & 0 & 0 & 0 \\ 0 & 0 & 0 & \frac{1211.52\,EI_z}{\rho Al^4} & 0 & 0 \\ 0 & 0 & 0 & 0 & \frac{3\,E}{\rho l^2} & 0 \\ 0 & 0 & 0 & 0 & 0 & \frac{3.6\,AGJ}{\rho I_x l^2} \end{array} \right] \end{array} \tag{2.130}$$

The modes corresponding to each column of Λ appear as labels above the columns. The correspondence can be determined by simple inspection of the eigenvalues themselves or by referring back to the eigenvector matrix of Equation (2.127).

Clamped-Free Beam Initial Stress Perturbation Results

Given a K_g perturbation the projection

$$\Psi_{kg}^c = {}^o\Phi_c^{-1}(M_c^{-1}(K + K_g)_c){}^o\Phi_c \tag{2.131}$$

yields the sensitivity matrix of Equation (2.133) which appears on page 88. Given a distributed geometric stiffness matrix perturbation, the projection

$$\Psi^{c}_{kgd} = {}^{o}\Phi_{c}^{-1}(M_{c}^{-1}(K + K_{gd})_{c})\,{}^{o}\Phi \tag{2.132}$$

yields the sensitivity matrix of Equation (2.134) which appears on page 89. Note that for reasons of compactness, the nodal load form for the nodal bending moments has been replaced with the equivalent single uniform shear term in the sensitivity matrices where possible, i.e.

$$\begin{aligned} M_y^A + M_y^B &= F_z l \\ M_z^A + M_z^B &= -F_y l \end{aligned}$$

Note also that the nodal form of the loading terms is only required for incorporating the stress stiffening effects in a discrete model and is not necessary here.

To facilitate the interpretation of Ψ_{kgd} three special cases are extracted from it: the no twisting moment, horizontal beam case (i.e. $\sin(\theta) = 0, M_x = 0$), the no twisting moment, vertical beam case (i.e. $\cos(\theta) = 0, M_x = 0$), and the artificial pure twisting moment case (i.e. $\sin(\theta) = 0, \cos(\theta) = 0$).

$$\Psi^{c}_{kgd}|_{\text{bend}} = {}^{o}\Phi^{-1}\left(M^{-1}\left(K + K_{gd}(\sin(\theta) = 0, M_x = 0)\right)\right){}^{o}\Phi \tag{2.135}$$

$$\Psi^{c}_{kgd}|_{\text{axial}} = {}^{o}\Phi^{-1}\left(M^{-1}\left(K + K_{gd}(\cos(\theta) = 0, M_x = 0)\right)\right){}^{o}\Phi \tag{2.136}$$

$$\Psi^{c}_{kgd}|_{\text{twist}} = {}^{o}\Phi^{-1}\left(M^{-1}\left(K + K_{gd}(\sin(\theta) = 0, \cos(\theta) = 0)\right)\right){}^{o}\Phi \tag{2.137}$$

The pure twist case is artificially isolated here as it is not possible to have zero gravity loading components in both the axial and transverse directions. The results of these projections are shown on page 90 in Equations (2.138), (2.139) and (2.140).

Similar analyses will now be performed for the pinned-pinned beam case and the free-free beam.

$$\Psi^{c}_{kg} = \frac{1}{\rho A l}\begin{bmatrix} \frac{12.48\left(EI_y+0.3848F_x l^2\right)}{l^3} & \frac{9.663F_x}{l} & 0 & \frac{-35.496M_x}{l^2} & \frac{3.498F_z}{l} & \frac{3.498M_z^A}{\sqrt{\frac{I_x}{A}}l} \\ \frac{9.663F_x}{l} & \frac{1212.\left(EI_y+0.04853F_x l^2\right)}{l^3} & \frac{35.496M_x}{l^2} & 0 & \frac{4.875F_z}{l} & \frac{4.875M_z^A}{\sqrt{\frac{I_x}{A}}l} \\ 0 & \frac{35.496M_x}{l^2} & \frac{12.48\left(EI_z+0.3848F_x l^2\right)}{l^3} & \frac{9.663F_x}{l} & \frac{-3.4979F_y}{l} & \frac{-0.8031(F_z l+4.3557M_y)}{\sqrt{\frac{I_x}{A}}l} \\ \frac{-35.496M_x}{l^2} & 0 & \frac{9.663F_x}{l} & \frac{1212.\left(EI_z+0.04853F_x l^2\right)}{l^3} & \frac{-4.875F_y}{l} & \frac{-6.193(F_z l+0.787M_y)}{\sqrt{\frac{I_x}{A}}l} \\ \frac{3.498F_z}{l} & \frac{4.875F_z}{l} & \frac{-3.498F_y}{l} & \frac{-4.875F_y}{l} & \frac{3EA}{l} & 0 \\ \frac{3.498M_z^A}{\sqrt{\frac{I_x}{A}}l} & \frac{4.875M_z^A}{\sqrt{\frac{I_x}{A}}l} & \frac{-0.8031(F_z l+4.356M_y)}{\sqrt{\frac{I_x}{A}}l} & \frac{-6.193(F_z l+0.787M_y)}{\sqrt{\frac{I_x}{A}}l} & 0 & \frac{3.6(0.8333F_x I_x+AGJ)}{I_x l} \end{bmatrix} \tag{2.133}$$

$$\Psi^{c}_{kgd} = \frac{1}{\rho A l}\begin{bmatrix} \frac{12.48\left(EI_y+(0.385F_x-0.127Agl\rho)l^2s\theta\right)}{l^3} & \frac{9.663(F_x-0.0294Agl\rho)s\theta}{l} & 0 \\ \frac{9.663(F_xs\theta-0.0294Agl\rho s\theta)}{l} & \frac{1211.5\left(EI_y+(0.0485F_x-0.00662Agl\rho)l^2s\theta\right)}{l^3} & \frac{35.496M_x}{l^2} \\ 0 & \frac{35.496M_x}{l^2} & \frac{12.48\left(EI_z+(0.385F_x-0.127Agl\rho)l^2s\theta\right)}{l^3} \\ \frac{-35.496M_x}{l^2} & 0 & \frac{9.663(F_x-0.0294Agl\rho)s\theta}{l} \\ \frac{0.4015(8.711F_z-Agl\rho)c\theta}{l} & \frac{3.097(1.574F_z-Agl\rho)c\theta}{l} & \frac{-3.498F_yc\theta}{l} \\ \frac{0.803\sqrt{\frac{A}{I_x}}(-F_yl+4.356M_z)c\theta}{l} & \frac{6.193\sqrt{\frac{A}{I_x}}(-F_yl+0.787M_z)c\theta}{l} & \frac{-0.2124\sqrt{\frac{A}{I_x}}\left(3.782F_zl+16.472M_y+Agl^2\rho\right)c\theta}{l} \end{bmatrix} \cdots$$

$$\begin{bmatrix} \frac{-35.496M_x}{l^2} & \frac{0.402(8.711F_z-Agl\rho)c\theta}{l} & \frac{0.803\sqrt{\frac{A}{I_x}}(-F_yl+4.356M_z)c\theta}{l} \\ 0 & \frac{3.097(1.574F_z-Agl\rho)c\theta}{l} & \frac{6.193\sqrt{\frac{A}{I_x}}(-F_yl+0.787M_z)c\theta}{l} \\ \frac{9.663(F_x-0.0294Agl\rho)s\theta}{l} & \frac{-3.498F_yc\theta}{l} & \frac{-0.212\sqrt{\frac{A}{I_x}}\left(3.782F_zl+16.472M_y+Agl^2\rho\right)c\theta}{l} \\ \frac{1211.5(EI_z+0.0485F_x-0.00662Agl\rho)s\theta}{l} & \frac{-4.875F_yc\theta}{l} & \frac{-3.848\sqrt{\frac{A}{I_x}}\left(1.61F_zl+1.267M_y+Agl^2\rho\right)c\theta}{l} \\ \frac{-4.875F_yc\theta}{l} & \frac{3EA}{l} & 0 \\ \frac{-3.848\sqrt{\frac{A}{I_x}}\left(1.61F_zl+1.267M_y+Agl^2\rho\right)c\theta}{l} & 0 & \frac{3.6(AGJ+(0.833F_x-0.417Agl\rho)I_xs\theta)}{I_xl} \end{bmatrix} \quad (2.134)$$

$$\Psi^{c}_{kgd}|_{\text{bend}} = \begin{bmatrix} \frac{12.48EI_y}{\rho Al^4} & 0 & 0 & 0 & \frac{(8.711F_z - Agl\rho)}{2.491\rho Al^2} & \frac{(-F_y l + 4.356M_z)}{1.245\rho\sqrt{I_x A}l^2} \\ 0 & \frac{1212.EI_y}{\rho Al^4} & 0 & 0 & \frac{(1.574F_z - Agl\rho)}{0.3229\rho Al^2} & \frac{(-F_y l + 0.787M_z)}{0.1615\rho\sqrt{I_x A}l^2} \\ 0 & 0 & \frac{12.48EI_z}{\rho Al^4} & 0 & \frac{-3.498F_y}{\rho Al^2} & \frac{-\left(3.782F_z l + 16.472M_y + Agl^2\rho\right)}{4.708\rho\sqrt{I_x A}l^2} \\ 0 & 0 & 0 & \frac{1212.EI_z}{\rho Al^4} & \frac{-4.875F_y}{\rho Al^2} & \frac{-\left(1.61F_z l + 1.267M_y + Agl^2\rho\right)}{0.2599\rho\sqrt{I_x A}l^2} \\ \frac{(8.71143F_z - Agl\rho)}{2.491\rho Al^2} & \frac{(1.574F_z - Agl\rho)}{0.3229\rho Al^2} & \frac{-3.498F_y}{\rho Al^2} & \frac{-4.875F_y}{\rho Al^2} & \frac{3EA}{\rho Al^2} & 0 \\ \frac{(-F_y l + 4.356M_z)}{1.245\rho\sqrt{I_x A}l^2} & \frac{(-F_y l + 0.787M_z)}{0.1615\rho\sqrt{I_x A}l^2} & \frac{-\left(3.782F_z l + 16.472M_y + Agl^2\rho\right)}{4.71\rho\sqrt{I_x A}l^2} & \frac{-\left(1.61F_z l + 1.267M_y + Agl^2\rho\right)}{0.2604\rho\sqrt{I_x A}l^2} & 0 & \frac{3.6AGJ}{\rho AI_x l^2} \end{bmatrix} \tag{2.138}$$

$$\Psi^{c}_{kgd}|_{\text{axial}} = \begin{bmatrix} \frac{\left(7.892EI_y + 3.037F_x l^2 - Agl^3\rho\right)}{0.6325\rho Al^4} & \frac{(34F_x - Agl\rho)}{3.519\rho Al} & 0 & 0 & 0 & 0 \\ \frac{(34F_x - Agl\rho)}{3.519\rho Al} & \frac{\left(151.1EI_y + 7.333F_x l^2 - Agl^3\rho\right)}{0.1247\rho Al^4} & 0 & 0 & 0 & 0 \\ 0 & 0 & \frac{\left(7.892EI_z + 3.037F_x l^2 - Agl^3\rho\right)}{0.6325\rho Al^4} & \frac{(34F_x - Agl\rho)}{3.519\rho Al} & 0 & 0 \\ 0 & 0 & \frac{(34F_x - Agl\rho)}{3.519\rho Al} & \frac{\left(151.1EI_z + 7.333F_x l^2 - Agl^3\rho\right)}{0.1247\rho Al^4} & 0 & 0 \\ 0 & 0 & 0 & 0 & \frac{3EA}{\rho Al} & 0 \\ 0 & 0 & 0 & 0 & 0 & \frac{(2F_x I_x + 2.4AGJ - AgI_x l\rho)}{0.667\rho AI_x l} \end{bmatrix} \tag{2.139}$$

$$\Psi^{c}_{kgd}|_{\text{twist}} = \begin{bmatrix} \frac{12.48EI_y}{\rho Al^4} & 0 & 0 & \frac{-35.496M_x}{\rho Al^3} & 0 & 0 \\ 0 & \frac{1212.EI_y}{\rho Al^4} & \frac{35.496M_x}{\rho Al^3} & 0 & 0 & 0 \\ 0 & \frac{35.496M_x}{\rho Al^3} & \frac{12.48EI_z}{\rho Al^4} & 0 & 0 & 0 \\ \frac{-35.496M_x}{\rho Al^3} & 0 & 0 & \frac{1212.EI_z}{\rho Al^4} & 0 & 0 \\ 0 & 0 & 0 & 0 & \frac{3EA}{\rho Al} & 0 \\ 0 & 0 & 0 & 0 & 0 & \frac{3.6AGJ}{\rho AI_x l} \end{bmatrix} \tag{2.140}$$

Pinned-Pinned Beam Unperturbed Eigensystem Characteristics

Constraining the translational degrees of freedom at both ends of the beam element results in a pinned-pinned beam with a single rotational rigid-body mode about its neutral axis. The unconstrained degrees of freedom for the pinned-pinned beam case are thus

$$U_{\mathrm{p}} = \left[\begin{array}{cccccc} U_A^4 & U_A^5 & U_A^6 & U_B^4 & U_B^5 & U_B^6 \end{array} \right] \tag{2.141}$$

The system property matrices for this boundary condition case will be denoted by M_{p} and K_{p}. The unnormalized eigenvectors for the pinned-pinned beam case are

$${}^{o}\Phi_{\mathrm{p}} = \left[\begin{array}{cccccc} 1 & 0 & 0 & 0 & 0 & -1 \\ 0 & -1 & 1 & 0 & 0 & 0 \\ 0 & 0 & 0 & -1 & 1 & 0 \\ 1 & 0 & 0 & 0 & 0 & 1 \\ 0 & 1 & 1 & 0 & 0 & 0 \\ 0 & 0 & 0 & 1 & 1 & 0 \end{array} \right] \tag{2.142}$$

Projecting the original pinned-pinned beam eigensystem onto itself yields the following diagonal matrix of eigenvalues

$${}^{o}\Psi_{\mathrm{p}} = \begin{array}{c} \begin{array}{cccccc} \text{rotation}_x & \text{bending}_{z_1} & \text{bending}_{z_2} & \text{bending}_{y_1} & \text{bending}_{y_2} & \text{torsion} \end{array} \\ \left[\begin{array}{cccccc} 0 & 0 & 0 & 0 & 0 & 0 \\ 0 & \frac{120.EI_y}{\rho Al^4} & 0 & 0 & 0 & 0 \\ 0 & 0 & \frac{2520.EI_y}{\rho Al^4} & 0 & 0 & 0 \\ 0 & 0 & 0 & \frac{120.EI_z}{\rho Al^4} & 0 & 0 \\ 0 & 0 & 0 & 0 & \frac{2520.EI_z}{\rho Al^4} & 0 \\ 0 & 0 & 0 & 0 & 0 & \frac{14.4GJ}{\rho I_x l^2} \end{array} \right] \end{array} \tag{2.143}$$

which will be compared to the perturbed system projection to identify which modes are directly stiffened or destiffened by the geometric stiffening and which modes be-

come coupled.

Pinned-Pinned Beam Initial Stress Perturbation Results

Applying the initial stress perturbation to the pinned-pinned beam system and performing the eigenprojection

$$\Psi_{kg}^{\mathrm{p}} = {}^{o}\Phi_{\mathrm{p}}^{-1}(M_{\mathrm{p}}^{-1}(K + K_g)_{\mathrm{p}})\,{}^{o}\Phi_{\mathrm{p}} \tag{2.144}$$

yields the sensitivity matrix of Equation (2.145) which appears on page 93 due to its size. If the perturbation is the distributed geometric stiffness matrix, the result is the sensitivity matrix Ψ_{kgd}^{p} which is also shown on page 93.

Free-Free Beam Unperturbed Eigensystem Characteristics

The free-free beam boundary condition case has of course six rigid-body modes which implies that there are six repeated eigenvalues at the origin. Unfortunately, if there exist multiple roots, the eigenvalue and eigenvector derivative relations presented in Section 2.3.2 do not hold. While the sensitivity matrix is useful in identifying stiffening and destiffening effects as well as couplings, it is no longer possible to physically relate the sensitivity matrix to exact eigensystem characteristics. The theory of eigenvalue and eigenvector derivatives in the presence of multiple eigenvalues and multiple eigenvalue derivatives is beyond the scope of this work: see References [64] and [65] for additional details. The previous analyses for the clamped-free and pinned-pinned beam had the advantage that multiple eigenvalues are not a necessary condition.

$$\Psi^{\mathrm{P}}_{kg} = \begin{bmatrix} 0 & 0 & 0 & 0 & 0 & 0 \\ 0 & \frac{10\left(12EI_y+F_xl^2\right)}{\rho Al^4} & 0 & 0 & \frac{-30M_x}{\rho Al^3} & 0 \\ 0 & 0 & \frac{42\left(60EI_y+F_xl^2\right)}{Al^4\rho} & \frac{210M_x}{\rho Al^3} & 0 & 0 \\ 0 & 0 & \frac{30M_x}{\rho Al^3} & \frac{10\left(12EI_z+F_xl^2\right)}{\rho Al^4} & 0 & \frac{-20F_zl}{\rho Al^3} \\ 0 & \frac{-210M_x}{\rho Al^3} & 0 & 0 & \frac{42\left(60EI_z+F_xl^2\right)}{Al^4\rho} & 0 \\ 0 & 0 & 0 & \frac{-2F_zl}{\rho I_xl} & 0 & \frac{14.4(0.833F_xI_x+AGJ)}{\rho AI_xl^2} \end{bmatrix} \tag{2.145}$$

$$\Psi^{\mathrm{P}}_{kgd} = \begin{bmatrix} 0 & 0 & 0 & \frac{-0.333Agl\,c\theta}{I_x} & 0 & 0 \\ 0 & \frac{5\left(24EI_y+2F_xl^2\,s\theta-\rho Agl^3\,s\theta\right)}{\rho Al^4} & \frac{2g\,s\theta}{l} & 0 & \frac{-30M_x}{\rho Al^3} & \frac{-20F_yl\,c\theta}{\rho Al^3} \\ 0 & \frac{14g\,s\theta}{l} & \frac{21\left(120EI_y+2F_xl^2\,s\theta-\rho Agl^3\,s\theta\right)}{\rho Al^4} & \frac{210M_x}{\rho Al^3} & 0 & 0 \\ \frac{-10g\,c\theta}{l} & 0 & \frac{30M_x}{\rho Al^3} & \frac{5\left(24EI_z+2F_xl^2\,s\theta-\rho Agl^3\,s\theta\right)}{\rho Al^4} & \frac{2g\,s\theta}{l} & \frac{-20F_zl\,c\theta}{\rho Al^3} \\ 0 & \frac{-210M_x}{\rho Al^3} & 0 & \frac{14g\,s\theta}{l} & \frac{21\left(120EI_z+2F_xl^2\,s\theta-\rho Agl^3\,s\theta\right)}{\rho Al^4} & \frac{-28g\,c\theta}{l} \\ 0 & \frac{-2F_yl\,c\theta}{\rho I_xl} & 0 & \frac{-2F_zl\,c\theta}{\rho I_xl} & \frac{-0.4A\,c\theta gl}{I_x} & \frac{6(2.4AGJ+2F_xI_x\,s\theta-\rho AgI_xl\,s\theta)}{\rho AI_xl^2} \end{bmatrix} \tag{2.146}$$

The unnormalized eigenvectors for the pinned-pinned beam case are

$$
{}^{o}\Phi_{f} = \left[\begin{array}{ccccccc|ccccc}
0 & 0 & 0 & 0 & 0 & 1 & 0 & 0 & 0 & 0 & -1 & 0 \\
-L & 0 & 0 & 0 & 1 & 0 & 0 & 0 & L & -L & 0 & 0 \\
0 & L & 0 & 1 & 0 & 0 & -L & L & 0 & 0 & 0 & 0 \\
0 & 0 & 1 & 0 & 0 & 0 & 0 & 0 & 0 & 0 & 0 & -1 \\
0 & 1 & 0 & 0 & 0 & 0 & -6 & 12 & 0 & 0 & 0 & 0 \\
1 & 0 & 0 & 0 & 0 & 0 & 0 & 0 & -6 & 12 & 0 & 0 \\
\hline
0 & 0 & 0 & 0 & 0 & 1 & 0 & 0 & 0 & 0 & 1 & 0 \\
0 & 0 & 0 & 0 & 1 & 0 & 0 & 0 & L & L & 0 & 0 \\
0 & 0 & 0 & 1 & 0 & 0 & -L & -L & 0 & 0 & 0 & 0 \\
0 & 0 & 1 & 0 & 0 & 0 & 0 & 0 & 0 & 0 & 0 & 1 \\
0 & 1 & 0 & 0 & 0 & 0 & 6 & 12 & 0 & 0 & 0 & 0 \\
1 & 0 & 0 & 0 & 0 & 0 & 0 & 0 & 6 & 12 & 0 & 0
\end{array}\right] \tag{2.147}
$$

and the eigenprojection of the original system yields the following diagonal matrix

of eigenvalues

$$
{}^{o}\Psi_{\mathrm{f}} = \begin{array}{c}
\begin{array}{cccccc} & & & & & & \text{bending}_{z_1} & \text{bending}_{z_2} & \text{bending}_{y_1} & \text{bending}_{y_2} & \text{axial} & \text{torsion} \end{array} \\
\begin{bmatrix}
0 & 0 & 0 & 0 & 0 & 0 & 0 & 0 & 0 & 0 & 0 & 0 \\
0 & 0 & 0 & 0 & 0 & 0 & 0 & 0 & 0 & 0 & 0 & 0 \\
0 & 0 & 0 & 0 & 0 & 0 & 0 & 0 & 0 & 0 & 0 & 0 \\
0 & 0 & 0 & 0 & 0 & 0 & 0 & 0 & 0 & 0 & 0 & 0 \\
0 & 0 & 0 & 0 & 0 & 0 & 0 & 0 & 0 & 0 & 0 & 0 \\
0 & 0 & 0 & 0 & 0 & 0 & 0 & 0 & 0 & 0 & 0 & 0 \\
0 & 0 & 0 & 0 & 0 & 0 & \frac{720EI_y}{\rho Al^4} & 0 & 0 & 0 & 0 & 0 \\
0 & 0 & 0 & 0 & 0 & 0 & 0 & \frac{8400EI_y}{\rho Al^4} & 0 & 0 & 0 & 0 \\
0 & 0 & 0 & 0 & 0 & 0 & 0 & 0 & \frac{720EI_z}{\rho Al^4} & 0 & 0 & 0 \\
0 & 0 & 0 & 0 & 0 & 0 & 0 & 0 & 0 & \frac{8400EI_z}{\rho Al^4} & 0 & 0 \\
0 & 0 & 0 & 0 & 0 & 0 & 0 & 0 & 0 & 0 & \frac{12EA}{\rho Al^2} & 0 \\
0 & 0 & 0 & 0 & 0 & 0 & 0 & 0 & 0 & 0 & 0 & \frac{14.4GJ}{\rho I_x l^2}
\end{bmatrix}
\end{array}
\tag{2.148}
$$

Free-Free Beam Initial Stress Perturbation Results

Clearly, it is not possible for a gravitational load field to apply initial stresses to an unconstrained beam, but it is desirable to understand the pure effects of the initial stress loading in order to study the case where the beam is suspended on a soft suspension system. Due to use of discrete attachment points it is not possible for its weight to be perfectly off-loaded and non-negligible residual stresses may exist in the structure.

Applying the geometric stiffness perturbation to the unconstrained beam and performing the eigenprojection

$$
\Psi^{\mathrm{f}}_{kg} = {}^{o}\Phi_{\mathrm{f}}^{-1}(M_{\mathrm{f}}^{-1}(K + K_g)_{\mathrm{f}})\,{}^{o}\Phi_{\mathrm{f}} \tag{2.149}
$$

yields the sensitivity matrix of Equation (2.150) which appears on page 97. The sensitivity matrix Ψ^{f}_{kgd}, which corresponds to the distributed geometric stiffness matrix perturbation, is not reproduced here due to its size.

2.3.4 Observations and Non-Dimensional Parameters

The general observations of Section 2.3.1 can now be quantified for the three different beam configurations studied. Examining Equations (2.133), (2.145) and (2.150) we can confirm that the nature of the modal couplings and eigenfrequency shifts predicted by direct inspection of K_g in Section 2.3.1 were correct. It is now possible, however, to evaluate more precisely the impact of a particular perturbing effect on the eigensystem of a clamped-free, pinned-pinned or free-free beam-like portion of a structure. This is best accomplished by establishing non-dimensional parameters which describe, in terms of general system properties, the system sensitivity to the stress stiffening gravity effect.

Recall that a pure perturbation to an eigenvalue is described by a change in the diagonal element of the sensitivity matrix, Ψ. Thus, a useful non-dimensional parameter for the eigenvalues is obtained by taking the square root of the ratio of the *perturbation* to the diagonal element, over the *original* diagonal element. From Equation (2.123) we have

$$\Gamma_{ii} = \frac{c_{ii}\Delta\beta_{ii}}{\Lambda_{ii}} \tag{2.151}$$

That this measure is an additive perturbation to the normalized squared resonant frequency was made clear in Equation (2.125) and is repeated here for clarity,

$$\frac{{}^{t}f_i}{{}^{o}f_i} = \sqrt{1 + \frac{c_{ii}\Delta\beta_{ii}}{\Lambda_{ii}}} = \sqrt{1 + \Gamma_{ii}} \tag{2.152}$$

Note that negative Γ_{ii} values correspond to destiffening while positive Γ_{ii} values correspond to stiffening. If Γ_{ii} equals negative one the perturbation effect corresponds to buckling. However, since the first order perturbation equations are based on a

$$\Psi_{kg}^{f} = \left[\begin{array}{cccccc|cccccc}
\frac{12F_x}{\rho Al^2} & 0 & \frac{-12F_z}{\rho Al^2} & 0\,0\,0 & \frac{72M_x}{\rho Al^3} & 0 & 0 & \frac{24F_x}{\rho Al^2} & \frac{-24F_y}{\rho Al^3} & \frac{12(F_z l-2M_y)}{\rho Al^3} \\
0 & \frac{12F_x}{\rho Al^2} & \frac{-12F_y}{\rho Al^2} & 0\,0\,0 & 0 & \frac{24F_x}{\rho Al^2} & \frac{-72M_x}{\rho Al^3} & 0 & \frac{24F_z}{\rho Al^3} & \frac{-12(F_y l+2M_z)}{\rho Al^3} \\
-\frac{F_z}{\rho I_x} & \frac{-F_y}{\rho I_x} & 0 & 0\,0\,0 & 0 & \frac{-2F_y}{\rho I_x} & 0 & \frac{-2F_z}{\rho I_x} & 0 & 0 \\
0 & \frac{-6F_x}{\rho Al} & \frac{6F_y}{\rho Al} & 0\,0\,0 & 0 & \frac{-12F_x}{\rho Al} & \frac{36M_x}{\rho Al^2} & 0 & \frac{-12F_z}{\rho Al^2} & \frac{6(F_y l+2M_z)}{\rho Al^2} \\
\frac{6F_x}{\rho Al} & 0 & \frac{-6F_z}{\rho Al} & 0\,0\,0 & \frac{36M_x}{\rho Al^2} & 0 & 0 & \frac{12F_x}{\rho Al} & \frac{-12F_y}{\rho Al^2} & \frac{6(F_z l-2M_y)}{\rho Al^2} \\
0 & 0 & 0 & 0\,0\,0 & 0 & 0 & 0 & 0 & 0 & 0 \\
\hline
\frac{30M_x}{\rho Al^3} & 0 & 0 & 0\,0\,0 & \frac{60\left(12EI_y+F_x l^2\right)}{\rho Al^4} & 0 & 0 & \frac{-240M_x}{\rho Al^3} & 0 & 0 \\
0 & \frac{14F_x}{\rho Al^2} & \frac{-14F_y}{\rho Al^2} & 0\,0\,0 & 0 & \frac{168\left(50EI_y+F_x l^2\right)}{\rho Al^4} & \frac{336M_x}{\rho Al^3} & 0 & \frac{28F_z}{\rho Al^3} & \frac{-14(F_y l+2M_z)}{\rho Al^3} \\
0 & \frac{-30M_x}{\rho Al^3} & 0 & 0\,0\,0 & 0 & \frac{240M_x}{\rho Al^3} & \frac{60\left(12EI_z+F_x l^2\right)}{\rho Al^4} & 0 & 0 & \frac{-20F_z}{\rho Al^2} \\
\frac{14F_x}{\rho Al^2} & 0 & \frac{-14F_z}{\rho Al^2} & 0\,0\,0 & \frac{-336M_x}{\rho Al^3} & 0 & 0 & \frac{168\left(50EI_z+F_x l^2\right)}{\rho Al^4} & \frac{-28F_y}{\rho Al^3} & \frac{14(F_z l-2M_y)}{\rho Al^3} \\
\frac{-6F_y}{\rho Al} & \frac{6F_z}{\rho Al} & 0 & 0\,0\,0 & 0 & \frac{12F_z}{\rho Al} & 0 & \frac{-12F_y}{\rho Al} & \frac{12EA}{\rho Al^2} & 0 \\
\frac{3(F_z l-2M_y)}{\rho I_x l} & \frac{-3(F_y l+2M_z)}{\rho I_x l} & 0 & 0\,0\,0 & 0 & \frac{-6(F_y l+2M_z)}{\rho I_x l} & \frac{-12F_z}{\rho I_x} & \frac{6(F_z l-2M_y)}{\rho I_x l} & 0 & \frac{(0.833F_x I_x+AGJ)}{0.0694\rho AI_x l^2}
\end{array}\right] \tag{2.150}$$

constant sensitivity slope, precision is lost in the case of large effects (i.e. large $\Delta\beta$). The accuracy of the change predicted by Γ is inversely proportional to the magnitude of the change. This accuracy loss is not catastrophic since the principal objective of the non-dimensional parameter is to allow for quickly identifying when it is necessary to model the gravity effect under consideration–it should not be used to predict the magnitudes of significant changes.

To predict the modal couplings we examine the off-diagonal elements of the sensitivity matrix Ψ. Based on Equation (2.126) a useful non-dimensional parameter is obtained by taking the ratio of the off-diagonal element and the difference in the corresponding original diagonal elements,

$$\Gamma_{ij} = \frac{c_{ji}\Delta\beta_{ji}}{{}^{o}\lambda_i - {}^{o}\lambda_j} \tag{2.153}$$

This corresponds to a coupling coefficient which describes the contribution of the j^{th} modeshape to the perturbed i^{th} modeshape. The results of these non-dimensional parameter computations for the three beam configuration cases are shown in Tables 2.2, 2.3 and 2.4.

To verify the validity of the non-dimensional parameters for large perturbation effects, it is reasonable to compare the predicted buckling force with the exact buckling force since the buckling load is proportional to the stiffness and the resonant frequency is proportional to the square root of the stiffness. The predicted force required for buckling in bending is determined by setting the non-dimensional parameter associated with a bending frequency perturbation to negative one and solving for F. For the clamped-free case the predicted buckling load, $\frac{-2.597EI}{l^2}$, is 5.2% greater than the exact buckling load, $\frac{-\pi^2 EI}{4l^2} \doteq \frac{-2.469EI}{l^2}$ [54]. This implies that eigenfrequency perturbations are underestimated by roughly 2.6% for large perturbations. For the pinned-pinned and free-free cases the buckling load predictions are the same which is promising since the exact buckling loads for the two configurations are known to be the same. It was found that the predicted buckling load for the two cases, $\frac{-12.05EI}{l^2}$, was 22.1% greater

than the exact buckling load, $\frac{-\pi^2 EI}{l^2} \doteq \frac{-9.87EI}{l^2}$ [54]. Thus, for large perturbations, the pinned-pinned and free-free non-dimensional parameters would underestimate the effect on the resonant frequency by approximately 10.5%. These errors are reasonable in light of the large perturbation magnitudes required to achieve buckling (the smaller the perturbation the more accurate the prediction). These results would seem to indicate that the methodology and results of this analysis are in order.

It should be mentioned here that even for small perturbations there is an error in the effect predicted by the non-dimensional parameter, due to the combined result of having used a single beam element in our analytical treatment, and the fact that the beam element was constructed using standard static deflection-based interpolation functions. Solving the general symbolic eigensystem equations for higher order multi-element configurations would have been preferable but was not successful (the existence of a solution is not guaranteed). For uniform beam elements subject to simple tip boundary conditions of the sort studied here it has been found that one can predict reasonably well as many eigenfrequencies as there are Hermitian[1] beam elements [66] (which is not true of isoparametric beam elements). Rough estimates can also be made of the next higher eigenfrequency. It is a characteristic of the finite element method that as the number of elements is increased, convergence in the eigenfrequency prediction is always achieved from above (i.e. adding elements always reduces the stiffness while increasing the accuracy). For a single element, clamped-free beam a typical error in the first eigenfrequency prediction is less than 0.5% (an excellent result which is to be expected since the interpolation functions resemble the dynamic clamped-free mode shapes). But for the pinned-pinned case (whose exact dynamic mode shape is a pure sinusoidal function and is not as well approximated by the interpolation functions) the error for the first single-element eigenfrequency prediction can be as high as 10%. For the second, single-element eigenfrequency prediction the error increases to 20% for the clamped-free beam and 25% for the

[1]As were used in this analysis, see Section 2.2.1.

Table 2.2: Non-Dimensional Parameters for Clamped-Free Beam Sensitivity to Gravity Load Effects

Load Type	Effect	Non-Dimensional Parameter
axial load	1st bending freq. pert.	$\frac{0.385Fl^2}{EI}$
(F_x)	2nd bending freq. pert.	$\frac{0.049Fl^2}{EI}$
	1st torsion freq. pert.	$\frac{0.833FI_x}{AGJ}$
	1st bending – 2nd bending coupling	$\frac{-0.0081Fl^2}{EI}$
bending load	1st bending – torsion coupling	$\frac{0.972M\sqrt{I_xA}l^2}{3.466EI_xI_y-AGJl^2}$
(M_y or M_z)	2nd bending – torsion coupling	$\frac{1.354M\sqrt{I_xA}l^2}{336.7EI_xI_y-AGJl^2}$
torsional load	1st z-bend. – 2nd y-bend. coupling	$\frac{-2.84Ml}{E(I_y-97.1I_z)}$
(M_x)	2nd z-bend. – 1st y-bend. coupling	$\frac{2.84Ml}{E(97.1I_y-I_z)}$

pinned-pinned beam. Thus, while the symbolic non-dimensional parameters are useful given their general form and ease of evaluation, they cannot be expected to yield exact dynamic perturbation effect predictions.

Inspecting Tables 2.2, 2.3 and 2.4 reveals that, in general, the impact of the initial stress loading is greatest on the fundamental eigenfrequencies. This supports the use of the single beam element approach which is only valid for the lowest eigenpairs. Tables 2.2, 2.3 and 2.4 also indicate, as expected, that the effects of initial stress stiffening can be very important on closely spaced modes. Given that closely spaced modes are a typical occurrence in structures at medium and high frequencies, and particularly for structures which have planes of symmetry, the effects of initial stress stiffening cannot be discounted at high frequencies.

Table 2.3: Non-Dimensional Parameters for Pinned-Pinned Beam Sensitivity to Gravity Load Effects

Load Type	Effect	Non-Dimensional Parameters
axial load (F_x)	1st bending freq. pert.	$\frac{0.083Fl^2}{EI}$
	2nd bending freq. pert.	$\frac{0.017Fl^2}{EI}$
	1st torsion freq. pert.	$\frac{0.833FI_x}{AGJ}$
	1st bending – 2nd bending coupling	0
bending load (M_y or M_z)	1st bending – torsion coupling	0
	2nd bending – torsion coupling	0
torsional load (M_x)	1st z-bend. – 2nd y-bend. coupling	$\frac{-1.75Ml}{E(I_y-21I_z)}$
	2nd z-bend. – 1st y-bend. coupling	$\frac{0.25Ml}{E(21I_y-I_z)}$

Table 2.4: Non-Dimensional Parameters for Free-Free Beam Sensitivity to Gravity Load Effects

Load Type	Effect	Non-Dimensional Parameters
axial load (F_x)	1st bending freq. pert.	$\frac{0.083Fl^2}{EI}$
	2nd bending freq. pert.	$\frac{0.02Fl^2}{EI}$
	1st torsion freq. pert.	$\frac{0.833FI_x}{AGJ}$
	1st bending – 2nd bending coupling	0
	xy or xz tilt stiffening	$\frac{0.166Fl}{EI}$
bending load (M_y or M_z)	1st bending (y or z) – torsion coupling	0
	2nd bending (y or z) – torsion coupling	$\frac{-0.833M_zAl^3}{583.3EI_xI_y-AGJl^2}$
	xy or xz tilt – torsion coupling	$\frac{-0.4Ml}{GJ}$
torsional load (M_x)	1st z-bend. – 2nd y-bend. coupling	$\frac{-0.466Ml}{E(I_y-11.7I_z)}$
	2nd z-bend. – 1st y-bend. coupling	$\frac{0.333Ml}{E(11.7I_y-I_z)}$
	xy or xz tilt – same plane 1st bending	$\frac{0.417Ml}{EI}$

2.4 Beam Element Initial Deformation Effects

2.4.1 General Observations

As detailed in Section 2.1.3, to describe the system property matrices and eigenvectors of a deformed structure in the original global coordinates, it is necessary to transform or rotate the individual elements prior to their assembly. For an n degree of freedom structure the global system property matrices M and K are n by n. If the elemental $K^{(m)}$ and $M^{(m)}$ matrices are written in the global n by n form (i.e. padded with zeros) we can write the global system property matrices as a sum of the element property matrices

$$^{o}K = \sum_{m} K^{(m)} \tag{2.154}$$

$$^{o}M = \sum_{m} M^{(m)} \tag{2.155}$$

When the structure undergoes initial deformation after being suspended in a gravity field, the individual $K^{(m)}$ and $M^{(m)}$ must be transformed prior to assembly

$$^{t}K = \sum_{m} T^{(m)^T} K^{(m)} T^{(m)} \tag{2.156}$$

and

$$^{t}M = \sum_{m} T^{(m)^T} M^{(m)} T^{(m)} \tag{2.157}$$

Unless all $T^{(m)}$ are the same, it is not generally possible to write the global system property matrices as a single global transformation of the assemblage, i.e.

$$^{t}K \neq T^T \left(\sum_{m} K^{(m)} \right) T \tag{2.158}$$

$$^{t}M \neq T^T \left(\sum_{m} M^{(m)} \right) T \tag{2.159}$$

Therefore the mass and stiffness matrices of the deformed structure, written in the original global coordinates, cannot generally be expressed as a projection of the original mass and stiffness matrices. It is possible however, in the case of a single element (or a portion thereof) undergoing initial deformation. In this case we can write the eigenproblem as

$$\left(T^T\left(M^{-1}K\right)T\right)T^{-1}\,{}^o\Phi = T^{-1}\,{}^o\Phi\Lambda \tag{2.160}$$

We can subsequently write the following simple relation for the effect of initial deformations on the eigenvectors of a single element

$${}^t\Phi = T^{-1}\left({}^o\Phi\right) \tag{2.161}$$

To make further observations it is necessary to identify T.

The transformation matrix $T^{(m)}$, for any element, will always be some combination of elemental rotations except in the case of distortion of the element. Given the assumption of large displacements and small strains, it is assumed here that there are a sufficient number of elements in the structure to represent the structural deformations without distorting the elements. The latter assumption should always be the case in a sound finite element model to ensure valid static and dynamic finite element model predictions [45]. Using the global reference frame depicted in Figure 2-3, and the same ordering of beam element degrees of freedom as in Equation (2.63), the elemental transformation matrix is

$$T^{(m)} = \begin{bmatrix} \mathcal{R} & 0 & 0 & 0 \\ 0 & \mathcal{R} & 0 & 0 \\ 0 & 0 & \mathcal{R} & 0 \\ 0 & 0 & 0 & \mathcal{R} \end{bmatrix} \tag{2.162}$$

Table 2.5: General Nature of Initial Deformation Effects on Beam

Deformation Type	Nature of Pre-Deformation Effect
Droop or Sag (R_y)	couples axial and vertical bending modes. couples torsion and horizontal bending modes.
Twist (R_x)	couples out-of-plane bending modes.

For a pure vertical plane rotation, which corresponds to droop or sag

$$\mathcal{R} = R_y = \begin{bmatrix} \cos(\theta) & 0 & -\sin(\theta) \\ 0 & 1 & 0 \\ \sin(\theta) & 0 & \cos(\theta) \end{bmatrix} \tag{2.163}$$

and for a twisting initial deformation about the beam neutral axis

$$\mathcal{R} = R_x = \begin{bmatrix} 1 & 0 & 0 \\ 0 & \cos(\theta) & \sin(\theta) \\ 0 & -\sin(\theta) & \cos(\theta) \end{bmatrix} \tag{2.164}$$

The role of rotation in the initial deformation class of gravity effects is plain here and not hidden as in the case of the initial stress effect (where infinitesimal rotations contribute to the non-linear strain which fundamentally leads to the geometric stiffening).

From the relation of Equation (2.161) it is possible to identify the very general nature of the initial deformation effect on a beam. Table 2.5 lists the couplings induced by the two initial deformation types.

In the case of droop, the perturbation to the vertical plane dynamics is limited to a coupling with the axial dynamics. Given the high axial stiffness as compared to the vertical bending stiffness (which is necessarily very low in the case of finite droop or sag), this coupling will have a minimal effect on the eigensystem of most

structures. The coupling of the torsional dynamics with the horizontal dynamics, on the other hand, has the potential to become a very important effect. The coupling of out-of-plane bending modes due to torsional initial deformations is another possibly important effect. However, given our assumption of a uniform beam cross-section, an out-of-plane structural mass would be required to impart an initial twisting deformation to the beam component.

2.4.2 Initial Deformations of an Assemblage

To rotate all degrees of freedom of a single element, whether it is clamped-free, pinned-pinned or free-free, simply results in a change of basis of the eigenvectors and does not fully capture the effects of initial deformation on the eigensystem of a structure. The fundamental nature of this effect, rather, is a relative deformation of two parts of a structure. Thus, to capture the effects of finite deformations of a structure due to gravity, it is necessary to study a free-free element with only one tip deformed, or to use two or more elements for other boundary conditions.

The configuration studied in this work is a free-free beam element where only one node is subject to the initial deformation effects. The two other configurations recommended for future study are a two-element clamped-free beam, where the second element has drooped some angle, say α, with respect to the first element and a pinned-pinned beam, where the two beams sag at an angle of α with respect to the horizontal (depicted in Figure 2-6). These configurations each have twelve degrees of freedom and are recommended for study before the more complex eighteen degree of freedom kinked, two element, free-free beam.

For the twelve degree of freedom free-free beam the effects of droop and twist are studied using the techniques developed in the previous section; i.e. the original free-free beam eigenvectors are used to project the perturbed eigensystem unto the original eigenspace and non-dimensional parameters are identified.

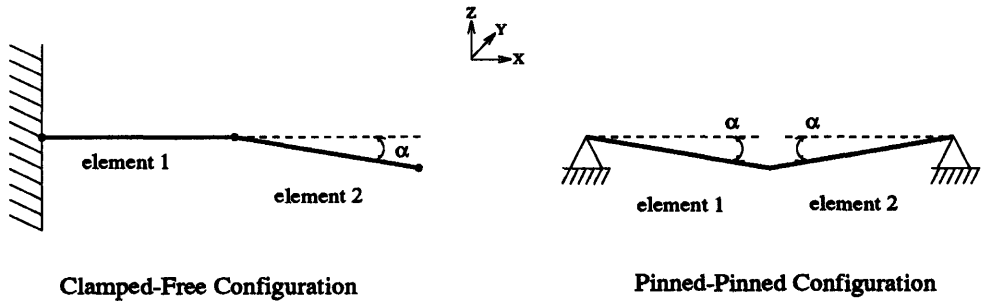

Figure 2-6: Droop Initial Deformation Effect Configurations Recommended for Analysis

2.4.3 Eigensystem Sensitivity Analysis

Beam Droop Effect

For a free-free horizontal beam element, for which one tip is subject to a rotation α in the vertical plane, we have a perturbation to the system matrices which when projected onto the original eigenspace with the transformation of Equation (2.165) yields a sensitivity matrix Ψ_{Ry} with first and second order sin and cos terms.

$$\Psi_{Ry} = {}^{o}\Phi^{-1} R_y^T \left(M^{-1}K\right) R_y {}^{o}\Phi \tag{2.165}$$

In the case of small deformations and small angles of rotation the result simplifies to Equation (2.167) shown on page 107.

Beam Twist Effect

For a beam element where one tip is subject to a small rotation α about the beam neutral axis (which corresponds to the global X axis in the convention adopted here) we have the transformation

$$\Psi_{Rx} = {}^{o}\Phi^{-1} R_x^T \left(M^{-1}K\right) R_x {}^{o}\Phi \tag{2.168}$$

which results in Equation (2.166) on page 107 when one assumes a small initial or incremental deformation.

$$\Psi_{Rx} = \frac{1}{\rho A l}\begin{bmatrix} \frac{12.48EI_y}{l^3} & 0 & \frac{12.48(-EI_y+EI_z)\beta}{l^3} & 0 & 0 & 0 \\ 0 & \frac{1212.EI_y}{l^3} & 0 & \frac{1212.(-EI_y+EI_z)\beta}{l^3} & 0 & 0 \\ \frac{12.48(-EI_y+EI_z)\beta}{l^3} & 0 & \frac{12.48EI_z}{l^3} & 0 & 0 & 0 \\ 0 & \frac{1212.(-EI_y+EI_z)\beta}{l^3} & 0 & \frac{1212.EI_z}{l^3} & 0 & 0 \\ 0 & 0 & 0 & 0 & \frac{3EA}{l} & 0 \\ 0 & 0 & 0 & 0 & 0 & \frac{3.6AGJ}{I_x l} \end{bmatrix} \tag{2.166}$$

$$\Psi_{Ry} = \frac{1}{\rho A l}\begin{bmatrix} \frac{12.48EI_y}{l^3} & 0 & 0 & 0 & \frac{\left(4.16EI_y-EAl^2\right)\beta}{0.3184l^3} & 0 \\ 0 & \frac{1212.EI_y}{l^3} & 0 & 0 & \frac{\left(-403.84EI_y+EAl^2\right)\beta}{2.456l^3} & 0 \\ 0 & 0 & \frac{12.48EI_z}{l^3} & 0 & 0 & \frac{\left(3.467EI_zI_x-AGJl^2\right)\beta}{2.023I_x\sqrt{\frac{I_x}{A}}l^2} \\ 0 & 0 & 0 & \frac{1212.EI_z}{l^3} & 0 & \frac{\left(-336.5EI_zI_x+AGJl^2\right)\beta}{2.818I_x\sqrt{\frac{I_x}{A}}l^2} \\ \frac{\left(4.16EI_y-EAl^2\right)\beta}{0.2859l^3} & \frac{\left(403.84EI_y-EAl^2\right)\beta}{0.2051l^3} & 0 & 0 & \frac{3EA}{l} & 0 \\ 0 & 0 & \frac{\left(-3.467EI_zI_x+AGJl^2\right)\beta}{0.173\sqrt{AI_x}l^4} & \frac{\left(-336.5EI_zI_x+AGJl^2\right)\beta}{0.02243\sqrt{AI_x}l^4} & 0 & \frac{3.6AGJ}{I_x l} \end{bmatrix} \tag{2.167}$$

2.4.4 Observations and Non-Dimensional Parameters

Inspecting the beam twist and beam droop sensitivity matrices Equations (2.166) and (2.167), shows that the effect of beam twist is limited to a coupling of the out-of-plane bending modes while the effect of beam droop is to couple axial modes with bending in the droop plane, and torsional modes with bending out of the droop plane. The nature of these effects of twist and droop correspond to the torsional load and bending load induced stress stiffening effects respectively (see Section 2.3.1), as one would expect.

Using the same approach as in Section 2.3.4 we can now identify non-dimensional parameters for the partially deformed free-free beam element using the sensitivity matrices of Equations (2.166) and (2.167). Since no pure eigenfrequency perturbations are evident in Equations (2.166) and (2.167) we are uniquely concerned with eigenmode coupling. As was done in the study of the stress stiffening effect on the eigenvectors, the initial deformation effect non-dimensional parameters are obtained by taking the ratio of the off-diagonal element and the difference in the corresponding original diagonal elements, i.e.

$$\Gamma_{ij} = \frac{c_{ji}\Delta\beta_{ji}}{{}^{o}\lambda_i - {}^{o}\lambda_j} \tag{2.169}$$

The results of these computations are listed in Table 2.6. It is interesting to note that the sensitizing effect of closely spaced modes (which is apparent in the eigenvalue difference of the coupling coefficient denominator, Equation (2.126)) is offset by the same difference in the numerator of the off-diagonal modal coupling terms.

2.5 Verification and Sample Problem Analysis

In this section we apply the technique of redefining a structure to capture initial deformation effects and the technique of updating the system stiffness with the geometric stiffness matrix K_g (or K_{gd}) to capture stress stiffening effects. The validity and performance of these methods in correctly computing the perturbations to the eigenstructure of a beam is tested for the case of a drooping beam.

Table 2.6: Non-Dimensional Parameters for Clamped-Free Beam Sensitivity to Initial Deformation Effects

Pre-Deform.	Effect is to Couple	Non-Dim. Parameter	Condition
twist	1st z-bending – 1st y-bend.	β	$EI_y \neq EI_z$
(R_x)	2nd z-bending – 2nd y-bend.	β	$EI_y \neq EI_z$
	1st vert. bending – axial	1.047β	$EI_y \neq \frac{EAl^2}{4.16}$
droop	2nd vert. bending – axial	0.1357β	$EI_y \neq \frac{EAl^2}{403.8}$
(R_y)	1st hor. bending – torsion	$0.1373\sqrt{\frac{A}{I_x}}\beta l$	$EI_zI_x \neq \frac{AGJl^2}{3.467}$
	2nd hor. bending – torsion	$0.0985\sqrt{\frac{A}{I_x}}\beta l$	$EI_zI_x \neq \frac{AGJl^2}{3.467}$

Comparisons between the effects of initial deformation and of stress stiffening are made. In addition the performance of the concentrated nodal load geometric stiffness matrix K_g is compared with that of the concentrated plus distributed load geometric stiffness matrix K_{gd} derived in section 2.2.3.

The verification case is the dynamic analysis of Minguet and Dugundji [30] in their study of a horizontal drooping slender beam. This case was found to be principally affected by initial deformation. Also studied is the case of a vertical beam under tension to verify the geometric stiffness refinement and to again compare the performance of K_{gd} versus K_g.

2.5.1 Effect of Distributed Bending Moment and Beam Droop

In this subsection we compare the eigensolutions predicted by an initial deformation refinement, and by a K_g and K_{gd} refinement with those predicted by Minguet and Dugundji in their study of the dynamics of long slender (helicopter-blade type) beams subject to uniform bending loads [30]. This latter case examines the modeling of bending-torsion coupling due to transverse loading and beam droop. Highlighted in the verification analysis is the derivation of expressions for the internal nodal loads (F_x^A, F_x^B, M_y^A, M_y^B, M_z^A, M_z^B, ...) which are the result of internal element stresses and

are not to be confused with the external applied nodal loads (R_x^A, R_x^B, etc...).

Nodal Load Computation

To compute the numerical geometric stiffness matrix $K_g^{(m)}$ or $K_{gd}^{(m)}$ of an element, (e.g. Equation (2.96) or Equation (2.97) for a beam element), it is necessary to first have computed the internal nodal loads of the element, $F^{(m)}$. Sophisticated finite element software typically performs the computation of $F^{(m)}$ by numerical integration of the following

$$F^{(m)} = \int_V^{(m)} B^{(m)^T} \tau^{(m)} \, dV^{(m)} \tag{2.170}$$

where $B^{(m)}$ is the strain-displacement matrix (Equation (2.30)), and $\tau^{(m)}$ is the element stress vector obtained from the product of the strain vector $\epsilon^{(m)}$ and the constitutive matrix $C^{(m)}$ (Equation (2.4))

$$\tau^{(m)} = C^{(m)} \epsilon^{(m)} = C^{(m)} B^{(m)} U^{(m)} \tag{2.171}$$

If one knows the consistent external applied loads, integration is not necessary to obtain the internal nodal loads. The consistent external applied loads which correspond to a uniformly distributed load on a beam element are [48] as shown in Figure 2-7, and are determined by the integration

$$R^{(m)} = \int H^{(m)^T} f^{(m)} \, dV^{(m)} \tag{2.172}$$

The external nodal loads determined with Equation (2.172) are named consistent as they make use of the same interpolation matrix as used by the displacements, i.e. $H^{(m)}$. By integrating the distributed forces $f^{(m)}$ weighted by $H^{(m)}$ one is assured that the resulting nodal loads will perform the same work as the distributed loads when deforming the structure. This is in contrast to the use of "plain"lumped nodal forces which are determined by simply dividing the applied distributed loads equally

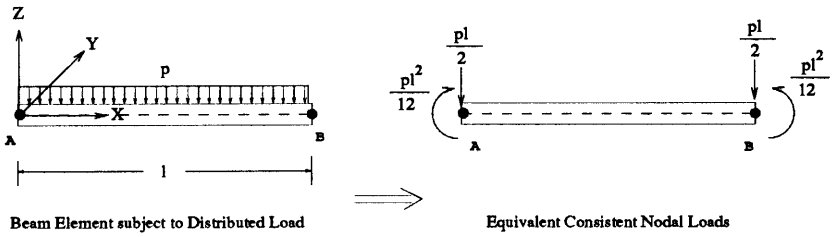

Figure 2-7: Example of Consistent Nodal Loads for a Beam Element subject to Uniform Distributed Transverse Load

between the element nodes. For example, the plain lumped forces for the loading of Figure 2-7 would not include the nodal bending moments.

The steps in computing the internal nodal loads given the consistent external nodal loads are:

1. compute reaction forces,
2. sum external nodal loads and reaction forces to obtain internal nodal forces at geometric boundary conditions, and
3. apply equilibrium principles to determine remaining internal nodal forces.

For a single horizontal beam element (of length h, density ρ, and cross-sectional area A) cantilevered at node A and subject to gravitational loading, the above procedure yields the following consistent nodal loads

$$\begin{aligned} F_z^A &= \frac{\rho A g h}{2} \\ F_z^B &= -\frac{\rho A g h}{2} \\ M_y^A &= -\frac{5\rho A g h^2}{12} \\ M_y^B &= -\frac{\rho A g h^2}{12} \end{aligned} \tag{2.173}$$

or, for an N element beam of length l ($n = 1, 2, 3 \ldots N$), the internal nodal loads of

the n^{th} element are

$$\begin{aligned} F_z^A &= \rho Agl - (\rho Agh)(n - \frac{1}{2}) \\ F_z^B &= -F_z^A \\ M_y^A &= \frac{\rho Agh^2}{12} - \frac{\rho Ag((N+1-n)h)^2}{2} \\ M_y^B &= -M_y^A - F_z^A h \end{aligned} \tag{2.174}$$

where the element length h is uniform, i.e. $h = l/N$.

If distributed forces are permitted in the load and stress state description, as must be the case when using K_{gd}, the equilibrium relations change to allow for the distributed forces and we now obtain the following internal nodal loads for the n^{th} element

$$\begin{aligned} F_z^A &= \rho Agl - \rho Ag(n-1)h \\ F_z^B &= -F_z^A + \rho Agh \\ M_y^A &= -\frac{\rho Ag((N+1-n)h)^2}{2} \\ M_y^B &= -M_y^A - F_z^A h + \frac{\rho Agh^2}{2} \end{aligned} \tag{2.175}$$

Analysis Procedure

Using the internal nodal forces of Equations (2.175) and the geometric stiffness matrix K_g of Equation (2.97), (or the internal nodal forces of Equations (2.176) and the distributed geometric stiffness matrix $K_g d$ of Equation (2.105)), as well as the transformation matrix of Equations (2.162) and (2.163) we are now in a position to study the effect of droop or sag on a beam or beam-type structure. To compute the eigensystem of the deformed beam, subject to geometric stiffening effects, the iterative procedure outlined in Figure 2-8 was followed.

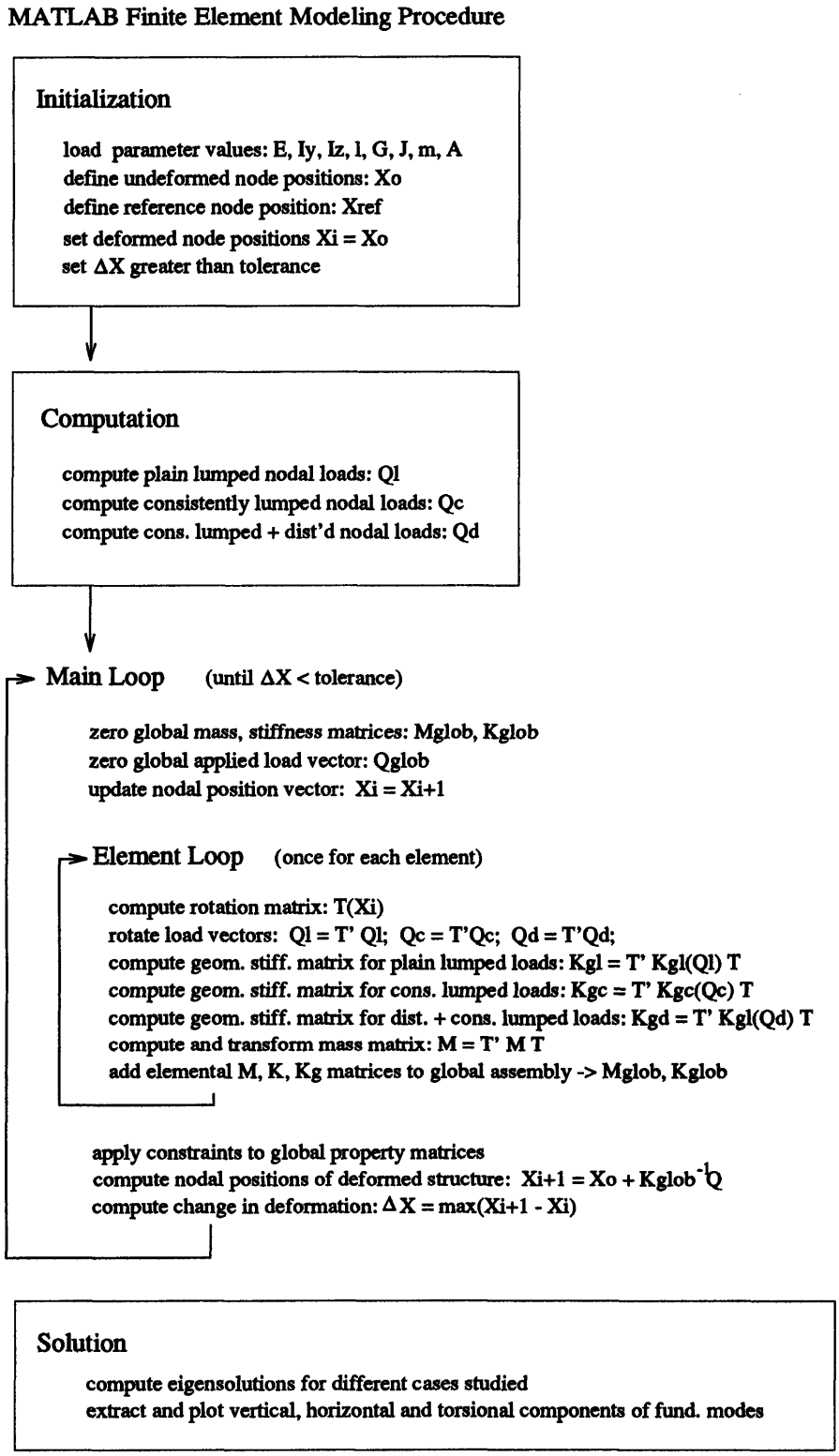

Figure 2-8: MATLAB-based Finite Element Procedure Flowchart

Non-Dimensional Parameter Computation

Based on the general observations of Section 2.3.1 and Section 2.4.1, and on Tables 2.1 and 2.5, we expect to observe coupling between the horizontal bending modes and the torsional modes of the clamped-free horizontal Minguet beam due to initial droop and a bending-moment-induced geometric stiffening. To evaluate the effectiveness of the non-dimensional sensitivity parameters derived in Sections 2.3.4 and 2.4.1 we compute here the two parameters describing the magnitude of the geometric stiffening non-dimensional parameter and the initial deformation non-dimensional parameter for the bending-torsion coupling case. Using homogeneous beam parameters which approximate the properties of the Minguet graphite-epoxy composite beam (listed in Appendix B) we obtain

$$\Gamma_{kg} = \frac{0.972M\sqrt{I_x A}\,l^2}{3.466EI_xI_y - AGJl^2} = -0.05075M \approx 0.003 \tag{2.176}$$

for the first bending-torsion coupling non-dimensional parameter based on the geometric stiffness parameter expression from Table 2.1. The very small value of Γ_{kg} indicates that the geometric stiffness effect is negligible for the clamped-free Minguet beam. Substituting the same Minguet beam properties in the initial deformation parameter expression from Table 2.5 for first bending-torsion coupling, we obtain

$$\Gamma_{def} = 0.1373\sqrt{\frac{A}{I_x}}l\beta = 8.078\beta \approx 1.57 \tag{2.177}$$

The non-dimensional parameter associated with the initial deformation effect indicates, on the other hand, very significant coupling between bending and torsion. In fact, since the coupling parameter is close to unity one would expect the new modes to have roughly equal contributions of the two original modes.

Results

Using 15 elements to model the horizontal clamped-free beam, as did Minguet and Dugundji [30], an unloaded or 0–g model was first derived using a load vector of zero. The first vertical bending, torsion, and horizontal bending modes of this model, along with associated eigenfrequencies, are shown in the lower-half of Figure 2-9 under the Minguet/Reference results for the unloaded beam. It can be seen quite clearly that the eigenmodes of the MATLAB model are nearly identical to the Minguet model eigenmodes and that the vertical bending frequencies are exactly the same. The torsion and horizontal bending frequencies on the other hand are quite different with errors of +10.6% and +3.8% respectively. These errors are the necessary result of modeling a 6 ply (3 ply symmetric) graphite-epoxy composite beam as a homogeneous beam while the more sophisticated model of Minguet and Dugundji included descriptions of each layer. The equivalent beam properties derived from the composite were tuned to obtain the proper mass and stiffness distribution in the vertical/droop plane. This resulted in an exact match between the computed tip deflection and Minguet's reported tip deflection of 2% of the beam length, i.e. 11.2 mm.

Three different 1–g models were then derived for comparison with the Minguet model 1–g results. The 1–g Minguet/Reference results are shown in the upper half of Figure 2-10. The first 1–g model derived, shown in Figure 2-10 beneath the Minguet results, was the best possible model and includes the effects of both initial deformations and K_{gd} geometric stiffening. The results are excellent in light of the original frequency discrepancy. The MATLAB model successfully reproduced the magnitude and shape of the coupled torsion–bending modes. The frequencies of the two new coupled modes shifted in the appropriate directions and by nearly the right magnitude but not quite sufficiently, i.e. the error in the lower torsion-bending mode is now +12.2% (instead of +10.6%) and the error in the second bending-torsion mode is now +2.3% (instead of +3.8%). The MATLAB-based model therefore did not destiffen the original torsional mode by as much as Minguet predicted (-6.5 Hz versus -7.0

Hz), and did not stiffen the original horizontal bending mode by as much as Minguet predicted (+3.9 Hz versus +5.5). As the modal coupling and eigenfrequency shift was well captured the verification of the gravity effect modeling method was deemed successful. The next figure, Figure 2-11, shows the eigensolutions for the case of only including the effects of the initial deformation without a geometric stiffening refinement, and the case of only including the effects of geometric stiffening without a structure re-definition due to initial deformations. The initial deformation case very nearly reproduces the results of Figure 2-10 while the pure geometric stiffness case captures only the slightest amount of coupling. Clearly, in the case of a slight droop or sag, the major part of the gravity effect is captured by solving for the initial deformation and transforming the system matrices to global coordinates. This confirms the predictions made by the non-dimensional parameters in the prior subsection. As an aside it should be mentioned that the gravitational load applied by Minguet was actually upwards which was reflected in the MATLAB based model by the application of -1 g. A sign reversal has the effect of changing the relative phasing of the bending-torsion coupling.

2.5.2 Effect of Beam Tension

The second verification/sample problem studied is the case of a clamped-free vertically suspended beam. The effect of tension on the dynamics of a beam in bending is an extensively well-studied problem. Examined here however is the effectiveness of the finite element geometric stiffness method and in particular a comparison is made between the results obtained using K_g versus K_{gd}.

The homogeneous beam properties used in the previous horizontal beam study are used here again, i.e. the Minguet beam properties. Rather than apply a fixed gravity load of 1 g we examine here the effect of various load levels on the eigensystem. The axial load is expressed in units of the first bending frequency non-dimensional parameter, where a value of -1 corresponds to buckling. For ease of reference the

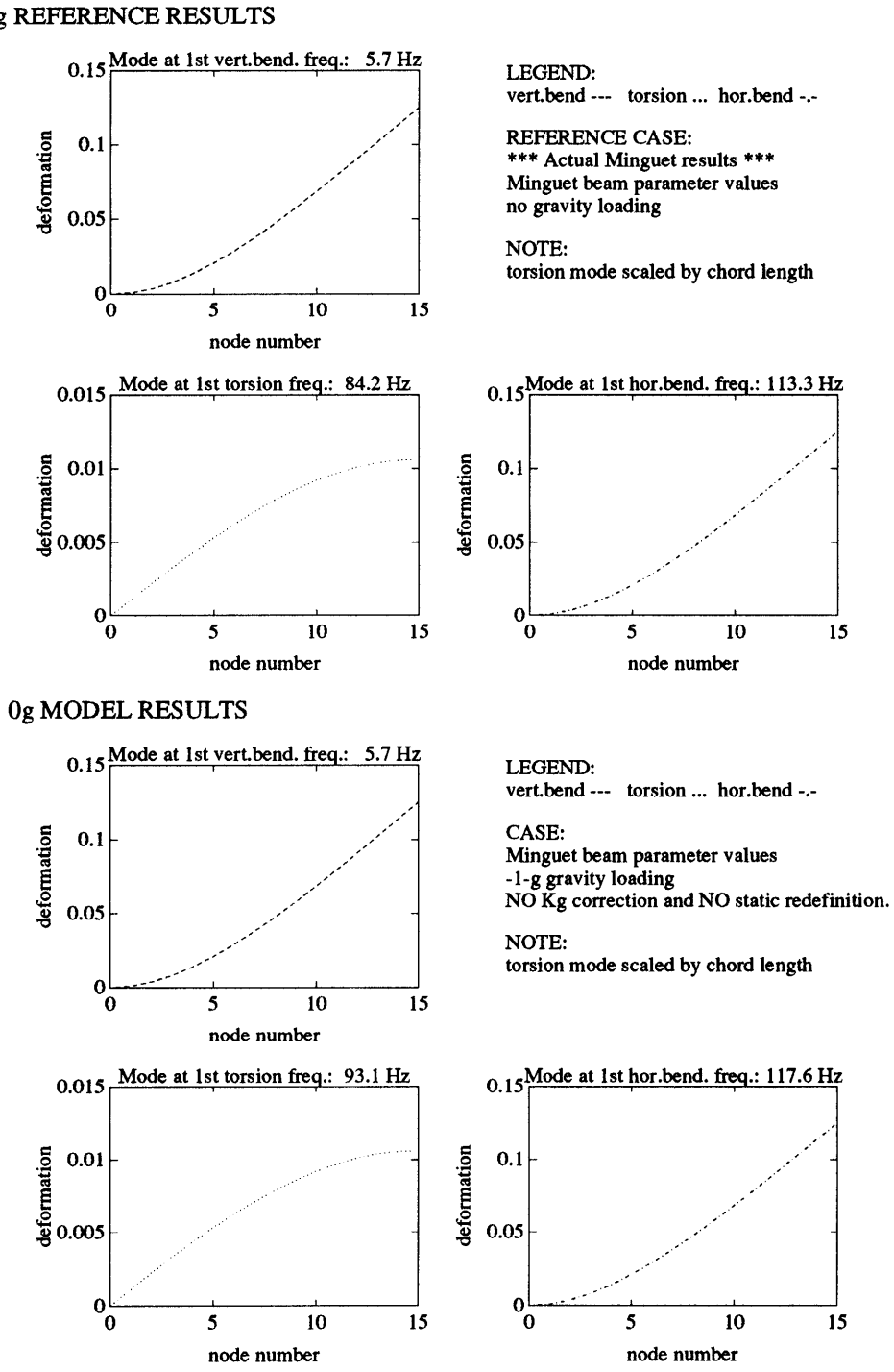

Figure 2-9: Comparison of 0–g Model Results with Minguet 0–g Results

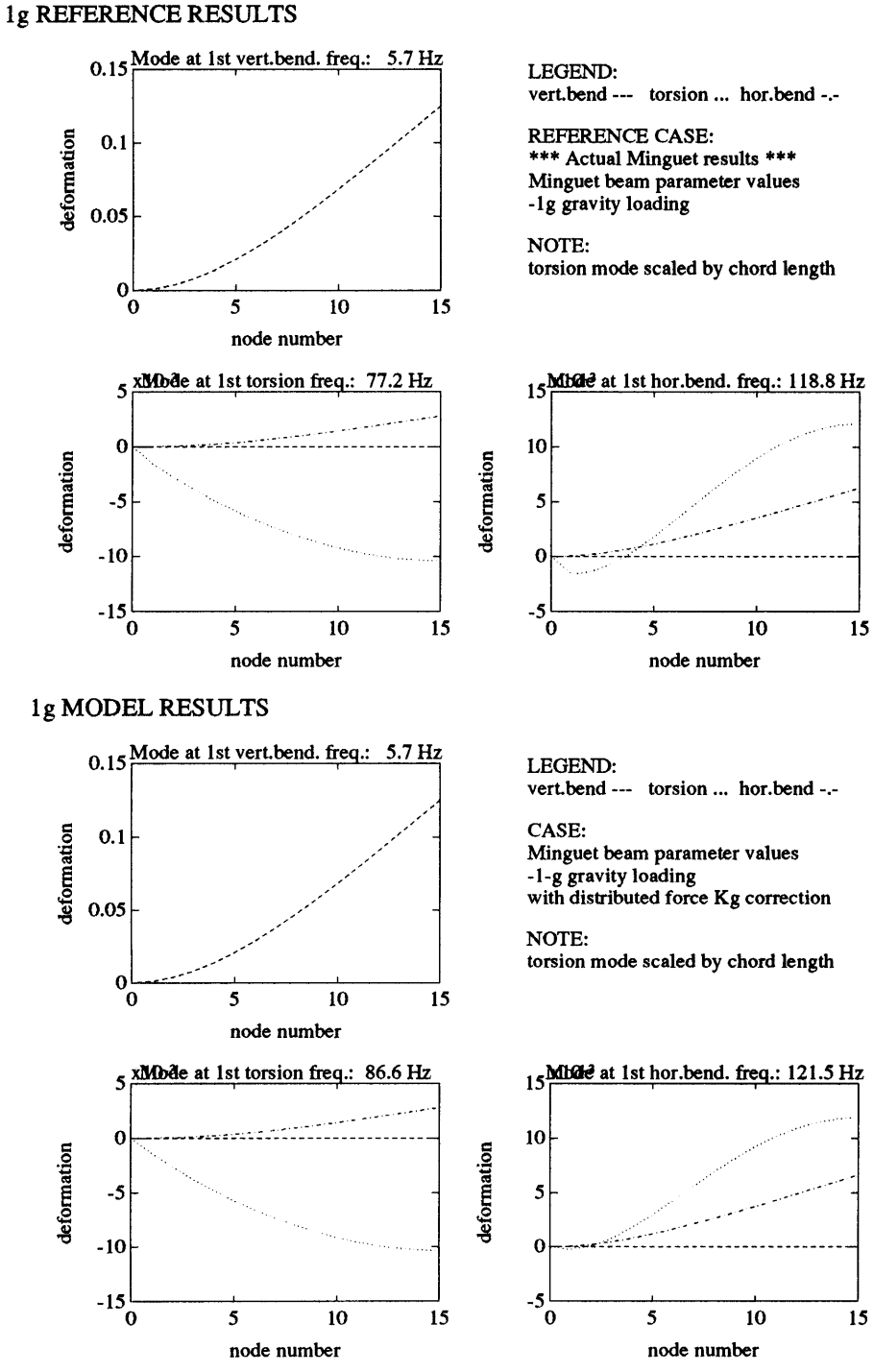

Figure 2-10: Comparison of 1–g Eigensystem Prediction with Minguet 1–g Results

1g MODEL RESULTS: Static re-definition only.

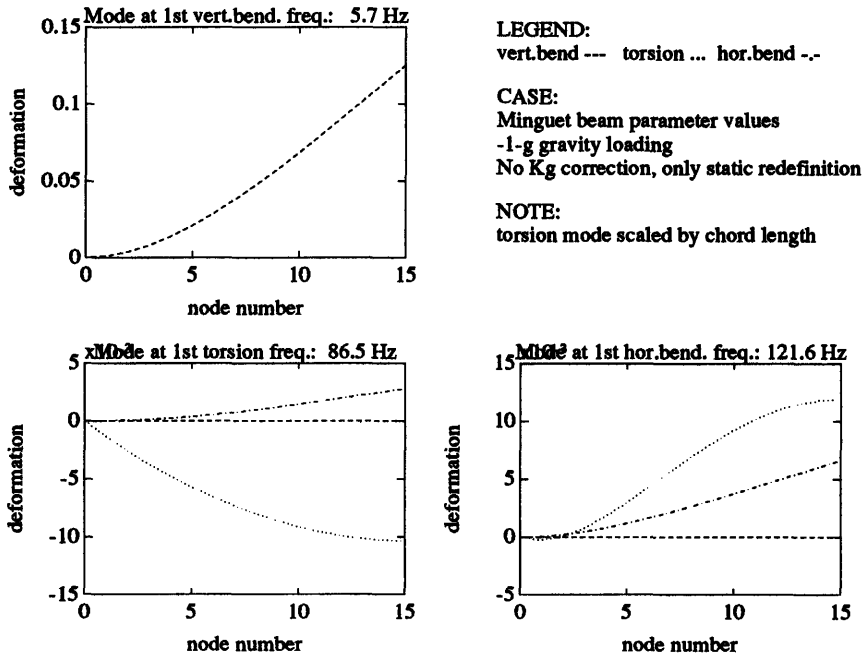

1g MODEL RESULTS: Kg correction only.

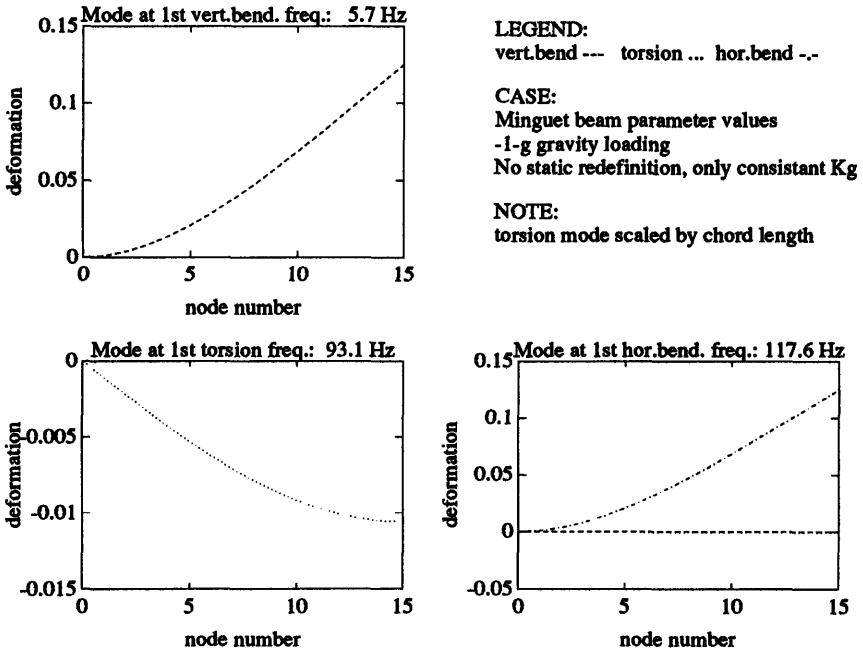

Figure 2-11: Comparison of Eigensystems Predicted using only an Initial Deformation Transformation and only a Geometric Stiffness Update for the case of a Drooping Beam

geometric stiffness non-dimensional parameter for an axial load induced perturbation to the first bending frequency is reproduced here from Table 2.1:

$$\Gamma_{kg} = \sqrt{\frac{0.385Fl^2}{EI}} \tag{2.178}$$

Nodal Load Computation

The internal nodal loads which correspond to the distributed gravitational loading of a vertically suspended clamped-free beam for the consistent nodal load case are

$$F_x^A = -\frac{\rho Agh(N-n+1)}{2} \tag{2.179}$$

$$F_x^B = \frac{\rho Agh(N-n+1)}{2} \tag{2.180}$$

where A is the clamped node, B is the free node, n is the element number from 1 to N, and the element lengths h are constant, i.e. $h = l/N$. Note the staircase nature of the loading. When using K_{gd} distributed loads are permitted between the discrete nodal loads so that the internal loads for this case are given by

$$F_x^A = -\rho Agh(N-n+1) \tag{2.181}$$

$$F_x^B = \rho Agh(N-n) \tag{2.182}$$

Analysis Procedure

The same methodology used in the beam droop case was used here, i.e. the MATLAB-based iterative finite element modeling procedure illustrated in Figure 2-8. Note that for the case of pure axial loads the deformations are typically negligible and the modeling process essentially consists of a single geometric stiffness refinement.

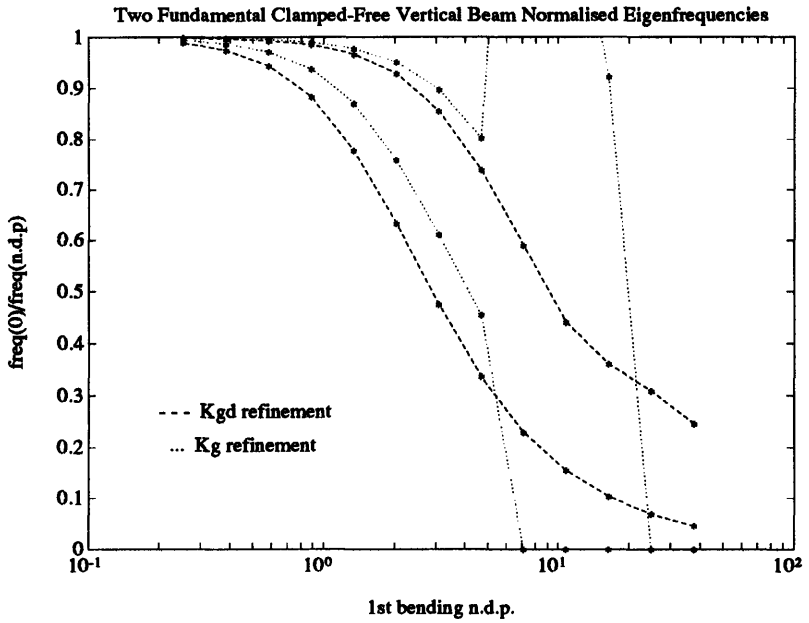

Figure 2-12: Effect of Distributed Axial Load on Eigenfrequencies of Clamped-Free Hanging Beam

Results

The eigenfrequencies of the two fundamental modes of the clamped-free beam are tracked versus increasing load in Figure 2-12. The eigenfrequencies are normalized and inverted for a compact plot. A downward slope indicates stiffening of the structure. For a non-dimensional parameter of one the first resonant frequency has increased by a factor of nearly ten-fold. Clearly, when the non-dimensional gravity effect sensitivity parameter is non-negligible with respect to one the geometric stiffening effect is important. Figure 2-12 also shows the improved performance obtained by using the distributed geometric stiffness matrix K_{gd} versus the pure consistent load derived geometric stiffness matrix K_g. The K_{gd} case is more stable under large loads and is more sensitive than using K_g. In terms of the effects on the eigenmodes the use of K_{gd} was again found to be more sensitive than the use of K_g. This can be seen in Figure 2-13 by comparing the lower three K_{gd} plots to the upper three K_g plots. It should be pointed out that the magnitude of the loads required to obtain a

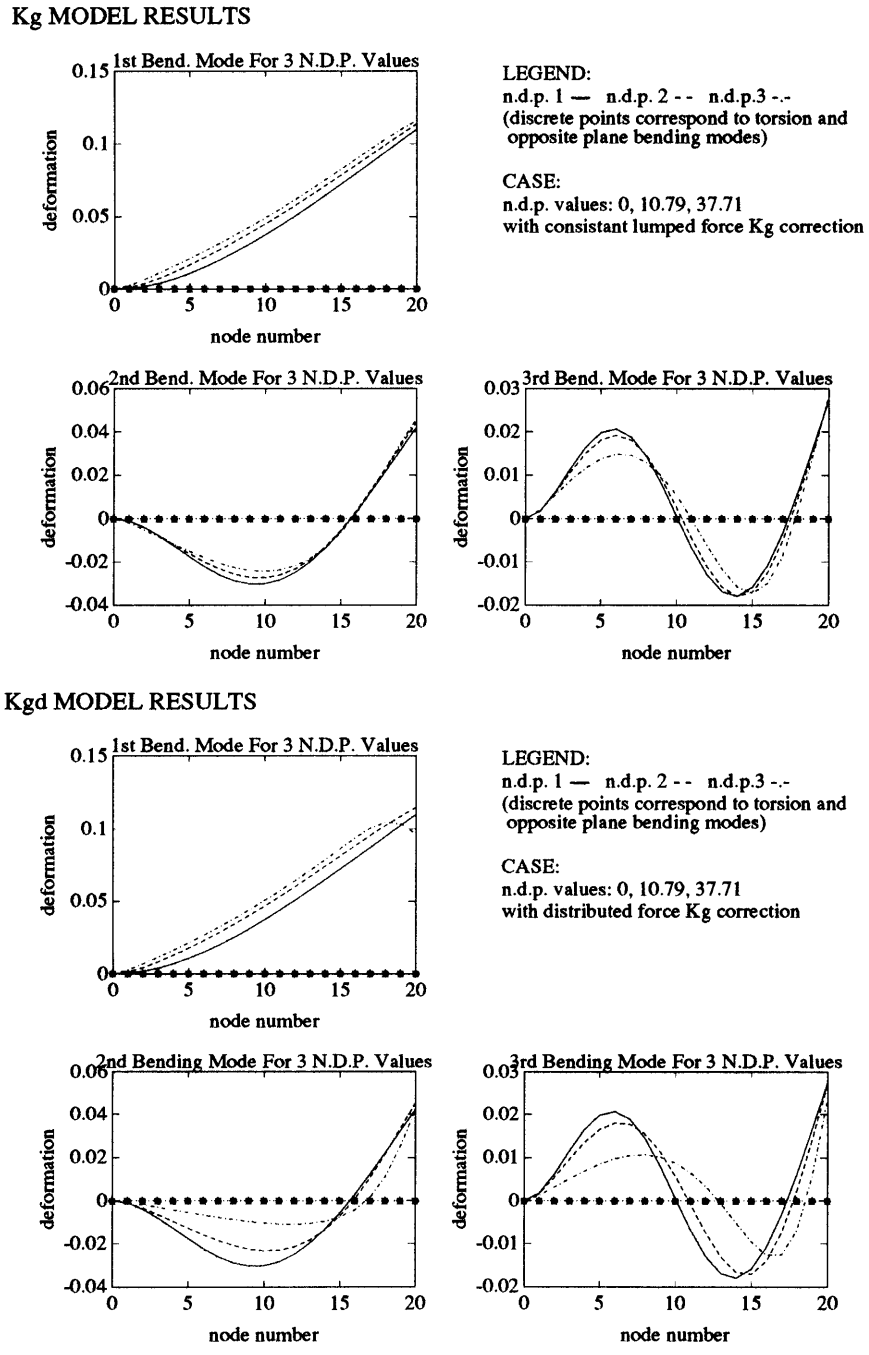

Figure 2-13: Effect of Distributed Axial Load on Eigenmodes of Clamped-Free Hanging Beam

substantial difference between the two predictions is large and therefore encountered less often. However, in cases where the loads are purely distributed and the axial component is large it would appear to be advantageous to use the geometric stiffness matrix derived in this thesis, i.e. K_{gd}, over the more common closed-form geometric stiffness matrix K_g.

Chapter 3

Suspension Effects on Structures

When performing ground-based tests of flexible space structures it is advantageous to support the structure in a manner which simulates the unrestrained boundary conditions of space as much as possible. The obvious goal is to minimize the effect of the suspension system on the dynamics of the test article so as to facilitate and enhance the prediction of on-orbit behavior and performance.

The fundamental approach is to minimize the mass, stiffness, damping and friction of the suspension system which participate in any modal behavior of the structure within the bandwidth of interest. For full three dimensional tests the result is typically a multi-attachment point suspension system with long pendular cables to minimize pendular stiffening and soft vertical springs. (Other gravity compensation techniques which allow full spatial motion such as neutral buoyancy environments, drop tube chambers and ballistic airplane flights are not viable for the respective reasons of high viscous damping, short test window and routine testing impracticality among others.) A typical goal is to have the suspension fundamental frequencies half a decade below the structure's first resonance [6, 67]. In one's attempt to keep the suspension system dynamics outside the test article's bandwidth of interest, it is sometimes necessary to push the higher suspension frequencies, e.g. cable modes and surge modes, above the highest structural eigenfrequency of interest. This objective, however, is in direct conflict with the objective of a soft suspension, complicating the

design of a simple spring suspension system; see Appendix C for details. Numerous suspension system designs which achieve very low bounce frequencies and overcome the practical limits of a simple extensional spring suspension have been proposed and successfully implemented, e.g. pneumatic-electric devices [16,17,21], spring lever arrangements [16, 68], zero-spring rate mechanisms [16, 68, 21], and active disk suspension systems [69]. Active control strategies are sometimes used to reduce any remaining coupling by generating cancellation forces to compensate for the participation of suspension inertias, stiffnesses, damping or friction. While these technologies have yielded promising results it is clear that achieving the required separation between the test article dynamics and the suspension dynamics is not always feasible, especially in the case of lightweight low frequency test articles. It is therefore typically required to augment the states of the system model to include the suspension system.

Whether or not one need include the suspension system in the plant model, and to what degree of fidelity, is a function of many things including: the magnitude of the frequency separation between the test article and the suspension system, the performance objective of the spacecraft (i.e. do the rigid-body modes affect the performance metric?), the authority of the control system (i.e. are the levels of control effort so high as to make important even small perturbations?), and the amount of initial deformation and gravity stiffening present since the attachment point boundary conditions are required for the computation of the loads and subsequent gravity effects on the structure. If the need to incorporate the suspension system is not immediately obvious, an appropriate first step towards answering these questions is to examine the correlation between the data and the model results. An appropriate second step is to model the suspension system using simple spring elements at the attachment points which captures the fundamental stiffening of the rigid-body modes. Finally, if the model to data correlation is poor it may be necessary to model the higher order suspension behavior such as cable modes where the dynamic behavior of the

cable mass is no longer neglected. Cable mode or surge mode behavior is typically easily identified in a transfer function as closely-spaced pole-zero pairs which appear as small "blips" at regular intervals in the transfer function. This observation is based on data from the MODE ground-based testbed and the MIT SERC Interferometer.

It is difficult to identify general suspension effects on a controlled flexible spacecraft given the dependence on the specific structural configuration and suspension configuration. In keeping with the focus on gravity effects on beam-type structures this chapter will briefly examine in an analytical manner (as opposed to the numerical treatment of Chapter 5 for the MACE test article) the effects of a soft suspension system on a suspended horizontal beam.

3.1 Static Stiffening Effects

The principal perturbing effect of the suspension system is to stiffen the rigid-body modes. This effect can be captured using static stiffness elements at the attachment points. This approach can be used in practice as a rudimentary suspension model if the higher frequency suspension behavior is well outside the test article bandwidth of interest. The spring constants in translation are established based on the bounce frequency ω_b, and the pendular frequency ω_p. The vertical stiffness, k_v, is given by

$$k_v = \omega_b^2 \, m_v \tag{3.1}$$

where m_v is the mass at the attachment point associated with the vertical deflection. The horizontal stiffness, k_h, is given by

$$k_h = \omega_p^2 \, m_h = \frac{m_h g}{l_s} \tag{3.2}$$

where m_h is the attachment point mass which is associated with the horizontal degree-of-freedom and l_s is the length of the suspension cable. This constrains five of the six

rigid-body modes. Assuming that spherical joints are used at the attachment points and that the center-of-mass of the uniform cross-section is below the attachment point, we can model the roll stiffness in terms of the test article double pendulum frequency ω_{p_2}. The torsional spring stiffness at the attachment point about the neutral axis is thus given by

$$k_\theta = \omega_{p_2}^2 \, I_\theta \tag{3.3}$$

where I_θ is the lumped inertia about the neutral axis for the given attachment point. The result is a set of three orthogonal extensional springs and a torsional spring along the beam axis at each attachment point as illustrated in Figure 3-1. The approximation here is that the suspension attachment points coincide with the beam neutral axis. In practice it may be necessary to refine further the torsional spring constant used to capture the rotational stiffening due to additional stiffening provided by the offset translational springs.

These natural boundary conditions are incorporated directly into the stiffness matrix by adding the spring constant to the diagonal element of K_o which corresponds to the degree-of-freedom which is constrained. In the case of a single beam element

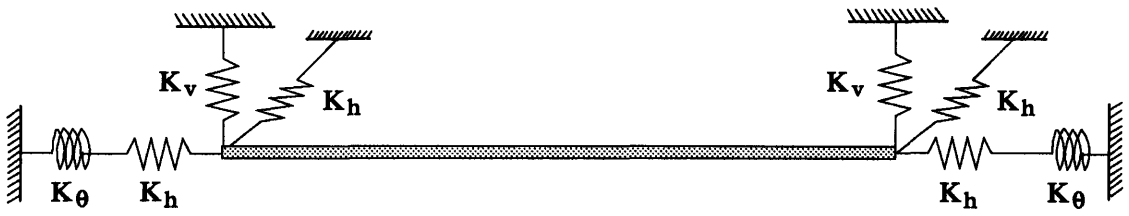

Figure 3-1: Static Modeling of Cable Suspension System

with a suspension cable attachment at each tip, we have

$$K_{susp} = \left[\begin{array}{cccccc|cccccc} \frac{AL\rho\omega_p^2}{2} & 0 & 0 & 0 & 0 & 0 & 0 & 0 & 0 & 0 & 0 & 0 \\ 0 & \frac{AL\rho\omega_p^2}{2} & 0 & 0 & 0 & 0 & 0 & 0 & 0 & 0 & 0 & 0 \\ 0 & 0 & \frac{AL\rho\omega_b^2}{2} & 0 & 0 & 0 & 0 & 0 & 0 & 0 & 0 & 0 \\ 0 & 0 & 0 & \frac{I_x L\rho\omega_{p_2}^2}{2} & 0 & 0 & 0 & 0 & 0 & 0 & 0 & 0 \\ 0 & 0 & 0 & 0 & 0 & 0 & 0 & 0 & 0 & 0 & 0 & 0 \\ 0 & 0 & 0 & 0 & 0 & 0 & 0 & 0 & 0 & 0 & 0 & 0 \\ \hline 0 & 0 & 0 & 0 & 0 & 0 & k_{s_{1\cdot1}} & 0 & 0 & 0 & 0 & 0 \\ 0 & 0 & 0 & 0 & 0 & 0 & 0 & k_{s_{2\cdot2}} & 0 & 0 & 0 & 0 \\ 0 & 0 & 0 & 0 & 0 & 0 & 0 & 0 & k_{s_{3\cdot3}} & 0 & 0 & 0 \\ 0 & 0 & 0 & 0 & 0 & 0 & 0 & 0 & 0 & k_{s_{4\cdot4}} & 0 & 0 \\ 0 & 0 & 0 & 0 & 0 & 0 & 0 & 0 & 0 & 0 & 0 & 0 \\ 0 & 0 & 0 & 0 & 0 & 0 & 0 & 0 & 0 & 0 & 0 & 0 \end{array}\right] \tag{3.4}$$

and the perturbation to the system free-free stiffness matrix is simply $K = K_o + K_{susp}$.

3.1.1 Eigensystem Sensitivity Analysis

Unperturbed Eigensystem Characteristics

For the free-free beam the unnormalized eigenvectors are again written as the columns of the eigenvector matrix ${}^{o}\Phi$

$$
{}^{o}\Phi = \begin{bmatrix}
0 & 0 & 0 & 0 & 0 & 1 & 0 & 0 & 0 & 0 & -1 & 0 \\
-L & 0 & 0 & 0 & 1 & 0 & 0 & 0 & L & -L & 0 & 0 \\
0 & L & 0 & 1 & 0 & 0 & -L & L & 0 & 0 & 0 & 0 \\
0 & 0 & 1 & 0 & 0 & 0 & 0 & 0 & 0 & 0 & 0 & -1 \\
0 & 1 & 0 & 0 & 0 & 0 & -6 & 12 & 0 & 0 & 0 & 0 \\
1 & 0 & 0 & 0 & 0 & 0 & 0 & 0 & -6 & 12 & 0 & 0 \\
0 & 0 & 0 & 0 & 0 & 1 & 0 & 0 & 0 & 0 & 1 & 0 \\
0 & 0 & 0 & 0 & 1 & 0 & 0 & 0 & L & L & 0 & 0 \\
0 & 0 & 0 & 1 & 0 & 0 & -L & -L & 0 & 0 & 0 & 0 \\
0 & 0 & 1 & 0 & 0 & 0 & 0 & 0 & 0 & 0 & 0 & 1 \\
0 & 1 & 0 & 0 & 0 & 0 & 6 & 12 & 0 & 0 & 0 & 0 \\
1 & 0 & 0 & 0 & 0 & 0 & 0 & 0 & 6 & 12 & 0 & 0
\end{bmatrix} \tag{3.5}
$$

The projection of the original twelve degree-of-freedom system onto its own eigenspace, i.e. ${}^{o}\Phi^{-1\,o}(M^{-1}K)\,{}^{o}\Phi$, yields the diagonal matrix of eigenvalues Λ as expected. Note

the presence of the six zero frequency rigid body modes.

$$
{}^{o}\Psi = \begin{array}{c}
\begin{array}{cccccc} & & & & & & \text{bending}_{z_1} & \text{bend.}_{z_2} & \text{bend.}_{y_1} & \text{bend.}_{y_2} & \text{axial} & \text{torsion} \end{array} \\
\begin{bmatrix}
0 & 0 & 0 & 0 & 0 & 0 & 0 & 0 & 0 & 0 & 0 & 0 \\
0 & 0 & 0 & 0 & 0 & 0 & 0 & 0 & 0 & 0 & 0 & 0 \\
0 & 0 & 0 & 0 & 0 & 0 & 0 & 0 & 0 & 0 & 0 & 0 \\
0 & 0 & 0 & 0 & 0 & 0 & 0 & 0 & 0 & 0 & 0 & 0 \\
0 & 0 & 0 & 0 & 0 & 0 & 0 & 0 & 0 & 0 & 0 & 0 \\
0 & 0 & 0 & 0 & 0 & 0 & 0 & 0 & 0 & 0 & 0 & 0 \\
0 & 0 & 0 & 0 & 0 & 0 & \frac{720.EI_y}{\rho AL^4} & 0 & 0 & 0 & 0 & 0 \\
0 & 0 & 0 & 0 & 0 & 0 & 0 & \frac{8400.EI_y}{\rho AL^4} & 0 & 0 & 0 & 0 \\
0 & 0 & 0 & 0 & 0 & 0 & 0 & 0 & \frac{720.EI_z}{\rho AL^4} & 0 & 0 & 0 \\
0 & 0 & 0 & 0 & 0 & 0 & 0 & 0 & 0 & \frac{8400.EI_z}{\rho AL^4} & 0 & 0 \\
0 & 0 & 0 & 0 & 0 & 0 & 0 & 0 & 0 & 0 & \frac{12.EA}{\rho AL^2} & 0 \\
0 & 0 & 0 & 0 & 0 & 0 & 0 & 0 & 0 & 0 & 0 & \frac{14.4GJ}{\rho I_x L^2}
\end{bmatrix}
\end{array}
\tag{3.6}
$$

The modes corresponding to each column of Λ appear as labels above the columns. Recall that the z and y subscripts correspond to the vertical and horizontal axes respectively.

Using the original eigenvectors to project the suspension constrained system onto the original eigenspace (as was performed in the previous chapter), i.e.

$$\Psi_{susp} = {}^{o}\Phi^{-1}\left(M^{-1}(K + K_{susp})\right){}^{o}\Phi \tag{3.7}$$

yields the sensitivity matrix of Equation (3.8) on page 132. The first six columns of Equation (3.8) correspond to the suspension modes of rotational-swing, tilt, double-pendulum, bounce, horizontal or y pendulum, and axial pendulum. The rotational-swing mode corresponds to a rotation of the beam in the horizontal plane about its center and the tilt mode corresponds to a rotation of the beam in the vertical plane

$$\Psi_{susp} = \left[\begin{array}{cccccc|cccccc}
3\omega_p^2 & 0 & 0 & 0 & 0 & 0 & 0 & 0 & 0 & 6\omega_p^2 & 0 & 0 \\
0 & 3\omega_b^2 & 0 & 0 & 0 & 0 & 0 & 6\omega_b^2 & 0 & 0 & 0 & 0 \\
0 & 0 & \omega_{p_2}^2 & 0 & 0 & 0 & 0 & 0 & 0 & 0 & 0 & 0 \\
0 & -L\omega_b^2 & 0 & \omega_b^2 & 0 & 0 & -L\omega_b^2 & -3L\omega_b^2 & 0 & 0 & 0 & 0 \\
L\omega_p^2 & 0 & 0 & 0 & \omega_p^2 & 0 & 0 & 0 & L\omega_p^2 & 3L\omega_p^2 & 0 & 0 \\
0 & 0 & 0 & 0 & 0 & \omega_p^2 & 0 & 0 & 0 & 0 & 0 & 0 \\
\hline
0 & -2.5\omega_b^2 & 0 & \frac{-5\omega_b^2}{L} & 0 & 0 & \frac{720EI_y}{\rho AL^4} + 5\omega_b^2 & 0 & 0 & 0 & 0 & 0 \\
0 & 3.5\omega_b^2 & 0 & 0 & 0 & 0 & 0 & \frac{8400EI_y}{\rho AL^4} + 7\omega_b^2 & 0 & 0 & 0 & 0 \\
-2.5\omega_p^2 & 0 & 0 & 0 & \frac{5\omega_p^2}{L} & 0 & 0 & 0 & \frac{720EI_z}{\rho AL^4} + 5\omega_p^2 & 0 & 0 & 0 \\
3.5\omega_p^2 & 0 & 0 & 0 & 0 & 0 & 0 & 0 & 0 & \frac{8400EI_z}{\rho AL^4} + 7\omega_p^2 & 0 & 0 \\
0 & 0 & 0 & 0 & 0 & 0 & 0 & 0 & 0 & 0 & \frac{12EA}{\rho AL^2} + 3\omega_p^2 & 0 \\
0 & 0 & 0 & 0 & 0 & 0 & 0 & 0 & 0 & 0 & 0 & \frac{14.4GJ}{\rho I_x L^2} + 3\omega_{p_2}^2
\end{array}\right] \tag{3.8}$$

about its center. The other suspension modes are self-explanatory.

It can be seen by inspection of Equation (3.8) that the suspension bounce mode and tilt mode only affect vertical bending behavior while the horizontal pendulum mode and swing mode only affect the horizontal bending behavior as one would expect. It is interesting to note that the while the latter perturbations affect both the eigenmodes and eigenfrequencies the axial pendular stiffening and double-pendular stiffening only perturb the axial and torsion eigenfrequencies respectively and do not affect the corresponding eigenmodes (as revealed by the absence of off-diagonal terms for the eleventh and twelfth rows and columns of Ψ_{susp}).

3.1.2 Non-Dimensional Parameters

Normalizing the perturbations to the diagonal elements of Ψ_{susp} by the original diagonal modal frequencies and taking the square root yields the non-dimensional parameters of Table 3.1. Note that the suspension tilt mode eigenfrequency was expressed as a function of the bounce mode eigenfrequency, ω_b, and the two combine to stiffen the vertical flexible modes. Similarly the rotational swing mode (or center pivot mode) was expressed as a function of the horizontal pendular frequency, ω_p, and the two combine to stiffen the horizontal flexible modes.

Inspection of Table 3.1 also reveals that the suspension does not introduce coupling between the flexible modes of the structure for the configuration studied. There is however a certain amount of coupling between the suspension modes and the fundamental flexible modes. Unfortunately, given the repeated roots associated with the rigid-body modes of the original system, the off-diagonal elements of Ψ_{susp} do not correspond to the frequency separation weighted eigenvector derivatives. This is to say that the theory presented in Section 2.3.2 is only valid for systems with distinct eigenvalues.

It is known however that as the number of suspension points is increased the system bending behavior asymptotically approaches that of a beam on an elastic

Table 3.1: Non-Dimensional Parameters for Beam Sensitivity to Suspension Effects

Suspension Mode	Stiffening Effect on	Non-Dim. Parameter
bounce & tilt modes	1st vert. bending freq.	$5\omega_b^2/\omega_{z_1}^2$
	2nd vert. bending freq.	$7\omega_b^2/\omega_{z_2}^2$
horiz. pend. and	1st hor. bending freq.	$5\omega_p^2/\omega_{y_1}^2$
rotational swing modes	2nd hor. bending freq.	$7\omega_p^2/\omega_{y_2}^2$
axial pend. mode	1st axial freq.	$3\omega_p^2/\omega_x^2$
double pend. mode	1st torsional freq.	$3\omega_{p_2}^2/\omega_{\theta x}^2$

foundation. By increasing the number of suspension attachment points and recomputing the sensitivity matrix Ψ_{susp} we would thus expect the off-diagonal terms to become smaller. For a beam on an elastic foundation it is known that the eigenmodes of the structure are unaffected if the elastic foundation is massless [54]. The bending eigenfrequencies of the suspended structure on the other hand all undergo a uniform shift which becomes negligible at higher frequencies [54]

$$\omega'_{\text{bending}_i} = \left(\omega^2_{\text{bending}_i} + \omega^2_{\text{bounce}_i}\right)^{1/2} \tag{3.9}$$

In the case where the beam or structure principal axes are not aligned with the horizontal and vertical planes there is a loss of the proportional stiffening property of the bending modes. This property occurs when the structure is suspended in a manner which leaves it undeformed and level. If the structure is level the vertical stiffnesses are mass proportional and the bounce frequency is uniform at every attachment point (decoupling thus the flexible modes from the suspension bounce modes). If the structure is level and the suspension cables are the same length the pendular stiffening is also proportional as it will be the same at every attachment point. The advantage of proportional stiffening is that the impact on the structure's bending eigenmodes is

minimized and only the eigenfrequencies are affected.

3.2 Dynamic Effects

When the suspension system exhibits dynamic behavior (i.e. cable/bending modes, surge/axial modes, and twist/torsion[1] modes) within a half-decade of the structure's bandwidth of interest it is necessary to include the suspension system mass and distributed stiffness properties in the system model. The distinction between the suspension system and the structure disappears somewhat as the effects of gravity now act on the combined dynamic system. For this reason, and recognizing the higher order nature of the problem, the impact of dynamic suspension effects such as cable and surge behavior is not investigated in a general manner here. A generalized study of the perturbations of a suspension system with its own dynamics on the eigenstructure of a suspended beam-type structure is left for future study. What will be discussed here is how geometric stiffening applied to the combined suspension–structure model effectively models the suspension dynamics and the suspension–structure interactions.

3.2.1 Gravity Effect on Suspension System

By incorporating the suspension system into the structural model and computing the effects of initial stress on the loaded suspension system (as described in Chapter 2) one is able to accurately model the suspension system dynamics and the dynamic coupling between the suspension system and the test article. This is an excellent example of the power of the geometric stiffness model updating technique. For example, the geometric stiffening effect correctly describes the pendular stiffening of the suspension and structure due to gravity as well as the effect of the axial load on the cable modes.

As a demonstration of the correct application of pendular stiffening by geometric

[1]Twist or torsion of the suspension springs or cables is typically a negligible effect given the small polar mass moment of inertia of the cables or springs

stiffening we examine here a simple pinned-free beam element hanging vertically. To simplify the analysis we restrict the beam to motion in the vertical plane. The beam element has thus the following five degrees of freedom

$$U_c = \left[\theta y_A \; x_B \; z_B \; \theta x_B \; \theta y_B \right] \tag{3.10}$$

The gravity-free modeshapes of this system are given by,

$$^{o}\Phi_{pend} = \begin{bmatrix} 1 & -0.777 & 0.523 & 0 & 0 \\ 0 & 0 & 0 & 1 & 0 \\ -l & -0.217l & -0.093l & 0 & 0 \\ 0 & 0 & 0 & 0 & 1 \\ 1 & 1 & 1 & 0 & 0 \end{bmatrix} \tag{3.11}$$

and the eigenfrequencies corresponding to the above swing, 1st cable bending, 2nd cable bending, axial, and torsion modes are

$$\lambda_i = \left(0 \;\; \frac{307.805EI_y}{\rho Al^4} \;\; \frac{4912.19EI_y}{\rho Al^4} \;\; \frac{3EA}{\rho Al^2} \;\; \frac{3.6GJ}{\rho I_x l^2} \right) \tag{3.12}$$

To best identify the nature of the geometric stiffening here, a general eigenprojection analysis is first performed. Applying the properly constrained geometric stiffness matrix K_g from Equation (2.97) to the suspended pendulum stiffness matrix and projecting the result onto the original eigenspace yields,

$$\Psi_{pend} = \begin{bmatrix} \frac{3F_x}{\rho Al^2} & \frac{0.651F_x}{\rho Al^2} & \frac{0.279F_x}{\rho Al^2} & \frac{3F_x l}{\rho Al^4} & \frac{3M_z^A}{\rho Al^3} \\ \frac{20.27F_x}{\rho Al^2} & \frac{29.21\left(10.54EI_y+F_x l^2\right)}{Al^4\rho} & \frac{7.166F_x}{\rho Al^2} & \frac{20.27F_z}{\rho Al^3} & \frac{20.27M_z^A}{\rho Al^3} \\ \frac{81.73F_x}{\rho Al^2} & \frac{67.36F_x}{\rho Al^2} & \frac{102.79\left(47.79EI_y+F_x l^2\right)}{Al^4\rho} & \frac{81.73F_z}{\rho Al^3} & \frac{81.73M_z^A}{\rho Al^3} \\ \frac{3.F_z}{\rho Al} & \frac{0.651F_z}{\rho Al} & \frac{0.279F_z}{\rho Al} & \frac{3EA}{\rho Al} & 0 \\ \frac{3M_z^A}{\rho I_x l} & \frac{0.651M_z^A}{\rho I_x l} & \frac{0.279M_z^A}{\rho I_x l} & 0 & \frac{3.6(0.833F_x I_x+AGJ)}{AI_x l^2\rho} \end{bmatrix} \tag{3.13}$$

Clearly, the swing mode has been grounded by the application of the gravitational

load effect as the zero diagonal element has been replaced by the new squared eigenfrequency

$$\frac{3F_x}{\rho A l^2} \tag{3.14}$$

Since the axial load for the beam subject to its own weight is

$$F_x = \rho A l g \tag{3.15}$$

the pendular mode frequency (no longer a rigid-body swing mode) is given by

$$\lambda_1 = \sqrt{\frac{3g}{l}} \tag{3.16}$$

which is the exact pendular frequency of a tip suspended beam with a uniformly distributed mass [54]. Were the above analysis performed on a rigid-link with a concentrated tip mass the familiar pendular frequency of $\sqrt{g/l}$ would have been obtained.

3.2.2 Predicting Suspension Surge and Violin Mode Frequencies

For reference purposes this section describes the vital yet simple calculations one should always perform to estimate the principal suspension resonant frequencies and assess the minimum initial modeling order required for the suspension system.

The surge modes of a simple translational spring can be very well approximated by modeling the spring as a uniform pinned-pinned rod for which the axial resonant frequencies are [54]

$$(f_s)_i = \frac{i}{2x_s}\sqrt{\frac{3 \cdot k_u}{\mu}} \tag{3.17}$$

where

$(f_s)_i$	=	i'th surge mode eigenfrequency	$[Hz]$
k_u	=	unit spring stiffness	$[in \cdot lb/in]$
x_s	=	undeformed spring length	$[in]$

μ = spring mass density $[slugs/in]$

Note the regular harmonic spacing of the surge modes which typically drives the spring design length to be as short as possible so that the first surge mode is above the bandwidth of interest.

The violin modes of the suspension cables are those modes where the suspension rods or cables behave as pinned-pinned strings of a violin. These modes are also referred to as cable modes, piano modes, etc. Estimating the violin mode eigenfrequencies first requires an estimate of the tension on each cable. For an overdetermined system this information is best obtained by solving for the reaction forces in the finite element analysis. The violin mode eigenfrequencies are given by [54]

$$(f_v)_i = \frac{i}{2l}\sqrt{\frac{T_o}{\rho A}} \tag{3.18}$$

where

$(f_v)_i$ = i'th violin mode eigenfrequency
l = suspension cable length
T_o = tension in the suspension cable
ρ = suspension cable density
A = cable cross-sectional area

3.2.3 Summary

The effect of a laboratory suspension system on the dynamics of a suspended space structure is principally to replace the structure's rigid-body modes with bounce, tilt, and pendular modes, and to stiffen the fundamental flexible modes of the structure when there is insufficient frequency separation between the fundamental suspension dynamics and the fundamental structural flexible modes. If the rigid-body modes affect the performance metric it is crucial to include at least a static representation

of the suspension system in the model. If the experimental transfer function data indicates the presence of suspension dynamic behavior, i.e. violin or surge modes, it is necessary to model the suspension cables themselves as flexible beam elements. Whether the suspension system is modeled as soft spring supported rigid rods, or soft spring supported flexible rods it is necessary to include the suspension description in the system model prior to the solution for the initially deformed structure and the incorporation of geometric stiffening effects. The geometric stiffness refinements capture gravity's stiffening effect on the rigid-body modes of the suspended structure as well as the coupling effects between the loaded suspension system and the flexible structure.

Chapter 4

Gravitational Load Effects on Sensors and Actuators

This chapter identifies and develops models of the fundamental gravity effects on sensors and actuators viable for use in the control of flexible spacecraft. The two devices which have been found to have a fundamental operational principle which is affected by the gravitational field are the accelerometer and proof-mass actuator. Non-dimensional measures are established which describe when these fundamental gravity effects are non-negligible. The MACE testbed is used as an example of the application of the non-dimensional measures. The implementation of the gravity effect modeling technique on MACE was found to improve transfer function predictions.

The approach adopted here is to focus on the dynamic effects of gravity and ignore the static effects on device performance as the latter are typically eliminated using zeroing techniques prior to their operation. After the identification of the fundamental perturbation mechanism, the gravity effects are incorporated into exact dynamic input or output equations which are used to generate the modal input or output equations more practical for implementation into the discrete controlled structure model. The non-dimensional parameters are then extracted from the modal form of the input or output equations.

4.1 Background

4.1.1 Controlled Structure Model

The dynamics of a controlled flexible structure can be represented in state space form as

$$\begin{bmatrix} \dot{X} \\ Y \end{bmatrix} = \begin{bmatrix} A & B \\ C & D \end{bmatrix} \begin{bmatrix} X \\ U \end{bmatrix} \tag{4.1}$$

where the modal amplitude state vector is X, the output vector is Y and the input vector is U. The homogeneous system dynamics matrix is A, the B and C matrices are the control and output matrices respectively and the D matrix is the static correction matrix or feed-forward matrix. A standard partitioning of the state vector is to group the modal amplitudes and modal amplitude rates as follows

$$X = \left[\begin{array}{c|c} \eta & \dot{\eta} \end{array} \right]^T \tag{4.2}$$

The resulting form of the system matrix A, in the case of proportional damping, is

$$A = \left[\begin{array}{c|c} 0 & I \\ \hline -M^{-1}K & -CM^{-1}K \end{array} \right] \tag{4.3}$$

where C is a diagonal matrix of damping coefficients.

4.1.2 Direct and Indirect Effects

The initial stress and pre-deformation effects of gravity on the M and K matrices described in Chapter 2 are direct effects on the structure. This chapter on the other hand is concerned with the direct effects on the sensors and actuators which corresponds to direct effects on the control and output matrices B and C. Indirect effects to the B and C matrices are those effects which result from perturbations to the A matrix, i.e. effects on the eigensystem as described in Chapter 2.

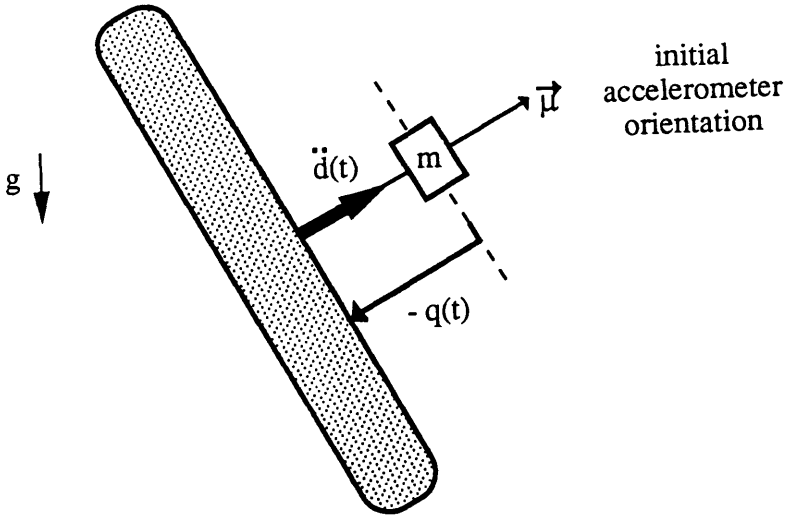

Figure 4-1: Accelerometer Output Model Schematic

4.2 Gravity Effect on Accelerometer Output

The internal mass of an accelerometer is stiffly connected to the accelerometer base such that internal inertial and damping forces are negligible within the device's effective bandwidth. The acceleration of the base is inferred by measuring the relative displacement of the internal mass to the base. The output of an accelerometer is thus given by

$$a(t) = -\omega_n^2 \, q(t) = \ddot{d}(t) \tag{4.4}$$

where ω_n is the accelerometer natural frequency, $q(t)$ is the relative displacement of the internal mass and $d(t)$ is the displacement component of the structure along $\vec{\mu_o}$ as depicted in Figure 4-1. (For details of accelerometer operation see Reference [27]).

When the structure undergoes rotation a *change* in the translational gravity load

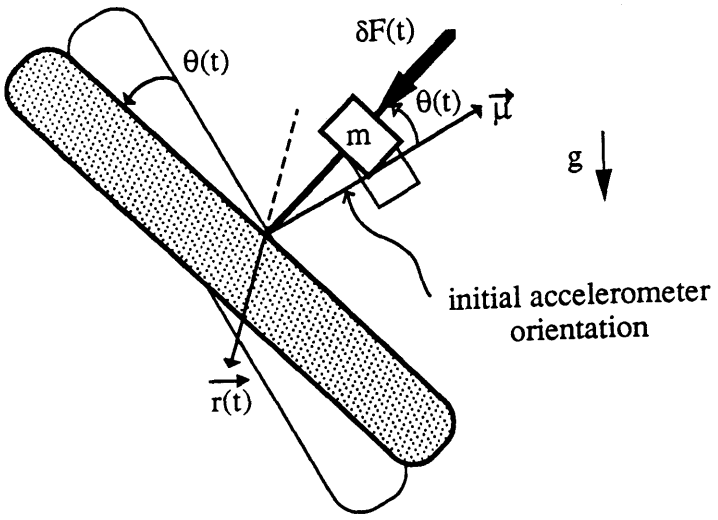

Figure 4-2: Schematic of Accelerometer Rotation in Gravity Field

is induced and for small rotations the accelerometer output is now given by:

$$a(t) = \ddot{d}(t) + \vec{g} \cdot (\vec{\mu_o} \times \vec{r}(t)) \tag{4.5}$$

where $\vec{\mu_o}$ is the initial accelerometer axis unit vector and $\vec{r}(t)$ is the right-hand rule rotation vector associated with $\theta(t)$, see Figure 4-2. This representation holds for arbitrary accelerometer orientations and rotations in three dimensions where θ is positive for an upwards rotation and the gravity vector $\vec{g}$ is positive when downwards pointing. As captured by the dot product of Equation (4.5), the gravity effect is clearly null when the rotation is about the sensitivity axis of the accelerometer or about the vertical axis.

This rotation induced gravity effect on the accelerometer can lead to important dynamic performance perturbations at low frequencies as will be shown in Section 4.4 and demonstrated in Section 4.6 after a brief description of the complementary gravity effect on the output of a proof-mass actuator.

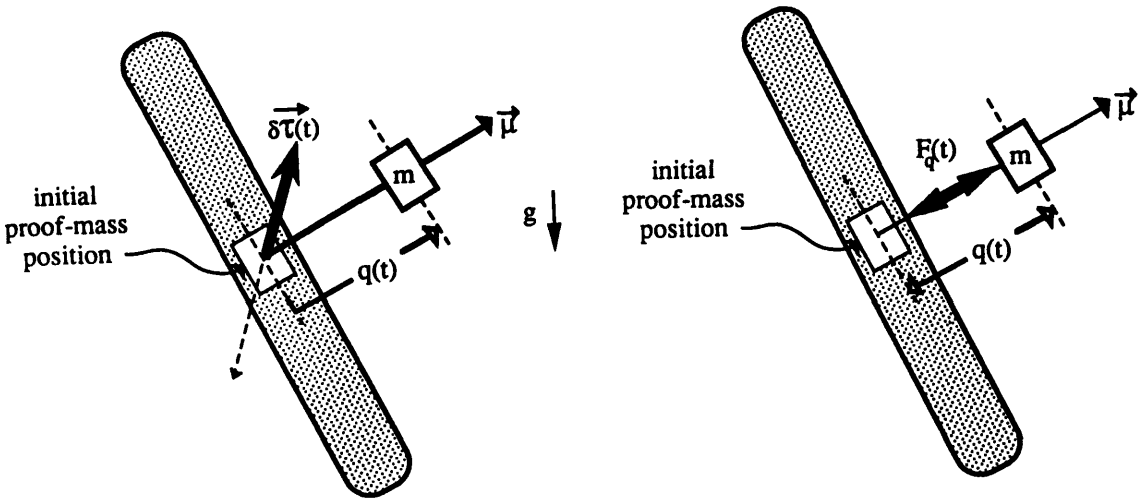

Figure 4-3: Proof-Mass Actuator Input Model Schematic

4.3 Gravity Effect on Proof-Mass Actuator Input

Assuming high authority local control is used to reject disturbance forces, the proof-mass actuator force input to the structure along $\vec{\mu_o}$ is prescribed by the controlled acceleration of the proof-mass. The proof-mass actuator force input to the structure along $\vec{\mu_o}$ is thus

$$F_q(t) = -m\,\ddot{q}(t) \tag{4.6}$$

as portrayed in Figure 4-3. When the proof-mass translates in a gravity field along any axis other than the vertical, the translation induces a change in the torque on the structure as the moment arm is changed. In general, for small rotations, the proof-mass actuator input is thus a simultaneous force and torque input:

$$F_q(t) = -m\,\ddot{q}(t) \tag{4.7}$$

$$\vec{T}_q(t) = m\,q(t)\,(\vec{\mu_o} \times \vec{g}) \tag{4.8}$$

where $q(t)$ is the dynamic proof-mass displacement along the actuation axis, see Figure 4-3.

To incorporate this effect and the accelerometer gravity effect into the controlled structure model we now proceed to a modal representation of the sensor and actuator dynamics making use of the fact that the devices are fixed at discrete locations on the structure and that the structure has been modeled and its modal properties are known.

4.4 Modal Modeling

The key to a compact and elegant representation of the effects of gravity on the performance of flexible structure sensors and actuators is to recognize that the mode-shapes $\vec{\Phi}_j$ can be divided into translational components $\vec{\Phi}_j^D$ and rotation components $\vec{\Phi}_j^R$. This is equivalent to expressing the deflection $d(t)$ at x as a weighted sum of translational modal amplitudes,

$$d(x,t) = \sum_{j=1}^{N} \eta_j(t)\, \vec{\Phi}_j^D(x) \cdot \vec{\mu_o} \tag{4.9}$$

and the rotation vector $r(t)$ at x as a weighted sum of rotational modal amplitudes,

$$\vec{r}(x,t) = \sum_{j=1}^{N} \eta_j(t)\, \vec{\Phi}_j^R(x) \tag{4.10}$$

Taking the Fourier transform of Equation (4.5) and making use of the modal displacement and rotation relations allows us to write the output equation for an accelerometer as

$$a(t) = -\sum_{j=1}^{N} \left\{ \omega^2 \left(\vec{\Phi}_j^D(x) \cdot \vec{\mu_o} \right) + \vec{g} \cdot \left(\vec{\Phi}_j^R(x) \times \vec{\mu_o} \right) \right\} \eta_j(t) \tag{4.11}$$

For the i^{th} accelerometer located at x_i the corresponding row vector of output matrix

terms C_{ij} is therefore given by

$$C_{ij} = -\sum_{j=1}^{N} \left\{ \omega_i^2 \left(\vec{\Phi}_j^D(x_i) \cdot \mu_{o_i} \right) + \vec{g} \cdot \left(\vec{\Phi}_j^R(x_i) \times \mu_{o_i} \right) \right\} \tag{4.12}$$

Note that the output matrix will have the form

$$C = \left[\; C_{ij} \; \middle| \; 0 \; \right] \tag{4.13}$$

for the state vector partitioning described by Equation (4.2).

The proof-mass actuator input equation derivation is somewhat more involved as the equations must be written in terms of the commanded force to obtain the appropriate form for the input matrix terms. From Equation (4.8) we can write the translation of the proof-mass as the doubly integrated time history of the commanded forcing,

$$q(t) = -\frac{1}{m} \iint_{t_o}^{t_f} F_q(t)\, dt^2 \tag{4.14}$$

which can be substituted into the gravity induced torque equation (4.8) to yield

$$\vec{T}_q(t) = \iint_{t_o}^{t_f} F_q(t)\, dt^2 \, (\vec{g} \times \vec{\mu_o}) \tag{4.15}$$

Note that the order of the cross-product was flipped to maintain a positive expression for the moment on the structure. Making use of the modal displacement and rotation relations of Equations (4.9) and (4.10) we can write the translational modal forcing as

$$\mathcal{F}_j^D(t) = \left(\vec{\Phi}_j^D(x) \cdot \vec{\mu_o} \right) F_q(t) \tag{4.16}$$

and the rotational modal forcing as

$$\mathcal{F}_j^R(t) = \vec{\Phi}_j^R(x) \cdot \vec{T}_q(t) = -\frac{1}{\omega^2}\left(\vec{\Phi}_j^R(x) \cdot (\vec{g} \times \vec{\mu_o})\right) F_q(t)$$
$$= \frac{1}{\omega^2}\left(\vec{g} \cdot \left(\vec{\Phi}_j^R(x) \times \vec{\mu_o}\right)\right) F_q(t) \qquad (4.17)$$

where the Fourier transform was used to eliminate the double integration. The entire $\mathcal{F}_j^R(t)$ term here is the gravity induced input perturbation. For the i^{th} proof-mass actuator located at x_i the corresponding column vector of input matrix terms B_{ji} is therefore given by

$$B_{ji} = \left(\vec{\Phi}_j^D(x) \cdot \vec{\mu_o}\right) + \frac{1}{\omega^2}\left(\vec{g} \cdot \left(\vec{\Phi}_j^R(x) \times \vec{\mu_o}\right)\right) \qquad (4.18)$$

where the B matrix is of the form

$$B = \left[\begin{array}{c|c} 0 & B_{ij} \end{array}\right]^T \qquad (4.19)$$

for the state vector partitioning described in Equation (4.2).

4.5 Non-Dimensionalization

Using the modal input and output relations of Equations (4.18) and (4.12) very useful non-dimensional parameters can be derived for evaluating the impact of gravity on the performance of a flexible structure mounted accelerometer or proof-mass actuator. The derivation of the non-dimensional parameters is very straightforward since the perturbation to both the accelerometer and the proof-mass actuator performance is additive. To obtain the non-dimensional parameter for an additive perturbation we simply take the ratio of the perturbing quantity to the unperturbed quantity. The resulting ratio for both the sensing and the actuation case is in fact the same and is

given by

$$\Gamma_j = \frac{\vec{g} \cdot \left(\vec{\Phi}_j^R(x) \times \vec{\mu_o} \right)}{\omega^2 \left(\vec{\Phi}_j^D(x) \cdot \vec{\mu_o} \right)} \tag{4.20}$$

or, for beam mounted devices we can normalize by the beam length to obtain a non-dimensional parameter

$$\Gamma_j = \frac{\vec{g} \cdot \left(\vec{\Phi}_j^R \left(\frac{x}{l} \right) \times \vec{\mu_o} \right)}{\omega^2 \, l \left(\vec{\Phi}_j^D \left(\frac{x}{l} \right) \cdot \vec{\mu_o} \right)} \tag{4.21}$$

When the non-dimensional ratio of Equation (4.21) is finite or large with respect to unity the effect of gravity on the dynamic performance of an accelerometer or proof-mass actuator is important and should not be neglected.

4.5.1 Observations

A number of interesting observations can be made concerning the effect of gravity on a flexible structure borne accelerometer or proof-mass actuator . The most interesting is that the non-dimensional parameter is the same for the two devices so that they are gravity effect sensing and actuation duals.

The effect of gravity on the accelerometer is such that all rotations other than about the vertical or about $\vec{\mu_o}$ (for which $\Gamma_j = 0$) are sensed to some degree by the accelerometer. In fact, the most sensitive orientation for both devices is clearly the horizontal orientation (as the cross-product quantity will yield a vertical vector which will be parallel to the gravity vector and the dot product or projection will be equivalent to a multiplication by plus or minus one). The additive perturbation can be constructive, i.e. $\Gamma_j > 0$, or destructive, i.e. $\Gamma_j < 0$, depending on the relative sign between the perturbation and the unperturbed signal. The result is thus an amplification of the accelerometer signal or an attenuation which can lead to a near cancellation of the signal or to a phase reversal of the signal which can be catastrophic if the accelerometer is a feedback element of a control system.

It is not surprising to observe that the effect of gravity on the proof-mass actuator is such that the proof-mass actuator will not excite rotations about the vertical or about its actuation axis. As with the accelerometer the additive gravity perturbation can be constructive ($\Gamma_j > 0$) or destructive ($\Gamma_j > 0$) either enhancing the ability of the proof-mass actuator to excite a given mode or reducing its effectiveness.

Clearly the impact of the gravity perturbation for both the accelerometer and the proof-mass actuator is most important at low frequencies or at modes with a small displacement component: $\Gamma_j \gg 0$, or, $\Gamma_j \ll 0$. It is for the latter cases in particular that the effect of gravity on the system controllability and observability should be taken into account. Note that a judicious placement and orientation of the device can eliminate or significantly reduce the effect of gravity.

A few additional observations can be made for two special cases which correspond to the two pure modal origins of the modal rotation component, i.e. pure bending and pure torsion. When $\vec{\Phi}_j^R(x_i)$ is due entirely to a twisting about the neutral axis we have a pure torsion effect, ($\Gamma_j \to \infty$). When $\vec{\Phi}_j^R(x)$ is due entirely to a neutral axis displacement we have a pure bending gravity effect.

For the accelerometer in the pure torsion gravity effect case, the gravity perturbation is about an otherwise null signal which therefore makes the otherwise unobservable torsion modes observable. This can be advantageous for ground-based systems if the output matrix of the system model reflects this effect, but if unmodeled this effect can lead to harmful spillover. Similarly, the torsional gravity perturbation to the proof-mass actuator imparts some controllability to the torsional mode in question. It is important to recognize that this enhanced observability and controllability of torsion disappears in space and the orbital control system must take this into account.

For the pure bending gravity effect case the relative phasing of the gravity perturbation and the unperturbed input or output can easily be determined by inspection for a given mode. One need only identify if the local component of rotation in the ver-

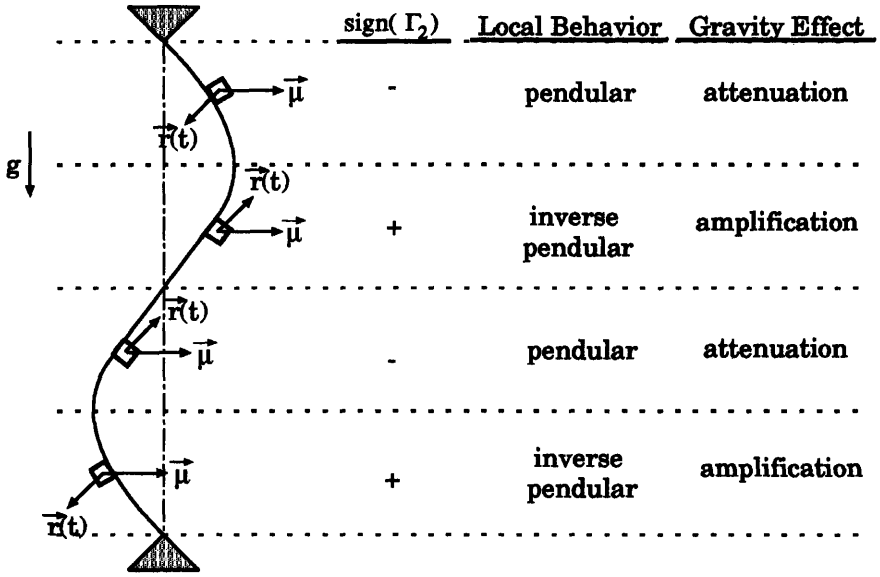

Figure 4-4: Example of the Perturbation Phases for Various Accelerometer Positions on a Pinned-Pinned Beam in the Second Flexible Mode of Bending Vibration.

tical plane is pendular or inverse pendular, see Figure 4-4. (The accelerometer gravity effect due to bending was the special case treated by Nor et al. [27, 70] who only recognized the attenuating effect of gravity in their pendular vertical plane structure.)

4.6 MACE Accelerometer Output Experiment

The Middeck Active Control Experiment, or MACE testbed is a flexible multi-body dynamics test-bed with articulating payloads. The experiment is more fully described in Section 5.1, but briefly it can be described as a scaled-down space platform with an attitude control system and double gimballed pointing payload. The performance metric is a weighted contribution of the payload pointing stability and jitter. The objective of the experiment is to study the control structure issues involved in verifying the performance of a controlled structure for space flight. This includes the study of gravity and suspension effects as well as the management of interacting control systems separated by a flexible bus.

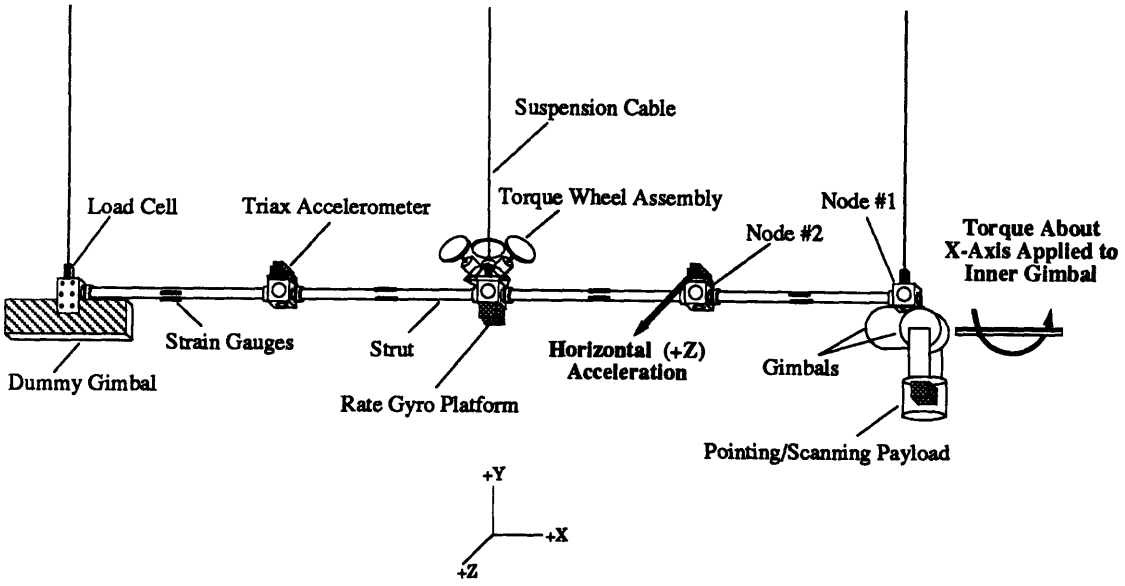

Figure 4-5: Middeck Active Control Experiment (MACE) Testbed Schematic

The key measure of how good a model is for control is how well the model predicts the different possible transfer functions. This section examines the improvement in transfer function prediction brought about by incorporating the direct effects of gravity on the output of the horizontally oriented accelerometer on Node 2 of the MACE test article, see Figure 4-5. This particular output quantity we know from Section 4.5.1 will be most susceptible to the gravity perturbation. The input which most excites horizontal acceleration is the Inner Gimbal, or X–Gimbal, so that the transfer function under study here is Inner Gimbal Torque to Acceleration at Node 2.

4.6.1 Application of Non-Dimensional Parameter

No matter where the sensor or actuator is placed on a structure, at some frequencies the modal rotation participation will be significant. This can be seen in the top histogram of Figure 4-6 for the MACE structure, which shows the phase and magnitude of the modal rotation about X at Node 2 where the accelerometer is located. It would be incorrect to assume that gravity will only affect the higher frequencies

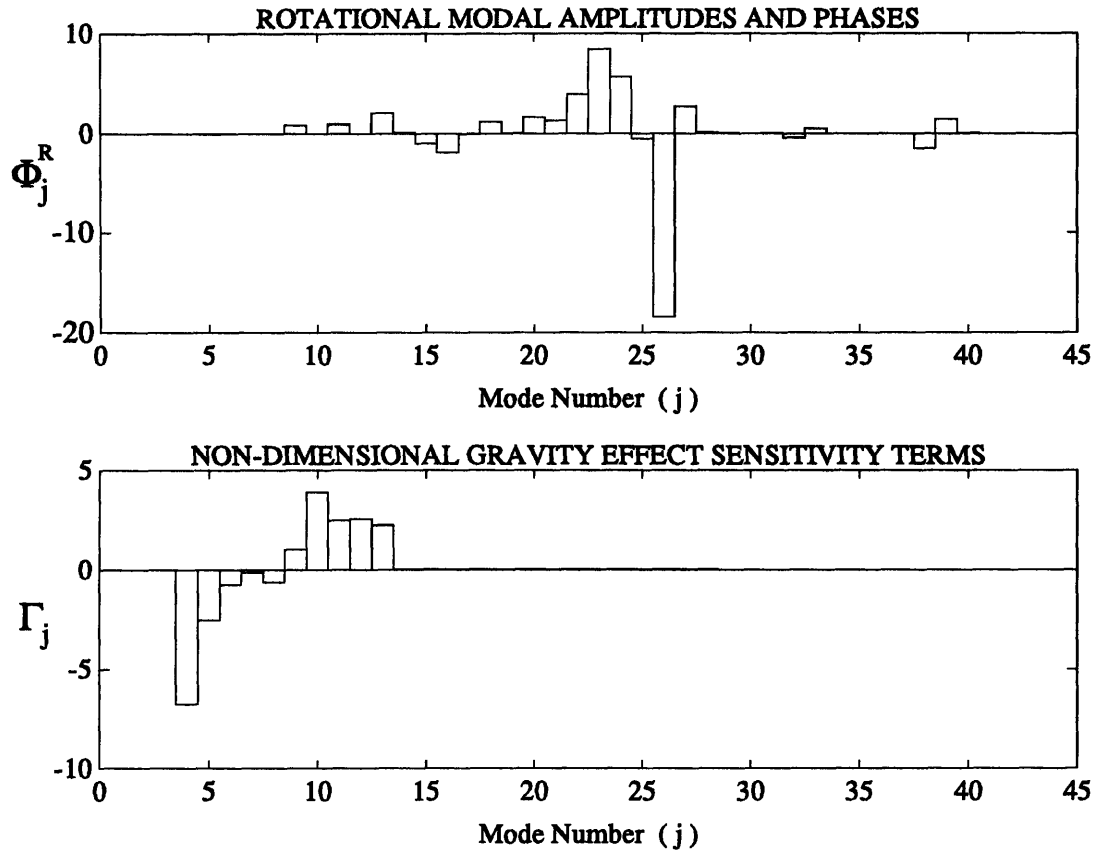

Figure 4-6: Torsional Modal Amplitudes and Non-Dimensional Gravity Effect Sensitivity Ratios for MACE

as indictated since the frequency weighting and modal translation weighting of the non-dimensional measure have yet to be incorporated. The lower histogram depicts the phase and magnitude of the non-dimensional parameters (Equation (4.21)) for the horizontal accelerometer at Node 2. Each visible bar on the histogram indicates a significant perturbation at the frequency associated with that mode number. Clearly, the direct effect of gravity on the Node 2 accelerometer should be incorporated into the system output matrix.

Since the MACE test article has six rigid-body modes and five articulation modes (one double gimbal and three torque wheels) Figure 4-6 indicates that six of the eleven rigid-body modes are affected and the first three flexible modes are also affected. By examining the modeshapes of the affected modes it was determined that the

greatest direct gravity effects were due to the modal rotation imparted by the pendular swinging of the structure. This important observation recommends thus the use of a suspension system which is not co-planar if the control system makes use of any horizontally mounted accelerometers; (a non co-planar suspension system will allow for a similar lateral swing but will not impose large rotations of the test article).

4.6.2 Transfer Function Results

Depicted in Figure 4-7 are three transfer-function curves for the Outer Gimbal to Node 2 Horizontal Accelerometer. The discrete points are experimental data, the solid line is the model without the direct gravity effect and the dashed line is the improved transfer function after incorporating the direct gravity effect on the accelerometer output (using Equation (4.12)). The correction effect on the poles was minimal but the effect on the zeros was significant as would be expected since the gravity effect influences sensing. Of particular note is the improvement in the 0.8 Hz and 1.1 Hz zero prediction.

4.7 Summary

The following items summarize the principal observations of this chapter.

- The non-dimensional gravity effect sensitivity ratio is the same for both the PMA and the accelerometer.
- Direct gravity effects on accelerometers and proof-mass actuators can be very important.
- Calculation of the non-dimensional gravity effect ratio is recommended, especially over low frequencies.
- The gravity effect can make observable otherwise unobservable modes.
- The gravity effect can make controllable otherwise uncontrollable modes.

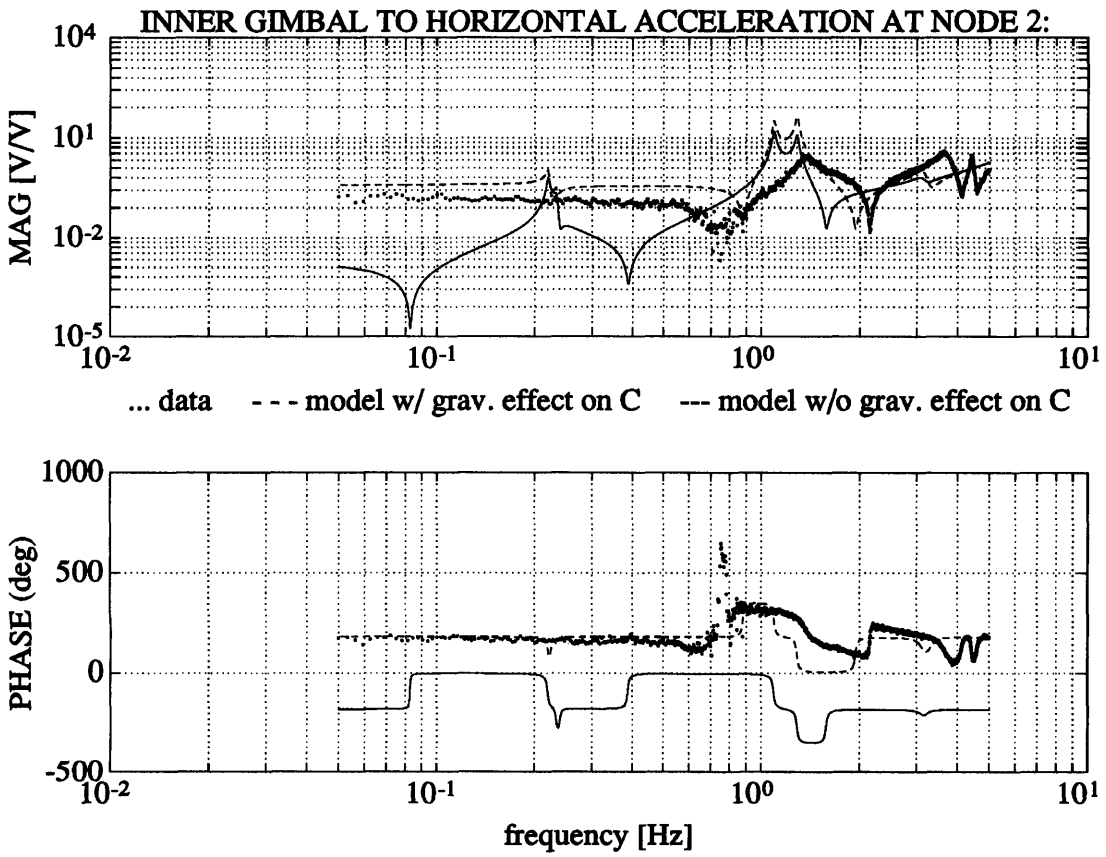

Figure 4-7: Gravity Effect on Horizontal Accelerometer Output for MACE

Chapter 5

MACE Testbed Case Study

This chapter presents a numerical analysis of gravity and suspension effects performed by computationally applying the gravity and suspension modeling techniques described in Chapters 2 and 3. The techniques are first applied to a simplified model of the Middeck Active Control Experiment test article (MACE) and to a set of parametric variations thereof. Two models are derived for each configuration studied: a 0–g model, which is gravity and suspension free, and a 1–g model, which includes gravity and suspension effects. The gravity and suspension modeling techniques were also used to improve the higher order model of the actual testbed for comparison with experimental data. These results however are not contained in this thesis except for a description of the modeling of the MACE Development Model testbed and a sample overlay of typical 0–g , 1–g , and experimental transfer functions in Appendix A.3.2 An experimental analysis of the effects of initial deformation is performed by fitting MACE with flexible appendages and simulating the 0–g and 1–g droop of the appendages. The principal objectives of this chapter are thus:

- to gain insight into the realistic nature of gravity and suspension effects on a beam-like spacecraft model,
- to evaluate the ability of the non-dimensional, gravity and suspension effect sensitivity ratios in predicting eigenfrequency shifts and modal couplings, and

- to evaluate the improvements of the high fidelity, finite element model of the testbed after incorporating gravity and suspension effects.

The chapter opens with a general description of the MACE testbed and an overview of the scaling analysis performed for the MACE test article. The scaling analysis culminates in a discussion of the scaling of the effects of gravity. After a description of the simplified MACE model and the different variations thereof for the parametric variation study, this chapter outlines the practical steps involved in modeling gravity and suspension effects with off-the-shelf finite element modeling software (Appendix A provides a self-contained description of gravity and suspension effect modeling with ADINA, for reference purposes). A summary table of predicted gravity and suspension effects is presented for the parametric variation analysis before presenting the results of the ADINA 0–g and 1–g modeling. The chapter closes with the results of the flexible appendage experiment.

5.1 Testbed Description

The MACE testbed was designed as an experimental platform for the research and development of modeling, control and qualification technologies for the next generation of space platforms whose control bandwidth encompasses structural flexible modes. As such the test article has a flexible slender bus with articulating payloads at each end and a torque wheel attitude control system at its midpoint. Figure 5-1 shows an artist's portrayal of the MACE Flight Model aboard the Space Shuttle middeck with the Experiment Support Module and middeck lockers in the background. The experiment is fully instrumented and various bus attitude and gimbal pointing control laws can be implemented on a real time computer which drives the system [71]. The testbed is equipped with state-of-the-art suspension devices to address and identify the real problems associated with the qualification of flexible spacecraft. The test program includes plans to fly the MACE test article aboard the Shuttle middeck

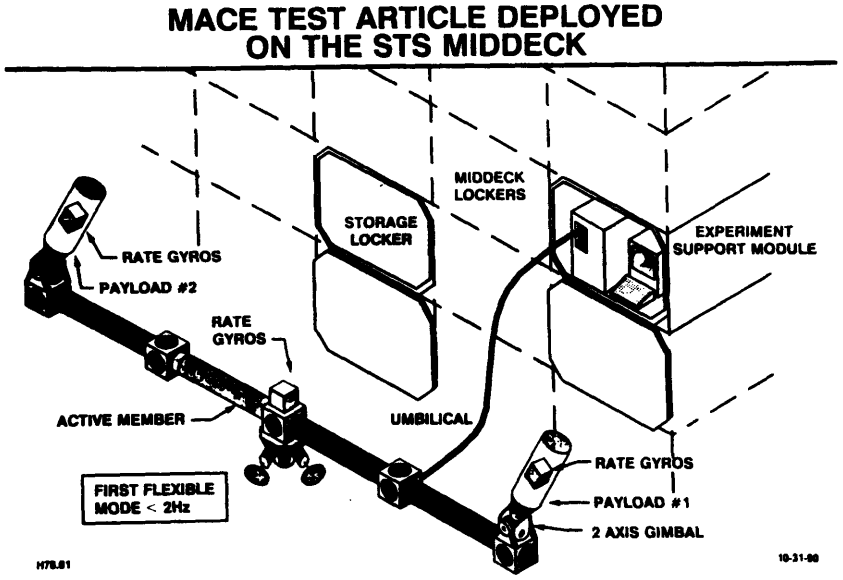

Figure 5-1: Schematic of the Middeck Active Control Experiment aboard the Shuttle middeck

to evaluate the level of fidelity of the 0–g a-priori modeling and the performance of different measurement and model based control systems developed on the ground. In-flight identification information will also be transmitted to the ground for a control system redesign with subsequent reevaluation at a later point in the flight.

Test Article

The bus is composed of four tubular section lexan struts held together end-to-end with square aluminium nodes. The connections are designed in a quick connect fashion to allow for easy assembly and disassembly by the Shuttle astronauts. This modularity was also incorporated into the design to permit storage in a Shuttle middeck locker. At the time of writing of this thesis, the test article was in its Development Model configuration (a precursor to the Engineering and Flight Models). The Development Model, which makes use of preliminary gimbal and torque wheel designs, is only fitted with one double gimbal/payload assembly. The Engineering Model will be fitted with two gimbal assemblies and will use redesigned gimbal and torque wheel hardware in addition to new sensor and actuator hardware such as an active (piezoelectric) strut.

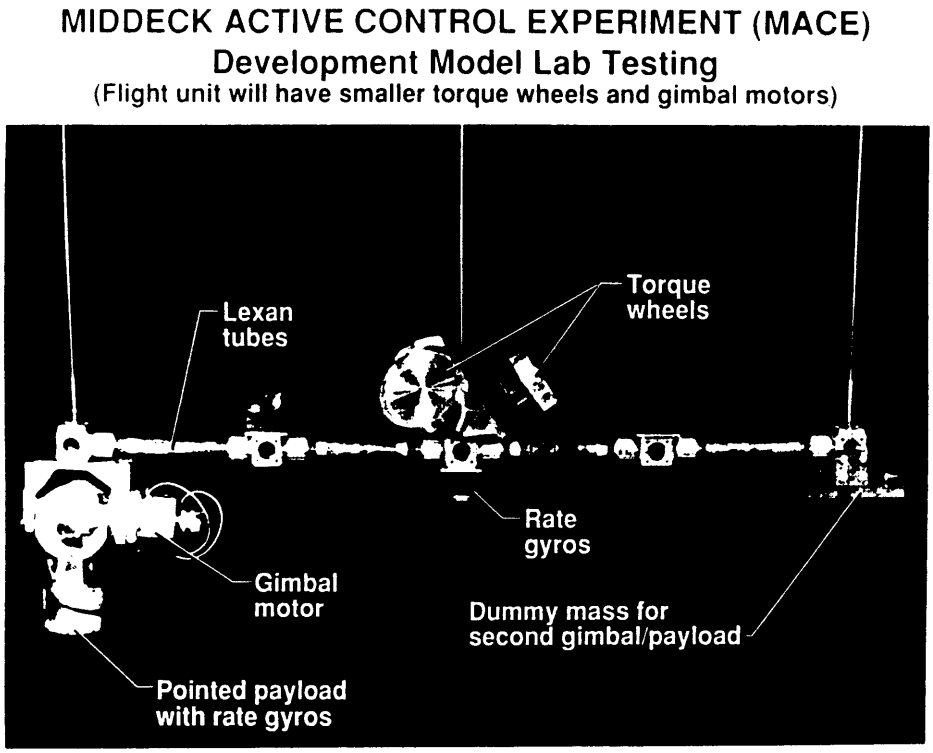

Figure 5-2: MACE Development Model Testbed

The Development Model is fitted with two tri-axis rate gyro packages (one mounted on the articulated payload and one mounted underneath the central node), two tri-axis accelerometer packages (mounted on the intermediate nodes 2 and 4), sixteen strain gauges (mounted in opposition on the surface of each strut at its center), two optical encoders (one per axis of the double gimbal assembly) and three load cells (one at each test article suspension attachment point). The double gimbal provides a conical pointing envelope for the payload.

The fundamental vertical flexible bending mode of the test article is approximately 1.8 Hz and the fundamental horizontal flexible mode is approximately 3 Hz.

Suspension System

Three pneumatic-electric suspension devices support the MACE test article with a bounce frequency from 0.1 to 0.5 Hz. The test article is suspended by three 4.6 meter

long, 1/32" diameter, steel rods attached to the test article end nodes and center node with small universal joints. The upper end of each rod is fixed to a suspension carriage which is constrained to pure vertical motion by air bearing shafts. Fixed to the top of the suspension carriage is a piston which is connected to an 80 gallon air tank. Each of the air tanks is individually pressurized to provide the proper upwards force on the piston to offload the test article weight in a level fashion. It is the large air plenum which provides the soft vertical stiffness, see [16] or [17] for details. The electric component of the pneumatic/electric devices are the electric displacement transducers attached to the suspension carriages to provide a D.C. restoring force to control piston drift. The electric stiffnesses can be controlled to compensate for the carriage mass.

5.1.1 Scaling Analysis

To ensure that the MACE test article was addressing realistic issues concerning the qualification of controlled flexible spacecraft, a scaling analysis was performed to determine the key physical properties of MACE. Using the physical properties of candidate flexible spacecraft missions deemed susceptible to control structure interaction problems, (e.g. Space Station Freedom, Hubble Space Telescope, Earth Observation Platforms: EOS-A, EOS-B and GEOS) a consistent multiple scaling was performed for the MACE test article [72]. The need to perform a multiple scaling parameter scaling versus a single scaling parameter scaling (e.g. replica scaling) was the result of criteria beyond the simple physical size of the scaled test article. It was necessary to take into account the mass and length constraints imposed by the Space Shuttle middeck (given the objective of having the MACE test article eventually fly as a payload aboard the Shuttle) as well as the scientific criterion of unity time and rotation scaling.

The Shuttle middeck imposes constraints of a test article length less than 6 feet and total mass less than 54 lbs, this roughly fixes two scaling parameters: a geom-

etry parameter, λ_l, and a mass parameter λ_m. Given platform sizes of the order of magnitude of 50 feet and platform masses of the order of 10,000 lbs we have

$$\lambda_l = \frac{\text{length}_{\text{MACE}}}{\text{length}_{\text{platform}}} \approx \frac{\mathcal{O}(5)}{\mathcal{O}(50)} = \frac{1}{10} \tag{5.1}$$

$$\lambda_m = \frac{\text{mass}_{\text{MACE}}}{\text{mass}_{\text{platform}}} \approx \frac{\mathcal{O}(100)}{\mathcal{O}(10000)} = \frac{1}{100} \tag{5.2}$$

To simplify interpretation of system performance the frequencies and the rotations or strains[1] were selected to scale as unity. The resulting time scaling parameter, λ_t, and rotation scaling parameter, λ_θ, are thus fixed to be one

$$\lambda_t = \frac{\text{resonant freq}_{\text{MACE}}}{\text{resonant freq}_{\text{platform}}} \approx \frac{\mathcal{O}(1Hz)}{\mathcal{O}(1Hz)} = 1 \tag{5.3}$$

$$\lambda_\theta = \frac{\text{rotations}_{\text{MACE}}}{\text{rotations}_{\text{platform}}} \approx \frac{\mathcal{O}(1)}{\mathcal{O}(1)} = 1 \tag{5.4}$$

The above selection of unity scaling for both time and rotation (or strain) has the advantageous result of facilitating the interpretation of experimental results since rotation and rotation rate both scale as unity and the two are directly linked to the performance metric which weights pointing stability and jitter of the payload inertial angle and bus attitude.

Having established the four scaling parameters, λ_l, λ_m, λ_t, and λ_θ, all other system physical properties are fixed by unique scaling parameters derivable by non-dimensionalizing the system equations of motion. The scaling of forces, deflections, stiffnesses, etc. are thus expressed in terms of λ_l, λ_m, λ_t, and λ_θ, and are presented in Table 5.1 for reference purposes. To better appreciate the advantages of the multiple scaling used for MACE, Table 5.1 also includes the scaling values which would result from replica scaling (where all properties are scaled based on a single geometry scaling parameter). The replica scaling values are those associated with a 1/10th scale model.

[1]It can be shown by elasticity first principles that strain scales as rotation.

Table 5.1: Summary Table of MACE Scaling Factors

Quantity	Symbol	MACE Multiple Scaling		Replica Scaling	
length	l	λ_g	10^{-1}	λ	10^{-1}
mass	m	λ_m	10^{-2}	λ^3	10^{-3}
time	t	λ_t	1	λ	10^{-1}
rotation & strain	θ	λ_θ	1	1	1
displacement	δ	$\lambda_g\lambda_\theta$	10^{-1}	λ	10^{-1}
force	F	$\lambda_m\lambda_g\lambda_\theta/\lambda_t^2$	10^{-3}	λ^2	10^{-2}
acceleration	a	$\lambda_g\lambda_\theta/\lambda_t^2$	10^{-1}	λ^{-1}	10
torque	τ	$\lambda_m\lambda_g^2\lambda_\theta/\lambda_t^2$	10^{-4}	λ^3	10^{-3}
flexural stiffness	EI	$\lambda_m\lambda_g^3/\lambda_t^2$	10^{-5}	λ^4	10^{-4}
axial stiffness	EA	$\lambda_m\lambda_g/\lambda_t^2$	10^{-3}	λ^2	10^{-2}
angular velocity	$\dot{\theta}$	λ_θ/λ_t	1	λ^{-1}	10
angular accel.	$\ddot{\theta}$	$\lambda_\theta/\lambda_t^2$	1	λ^{-2}	100
gravity effects	–	λ_θ	1	1	1

The multiple scaling is clearly preferable to the replica scaling in its scaling of angular rate and angular acceleration, as well as in its scaling of frequencies (i.e. time) which would be too low in the replica scaling case.

We come now to the interesting question of how the effects of gravity scale. Clearly the gravitational acceleration is independent of the scale of the model so that g does not scale. The *effects* of g, on the other hand, do scale and are a function of the type of scaling adopted for the spacecraft model. The magnitude of the stress stiffening effect of g on the structure's eigenfrequencies and eigenmodes is captured by the non-dimensional parameters derived in Chapter 2. Thus, by evaluating the scaling of the non-dimensional parameters, we evaluate the scaling of the effect of gravity. Applying the appropriate multiple scaling parameters used for MACE (from Table 5.1) to the various properties which make up a given non-dimensional parameter we obtain the

following

$$\text{axial load n.d.p.} \rightarrow \text{scales as } \left(\frac{Fl^2}{EI}\right) \rightarrow \lambda_\theta \tag{5.5}$$

$$\text{bending load n.d.p.} \rightarrow \text{scales as } \left(\frac{M\sqrt{IA}l^2}{EI^2 - AGJl^2}\right) \rightarrow \lambda_\theta \tag{5.6}$$

$$\text{torsional load n.d.p.} \rightarrow \text{scales as } \left(\frac{Ml}{EI}\right) \rightarrow \lambda_\theta \tag{5.7}$$

It is very interesting to discover that the effect of gravity scales as the rotation scales, which for the case of the MACE testbed is unity. This observation further strengthens the proposition that infinitesimal or elemental rotations of the structure in the gravity field are the underlying or unifying source of the family of gravity effects (as discussed in Sections 2.1.2, 2.4.1 and 4.5.1 for the role of rotation in initial stress, initial deformation and sensor/actuator gravity effects respectively.)

5.2 Parametric Variation Study

To examine the realistic nature of gravity effects on a beam-like test article and explore the practicality of predicting the magnitude of gravity and suspension effects with the non-dimensional parameters of Chapters 2 and 3, a parametric variation study was performed. A simplified MACE model was developed along with four variation cases where a single geometric, material or configurational change was made for each case. The ADINA finite element modeling software was used to develop both 0–g and 1–g models for each case. The shifts in eigenfrequencies and the changes in the eigenmodes from 0 g to 1 g are examined in addition to examining the changes in two key system transfer functions.

5.2.1 Baseline Simplified MACE Model

To capture the fundamental physics of the MACE test article dynamics with a low order model, a simplified MACE model was developed. The simplified model from which the parametric variation cases are derived is called the baseline simplified MACE model. As illustrated in Figure 5-3 the essential configuration features a planar structure composed of four lexan struts with 5 nodal point masses, a torque wheel point mass raised above the bus axis, 2 double gimbal assembly point masses and 2 payload point masses. All point masses have appropriate rotary inertia properties. The 0–g model has 6 rigid-body modes and 4 mechanism modes given the 2 double gimbal mechanisms. The lexan struts have a density of 1200 kg/m^3 and a Young's modulus of 3.3575e9 Nm^2 (increased from the nominal 2.3e9 Nm^2 specification to obtain the correct first flexible frequency of approximately 1.72 Hz and capture the stiffening effect of the unmodeled attachment nodes and collars). Other details of the baseline case are provided in Table 5.2 which summarizes the fundamental properties of each parametric variation case. The rigid links are modeled as having a stiffness two orders of magnitude greater than the lexan struts and a density one tenth that

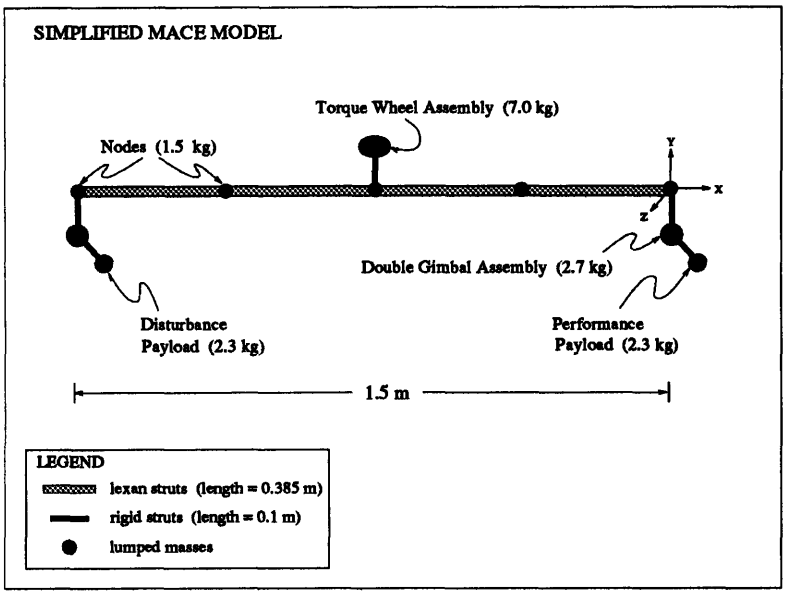

Figure 5-3: Simplified MACE Model Geometry and Lumped Mass Distribution for 0–g Analysis

of the struts.

5.2.2 Suspended Baseline Simplified MACE Model

The suspended simplified model is also referred to as the simplified 1–g model. As shown in Figure 5-4, three devices are used to support the MACE test article. The pneumatic-electric suspension devices are modeled as soft translational springs fixed between the ceiling and a suspension carriage. All carriage degrees of freedom are constrained except for the vertical (Y axis) degree of freedom. The carriages are modeled as massless. A single rigid beam element is used to model the suspension rods. Universal pin joints are included in the model at each end of the rods.

5.2.3 Parametric Variation Cases of Simplified MACE Model

Four different variations of the baseline case, case C0, were modeled using the ADINA finite element modeling software. The first case, C1, is the 1 Hz case where the Young's modulus of the lexan was reduced to obtain a fundamental vertical bending

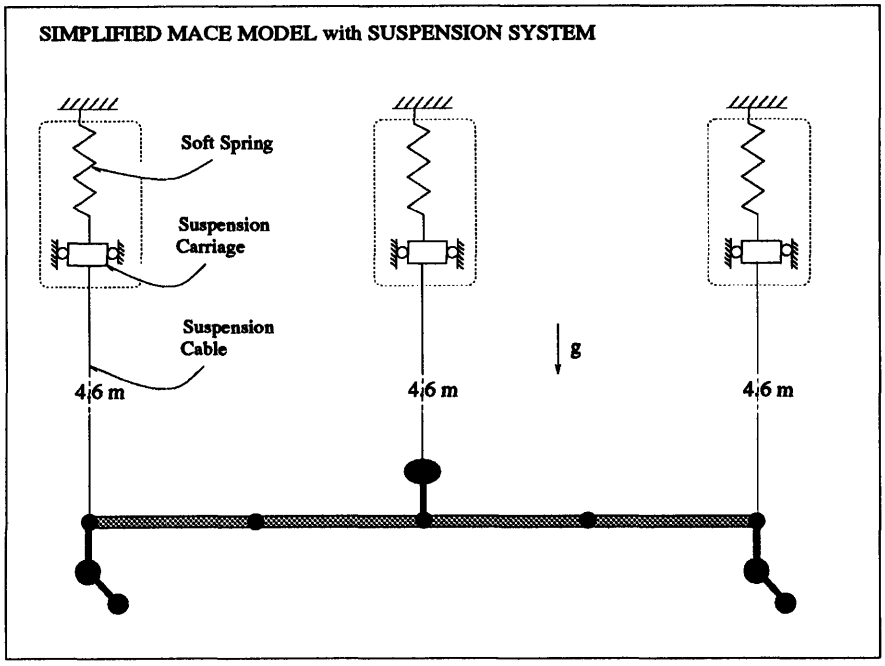

Figure 5-4: Simplified MACE Model with Suspension System for 1–g Analysis

frequency of 1 Hz, and simultaneously destiffen all flexible modes. It is expected that all gravity effect sensitivity parameters will increase for this change from the baseline. The second and third cases, C2 and C3, are rectangular cross-section cases where I_y and I_z were reduced by a factor of 3, respectively, for the two cases. For C2 the first vertical bending frequency remains unchanged and for C3 the first horizontal bending frequency remains unchanged. In both cases the opposite plane bending mode frequency is reduced by a factor of $\sqrt{1/3}$. The fourth case, C4, is identical to the baseline case except for the orientation of the performance payload which it kept at 45 degrees to the vertical but is rotated out of the suspension plane by 45 degrees. This introduces a torsional load on the MACE bus.

5.2.4 Application of Non-Dimensional Parameters

Since the principal structural component of the MACE test article is beam-like it is definitely suitable for the application of the non-dimensional parameters derived in this thesis.

Table 5.2: Summary Table of Fundamental Properties of Simplified MACE Model Baseline and Parametric Variation Cases

CASE	E (Nm^2)	G (Nm^2)	Ix (m^4)	Iy (m^4)	Iz (m^4)	J (m^4)	Area (m^2)	1st vert. flex. [Hz] / #	1st hor. flex. [Hz] / #	1st torsion [Hz] / #	2nd hor. flex. [Hz] / #	2nd vert. flex. [Hz] / #
Baseline	3.3575e9	1.262e9	2.8e-8	1.4e-8	1.4e-8	2.8e-8	2.232e-4	1.721 / #1	2.30 / #2	5.445 / #3	6.477 / #4	7.217 / #5
C1	**1.337e9**	**5.026e8**	2.8e-8	1.4e-8	1.4e-8	2.8e-8	2.232e-4	**1.00 / #1**	**1.335 / #2**	**3.164 / #3**	**3.764 / #4**	**4.194 / #5**
C2	3.3575e9	1.262e9	**1.867e-8**	1.4e-8	**4.667e-9**	**1.217e-8**	3.114e-4	1.717 / #2	**1.322 / #1**	**4.451 / #4**	**3.689 / #3**	7.162 / #6
C3	3.3575e9	1.262e9	**1.867e-8**	**1.867e-8**	1.4e-8	**1.217e-8**	3.114e-4	**0.991 / #1**	2.288 / #2	**4.135 / #4**	**4.456 / #3**	**5.393 / #5**
C4	3.3575e9	1.262e9	2.8e-8	1.4e-8	1.4e-8	2.8e-8	2.232e-4	1.718 / #1	2.30 / #2	5.44 / #3	6.454 / #4	7.218 / #5

CROSS-SECTIONS

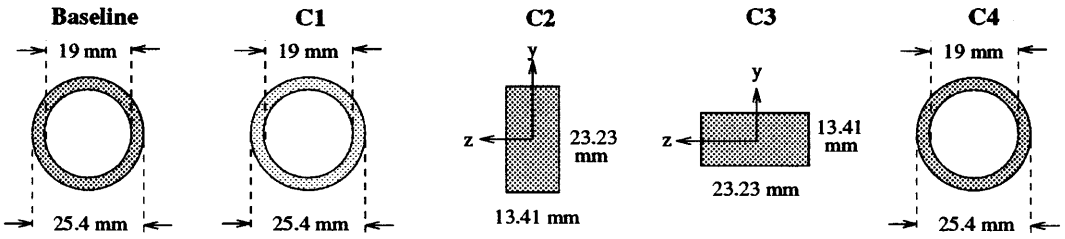

To estimate the sensitivity of the various configurations to the effects of gravity it is necessary to estimate the internal loads on the MACE bus and the magnitude of the initial deformations if any. To evaluate the sensitivity to the fundamental suspension stiffening effects it is necessary to know or have estimates of the suspension bounce mode, pendulum mode, and double-pendulum mode frequencies, as well as knowledge of the fundamental resonant frequencies and mode-shapes of the test article which can be obtained from the 0–g model.

Given the canceling effect of the bending moments induced by the two 45 degree gimballed payloads at each end of the test article, and the fact that all significant point masses are off-loaded it was estimated that the internal nodal loads were not significant (and largely due to shear if they were non-negligible). Similarly, the effects of initial deformations were considered to be negligible for all of the configurations studied here. These two assumptions proved to be incorrect as will be demonstrated in the following section. The non-dimensional parameters associated with geometric stiffening and initial deformation should in fact have been computed.

The torsional load due to the out-of-plane gimbal in case 4, i.e. C4, was deemed important and the following torsional internal load was estimated

$$M_x = \frac{0.1}{\sqrt{2}}(2.3)(9.8) = 1.6 \text{ Nm} \tag{5.8}$$

To determine the suspension system non-dimensional parameters it is necessary to identify the fundamental suspension resonances. The spring stiffnesses are tuned to achieve a level structure with a bounce frequency f_b of 0.1 Hz, the pendular frequency f_p is approximately 2.3 Hz (from $f_p = 1/2\pi\sqrt{(g/l)}$) and the double-pendular frequency was found to be approximately 0.63 Hz.

NDP's for Suspension Effect

Treating the beam as a free-free beam and using the parameters of Table 5.2 with the suspension resonant frequencies described above we can estimate the stiffening effect

on the system fundamental modes. The results of these computations are tabulated in Table 5.3 where, recall, the label C0 is used to indicate the Baseline case. A sample calculation follows for the stiffening effect of the suspension pendular behavior on the 1st horizontal flexible mode

$$\Gamma_{h1} = \frac{5(0.23)^2}{(2.3)^2} \doteq 0.05 \tag{5.9}$$

The resulting impact on the resonant frequency is then

$$\frac{{}^{t}f_{h1}}{{}^{o}f_{h1}} = \sqrt{1 + 0.05} = 1.025 \tag{5.10}$$

which corresponds to a stiffening of +2.5%.

5.2.5 ADINA Modeling Procedure

The ADINA finite element modeling software [31] was used to generate 0–g and 1–g models of the baseline simplified MACE test article and the different parametric variations thereof. As described in more detail in Appendix A capturing gravity effects with ADINA is a multi-step procedure. The initial step consists of developing an unsuspended model of the test article (this is the 0–g model). Three different ADINA input files are then required to derive the 1–g model. The first step in deriving the 1–g model is to add the suspension system description to the 1–g model and constrain the lower end of each spring so that the suspension system is rigid. A description of the mass-proportional loading is then added to the model and a non-linear iterative analysis (with geometric stiffness refinements) is performed to compute initial deflections and reaction forces. A linear analysis could equally be performed but better results are obtained in the subsequent non-linear steps if this first step is also non-linear. The reaction forces F_R at the suspension upper attachment points are then used to calculate the suspension spring stiffnesses $k_{\mathbf{susp}}$ which will yield a level

Table 5.3: Summary Table of Model Output and Non-Dimensional Parameter Predictions of Gravity and Suspension Effects on MACE Simplified Model Eigenfrequencies

		1^{st} v. bend.	1^{st} h. bend.	1^{st} tors.	2^{nd} h. bend.	2^{nd} v. bend.
	Predicted	0.85%	2.5%	2.1%	0.4%	$\sim$ 0%
C0	Output	2.3%	3.1%	5.1%	0.25%	0.5%
	(mode #)	1	2	3	4	5
	Predicted	2.5%	7.1%	5.8%	1.2%	0.2%
C1	Output	10.0%	7.5%	14.0%	1.1%	1.2%
	(mode #)	1	2	3	4	5
	Predicted	0.85%	7.3%	2.9%	1.3%	$\sim$ 0%
C2	Output	2.4%	8.0%	-9.8%	$\sim$ 0%	-6.3%
	(mode #)	2	1	4	3	6
	Predicted	2.5%	2.5%	3.0%	1.9%	0.2%
C3	Output	10.0%	2.4%	-9.7%	0.6%	1.5%
	(mode #)	1	2	4	6	3
	Predicted	0.85%	2.3%	2.1%	0.4%	$\sim$ 0%
C4	Output	2.7%	4.7%	4.85%	-1.5%	4.5%
	(mode #)	1	2	3	4	5

structure with the correct bounce frequency f_b, i.e.

$$k_{\text{susp}_i} = \frac{4\pi^2 f_b^2 F_{R_i}}{g} \tag{5.11}$$

This first step is appropriate for suspension systems such as pneumatic-electric suspension devices where the suspension device stiffnesses are tuned to obtain a level structure. The tuning process is equivalent to setting the spring stiffnesses to be mass-proportional. An alternate method of suspending a structure is to use fixed

stiffness translational springs and to adjust the cable lengths[2] and hence the off-loaded mass so as to obtain a set of mass-proportional suspension stiffnesses and a level structure. If this method is used it is necessary once again to determine the reaction forces, preferably by constraining (i.e. pinning) the structure in a level configuration directly at the suspension–structure attachment points. The dislocation method can then be used to compute the change in cable length required to obtain mass-proportional stiffening [19]

$$\Delta l_i = \frac{l_i}{1 + \frac{F_{R_i}}{(EA)_i}} - l_i \tag{5.12}$$

Having determined the approximate suspension stiffnesses the second step is to release the constrained springs and perform the non-linear iterative analysis which will solve for the initial deformations of the system subject to geometric stiffness effects. The non-linear iterative analysis with geometric stiffness refinements is an automated feature of the ADINA finite element modeling software. This step yields the sought after system property matrices for the deformed system (in global coordinates) subject to geometric stiffness effects capturing thus the effects of the suspension system, initial deformations and geometric stiffening. The third and final step consists of performing the eigensolution for the system described at the end of step two. More details of the ADINA modeling procedure are provided in Appendix A.

5.2.6 Results

Several different methods are used here to compare the dynamics of the 0–g and 1–g systems: eigenratio plots, eigenmode cross-orthogonality plots, and superimposed 0–g and 1–g transfer function plots.

[2] typically with turnbuckles

Eigensystem Comparison Methods

The eigenvalues of the first 15 flexible modes[3] are compared in eigenratio histogram plots where the the 1–g resonant frequency is normalized by the 0–g frequency (see Figures 5-5 to 5-9). An alternate normalization technique for the eigenfrequencies is to take the difference between the 1–g and 0–g frequencies and normalize by half of the half-power bandwidth. The motivation for this approach of plotting the eigenfrequency shifts in units of half-power bandwidths is to provide a useful measure for estimating the importance of the eigenfrequency shift based on the assumption that robust control strategies have difficulty coping with eigenfrequency shifts of greater than a half-power bandwidth. This approach sensitizes the measure of the gravity effect to the amount of damping at each resonance. However, since no experimental data exists for the hypothetical simplified MACE model a uniform damping ratio of 1% was used. The half half-power bandwidth normalized plots therefore correspond to histograms of the percent shift in frequency.

Before discussing these results, the eigenmode cross-orthogonality plots are explained. The two mesh plots in each of Figure 5-5 to 5-9 are two views of the same mesh. The mesh is obtained by taking the absolute value of the inner product of the 0–g and 1–g eigenvector matrices: i.e. $|\Phi_{0g}^T \Phi_{1g}|$. If the eigenvector matrices were identical the modal cross-orthogonality mesh would be diagonal. Non-zero off-diagonal terms correspond to couplings between modes. The first fundamental mode (i.e. the bounce mode in the 1–g case) is in the upper left corner of the mesh while the highest frequency mode (the 32^{nd}) is in the lower right corner as indicated. Note that the modal cross-orthogonality meshes include the effect on the original rigid body modes while the eigenratio plots only summarize the effects on the flexible modes.

For a detailed interpretation of the cross-orthogonality meshes it is necessary to identify the (i, j) position of the peak or point we are interested in to be able to identify the modes involved. Recall that the first 10 modes are fundamental suspension modes;

[3]recall that there are 10 rigid-body or mechanism modes

they are listed here for reference purposes

1.	bounce	0.1 Hz
2.	tilt	0.132 Hz
3.	xz pendular (d)	0.227 Hz
4.	axial pendular	0.2319 Hz
5.	xz pendular (p)	0.2331 Hz
6.	bus rocking	0.465 Hz
7.	double gimbal (p)	0.633 Hz
8.	double gimbal (d)	0.659 Hz
9.	gimbal (d)	0.811 Hz
10.	gimbal (p)	0.815 Hz

For the fundamental flexible modes refer to the flexible mode numbers in Table 5.3 since the order varies depending on the configuration.

General Observations

At a glance, the modal cross-orthogonality meshes reveal that the principal effect of adding suspension and gravity effects to the 0–g model is to highly couple the rigid-body eigenspace and introduce slight or important couplings between various eigenmode pairs. The important couplings tend to occur between adjacent modes as expected. This is apparent in the modal cross-orthogonality meshes where separate peaks merge at their midpoint. In the case of very large couplings where modes essentially switch, the adjacent peaks each shift off the diagonal and form a large off-diagonal pair. Smaller couplings occasionally occur between non adjacent modes, including couplings between flexible modes and fundamental suspension modes.

Table 5.3 summarizes the eigenfrequency shifts observed from the 0–g model to the 1–g model along with the eigenfrequency shifts predicted by the static suspension stiffening non-dimensional parameters. Non-dimensional parameter predictions for the 1st mode horizontal case were very successful while the vertical mode eigenfre-

quency shifts were underestimated. This is due to the fact that the static suspension stiffening effects were derived based on a two point suspension system while the MACE simplified model has a third suspension spring at the beam midpoint. The additional vertical suspension spring naturally stiffens the first vertical bending mode as well as the other symmetric vertical bending modes. Clearly, there is a need to derive static suspension stiffening non-dimensional parameters which are a function of the number of attachment points. This is recommended for future work. Table 5.3 also makes clear the need to have included geometric stiffening and initial deformation effect contributions. Couplings between 1^{st} torsion and 2^{nd} horizontal bending are very evident but were not predicted.

Effects on C0: Baseline MACE Model

It is interesting to note that only the eigenfrequencies of the baseline model are affected and not its eigenmodes. Since the higher suspension frequencies are as high as one half of the first fundamental resonance of the Baseline it is not surprising to witness a stiffening of the first three fundamental modes: vertical bending, horizontal bending, and torsion. The reduced sensitivity of higher modes was well predicted by the non-dimensional parameter calculation.

Effects on C1: 1 Hz MACE Model

As expected and as predicted the sensitivity of the 1 Hz MACE Model to all gravity effects increased as the resonances all dropped significantly closer to the suspension resonances. Again, the fundamental flexible mode eigenfrequencies are the most affected. A new development is the introduction of several modal couplings. The fundamental flexible mode is now coupled to the suspension gimbal mode, the third and fourth modes are strongly coupled (i.e. torsion and 2^{nd} horizontal bending), and slight couplings exist between various flexible modes and suspension modes. It is not clear that the initial deformation or geometric stiffening non-dimensional parameters

would successfully have captured the torsion and 2nd horizontal bending coupling since the parameters predict a larger coupling between the 1st horizontal bending and torsion which did not occur. The effect of lumped masses and the participation of the gimbals substantially differentiate this model from the uniform beam model used to derive the non-dimensional parameters. This test case has exposed thus, unfortunately, the limited applicability of the non-dimensional parameters for complex structures.

Effects on C2, C3: Rectangular Bus MACE Models

These two cases are the most susceptible to significant eigenfrequency shifts and modal couplings. This is due to both the softening of bending modes in one plane of vibration, and the rectangular bus which increases the bus sensitivity to torsion-bending coupling in the presence of initial deformations and geometric stiffening. Notice the very strong couplings between torsion and 2nd horizontal bending again (in fact in C3 the modes cross-over) and the addition of a very strong coupling of flexible modes 6 and 7 which in both cases cross-over. For the C2 case this corresponds to an exchange between 2nd vertical bending and a combined 2nd torsion and 1st horizontal bending. For the C3 case it corresponds to an exchange of 2nd horizontal bending, and the same 2nd torsion and 1st horizontal bending. Note also the couplings between adjacent higher frequency modes in both cases.

Effects on C4: Out-of-Plane Payload

This case is very interesting in that no modal cross-overs occur but the non-planar structure has significantly sensitized the structure to gravity effects even at medium and high frequencies. Strong couplings between adjacent pairs of horizontal and vertical bending modes are the norm. Frequencies alternately rise and fall except for the fundamental three flexible frequencies which are stiffened by the fundamental suspension modes.

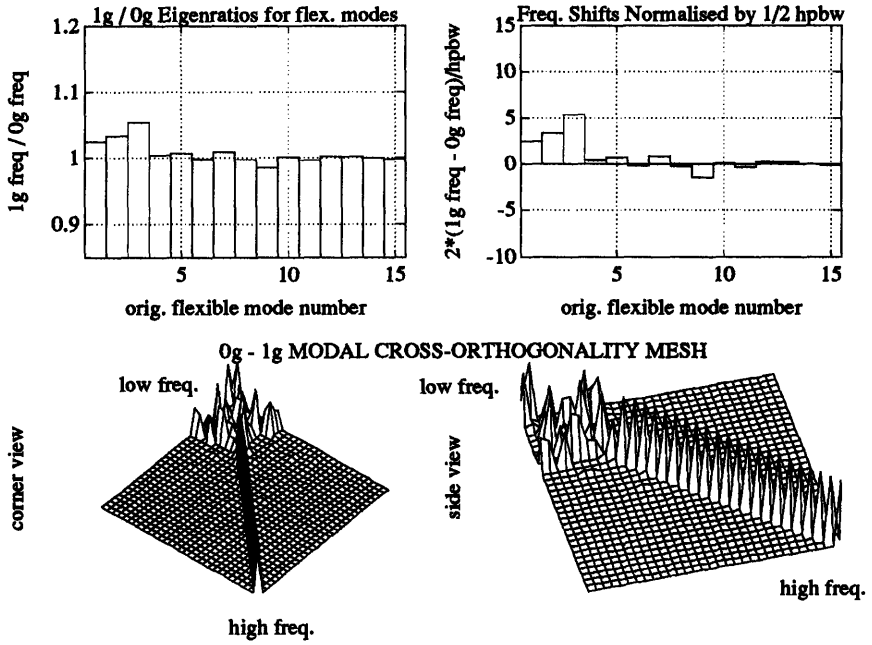

Figure 5-5: Gravity and Suspension Effects on C0: Baseline Simplified MACE Model

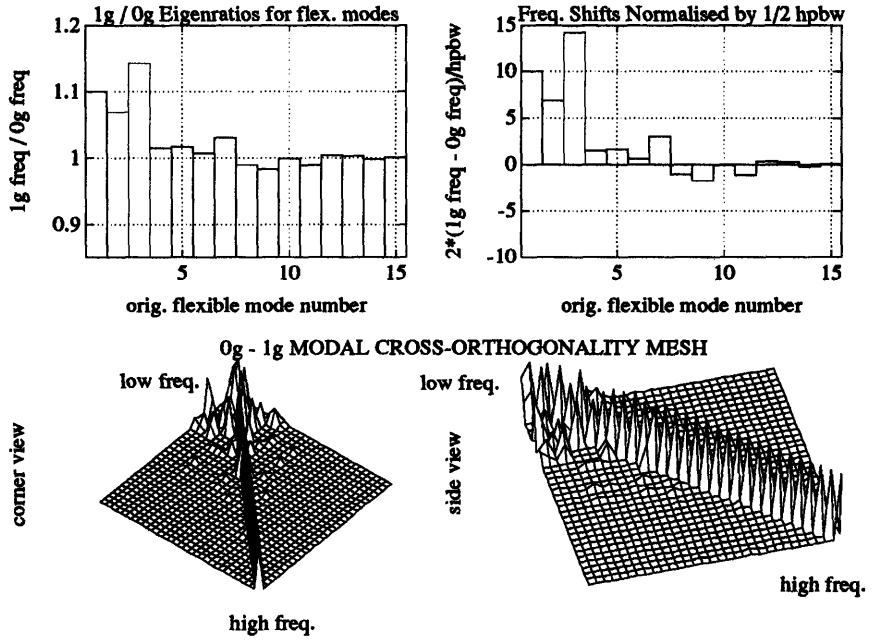

Figure 5-6: Gravity and Suspension Effects on C1: 1 Hz First Flexible Frequency Simplified MACE Model

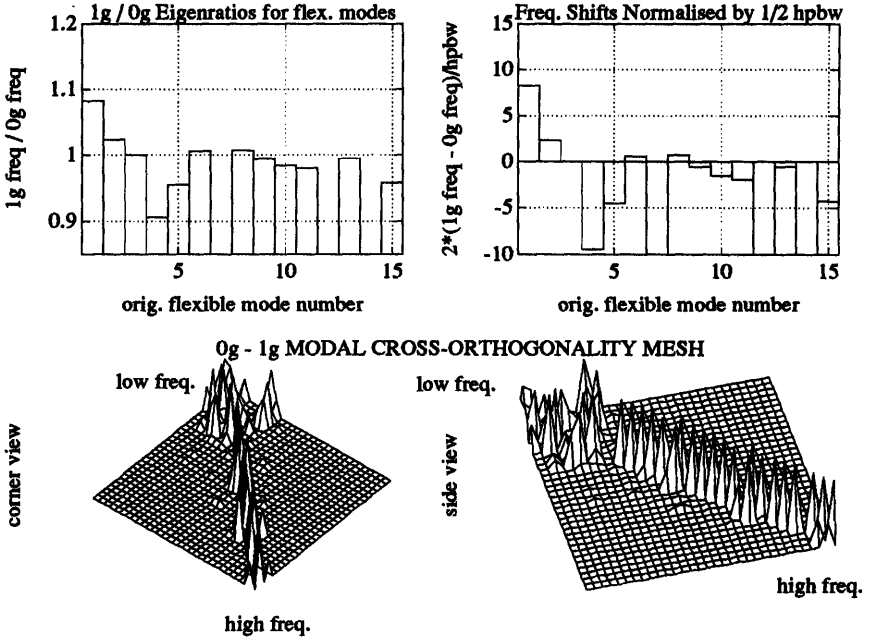

Figure 5-7: Gravity and Suspension Effects on C2: Reduced Y-Inertia Rectangular Bus Simplified MACE Model

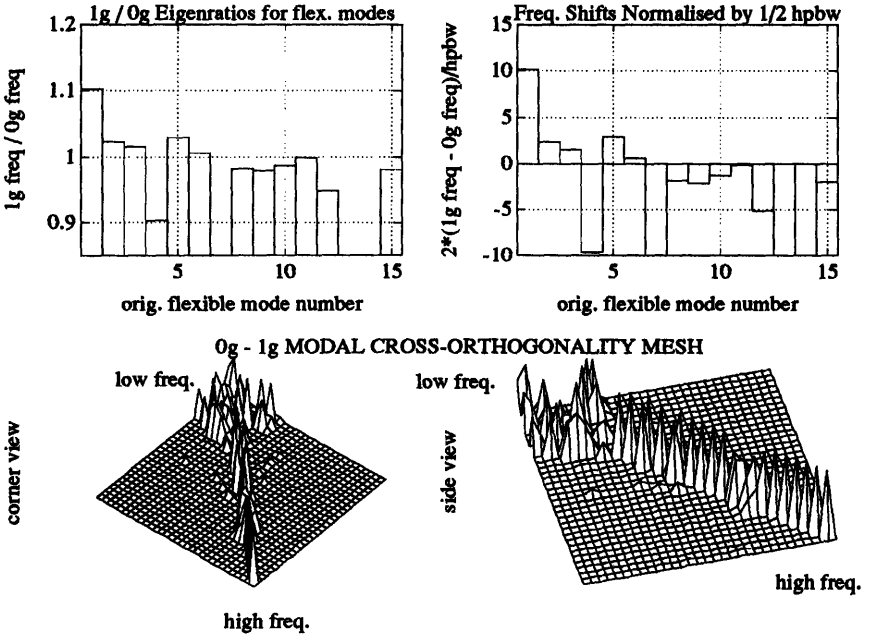

Figure 5-8: Gravity and Suspension Effects on C3: Reduced Z-Inertia Rectangular Bus Simplified MACE Model

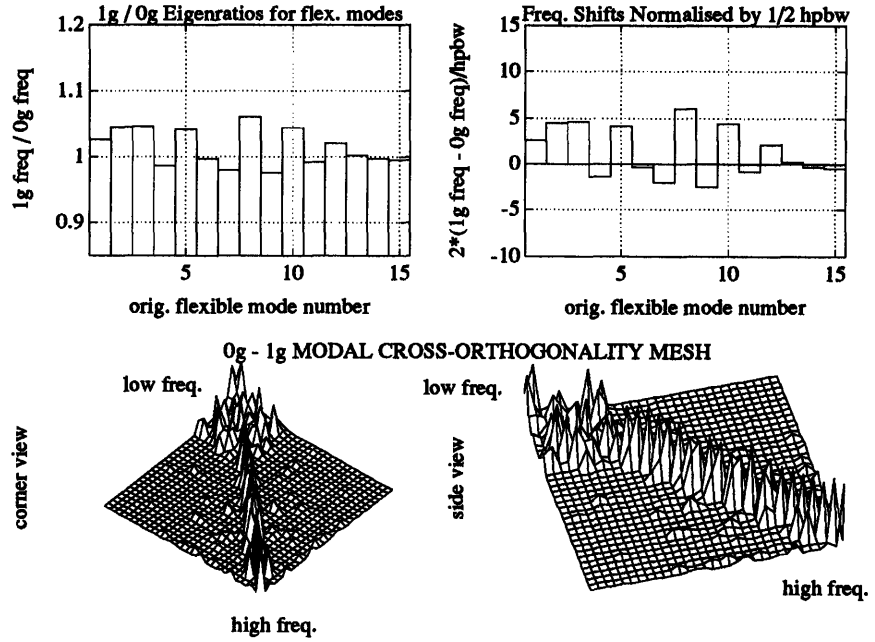

Figure 5-9: Gravity and Suspension Effects on C4: Simplified MACE Model with Performance Payload 45 Degrees Out-of-Plane

5.2.7 0–g and 1–g Transfer Functions

Having established the effects of gravity and of a laboratory suspension system on the eigensystem of the various MACE model parametric variations it is now possible to examine the nature of these same effects on a measure more directly applicable to the control of the structure–the key transfer functions.

Using the techniques described in Chapter 4, e.g. Equations (4.1) and (4.3), a state space model of the 0–g and 1–g MACE structures was developed for each parametric variation case, making use of the system property matrices and assuming proportional 1% damping. Appropriate input and output matrices were derived using eigenmode information at the point of actuation or sensing (see [1] for details). The results of the computed transfer functions for each case are plotted in Figures 5-10 to 5-14. The 0–g and 1–g transfer functions are superimposed on each plot (the 0–g transfer function is the solid line and the 1–g transfer function is the dashed line). The outer performance gimbal is the θ_Z gimbal on the right in Figure 5-3, while the

inner performance gimbal is the θ_X gimbal on the right. Node 2 is the node next to the performance gimbal node.

The most important effect in all transfer functions is the addition of suspension dynamics at low frequency. For the vertical accelerometer suspension bounce and tilt dynamics are readily apparent, for the horizontal accelerometer suspension bifilar pendular, transverse pendular, and double-gimbal pendular are readily apparent. The baseline model is otherwise largely unaffected. For the outer gimbal transfer function of the 1 Hz model, the first flexible mode pole is shifted upwards due to the suspension system while the inner gimbal transfer function shows a pole shift in the second flexible mode. In cases C2 and C3 the first flexible mode is similarly affected but of note are the very significant changes to the horizontal acceleration transfer functions over a large frequency spectrum. Clearly, gravity and suspension effects are not limited to low frequency effects when higher frequency modal couplings are introduced. In case C4 it is interesting to note that both horizontal and vertical transfer functions are significantly affected (as one would expect) based on the pervasive coupling introduced by gravity on the horizontal and vertical dynamics of the system with the out-of-plane gimbal.

It can be seen in Appendix A.3.2 that the general nature of the observations in this section on the simplified MACE model also holds true for the MACE Development Model.

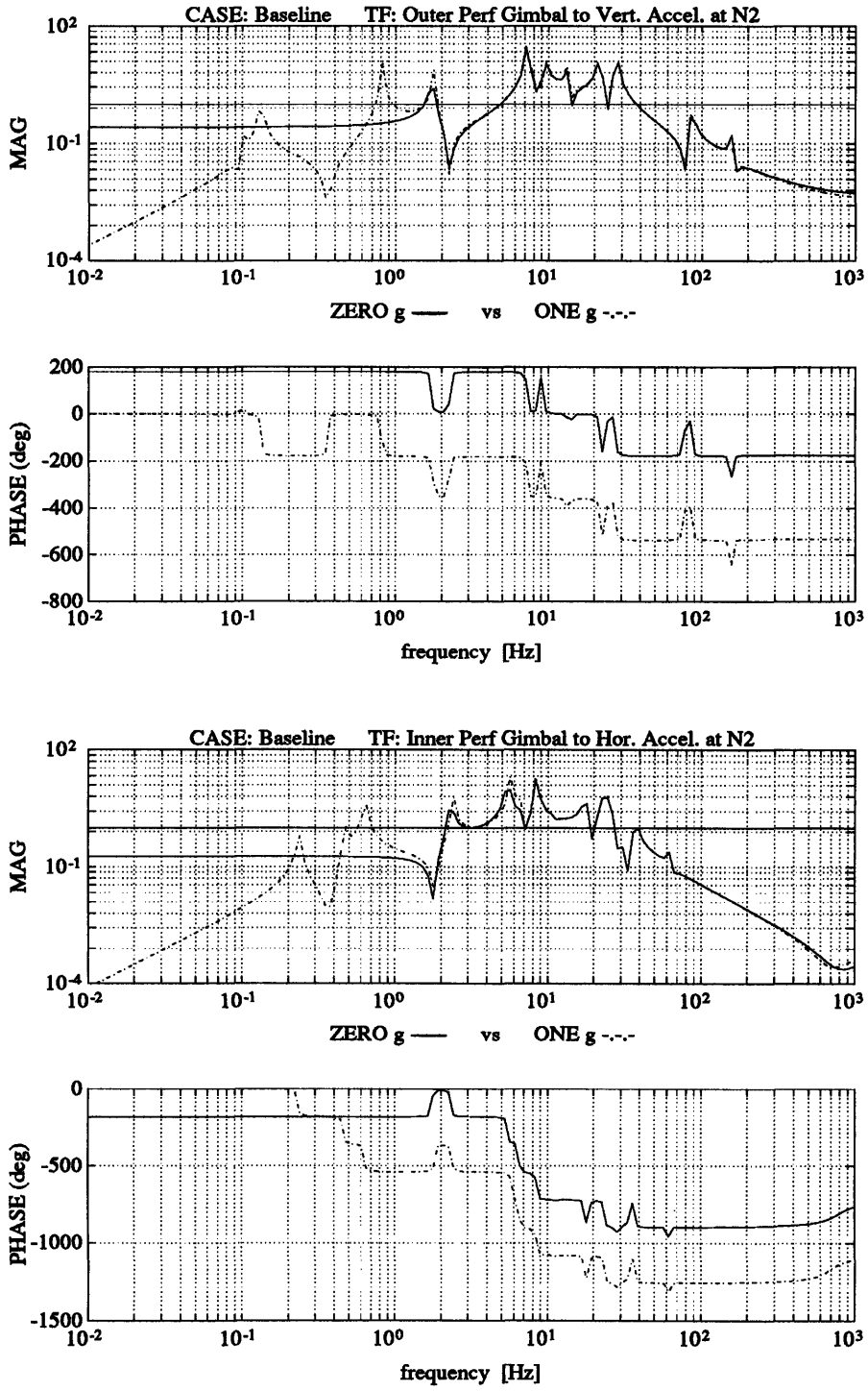

Figure 5-10: 0–g and 1–g Transfer Functions for C0 the Baseline Simplified Mace Model: Outer and Inner Performance Gimbals to Vertical and Horizontal Acceleration at Node 2

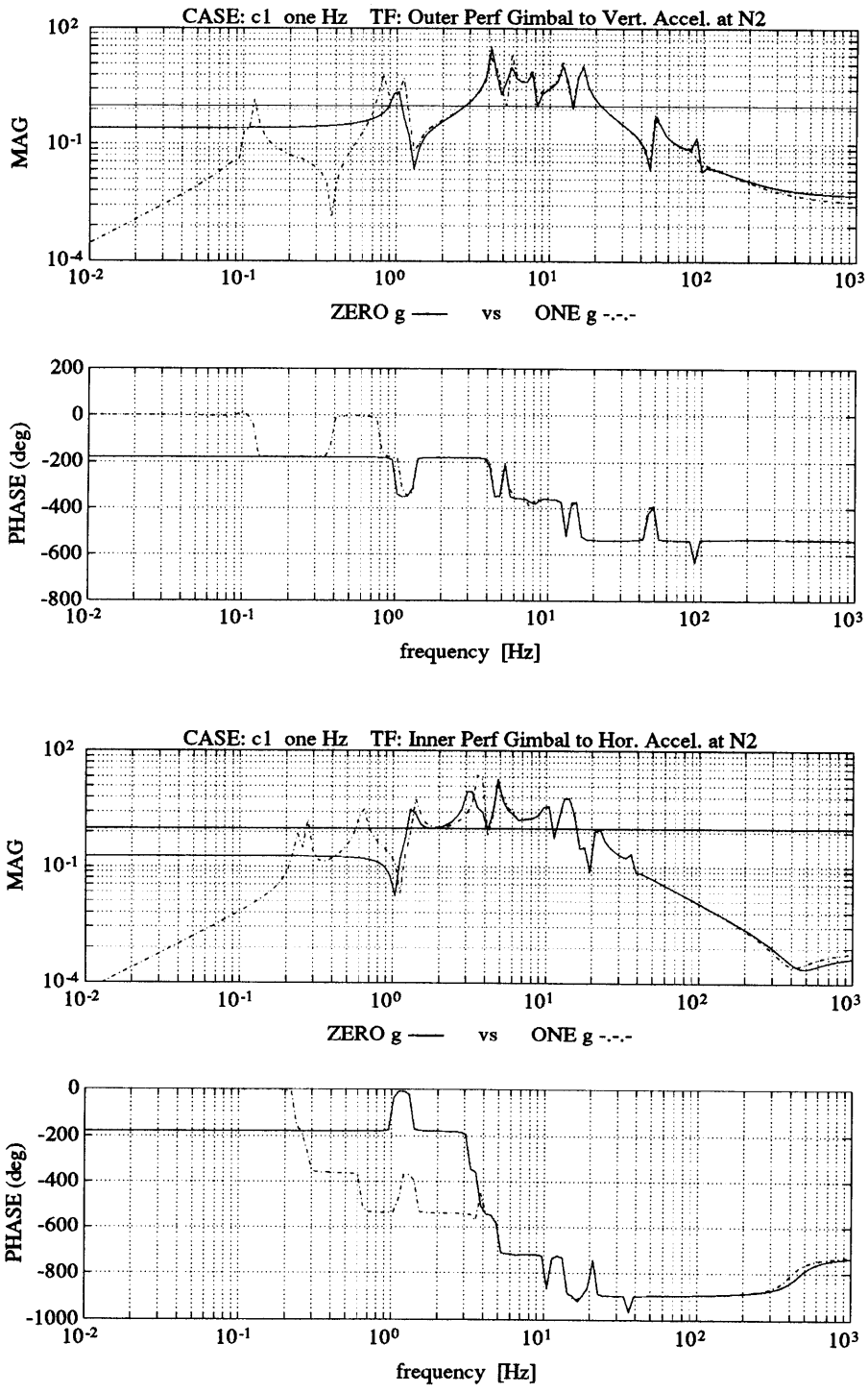

Figure 5-11: 0–g and 1–g Transfer Functions for C1 the 1 Hz Bus Simplified Mace Model: Outer and Inner Performance Gimbals to Vertical and Horizontal Acceleration at Node 2

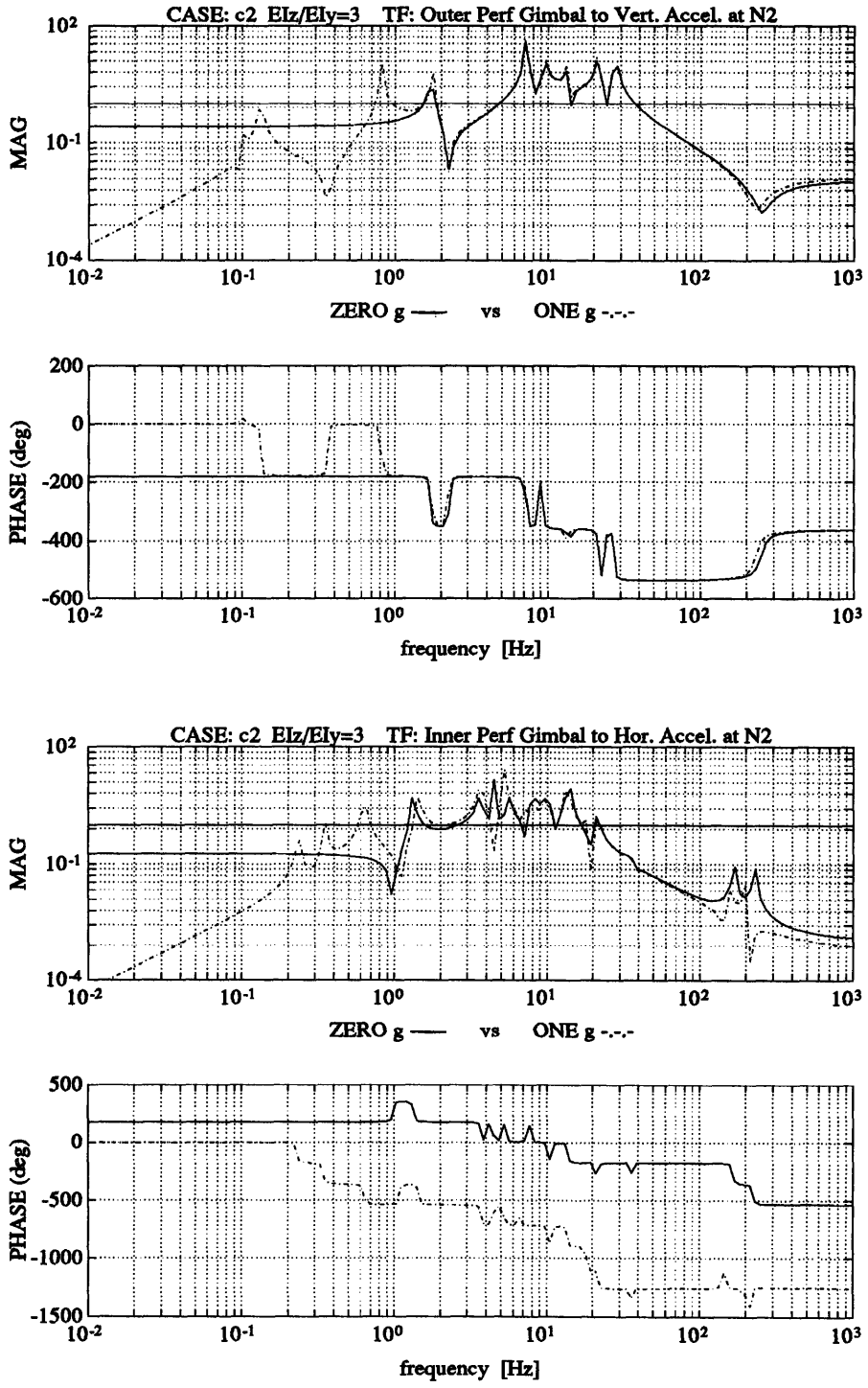

Figure 5-12: 0–g and 1–g Transfer Functions for the Reduced Iy, Rectangular Bus, Simplified Mace Model: Outer and Inner Performance Gimbals to Vertical and Horizontal Acceleration at Node 2

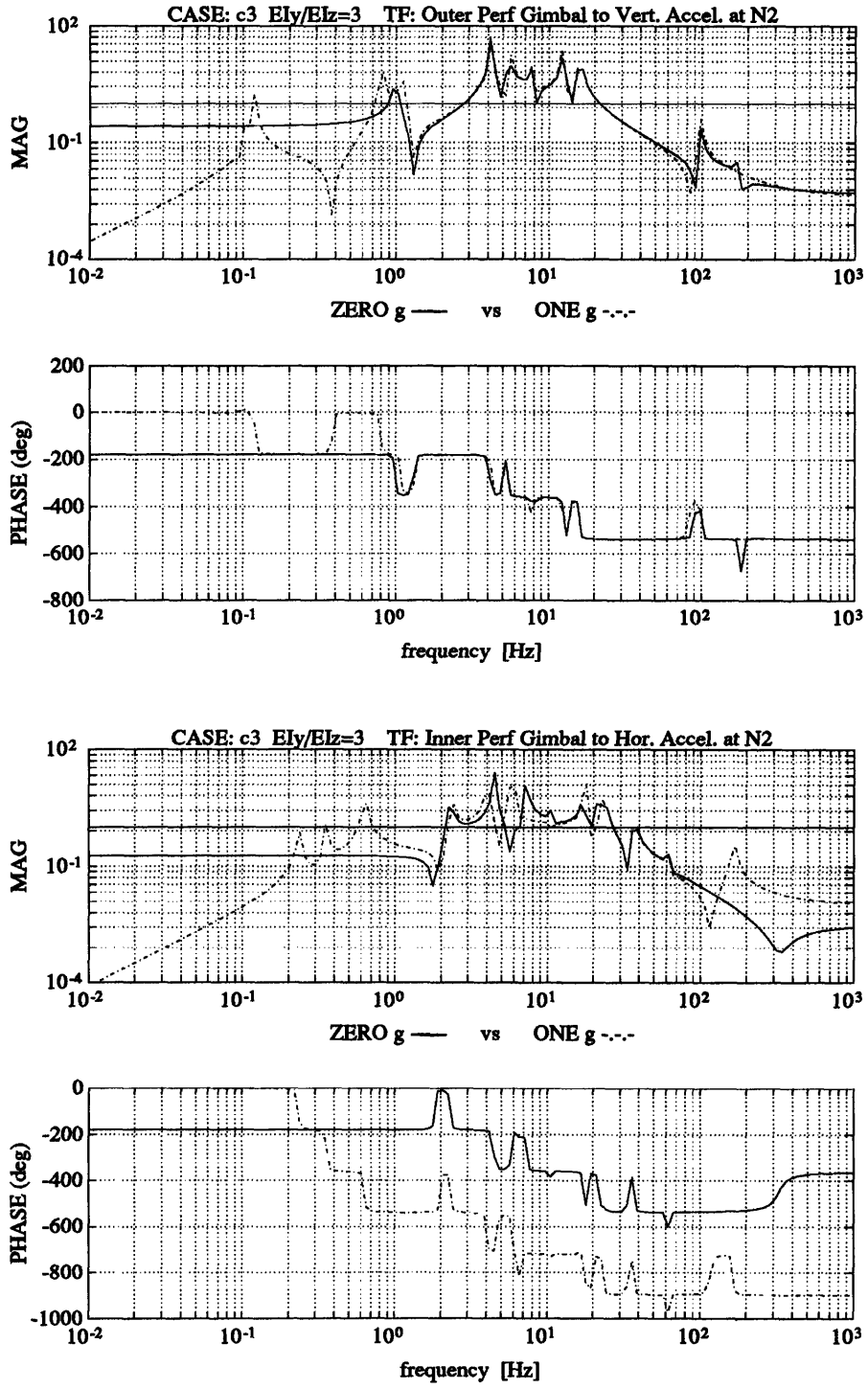

Figure 5-13: 0–g and 1–g Transfer Functions for C3 the Reduced Iz, Rectangular Bus, Simplified Mace Model: Outer and Inner Performance Gimbals to Vertical and Horizontal Acceleration at Node 2

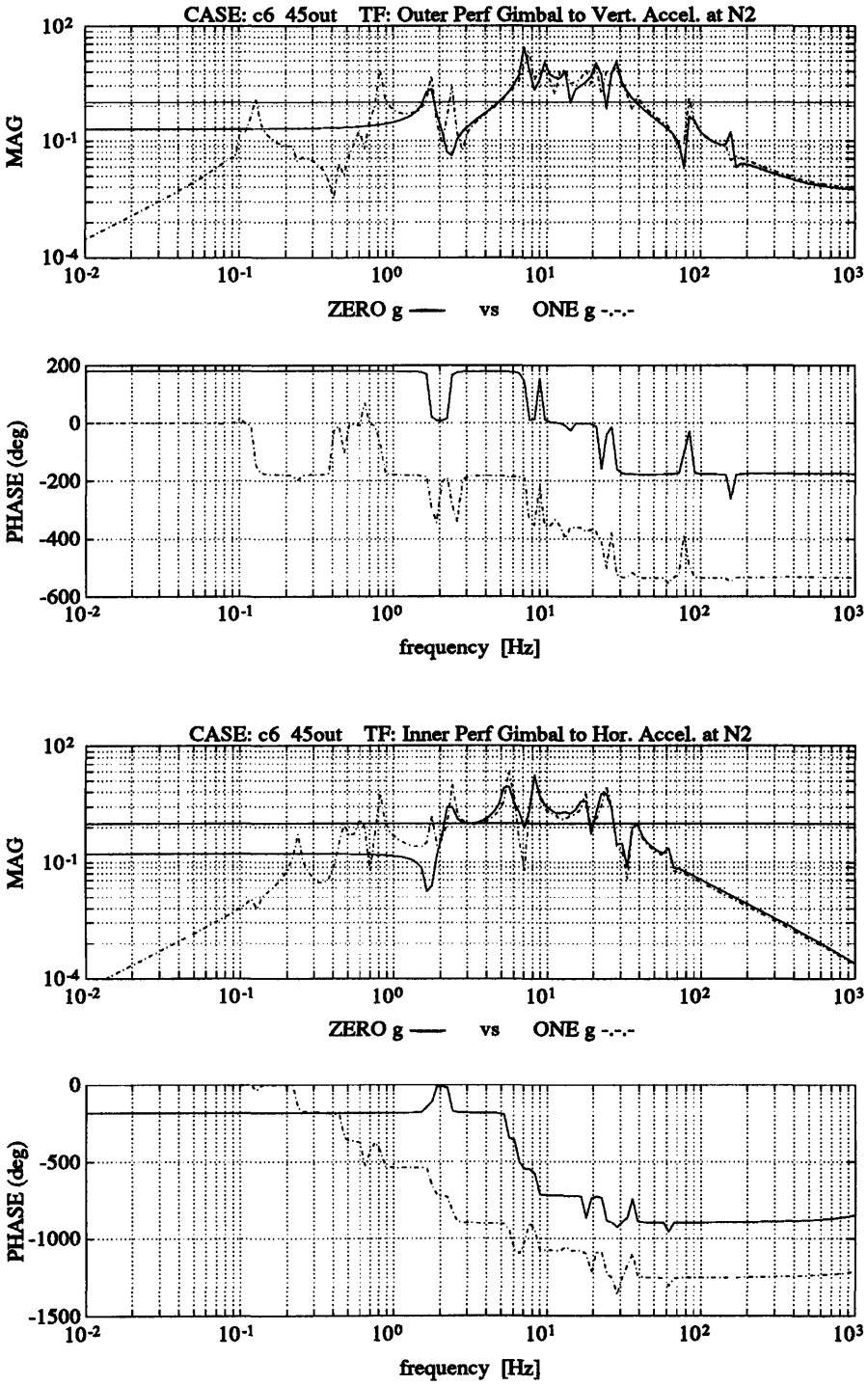

Figure 5-14: 0-g and 1-g Transfer Functions for C4 the Simplified Mace Model with Payload at 45 degrees to Suspension Plane: Outer and Inner Performance Gimbals to Vertical and Horizontal Acceleration at Node 2

5.3 MACE Flexible Appendage Experiment

This brief section presents the results of an experiment designed to sensitize the MACE Development Model to initial deformation effects in a manner realistic to the ground-based testing of controlled space structures. The motivation here is a realistic assessment of the nature of initial deformation effects on a suspended flexible spacecraft. Flexible appendages were attached to the MACE test article in a fashion representative of solar array models. The flexible appendages were attached to the test article node above the performance gimbal in a horizontal orientation–forming a T with the MACE test article as shown in Figure 5-15. -1z The same Minguet graphite-epoxy composite beams studied in Chapter 2 were selected for this experiment, the advantage being the known magnitude of the horizontal bending-torsion coupling and resonant frequency shifts under 1–g loading. From the many beams available two were selected which had a manufactured curvature very close to that induced by gravity were it cantilevered. Therefore, by attaching the beams to the MACE test article with the curvature up it was possible to simulate a 0 g initial deformation and with the curvature pointing down it was possible to simulate a 2 g or "Full Droop" case. The magnitude of the tip deflection was approximately 0 mm in the first case and approximately 20 mm in the second case.

5.3.1 Approach

It was originally attempted to model the flexible appendages in ADINA but, as with the MATLAB-based model, results were very poor in capturing both the proper horizontal bending and torsion dynamics of the composite beam. It appears to be insufficient to model the multi-layer composite beam as a uniform orthotropic plate element. Given the analysis of Section 2.5 it is valuable nonetheless to perform a purely experimental test and observe whether a tip deflection of 4% of the appendage length can have a significant effect on the overall system dynamics. Based on the

results of Section 2.5 it is expected that the torsional appendage mode at 84 Hz will couple with the horizontal bending mode at 113 Hz and will shift down to 77 Hz, or less, while the 113 Hz mode will shift up to 119 Hz or greater. Whether these effects occur and whether they impact the key MACE Development Model transfer functions will be determined experimentally.

5.3.2 Experiment Description

As described, simulation of 0 g , i.e. the "No Droop" case, was possible by mounting the curved appendages such that the gravitational loading corrected the pre-curvature and straightened the appendages. The "Full Droop" case was obtained by mounting the beams with the slight curvature pointing downwards such that the gravitational loading exacerbated the drooping. Photographs of the "No Droop" and "Full Droop" configurations are reproduced in Figures 5-15 and 5-16.

5.3.3 Results

It was possible to observe the impact of the flexible appendage droop in certain key transfer functions where a shift in the pole-zero structure was observed in the region of the original torsional frequency of the flexible appendages. As expected this frequency dropped when the torsional mode became coupled with horizontal (fore-aft) bending. This can be seen in both figures 5-17 and 5-18 where a zero-pole pair shift occured from 65 Hz to 48 Hz. That the original torsional frequency is lower than the expected 84 Hz is thought to be the result of having the two beams end to end about a lumped mass. The upwards shift in the fore-aft eigenfrequency which coupled with torsion was not measured given the limited bandwidth of the sensors.

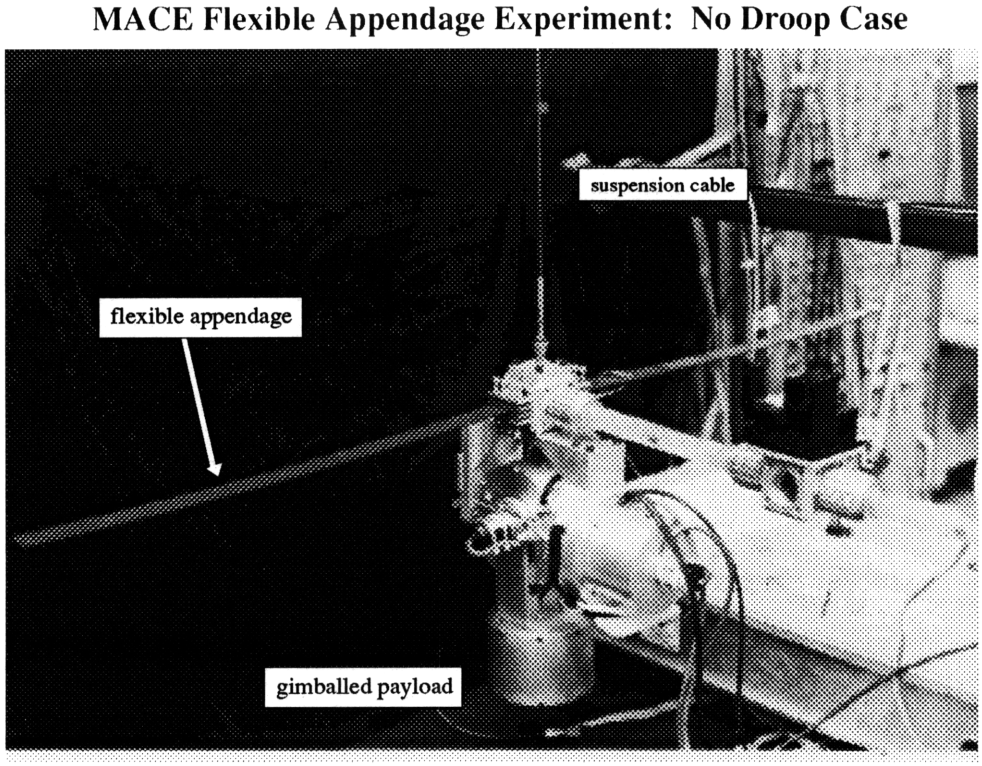

Figure 5-15: Photograph of the MACE Flexible Appendage Experiment: No Droop Case

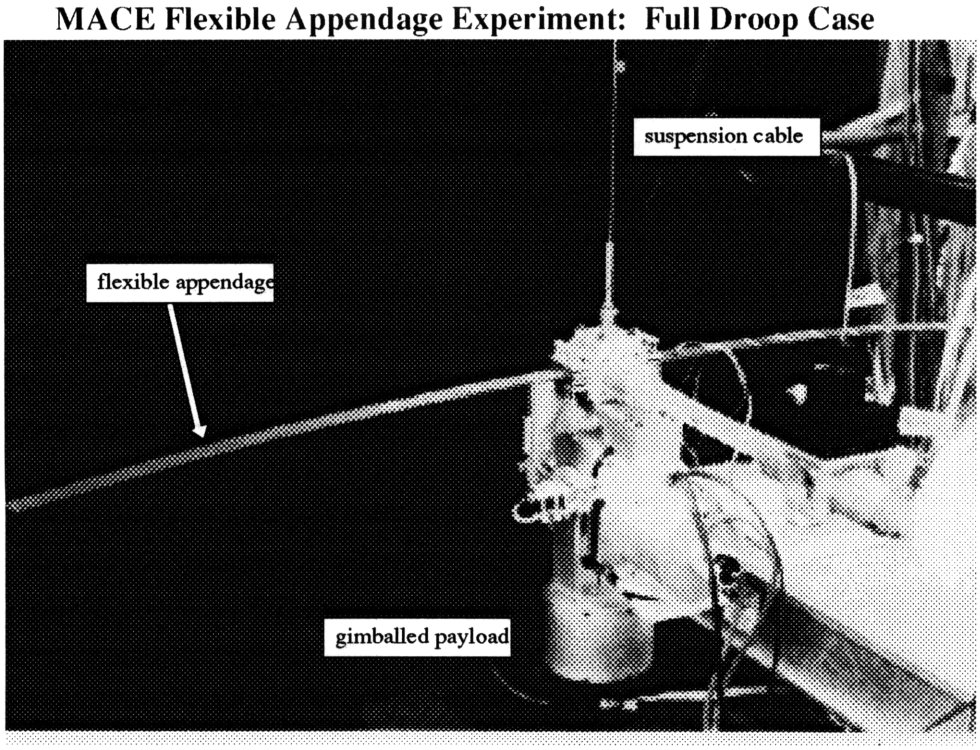

Figure 5-16: Photograph of the MACE Flexible Appendage Experiment: Full Droop Case

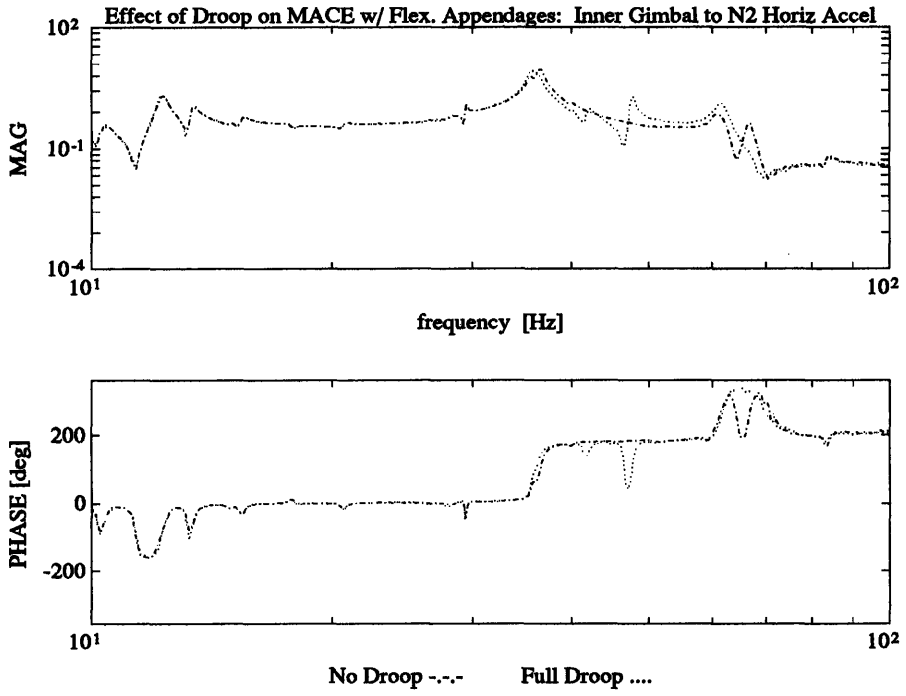

Figure 5-17: Effect of Flexible Appendage Droop on MACE Inner Gimbal to Horizontal Acceleration at Node 2 Transfer Function

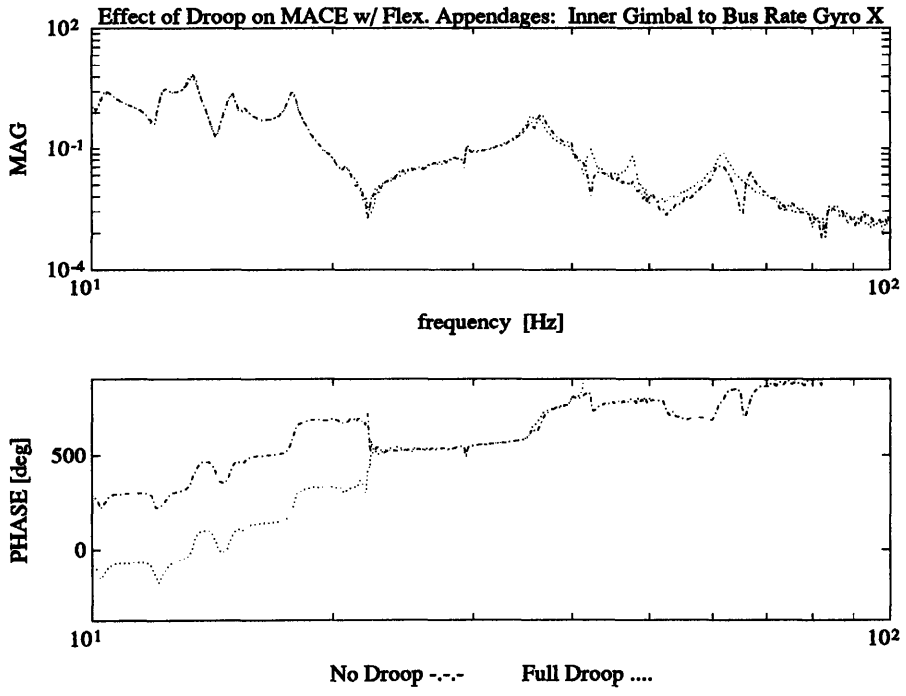

Figure 5-18: Effect of Flexible Appendage Droop on MACE Inner Gimbal to Bus Axial Rate Gyro Transfer Function

Chapter 6

Conclusions

6.1 Major Conclusions

Four different fundamental types of linear gravity and suspension effects on the dynamics of a controlled flexible spacecraft have been identified along with fundamental methods for modeling them. These effects,

1. Suspension Effects,
2. Direct Gravity Effects on Structure via Geometric Stiffening,
3. Direct Gravity Effects on Structure via initial deformation Effects, and
4. Direct Gravity Effects on Sensors and Actuators

were studied at length. Finite element modeling techniques have been derived for the direct gravity effects on the structure and on the structural sensors and actuators. A technique for modeling the static effects of a suspension system has been presented and the proper approach to modeling the dynamic suspension influences has been discussed. It has been found that by augmenting the finite element model of the structure with the suspension system model before incorporating the direct gravity effects one is able to comprehensively capture the entire family of linear gravity effects,

including dynamic suspension effects and couplings between the flexible structure and the suspension system.

The effects of gravity and of a suspension system on the dynamics of a controlled flexible structure have been shown to be very important for those low resonant frequency structures which have less than a decade of frequency separation between their fundamental modes and the suspension fundamental modes. It has been shown that gravity and suspension effects can degrade system performance and even destabilize the controlled system.

In general, the greatest impact of gravity and of the suspension system has been found to be a stiffening of the rigid-body modes and the introduction of couplings between the suspension system and the flexible test article. The second most important effect of gravity and the suspension system on the test article dynamics has been found to be the introduction of couplings between closely spaced or adjacent modes. It has been demonstrated that as the eigenmodes couple, the eigenfrequencies separate, essentially repelling each other. It has also been found that the sensitivity of the structure to gravity and suspension perturbations generally drops with the square of the resonant frequency (except for the coupling of closely spaced modes).

Non-dimensional gravity and suspension effect sensitivity parameters have been derived for the cases of a clamped-clamped, pinned-pinned, and free-free beam element subject to bending, axial and torsional initial stress effects, and for the case of a free-free beam element subject to static suspension effects.

The fundamental nature of the initial stress stiffening effect has been shown to be an additive perturbation to the system stiffness matrix, while the fundamental nature of the initial deformation effect has been shown to be a linear transformation of both the mass and stiffness matrices. The fundamental nature of the static suspension effects has been shown to a stiffness boundary condition change.

The technique of projecting the perturbed eigensystem onto the original eigenspace has been shown to be an excellent technique for rapidly, and compactly, identifying

the perturbation effects on the original eigenfrequencies and eigenmodes.

This completes the summary of the major thesis conclusions. A number of more specific conclusions can also be made.

6.2 Minor Conclusions

A beam element geometric stiffness matrix which allows for distributed loads in addition to concentrated nodal loads has been derived for the Bernoulli-Euler beam but it has been found that the use of the regular geometric stiffness matrix was sufficient if one uses consistent nodal loads as opposed to lumped nodal loads.

The role of infinitesimal element or finite element rotations has been identified as a common factor in the origin of the effects of gravity for both types of direct gravity effects on a structure, and for the direct gravity effects on sensors and actuators. For the initial stress effects, the perturbation to the stiffness matrix has been shown to be a result of infinitesimal element rotations (typically described as non-linear strains) which were not negligible with respect to the linear strains in the presence of external loads. The effects of initial deformations of the suspended structure due to gravity have been shown to be due to rotational transformations of the individual finite elements, whose reassembly results in a new reference structure. The key to describing the effects of gravity on structural sensors and actuators has been shown to be a partitioning of the structural modeshapes into translational components and rotational components. The non-dimensional, gravity effect sensitivity parameter for both the accelerometer and the proof-mass actuator, has been found to be the ratio of the rotational modal component over the translational modal component, weighted by the ratio of the gravitational acceleration over the product of the element length and the resonant frequency squared.

The gravity perturbation to the dynamics of the accelerometer and a proof-mass actuator has been shown to be a positive, or negative, additive perturbation to the

controlled flexible structure output or control matrix respectively. The sensor gravity effect correction has been shown to improve transfer function predictions for a horizontally mounted accelerometer on the MACE test article due to the important rotational contribution of the suspension system at low frequencies.

6.3 Recommendations for Future Research

Given the breadth of material which falls under the topic of gravity and suspension system effects on controlled flexible structures, it was not possible to bring to closure all pertinent items which were of interest and which would have enhanced the thesis. There are four items which were the particular subject of a considerable amount of work, but successful or succinct results were not obtained in time for their incorporation into this thesis.

The following items are recommended therefore for further investigation:

- *Derivation of non-dimensional parameters for initial deformation effects.* To accomplish this using the eigenprojection technique used for the initial stress stiffening and static suspension effects would require the identification of symbolic eigenvectors for at least a two-element beam. The perturbation introduced to the two-element assemblage should be to kink the beam by rotating one element with respect to the other. Two configurations should be studied here: a clamped-free beam subject to droop and a pinned-pinned beam subject to sag. It should be pointed out that there is no guarantee that a solution can be found to the twelfth-order symbolic characteristic polynomial while solving for the eigenpairs.

- *Derivation of non-dimensional parameters which are a function of the number of suspension cables or springs for static suspension stiffening effects.* In Chapter 3 non-dimensional parameters were derived for predicting the importance of stiffening due to the fundamental suspension modes. This analytical

(symbolic) derivation used a suspension cable at each end of a single beam element. In Chapter 5 it was found that the vertical plane stiffening effects were underestimated given the presence of three suspension cables. To derive non-dimensional parameters for suspended beam configurations with additional suspension springs it would be necessary to use additional beam elements which may become a computational obstacle in the case of a general symbolic derivation.

- *General analytical study of dynamic suspension effects.* While the different types of dynamic suspension effects were discussed in this thesis, along with a description of how they should be incorporated into the structural dynamics model, time did not permit the study of the particular nature of dynamic suspension effects on suspended beam-like structures. The latter is recommended even though doing so in a general symbolic manner for various beam configurations would require considerable effort. The approach recommended here is to assemble a finite-element model with two pinned-free vertical beam elements (with a cable-like cross-section) attached to the tips of a horizontal free-free beam, and then to solve for the general symbolic eigenpairs of the system after having applied the geometric stiffening effects to capture the dynamic suspension behavior. The use of symbolic mathematics software is recommended. Given the order of the system it is not guaranteed that the software will succeed in its attempt to solve for the general eigenpairs. If an analytic solution cannot be achieved it is recommended to reduce the number of symbolic system parameters by numerical substitution until a solution is reached. Every numerical substitution unfortunately reduces the generality of the solution.

- *Examination of additional beam configuration sample problems.* In Chapter 2 the initial deformation and geometric stiffening effect modeling approach was verified by a multi-element, numerical study, (using an original MATLAB-based finite element program) of a clamped-free horizontal and vertical beam under

gravitational loads, and comparing the eigenperturbation results to numerical solutions which had previously been published. Additional numerical analysis of other "sample problems" (i.e. simple configurations which capture the fundamental physics of the various possible effects) would complement well the general analytical work of this thesis, which focused on a single beam element, and the ADINA analysis, which focused on variations of the MACE test article. The study of gravity effects on a higher order pinned-pinned and free-free beam is recommended.

- *Development of a high-order MACE Development Model model with flexible appendages.* The nature of the experimental results of Chapter 5 was predicted based on the clamped-free beam verification analysis of Chapter 2. A significant effort to model the flexible appendages under 0g and 1g was made using both the author's own finite element program and the ADINA finite element modeling package. The attempts were unsuccessful due to the difficulty of identifying the correct homogeneous-beam approximations for the multi-ply composite beam. While the two dynamic bending behaviors could be properly captured the dynamic torsional behavior of the appendage could not. Additional work along this path is recommended to evaluate ADINA's performance in capturing the effects of initial deformation. Required is some research into the homogeneous beam equivalent modeling of a multi-ply laminate.

- *Establish how to include the effects of modal couplings in the relationship between the perturbed eigenfrequencies ${}^{t}\lambda_i$, the original eigenfrequencies ${}^{o}\lambda_i$, and the sensitivity matrix elements Ψ_{ij}.* The relationship between the perturbed eigenfrequencies and the eigenprojection sensitivity matrix terms was identified but it is not clear if the expression captures the effect of modal couplings or is limited to pure frequency perturbations.

The following research items are less pertinent to the general thrust of the thesis

but are recommended as potential areas for broadening the scope of this work:

- *Further generalize the beam element, and the beam element loads, used in the gravity and suspension effects study.* Repeat the analysis while allowing for a non-homogeneous beam, with shear degrees of freedom (i.e. Timoshenko beam), subject to axial loads which are not directed through the centroid, and shear forces and moments which are not do not pass through the shear center. A higher order torsional interpolation could also be used to refine the study of torsion effects by adding a twist slope degree of freedom at the beam tips.

- *Repeat the analysis while focusing on an element type other than a beam element.* A plate element would be the next logical step followed by a further generalization to the shell element. This topic is of potential engineering value particularly with respect to the study of gravity and suspension effects on large surface area structures such as large flexible antennas, synthetic aperture radar or large solar arrays.

- *Study the effect of higher-order pneumatic-electric suspension device dynamics.* In the present study, the MACE pneumatic-electric suspension devices were modeled as soft vertical springs whose stiffness is always proportional to the off-loaded test article mass because of the test article leveling procedure used in the iterative modeling. This modeling approach mimics the real procedure of leveling the structure by tuning the pressures in the air plenums. In reality, an electric stiffness exists in parallel to the pneumatic stiffness and operates using displacement feedback of the suspension carriage. Ideally, the electric stiffness does not interfere with the proportional stiffness tuning as it simply represents an offset which is smaller than the required stiffness, however, the dynamics of the electric stiffness control circuit are potentially non-negligible.

- *Investigate the effect of neglecting to update the mass matrix in the presence of initial deformations.* Presently, the ADINA finite element modeling software

does not update the mass matrix when initial deformations of the structure occur in the non-linear gravity effect analysis. To desensitize the mass matrix to initial deformation effects the mass matrix is of the lumped mass type. This deficiency in ADINA is not of capital importance to the MACE test program due to the negligible initial deformations of the test article when it is not fitted with flexible appendages. Nonetheless, it would be valuable to quantify when this effect becomes significant.

- *Investigate the modeling of suspension system damping effects.* Since the damping inherent in a structure is typically incorporated into a model based on test measurements rather than by an a priori calculation it would be extremely valuable to derive modeling techniques which can accurately predict the damping imparted to the structure's flexible modes by the suspension system. Alternatively, experimental techniques could be designed to attempt to identify the damping contributed by the suspension system. This problem is definitely of a doctoral dissertation calibre.

Appendix A

Gravity Effect Modeling with ADINA

This appendix briefly describes the procedure for modeling the the direct effects of gravity and of a laboratory suspension system on the dynamics of a structure using the ADINA non-linear finite element modeling software [31]. An outline of the procedure is given, general advice and comments are provided to assist those individuals who are developing models of suspended structures in a gravity field, and sample ADINA input runstreams are provided.

A.1 General Procedure

To capture gravity and suspension effects in an ADINA model of a suspended structure a minimum of two input files are required. The first to perform a large displacement non-linear analysis which computes the initial deformations of the structure subject to geometric stiffening effects, and the second to compute the eigensolution for the structure about the deformed reference in global coordinates. A third initial input file can be used to solve for the reaction forces of the overdetermined system (as described in Section 5.2.5) for the purposes of tuning the suspension system stiffnesses or cable lengths.

The non-linear analyses use a dummy time variable to increment the loading and compute a stable deformed equilibrium at each step. Geometric stiffness refinements are performed at every step (if desired). Bias torques must be added at any free rotary mechanisms to offset the gravity induced torque. The bias torque can easily be weighted by the same time function used to weight the mass proportional loading. Damping must be added to the suspension springs and to any mechanisms to stabilize the large displacement analysis. The concentrated dampers are ignored by the eigensolution step.

The general steps are thus as follows:

1. Develop regular model of unsuspended structure: (0g input file).

2. Add finite element description of suspension system using beam elements for the cables, and truss elements or discrete spring elements for the springs.

3. Constrain springs and perform non-linear large displacement analysis to compute reaction forces at the spring attachment points: (1g_dd0 input file).

4. Determine suspension spring stiffness from the previous step which will yield an approximately level structure.

5. Update suspension spring stiffnesses and unconstrain springs before performing a second large displacement analysis with geometric stiffness refinements to compute the system property matrices of the deformed structure[1]: (1g_dd1 input file).

6. Compute the eigensolution by performing a non-linear large displacement analysis (1g_dd2 input file) for the deformed stiffened structure computed in the previous step. This is achieved by running this input file immediately after the previous one (1g_dd1 input file) and by having set this input file to have a

[1]ADINA does not update mass matrix so the use of a lumped mass matrix is recommended to desensitize the mass matrix to initial deformations.

start time equal to the final time of the 1g_dd1 input file. This is commonly referred to as a restart analysis and requires that appropriate flags be set in to two sequential input files to allow for the restart.

A.2 Recommendations

As when performing any non-linear analysis start with as simple a relevant model as possible before attempting to obtain the "final" answer. By gradually adding complexity to the model when convergence becomes difficult the culprit elements of the model are not hidden.

If convergence difficulties arise one can try to ramp up the load weighting function more slowly and if difficulties still persist the convergence tolerances can be iteratively reduced. The final solution should be closely examined in this case and compared with previous solutions to verify its legitimacy. Another trick is to increase the damping on the mechanisms or the soft suspension springs. Furthermore, by relating the problem equation numbers ADINA to appropriate degrees of freedom one can usually identify where the model is poorly conditioned.

Note that while the computation of reaction forces (in 1g_dd0) could be a linear analysis it is recommended to use the non-linear iterative solution approach in ADINA (with geometric stiffness refinements) to obtain results which are more compatible with the subsequent non-linear analysis.

Initially model suspension cables as a single beam element, which captures the fundamental stiffening effects of the suspension system, before increasing the number of elements to capture the suspension cable "violin" modes.

A.3 Sample ADINA-IN Runstreams

There are two types of input files in ADINA, a formatted *data deck* and an unformatted *ADINA-IN* input file which must be pre-processed. Use of the latter is

recommended as it optimizes the node numbering. Examples of both techniques are presented here. In the first subsection we have the four ADINA runstreams described above to develop 0–g and 1–g models of the baseline simplified MACE model described at length in Section 5.2. The second subsection contains a higher order ADINA-IN model (the dd1 input file) as an example of a non-linear ADINA-IN input file for a more complex structure. An ADINA mesh plot is provided to show the discretization the MACE DM model.

A.3.1 Sample ADINA Data Deck Sequence for Simplified MACE Model

```
 ZERO g:  Baseline 3d Bernoulli-Euler model of MACE test article
C  ---------------------------------------
C    Author: D. A. Rey
C    Date:   Oct. 7, 1991
C    File:   mace0g.inp
C
C               3d, NON-LINEAR DYNAMIC ADINA ANALYSIS
C
C    This is the only data deck required for the 0g model.
C
C    Note that the 2nd double gimbal joint is FREE at 45 for this dynamic analysis.
C
C  ---------------------------------------
C    678-1-2345678-2-2345678-3-2345678-4-2345678-5-2345678-6-2345678-7-2345678-8
C
C    1 - STRUCTURAL CONTROL CARD
C    col. 5: total number of nodes
C    col. 15,20: 0, number of non-linear element groups
C    col. 25: 1 for initial exec. mode
C    col. 30: NSTEPS - number of steps for incremental analysis
C    col. 40: delta t
C    col. 50: TSTART
C    678-1-2345678-2-2345678-3-2345678-4-2345678-5-2345678-6-2345678-7-2345678-8
C  %          %   %   %       %       %
  130000000  1   0   1   1       1.      0.   0   0   0   0   0   0
C
C
C    2 - STRUCTURAL CONTROL CARD
C
C    col. 20: 2 input and solution data saved to porthole
C    col. 59,60: 2,1 for stiffness matrices in output stream
C    678-1-2345678-2-2345678-3-2345678-4-2345678-5-2345678-6-2345678-7-2345678-8
C                %       %                       %%
  0   0   0   0   0   0   0   0   0
C
C
C    3 - LOAD CONTROL CARD      *** NO LOADS ***   LEAVE BLANK
C
C    col. 40: 1 for lumped mass proportional loading
C    col. 74: 1 for reaction force calculations
C    678-1-2345678-2-2345678-3-2345678-4-2345678-5-2345678-6-2345678-7-2345678-8
C                            IDGRAV          NCES            IREFOR
C                                %               %               %
  0   0   0   0   0   0   0   0   0   0   0   8   1   0   0
C
C
C    4 - MASS AND DAMPING CONTROL CARD
C
C    col. 5:  0 for static analysis, 1 for lumped, 2 for consistent mass
C    col. 10: IDAMP 1 for lumped damping present
C    col. 15: 1 for lumped masses present
C    col. 20: IDAMPN 1 for concentrated dampers present
C  %   %   %   %
  1   0   1   0
C   1   1   1   1       0       0
C
C
C    5 - EIGENVALUE SOLUTION CARD
  1   1  32      32   0
C
C    6 - TIME INTEGRATION METHOD CONTROL CARD
  0   0                   0   0   0   0   0
C
C    7 - INCREMENTAL SOLUTION STRATEGY CONTROL CARD  ** FOR NONLINEAR **
```

```
C
C   8 - PRINT OUT DIRECTIVES CONTROL CARD
C   col. 40: 1 for mass and stiffness matrix print-out to .mx (linear only)
  0   0   0   0   0   0   0   1
C
C   9 - PORTHOLE CREATION CONTROL CARD
  1   0   0   0   0             0   0   0   0
C
CC
C   - TIME FUNCTION CONTROL CARDS (IV)

C
C   - NODAL DATA CARDS
  1   0   0   0   0   0   0 -0.679289 0.1707107      0.0
  2  -2  -2  -2   0  -2   0 -0.750000       0.1      0.0
  3   0   0   0   0   0   0 -0.750000       0.1      0.0
  4   0   0   0   0   0   0 -0.750000       0.0      0.0
  5   0   0   0   0   0   0 -0.375000       0.0      0.0
  6   0   0   0   0   0   0       0.0       0.0      0.0
  7   0   0   0   0   0   0       0.0      -0.1      0.0
  8   0   0   0   0   0   0  0.375000       0.0      0.0
  9   0   0   0   0   0   0  0.750000       0.0      0.0
 10   0   0   0   0   0   0  0.750000       0.1      0.0
 11  -2  -2  -2   0  -2   0  0.750000       0.1      0.0
 12   0   0   0   0   0   0  0.820711 0.1707107      0.0
C  reference node
 13   1   1   1   1   1   1       1.0       1.0      0.0
C
C   678-1-2345678-2-2345678-3-2345678-4-2345678-5-2345678-6-2345678-7-2345678-8
C
C        Constraint Equations   (page V.24)
  8   0
  1   2   1   1
  3   1
  2   2   2   1
  3   2
  3   2   3   1
  3   3
C  4   2   4   1
C  3   4
  4   2   5   1
  3   5
C  6   2   6   1
C  3   6
  5  11   1   1
 10   1
  6  11   2   1
 10   2
  7  11   3   1
 10   3
  8  11   5   1
 10   5
C
C        Concentrated Mass Data   (VI.1)
C
C   payload
  1   0      2.3       2.3       2.3    2.7e-2    2.7e-2    2.7e-2
C   two super-imposed gimbal motors
  2   0     1.35      1.35      1.35    1.5e-2    1.5e-2    1.5e-2
  3   0     1.35      1.35      1.35    1.5e-2    1.5e-2    1.5e-2
C   nodes
  4   0     1.50      1.50      1.50    7.2e-3    7.2e-3    7.2e-3
  5   0     1.50      1.50      1.50    7.2e-3    7.2e-3    7.2e-3
  6   0     1.50      1.50      1.50    7.2e-3    7.2e-3    7.2e-3
C   torque wheel assembly
  7   0     6.50      6.50      6.50     1e-2      1e-2      1e-2
C   nodes
  8   0     1.50      1.50      1.50    7.2e-3    7.2e-3    7.2e-3
  9   0     1.50      1.50      1.50    7.2e-3    7.2e-3    7.2e-3
C   two super-imposed gimbal motors
 10   0     1.35      1.35      1.35    1.5e-2    1.5e-2    1.5e-2
 11   0     1.35      1.35      1.35    1.5e-2    1.5e-2    1.5e-2
C   payload
 12   0      2.3       2.3       2.3    2.7e-2    2.7e-2    2.7e-2
C   final node flag
 13   0      0.0       0.0       0.0      0.0       0.0       0.0
C
C        Concentrated Nodal Dampers   (VI.2)
C   678-1-2345678-2-2345678-3-2345678-4-2345678-5-2345678-6-2345678-7-2345678-8
C  16   0      0.0       0.0       0.0      0.0       0.0       5.0
C  17   0      0.0       0.0       0.0      0.0       0.0       0.0
C
C   - INITIAL CONDITIONS CONTROL CARD
  0   0   0   0   0
C
C
C   ---------------------------
C   - BEAM ELEMENT GROUP CONTROL CARD (XIV)
C   col. 12: 2 for non-linear beam element
C   col. 20: 0 for 2D action, 1 for 3D action (in non-linear analysis)
C   col. 28: 1 for rect. section, 2 for pipe section (in non-linear analysis)
C   col. 52: -1 for element nodal force and moment print-out
C   col. 64: number of different property sets
C   678-1-2345678-2-2345678-3-2345678-4-2345678-5-2345678-6-2345678-7-2345678-8
C     %   %   %   %   %   %             %           %   %
 4  9   0   0   1   0                   0           2
C
C   - LINEAR BEAM MATERIAL PROPERTY CARD 1 (LEXAN)
C   note: lexan stiffness tuned to capture collar stiffening effect
C  #       E         v      rho
```

```
C  %        %        %        %        %
   1  3.3575e9      .37     1200.       1
C
C    - SECTION PROPERTY CARD
C      Ir       Is       It       A
C        %        %        %        %
   2.8e-8    1.4e-8    1.4e-8   2.25e-4        0        0
C
C
C    - LINEAR BEAM MATERIAL PROPERTY CARD 2 (RIGID)
C  %        %        %        %        %
   2 3.3575e11      .33      120.       1
C
C    - SECTION PROPERTY CARD
C        %        %        %        %
   2.8e-8    1.4e-8    1.4e-8   2.25e-4        0        0
C
C
C    - ELEMENT DATA CARDS
     1    1    2   13    2    0    0        0    0    0           0
     2    3    4   13    2    0    0        0    0    0           0
     3    4    5   13    1    0    0        0    0    0           0
     4    5    6   13    1    0    0        0    0    0           0
     5    6    7   13    2    0    0        0    0    0           0
     6    6    8   13    1    0    0        0    0    0           0
     7    8    9   13    1    0    0        0    0    0           0
     8    9   10   13    2    0    0        0    0    0           0
     9   11   12   13    2    0    0        0    0    0           0
C
C
C    - EIGENVALUE SOLUTION CARD
C    col. 10: 0 for NO rigid body modes present
C    col. 30: optional cut-off frequency (250 * 2pi = 1570.7963)
C    678-1-2345678-2-2345678-3-2345678-4-2345678-5-2345678-6-2345678-7-2345678-8
C        %        %        %
  100    1     -10.0 1570.7963
C
C    678-1-2345678-2-2345678-3-2345678-4-2345678-5-2345678-6-2345678-7-2345678-8
C
STOP


      ONE g:  3d B.E. MACE model with suspension system, pre-def. and Kg
C     ------------------------------------------------------------------
C     Author: D. A. Rey
C     Date:   Oct. 8, 1991
C     File:   mace`1g`dd0.inp
C
C                3d, NON-LINEAR DYNAMIC ADINA ANALYSIS
C
C     *** DATA DECK 0, based on data deck 1 to compute the exact reaction ***
C     *** forces using constrained suspension carriage points.            ***

     Identical to the `1g`dd1.inp file which follows except for
     the single CCC-dd0 comment line regarding the spring constraints.

...


      ONE g:  3d B.E. MACE model with suspension system, pre-def. and Kg
C     ------------------------------------------------------------------
C     Author: D. A. Rey
C     Date:   Oct. 9, 1991
C     File:   mace`1g`dd1.inp
C
C                3d, NON-LINEAR DYNAMIC ADINA ANALYSIS
C
C     Data deck -1- for static/large deflection analysis with appropriate
C     flags for restarting an eigenanalysis using final M,K,(Kg).
C     Resultant deflections are calculated.
C
C     Note that suspension stiffnesses are (mass proportional) tuned to
C     yield the desired 0.1 Hz bounce frequency and a level suspended structure.
C
C     Nodal damping used here to damp out bounce.
C     ------------------------------------------------------------------
C
C     678-1-2345678-2-2345678-3-2345678-4-2345678-5-2345678-6-2345678-7-2345678-8
C
C     1 - STRUCTURAL CONTROL CARD
C     col. 5: total number of nodes
C     col. 15,20: number of linear element groups, 0
C     col. 25: 1 for initial exec. mode
C     col. 30: NSTEPS - number of steps for incremental analysis
C     col. 40: delta t
C     col. 50: TSTART
C     678-1-2345678-2-2345678-3-2345678-4-2345678-5-2345678-6-2345678-7-2345678-8
C  %           %   %   %        %        %
  190000000  0   2   1   45       1.       0.   0   0   0   0   0   0   0
C
C
C     2 - STRUCTURAL CONTROL CARD
C
C     col. 20: 2 input and solution data saved to porthole
C     col. 59,60: 2,1 for stiffness matrices in output stream
C     678-1-2345678-2-2345678-3-2345678-4-2345678-5-2345678-6-2345678-7-2345678-8
C               %        %                          %%
    0   0   0   0   0   0   0   0   0
C
```

```
C
C    3 - LOAD CONTROL CARD
C
C    col. 5:  number of concentrated load cards
C    col. 40: 1 for lumped mass proportional loading
C    col. 74: 1 for reaction force calculations
C    678-1-2345678-2-2345678-3-2345678-4-2345678-5-2345678-6-2345678-7-2345678-8
C   NLOAD                    IDGRAV        NCES          IREFOR
C   %                        %             %             %
     4   0   0   0   0   0   0   1   0   0   8   1   0   0   1
C
C
C    4 - MASS AND DAMPING CONTROL CARD
C
C    col. 5:  0 for static analysis, 1 for lumped, 2 for consistent mass
C    col. 10: IDAMP 1 for lumped damping present
C    col. 15: 1 for lumped masses present
C    col. 20: IDAMPN 1 for concentrated dampers present
C   %    %    %    %
     1    1    1    1        0        0
C
C
C    5 - EIGENVALUE SOLUTION CARD
     0    0    0        0    0
C    1    1   30       30    0
C
C
C    6 - TIME INTEGRATION METHOD CONTROL CARD
     0    2      0.5      0.25        0    0    0    0    0
C
C
C    7 - INCREMENTAL SOLUTION STRATEGY CONTROL CARD  ** FOR NONLINEAR **
C
C    col. 5:  0  for manual time stepping
C    col. 10: 3 for full Newton interation with line search
C    col. 16: 1 for last iteration data print-out, 2 for all iterations
C    col. 17: 1 for EF convergence criterion
C    col. 20: max. number of iterations per step
C
C    678-1-2345678-2-2345678-3-2345678-4-2345678-5-2345678-6-2345678-7-2345678-8
C   %    %    %% %                                                %        %
     0   -3   1 121 15        0        0        0        0       50       50
C
C
C    8 - PRINT OUT DIRECTIVES CONTROL CARD
C    col. 40: 1 for printout of M,K; (only if analysis is LINEAR)
C    678-1-2345678-2-2345678-3-2345678-4-2345678-5-2345678-6-2345678-7-2345678-
     1    1    1    1    0    0        0
C    0    0    0    0    0    0    0    0    1
C
C
C    9 - PORTHOLE CREATION CONTROL CARD
C    1    0    0    0    0              0    0    0    0
C
C
C      - BLOCK DEFINITION CARDS  (III.2)
C    678-1-2345678-2-2345678-3-2345678-4-2345678-5-2345678-6-2345678-7-2345678-
C   ISREFB - stiffness reformation
     1   45    1
C   IEQITB - equilibrium time steps
     1   45    1
C   IPRIB  - print-out time steps
     1   45    1
C   IPNODE - nodal quantities print-out
     1   19    1
C   INODB  - porthole nodal responses saving intervals
C    1   30   15
C   IELMB  - porthole element responses saving intervals
C    1   30   15
C
C
C      - TIME FUNCTION CONTROL CARDS  (IV)
C
     1    4
     1    4    0
C    678-1-2345678-2-2345678-3-2345678-4-2345678-5-2345678-6-2345678-7-2345678-8
C   rigid suspension time function
C        0        0        3      0.95         4        1       15        1
C   soft suspension time function
         0        0       24      0.95        27        1       45        1
C
C
C    - NODAL DATA CARDS
C
     1    0    0    0    0    0    0 -0.679289 0.1707107       0.0
     2   -2   -2   -2    0   -2    0 -0.750000       0.1       0.0
     3    0    0    0    0    0    0 -0.750000       0.1       0.0
     4    0    0    0    0    0    0 -0.750000       0.0       0.0
     5    0    0    0    0    0    0 -0.375000       0.0       0.0
     6    0    0    0    0    0    0       0.0       0.0       0.0
C    torque wheel assembly
     7    0    0    0    0    0    0       0.0      -0.1       0.0
     8    0    0    0    0    0    0  0.375000       0.0       0.0
     9    0    0    0    0    0    0  0.750000       0.0       0.0
    10    0    0    0    0    0    0  0.750000       0.1       0.0
    11   -2   -2   -2    0   -2    0  0.750000       0.1       0.0
    12    0    0    0    0    0    0  0.820711 0.1707107       0.0
C    reference node
    13    1    1    1    1    1    1       1.0       1.0       0.0
C    suspension carriage attachment points
```

```
  14   1   0   1   1   1   1 -0.750000     -4.6      0.0
  15   1   0   1   1   1   1      0.0      -4.6      0.0
  16   1   0   1   1   1   1  0.750000     -4.6      0.0
C    ceiling pneumatic "spring" attach points
  17   1   1   1   1   1   1 -0.750000    -9.176     0.0
  18   1   1   1   1   1   1      0.0     -9.176     0.0
  19   1   1   1   1   1   1  0.750000    -9.176     0.0
C
CCC-dd0 ****** for the dd0 input file:
C     Input lines 14,15, and 16 above should constrain the suspension carriages
C     in the y (vertical) direction with a 1 in the second column.
C
C    678-1-2345678-2-2345678-3-2345678-4-2345678-5-2345678-6-2345678-7-2345678-8
C
C         Constraint Equations    (page V.24)
   8   0
C    gimbals - both double-axis free: Ox, Oz
   1   2   1   1
   3   1
   2   2   2   1
   3   2
   3   2   3   1
   3   3
   4   2   5   1
   3   5
   5  11   1   1
  10   1
   6  11   2   1
  10   2
   7  11   3   1
  10   3
   8  11   5   1
  10   5
C
C
C         Concentrated Mass Data    (VI.1)
C
C     payload
   1   0      2.3      2.3      2.3    2.7e-2    2.7e-2    2.7e-2
C     two super-imposed gimbal motors
   2   0     1.35     1.35     1.35    1.5e-2    1.5e-2    1.5e-2
   3   0     1.35     1.35     1.35    1.5e-2    1.5e-2    1.5e-2
C     nodes
   4   0     1.50     1.50     1.50    7.2e-3    7.2e-3    7.2e-3
   5   0     1.50     1.50     1.50    7.2e-3    7.2e-3    7.2e-3
   6   0     1.50     1.50     1.50    7.2e-3    7.2e-3    7.2e-3
C     torque wheel assembly
   7   0     7.00     7.00     7.00     1e-2      1e-2      1e-2
C     nodes
   8   0     1.50     1.50     1.50    7.2e-3    7.2e-3    7.2e-3
   9   0     1.50     1.50     1.50    7.2e-3    7.2e-3    7.2e-3
C     two super-imposed gimbal motors
  10   0     1.35     1.35     1.35    1.5e-2    1.5e-2    1.5e-2
  11   0     1.35     1.35     1.35    1.5e-2    1.5e-2    1.5e-2
C     payload
  12   0      2.3      2.3      2.3    2.7e-2    2.7e-2    2.7e-2
C     final node flag
  19   0      0.0    0.0      0.0      0.0       0.0       0.0
C
C         Concentrated Nodal Dampers  (VI.2)
C    678-1-2345678-2-2345678-3-2345678-4-2345678-5-2345678-6-2345678-7-2345678-8
   2   0      0.0      0.0      0.0      3.0       0.0       3.0
  11   0      0.0      0.0      0.0      3.0       0.0       3.0
  14   0      0.0      9.0      0.0      0.0       0.0       0.0
  15   0      0.0      9.0      0.0      0.0       0.0       0.0
  16   0      0.0      9.0      0.0      0.0       0.0       0.0
  19   0      0.0    0.0      0.0      0.0       0.0       0.0
C
C    - INITIAL CONDITIONS CONTROL CARD
  0   0   0   0   0
C
C    ---------------------.
C    - TRUSS ELEMENT GROUP CONTROL CARD (XI)
C    col. 4: 1 for truss
C    col. 8: number of elements in group
C    col. 12: 2 for large displ. small strain
C    col. 20: 0 for general 3d truss
C    col. 28: max # of nodes per element (def. 2)
C    678-1-2345678-2-2345678-3-2345678-4-2345678-5-2345678-6-2345678-7-2345678-8
C      %   %     %    %                                %
  1   6   2      0      2                                4
C
C    - TRUSS MATERIAL AND SECTION PROPERTY CARDS spring 1 (XI)
C          Area       rho
C   #        %         %
    1        1         0
C
C        E
C        %
   12.3784
C
C    - TRUSS MATERIAL AND SECTION PROPERTY CARD spring 2 (XI)
C          Area       rho
C   #        %         %
    2        1         0
   19.4663
C
C    - TRUSS MATERIAL AND SECTION PROPERTY CARD spring 3 (XI)
C          Area       rho
C   #        %         %
```

```
   3       1       0
  13.1361
C
C    - TRUSS MATERIAL AND SECTION PROPERTY CARD stiff rods (XI)
C          Area      rho
C   #        %        %
   4        1       0
     1e7
C
C    - TRUSS ELEMENT DATA CARDS
C    col. 10: number of nodes per element
C    col. 15: 1 print elemental stresses and forces
C    col. 20: material property set number
C    col. 35: initial axial strain
C    678-1-2345678-2-2345678-3-2345678-4-2345678-5-2345678-6-2345678-7-2345678-8
C    col.  5: global node number of point 1
C    col. 10: global node number of point 2, etc...
C
C    rigid rods: carriage to test article
C   #    %    %    %            %
    1    2    1    4
C   %    %
    4   14
C
C   #    %    %    %            %
    2    2    1    4
    6   15
C
C   #    %    %    %            %
    3    2    1    4
    9   16
C
C    tuned suspension pneumatic springs
C   #    %    %    %            %
    4    2    1    1
C   %    %
   14   17
C
C   #    %    %    %            %
    5    2    1    2
   15   18
C
C   #    %    %    %            %
    6    2    1    3
   16   19
C
C    ------------------.
C    - BEAM ELEMENT GROUP CONTROL CARD (XIV)
C    col. 12: 2 for non-linear beam element
C    col. 20: 0 for 2D action, 1 for 3D action (in non-linear analysis)
C    col. 28: 1 for rect. section, 2 for pipe section (in non-linear analysis)
C    col. 52: -1 for element nodal force and moment print-out
C    col. 64: number of different property sets
C    678-1-2345678-2-2345678-3-2345678-4-2345678-5-2345678-6-2345678-7-2345678-8
C      %   %   %   %   %   %              %          %   %
  4   9   2   0   1   0   2              0          2
C
C    - NON-LINEAR BEAM MATERIAL AND SECTION PROPERTY CARDS 1 (LEXAN)
C
C      Ishear     rho       eta
C   %    %         %         %
    1    0     1200.         1
C
C        E         v        DO        DI
C        %         %         %         %
  3.3575e9      0.37    0.0254     0.019
C
C    - NON-LINEAR BEAM MATERIAL AND SECTION PROPERTY CARDS 2 (RIGID)
C
C      Ishear     rho       eta
C   %    %         %         %
    2    0     120.          1
C
C        E         v        DO        DI
C        %         %         %         %
 3.3575e11      0.37    0.0254     0.019
C
C
C    - BEAM ELEMENT DATA CARDS
    1    1    2   13    2    0    0        0    0    0           0
    2    3    4   13    2    0    0        0    0    0           0
    3    4    5   13    1    0    0        0    0    0           0
    4    5    6   13    1    0    0        0    0    0           0
    5    6    7   13    2    0    0        0    0    0           0
    6    6    8   13    1    0    0        0    0    0           0
    7    8    9   13    1    0    0        0    0    0           0
    8    9   10   13    2    0    0        0    0    0           0
    9   11   12   13    2    0    0        0    0    0           0
C
C
C
C    - APPLIED LOADS DATA CARDS  (XXXII)
C
C    - CONCENTRATED LOAD DATA
C    col. 5: concentrated load node number
C    col. 10: direction number (6 = Z rotation)
C    col. 15: time function number
C    col. 25: magnitude (-mglcosO = -(2.3)(9.8)(0.1)(0.707) = -1.5936)
C    678-1-2345678-2-2345678-3-2345678-4-2345678-5-2345678-6-2345678-7-2345678-8
C   %    %    %         %
```

```
   2   6   1  -1.5936
   3   6   1   1.5936
  10   6   1   1.5936
  11   6   1  -1.5936
C
C   - MASS PROPORTIONAL LOAD DATA
C   col. 45: gravitational constant (or multiple thereof)
C   678-1-2345678-2-2345678-3-2345678-4-2345678-5-2345678-6-2345678-7-2345678-8
C  %       x       y       z       %
  1       0       1       0     9.8
C
C
C   - EIGENVALUE SOLUTION CARD
C  100   1    -10.0       0
C
C   678-1-2345678-2-2345678-3-2345678-4-2345678-5-2345678-6-2345678-7-2345678-8
C
STOP


    ONE g: 3d B.E. MACE Model with Suspension System, Pre-def. and Kg
C   ------------------------------------------------------------------
C   Author: D. A. Rey
C   Date:   Oct. 9, 1991
C   File:   mace'1g'dd2.inp
C
C              3d, NON-LINEAR DYNAMIC ADINA ANALYSIS
C
C   Data deck -2-, for eigenanalysis using final M, K+Kg from mace'1g'dd1.inp
C   fortran output files; (deformed and stressed reference structure).
C
C   Note that suspension stiffnesses are (mass proportional) tuned to
C   yield the CORRECT 0.1 Hz bounce frequency and a level suspended structure.
C
C   Note that both double gimbal joints are FREE at 45 for this dynamic analysis.
C
C   Nodal damping was initially used to damp out bounce and payload swing.
C
C   No loading required for this eigensolution.
C   ------------------------------------------------------------------
C

   Identical to the preceding '1g'dd1.inp input file except for the
   following two differences concerning the start time and the eigensolution.

C   1 - STRUCTURAL CONTROL CARD
C   col. 5: total number of nodes
C   col. 15,20: 0, number of non-linear element groups
C   col. 25: 2 for restart mode
C   col. 30: NSTEPS - number of steps for incremental analysis
C   col. 40: delta t
C   col. 50: TSTART
C   678-1-2345678-2-2345678-3-2345678-4-2345678-5-2345678-6-2345678-7-2345678-8
C  %          %   %   %       %       %
 190000000  0   2   2   0      0.     45.   0   0   0   0   0   0   0
C
C

...

C
C   - EIGENVALUE SOLUTION CARD (XXXIII)
C   col. 10: 0 for NO rigid body modes present
C   col. 30: optional cut-off frequency
C   678-1-2345678-2-2345678-3-2345678-4-2345678-5-2345678-6-2345678-7-2345678-8
C      %
 100   1    -10.0    1500.
C
C   678-1-2345678-2-2345678-3-2345678-4-2345678-5-2345678-6-2345678-7-2345678-8
C
STOP
```

A.3.2 Sample ADINA-IN Input File for MACE DM Model

This subsection lists the dd1 ADINA-IN input file for the MACE Development Model. An ADINA mesh of the MACE DM test article follows the ADINA-IN listing along with a sample overlay of 0–g model, 1–g model and experimental data transfer functions. It was found in general that the impact of gravity and suspension effects on the MACE DM was very similar to those obtained for the Baseline Simplified MACE

Model. Incorporation of gravity and suspension effects has proven itself to be crucial to the low frequency modeling of the MACE DM test article.

```
*  ONE g:  3d B.E. MACE Dev Model with suspension system, pre-def. and Kg
*  ---------------------------------------------------------------------
*  Authors:  R.M. Glaese and D. A. Rey
*  Date:     Jan 14, 1992
*  File:     macedm1g_dd1.in
*
*            3d, NON-LINEAR DYNAMIC ADINA-IN ANALYSIS
*
*  ADINA-IN input file -1- for static/large deflection analysis with
*  appropriate flags for restarting an eigenanalysis using final M,K,(Kg).
*  Resultant deflections are calculated.
*
*  This is the model of the MACE Development Model currently being used in
*  preliminary ID experiments
*
*  This model includes the torque wheel assembly, one double-axis
*  gimbal, and all sensors.
*  ---------------------------------------------------------------------
*
FILEUNITS LIST=8
* LOG=7 ECHO=7
*
* DATABASE SCRATCH
*
FEPROGRAM ADINA
*
CONTROL NONINTERACTIVE ECHOPRINT=YES ERRORLIMIT=5 ERRORACTION=STOP
*
HEADING 'ONE g:  3d B.E. MACE Dev Model with suspension system, pre-def. and Kg'
*
MASTER REACTIONS=YES MODEX=EXECUTE NSTEP=35 DT=1. TSTART=0.
*
ANALYSIS TYPE=DYNAMIC MASSMATRIX=LUMPED ETA=1
*
KINEMATICS DISPLACEMENTS=LARGE
*
*FREQUENCIES SUBSPACE-ITERATION NEIG=40 NMODE=40 IRBM=1 RBMSH=0.0 INTERVAL=0
*
TOLERANCES TYPE=EF RNORM=50 RMNORM=50 PRINT=2 ITEMAX=30
*
STIFFNESS-STEPS 0 35 1
*
PRINTOUT IPDATA=0 IOUTPT=1 IDC=1 IVC=0 IAC=0
*
PRINTSTEPS
*
PORTHOLE VOLUME=MINIMUM NPUTSV=0 JDC=0 JVC=0 JAC=0 JTC=0 SAVEDEFAULT=NO
*
TIMEFUNCTION 1 IFLIB=1
      0       0
      6     0.1
      7   0.1498
      8   0.2353
      9   0.3689
     10     0.5
     11   0.6321
     12   0.8647
     13   0.9502
     14   0.9817
     15   0.9933
     16   0.9975
     17   0.9991
     18   0.9997
     19   0.9999
     20   1.0000
     35   1.0000
*
SYSTEM 0
COORDINATES
  ENTRIES NODE X Y Z
   1   0.0          0.0      0.0
   2   0.03175      0.0      0.0
   3   0.06350      0.0      0.0
   4   0.10807      0.0      0.0
   5   0.21933      0.0      0.0
   6   0.22568      0.0      0.0
   7   0.33693      0.0      0.0
   8   0.38150      0.0      0.0
   9   0.41325      0.0      0.0
  10   0.44500      0.0      0.0
  11   0.48957      0.0      0.0
  12   0.60083      0.0      0.0
  13   0.60718      0.0      0.0
  14   0.71843      0.0      0.0
  15   0.76300      0.0      0.0
  16   0.79475      0.0      0.0
  17   0.82650      0.0      0.0
  18   0.87107      0.0      0.0
  19   0.98233      0.0      0.0
  20   0.98868      0.0      0.0
  21   1.09993      0.0      0.0
  22   1.14450      0.0      0.0
  23   1.17625      0.0      0.0
  24   1.20800      0.0      0.0
```

```
  25    1.25257      0.0       0.0
  26    1.36383      0.0       0.0
  27    1.37018      0.0       0.0
  28    1.48143      0.0       0.0
  29    1.52600      0.0       0.0
  30    1.55775      0.0       0.0
  31    1.58950      0.0       0.0
*    Attachment Points
  32    0.03175   0.08100      0.0
  33    0.79475   0.08100      0.0
  34    1.55775   0.08100      0.0
*    Torque Wheel Assembly nodes
  35    0.79475   0.07433      0.0
  36    0.79475   0.10974   -0.09052
  37    0.87314   0.10974    0.04526
  38    0.71636   0.10974    0.04526
  39    0.79475   0.15038   -0.14800
  40    0.92292   0.15038    0.07400
  41    0.66658   0.15038    0.07400
  42    0.79475   0.15038   -0.14800
  43    0.92292   0.15038    0.07400
  44    0.66658   0.15038    0.07400
  45    0.79475   0.09958   -0.14800
  46    0.92292   0.09958    0.07400
  47    0.66658   0.09958    0.07400
*    Gimbal nodes
  48    1.47775  -0.12315      0.0
  49    1.55775  -0.11330      0.0
  50    1.55775  -0.11430      0.0
  51    1.55775  -0.11430      0.0
  52    1.54329  -0.11420   -0.00315
  53    1.55775  -0.11330      0.0
  54    1.55775  -0.11430      0.0
  55    1.55775  -0.11430      0.0
  56    1.55775  -0.14158    0.00151
*    Payload Can
  57    1.55775  -0.28575      0.0
*    Dummy Gimbal
  58    0.03175  -0.06350      0.0
*    Rate Gyro beneath Torque Wheel Assembly
  59    0.79475  -0.06985      0.0
*    Accelerometer Triax at Node 4
  60    0.40918   0.06553   -0.00407
*    Accelerometer Triax at Node 2
  61    1.17218   0.06553   -0.00407
*    reference node
  62    1.0       1.0       0.0
*    suspension carriage attachment points
  63    0.03175     4.6       0.0
  64    0.79475     4.6       0.0
  65    1.55775     4.6       0.0
*    ceiling pneumatic "spring" attach points
  66    0.03175     9.176     0.0
  67    0.79475     9.176     0.0
  68    1.55775     9.176     0.0
*
MASSES    NODES
*          Concentrated Mass Data
*    Elements with Nodal Mass Descriptions
   3    0.11137   0.11137   0.11137   3.36e-5   3.22e-5   3.22e-5
   4    0.05549   0.05549   0.05549   8.61e-6   4.32e-6   4.32e-6
   7    0.05549   0.05549   0.05549   8.61e-6   4.32e-6   4.32e-6
   8    0.11137   0.11137   0.11137   3.36e-5   3.22e-5   3.22e-5
  10    0.11137   0.11137   0.11137   3.36e-5   3.22e-5   3.22e-5
  11    0.05549   0.05549   0.05549   8.61e-6   4.32e-6   4.32e-6
  14    0.05549   0.05549   0.05549   8.61e-6   4.32e-6   4.32e-6
  15    0.11137   0.11137   0.11137   3.36e-5   3.22e-5   3.22e-5
  17    0.11137   0.11137   0.11137   3.36e-5   3.22e-5   3.22e-5
  18    0.05549   0.05549   0.05549   8.61e-6   4.32e-6   4.32e-6
  21    0.05549   0.05549   0.05549   8.61e-6   4.32e-6   4.32e-6
  22    0.11137   0.11137   0.11137   3.36e-5   3.22e-5   3.22e-5
  24    0.11137   0.11137   0.11137   3.36e-5   3.22e-5   3.22e-5
  25    0.05549   0.05549   0.05549   8.61e-6   4.32e-6   4.32e-6
  28    0.05549   0.05549   0.05549   8.61e-6   4.32e-6   4.32e-6
  29    0.11137   0.11137   0.11137   3.36e-5   3.22e-5   3.22e-5
*    Nodal Mass Representation of Nodes
   2    0.27050   0.27050   0.27050   3.04e-4   3.04e-4   3.04e-4
   9    0.27050   0.27050   0.27050   3.04e-4   3.04e-4   3.04e-4
  16    0.27050   0.27050   0.27050   3.04e-4   3.04e-4   3.04e-4
  23    0.27050   0.27050   0.27050   3.04e-4   3.04e-4   3.04e-4
  30    0.27050   0.27050   0.27050   3.04e-4   3.04e-4   3.04e-4
*    Lumped Mass and Inertia of TWA Base
  35    1.70030   1.70030   1.70030   2.61e-3   4.47e-3   2.68e-3
*    Lumped Mass and Inertia of TWA Motors
  36    0.77080   0.77080   0.77080   6.67e-4   3.38e-4   6.67e-4
  37    0.77080   0.77080   0.77080   6.67e-4   6.67e-4   3.38e-4
  38    0.77080   0.77080   0.77080   6.67e-4   6.67e-4   3.38e-4
*    Lumped Mass and Inertia of TWA Inertia Wheels
  42    1.09726   1.09726   1.09726   2.69e-3   5.28e-3   2.69e-3
  43    1.09726   1.09726   1.09726   2.69e-3   2.69e-3   5.28e-3
  44    1.09726   1.09726   1.09726   2.69e-3   2.69e-3   5.28e-3
*    Full Mass and Inertia Matrix for One Gimbal Stage(Base,Inner,Outer)
*    Note:  These inertias are the principal inertias and are referenced
*           to skew axes.
  48    2.99182   2.99182   2.99182 9.4269e-3 2.5266e-2 2.7566e-2
  52    2.92271   2.92271   2.92271 1.1876e-2 5.1450e-3 1.3503e-2
  56    1.06162   1.06162   1.06162 3.4409e-3 1.2802e-3 2.9162e-3
*    Payload Can and Rate Gyro
  57    1.29798   1.29798   1.29798   1.96e-3   2.07e-3   1.96e-3
*    Dummy MACE Gimbal Element Construction
```

```
  58   7.09984   7.09984   7.09984   5.32e-3   2.97e-2   2.90e-2
*   Rate Gyro beneath Torque Wheel Assembly
  59   1.07100   1.07100   1.07100   1.11e-3   7.88e-4   6.96e-4
*   Accel Triax on Node 4
  60   0.72968   0.72968   0.72968   2.67e-4   7.78e-5   2.67e-4
*   Accel Triax on Node 2
  61   0.66060   0.66060   0.66060   2.74e-4   8.00e-5   2.74e-4
*
DAMPERS  NODES
*         Concentrated Nodal Dampers  (VI.2)
*   Gimbals
  51   0.0       0.0       0.0       3.0       0.0       0.0
  55   0.0       0.0       0.0       0.0       0.0       3.0
*   Suspension carriages
  63   0.0      13.0       0.0       0.0       0.0       0.0
  64   0.0      13.0       0.0       0.0       0.0       0.0
  65   0.0      13.0       0.0       0.0       0.0       0.0
*
   2   0.0       0.0       0.0       4.0       0.0       0.0
  16   0.0       0.0       0.0       4.0       0.0       0.0
  30   0.0       0.0       0.0       4.0       0.0       0.0
*
SKEWSYSTEMS  EULERANGLES
*
   1   -54.739833       0.0       0.0
   2    26.242265 81.084306 -44.291621
   3    92.823587 49.841972 -157.70733
   4         90.0 20.998152     -90.0
   5   -89.314583 90.209326 -90.567411
   6   -0.1316743       0.0       0.0
*
NSKEWS  NODES
*
   39  1
   40  2
   41  3
   42  1
   43  2
   44  3
   48  4
   52  5
   56  6
*
MATERIAL 1 ELASTIC E=2.3E9   NU=0.37 DENSITY=1189.77
*     (LEXAN)
*
MATERIAL 2 ELASTIC E=69.0E9  NU=0.33 DENSITY=0.0
*     (ALUMINUM)
*
MATERIAL 3 ELASTIC E=69.0E10 NU=0.33 DENSITY=0.0
*     (RIGID)
*
MATERIAL 4 ELASTIC E=57.2130 NU=0.0  DENSITY=0.0
*     (SPRING 1)
*
MATERIAL 5 ELASTIC E=83.0270 NU=0.0  DENSITY=0.0
*     (SPRING 2)
*
MATERIAL 6 ELASTIC E=63.3390 NU=0.0  DENSITY=0.0
*     (SPRING 3)
*
MATERIAL 7 ELASTIC E=1E7     NU=0.0  DENSITY=0.0
*     (STIFF RODS)
*
EGROUP 1 TRUSS SUBTYPE=GENERAL DISPLACEMENTS=LARGE MATERIAL=4
  ENODES
  ENTRIES EL N1 N2
  1 63 66
  EDATA
  ENTRIES EL AREA PRINT
  1 1 NO
*
EGROUP 2 TRUSS SUBTYPE=GENERAL DISPLACEMENTS=LARGE MATERIAL=5
  ENODES
  ENTRIES EL N1 N2
  1 64 67
  EDATA
  ENTRIES EL AREA PRINT
  1 1 NO
*
EGROUP 3 TRUSS SUBTYPE=GENERAL DISPLACEMENTS=LARGE MATERIAL=6
  ENODES
  ENTRIES EL N1 N2
  1 65 68
  EDATA
  ENTRIES EL AREA PRINT
  1 1 NO
*
EGROUP 4 TRUSS SUBTYPE=GENERAL DISPLACEMENTS=LARGE MATERIAL=7
  ENODES
  ENTRIES EL N1 N2
  1 32 63
  2 33 64
  3 34 65
  EDATA
  ENTRIES EL AREA PRINT
  1 1 NO
  2 1 NO
  3 1 NO
*
```

```
EGROUP 5 BEAM SUBTYPE=DIM3 MATERIAL=1
  SECTION 1 SHAPE=PIPE H1=0.0254 H2=0.01905 SC=0 TC=0
  ENODES
*   Element Construction of the Struts
   1  62   4   5
   2  62   5   6
   3  62   6   7
   4  62  11  12
   5  62  12  13
   6  62  13  14
   7  62  18  19
   8  62  19  20
   9  62  20  21
  10  62  25  26
  11  62  26  27
  12  62  27  28
  EDATA
  ENTRIES EL SECTION PRINT
  1 1 NO
  2 1 NO
  3 1 NO
  4 1 NO
  5 1 NO
  6 1 NO
  7 1 NO
  8 1 NO
  9 1 NO
 10 1 NO
 11 1 NO
 12 1 NO
*
EGROUP 6 BEAM SUBTYPE=DIM3 MATERIAL=2
  SECTION 1 SHAPE=PIPE H1=0.04447 H2=0.01864 SC=0 TC=0
  ENODES
*   Elemental Construction of the Collar Assemblies
   1  62   3   4
   2  62   7   8
   3  62  10  11
   4  62  14  15
   5  62  17  18
   6  62  21  22
   7  62  24  25
   8  62  28  29
   EDATA
   ENTRIES EL SECTION PRINT
   1 1 NO
   2 1 NO
   3 1 NO
   4 1 NO
   5 1 NO
   6 1 NO
   7 1 NO
   8 1 NO
*
EGROUP 7 BEAM SUBTYPE=DIM3 MATERIAL=3
   SECTION 1 SHAPE=PIPE H1=0.0254 H2=0.01905 SC=0 TC=0
   ENODES
*   Elemental Representation of Nodes (Rigid)
   1  62   1   2
   2  62   2   3
   3  62   8   9
   4  62   9  10
   5  62  15  16
   6  62  16  17
   7  62  22  23
   8  62  23  24
   9  62  29  30
  10  62  30  31
*   Elemental Representation of Attachment Plates (Rigid)
  11  62   2  32
  12  62  16  33
  13  62  30  34
*   Elemental Representation of TWA components (Rigid)
  14  62  16  35
  15  62  35  36
  16  62  35  37
  17  62  35  38
  18  62  36  39
  19  62  37  40
  20  62  38  41
  21  62  42  45
  22  62  43  46
  23  62  44  47
*   Elemental Representation of one Gimbal Stage (Rigid)
  24  62  30  48
  25  62  48  49
  26  62  49  50
  27  62  51  52
  28  62  52  53
  29  62  53  54
  30  62  55  56
*   Payload Can and Rate Gyro (Rigid)
  31  62  56  57
*   Dummy MACE Gimbal Element Construction (Rigid)
  32  62   2  58
*   Rate Gyro beneath Torque Wheel Assembly (Rigid)
  33  62  16  59
*   Accel Triax on Node 4 (Rigid)
  34  62   9  60
*   Accel Triax on Node 2 (Rigid)
```

```
  35  62  23  61
  EDATA
  ENTRIES EL SECTION PRINT
  1  1 NO
  2  1 NO
  3  1 NO
  4  1 NO
  5  1 NO
  6  1 NO
  7  1 NO
  8  1 NO
  9  1 NO
  10 1 NO
  11 1 NO
  12 1 NO
  13 1 NO
  14 1 NO
  15 1 NO
  16 1 NO
  17 1 NO
  18 1 NO
  19 1 NO
  20 1 NO
  21 1 NO
  22 1 NO
  23 1 NO
  24 1 NO
  25 1 NO
  26 1 NO
  27 1 NO
  28 1 NO
  29 1 NO
  30 1 NO
  31 1 NO
  32 1 NO
  33 1 NO
  34 1 NO
  35 1 NO
*
LOADS MASSPROPORTIONAL 0 -1 0 9.807
*
*LOADS CONCENTRATED NODES
*   50  4  -.07456742937
*   51  4  .07456742937
*   54  6  .4144672254
*   55  6  -.4144672254
*
BOUNDARIES IDOF=111111 NODES
  62  66  67  68
*
BOUNDARIES IDOF=101111 NODES
  63  64  65
CONSTRAINTS OPTION=1
*
   42   1  39   1
   42   2  39   2
   42   3  39   3
   42   4  39   4
   42   6  39   6
   43   1  40   1
   43   2  40   2
   43   3  40   3
   43   4  40   4
   43   5  40   5
   44   1  41   1
   44   2  41   2
   44   3  41   3
   44   4  41   4
   44   5  41   5
   51   1  50   1
   51   2  50   2
   51   3  50   3
   51   5  50   5
   51   6  50   6
   55   1  54   1
   55   2  54   2
   55   3  54   3
   55   4  54   4
   55   5  54   5
*
ADINA
*
END
```

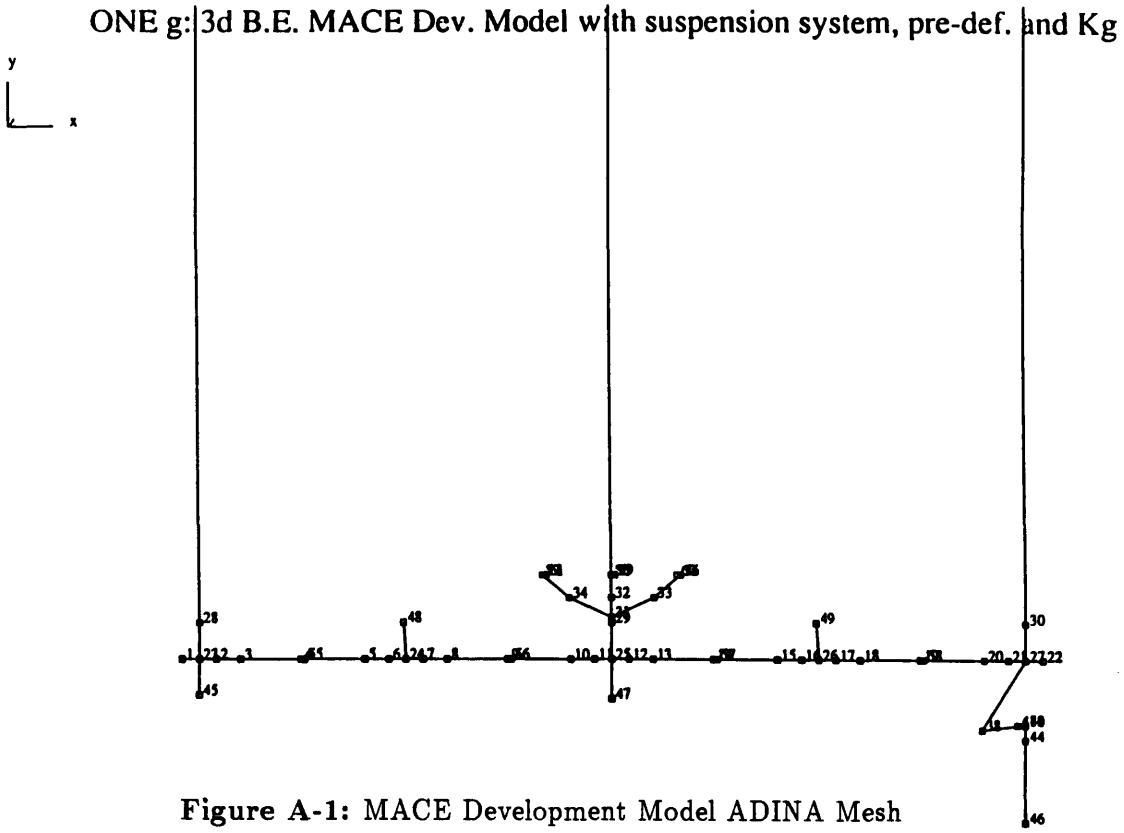

Figure A-1: MACE Development Model ADINA Mesh

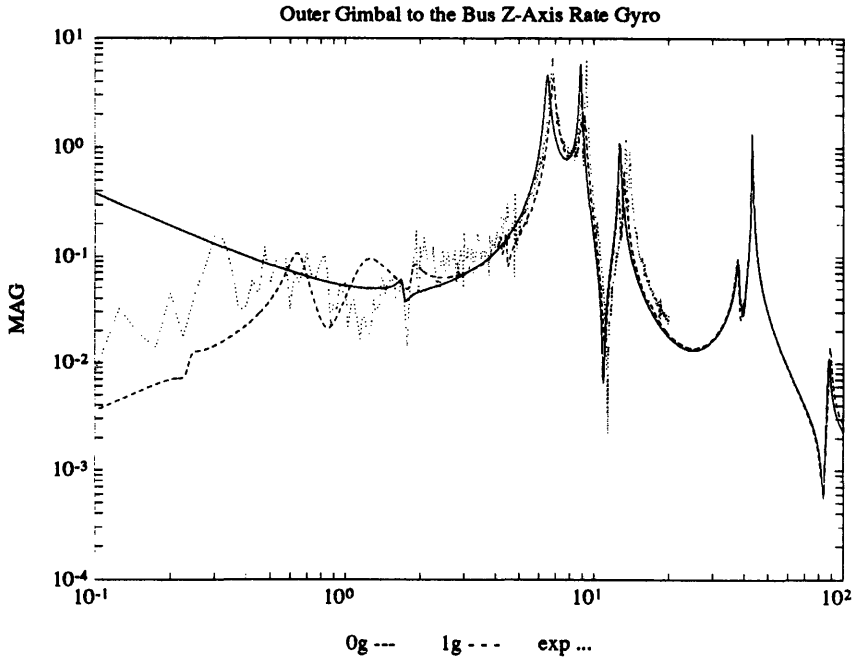

Figure A-2: Example of Transfer Function Improvement due to Incorporation of Gravity and Suspension Effects

Appendix B

MATLAB-based Finite Element Model with Kg, Kgd, and Initial Deformation Effects

This appendix contains the three most important MATLAB command files and function files used in Chapter 2 to study the effect of gravity on a cantilevered beam for comparison with the results of Minguet and Dugundji [30]. The main MATLAB command file is called **fembeamq.m** and is best described by the flowchart of Figure 2-8. It calls two other MATLAB routines: the first is **minguet.m** which simply initializes the beam properties, and the second is **beamkmkgq.m** which computes the elemental mass, stiffness, geometric stiffness, and distributed geometric stiffness matrices for a beam element.

B.1 MATLAB Finite Element Model Macro

```
%%%%%%%%%%%%%%%%%%%%%%%%%%%%%%%%%%%%%%%%%%%%%%%%%%%%%%%%%%%%%%%%%%%%%%%%%%%%
% fembeamq.m
%
% MATLAB macro to compute global mass and stiffness matrices of a
% clamped-free beam subject to gravitational loading and initial
% deformations.  Geometric stiffness effects are included.  Non-linear
% iterations are performed to compute the initial static deformation.
% Eigensolutions are computed for system without gravity loading, and
% with and without Kg or initial deformation effects for comparison
% purposes.
%
% author:  Daniel A. Rey                date:    July 01, 1991
% version: 4.0                          revised: Sept. 22, 1992
%
%%%%%%%%%%%%%%%%%%%%%%%%%%%%%%%%%%%%%%%%%%%%%%%%%%%%%%%%%%%%%%%%%%%%%%%%%%%%

% initialization
%-------------------------------------------------------------------------
 clear
 format short e

% load minguet parameter values for bending load test
%-------------------------------------------------------------------------
 minguet;
 nele = input('Number of elements: ')
 h = 1 / nele;       % uniform element lengths
 Ct = 6;                                        % rect. section (for Kgd)
 const=[EIy,EIz,EA,GIp,Ip,ECw,m,h,A,Iy,Iz,Ct];
 clear  EIy EIz EA GIp Ip ECw A Iy Iz Ct

% establish reference node co-ordinates and single element co-ordinates
%-------------------------------------------------------------------------
 Xref = [0 0 1]';
 X = zeros(3,2);

% establish initial ref structure co-ordinates [u, v, w, theta_x,_y,_z]
%-------------------------------------------------------------------------
 Xo = zeros(1:(6*(nele+1)),1);
 for i = 1:nele
     j = i*6;
     Xo((j+1):(j+6),1) = [(i*h) 0 0 0 0 0]';
 end
 Xo

% initialize deformed state vectors
%-------------------------------------------------------------------------
 Xo_KGQ = Xo;
 Xo_NOKG = Xo;

% initialize the deflection convergence measure
```

```
%-------------------------------------------------------------------
 delta = 99;
 tol = 1e-5;
 n_uncdof = (nele * 6) + 6;
 ndof = nele * 6;       % for cant.-free
 iterate = input('Perform non-linear iterations y/n (1/0)? ');
 if min(size(iterate)) == 0, iterate=0;end
 q_track =[];

% initialize lumped, consistent and cons/dist'd nodal load vectors
%-------------------------------------------------------------------
 Qe_l = zeros(12,nele);
 Qe_c = zeros(12,nele);
 Qe_d = zeros(12,nele);

% establish internal nodal load matrices for all elements of a
%   cantilevered hor. beam in g field
%-------------------------------------------------------------------
gs= 0  ;gc = 9.8;
magn = input('scale gravity loading by: ')
gs = gs * magn;gc = gc * magn;
g = [gs,gc];

 Fxa = 0; Fxb = 0;
 Fya = 0; Fyb = 0;
 Mxa = 0; Mxb= 0;
 Mza = 0; Mzb= 0;

% lumped translational forcing
%----------------------------
 for n = 1:nele
    Fza =  m*gc*l - m*gc*h*(n-0.5);
    Fzb = -Fza;
    Mya =  0;
    Myb =  0;
    Qe_l(:,n)=[Fxa, Fya, Fza, Mxa, Mya, Mza, Fxb, Fyb, Fzb, Mxb, Myb, Mzb]';
 end
% consistantly lumped nodal loads
%--------------------------------
 for n = 1:nele
    Fza =  m*gc*l - m*gc*h*(n-0.5);
    Fzb = -Fza;
    Mya =  m*gc*(h^2/12 - (((nele+1-n)^2*h^2)/2));
    Myb = -Mya-(Fza*h);
    Qe_c(:,n)=[Fxa, Fya, Fza, Mxa, Mya, Mza, Fxb, Fyb, Fzb, Mxb, Myb, Mzb]';
 end
% consistantly lumped nodal loads with dist'd forcing allowed
%-------------------------------------------------------------
 for n = 1:nele
    Fza =  m*gc*l - m*gc*h*(n-1);
    Fzb = -Fza + m*gc*h;
    Mya =  -(m*gc*((nele+1-n)*h)^2)/2;
```

```
    Myb = -Mya-(Fza*h) + (m*gc*h^2)/2;
    Qe_d(:,n)=[Fxa, Fya, Fza, Mxa, Mya, Mza, Fxb, Fyb, Fzb, Mxb, Myb, Mzb]';
  end
  clear Fxa Fya Fza Mxa Mya Mza Fxb Fyb Fzb Mxb Myb Mzb


%*********************************************************************
% MAIN LOOP: test for convergence and iterate if necessary
%*********************************************************************
loop_count = 0;
% echo on                                                    %debug tool
while delta > tol
 loop_count = loop_count + 1

  % perform assembly process for unconstrained simple beam
  %--------------------------------------------------------------------
   Kglob_NOKG  = zeros(n_uncdof,n_uncdof);
   Kglob_LKGQ  = zeros(n_uncdof,n_uncdof);
   Kglob_KGQ   = zeros(n_uncdof,n_uncdof);
   Kglob_DKGQ  = zeros(n_uncdof,n_uncdof);

   Mglob_NOKG = zeros(n_uncdof,n_uncdof);
   Mglob      = zeros(n_uncdof,n_uncdof);

   Qglob_NOKG = zeros(n_uncdof,1);
   Qglob      = zeros(n_uncdof,1);

% element-by-element sub-loop
%----------------------------
  for i = 1:6:nele*6
       j = i+11;

% solutions for different loading types
%--------------------------------------
       X(:,1) = Xo_KGQ(i:i+2,1);   % def'd x1 nodal u,v,w co-ord.
       X(:,2) = Xo_KGQ(i+6:i+8,1);          % def'd x2 nodal u,v,w co-ord.
       if i==1
          [Ke,Me,Kgl,Kg,dKg,T_Qe_c] = ...
            beam_kmkgq(const,X,Xref,Qe_1(:,i),Qe_c(:,i),Qe_d(:,i),g);
          Qglob(i:j,1) = T_Qe_c(:,1);
       else
          jj=(i+5)/6;
          [Ke,Me,Kgl,Kg,dKg,T_Qe_c] = ...
            beam_kmkgq(const,X,Xref,Qe_1(:,jj),Qe_c(:,jj),Qe_d(:,jj),g);
          Qglob(i:j,1) = Qglob(i:j,1) + T_Qe_c;
       end
       Kglob_LKGQ(i:j,i:j)  = Kglob_LKGQ(i:j,i:j) + Ke + Kgl;
       Kglob_KGQ(i:j,i:j)   =  Kglob_KGQ(i:j,i:j) + Ke + Kg;
       Kglob_DKGQ(i:j,i:j)  = Kglob_DKGQ(i:j,i:j) + Ke + dKg;
       Mglob(i:j,i:j) = Mglob(i:j,i:j) + Me;

% solution for no Kg reformation
```

```
%------------------------------
       X_NOKG(:,1) = Xo_NOKG(i:i+2,1); % no Kg def'd x1 nodal u,v,w co-ord.
       X_NOKG(:,2) = Xo_NOKG(i+6:i+8,1);       % no Kg def'd x2 nodal u,v,w co-ord.
       if i==1
          [Ke,Me,Kgl,Kg,dKg,T_Qe_c] = ...
            beam_kmkgq(const,X_NOKG,Xref,Qe_l(:,i),Qe_c(:,i),Qe_d(:,i),g);
            Qglob_NOKG(i:j,1) = Qglob_NOKG(i:j,1) + T_Qe_c(:,i);
       else
          jj=(i+5)/6;
          [Ke,Me,Kgl,Kg,dKg,T_Qe_c] = ...
           beam_kmkgq(const,X_NOKG,Xref,Qe_l(:,jj),Qe_c(:,jj),Qe_d(:,jj),g);
           Qglob_NOKG(i:j,1) = Qglob_NOKG(i:j,1) + T_Qe_c;
       end
       Kglob_NOKG(i:j,i:j) = Kglob_NOKG(i:j,i:j) + Ke;
       Mglob_NOKG(i:j,i:j) = Mglob_NOKG(i:j,i:j) + Me;

    end

   % apply constraints
   %-----------------
     Kglob_NOKG  = Kglob_NOKG(7:n_uncdof,7:n_uncdof);
     Kglob_LKGQ  = Kglob_LKGQ(7:n_uncdof,7:n_uncdof);
     Kglob_KGQ   = Kglob_KGQ(7:n_uncdof,7:n_uncdof);
     Kglob_DKGQ  = Kglob_DKGQ(7:n_uncdof,7:n_uncdof);

     Mglob_NOKG  = Mglob_NOKG(7:n_uncdof,7:n_uncdof);
     Mglob       = Mglob(7:n_uncdof,7:n_uncdof);

  % store NoKG & NoQ solution, also store the No Q update solution
  %  i.e. solution for unaltered stiffness matrix and solution for the
  %       linear, single Kg update of K (without iterative displacement
  %       based transformations of elemental matrices and loading).
  %-------------------------------------------------------------------------
    if loop_count == 1
        Kglobal_0 = Kglob_NOKG; Mglobal_0 = Mglob_NOKG;   % unperturbed
        Kglob_NOQ = Kglob_KGQ;  Mglob_NOQ = Mglob;        % no pre-def.
    end

  % no need to subtract reaction forces given the following few lines...
  % for a cantilever-free beam
  %-------------------------------------------------------------------------
    Qglob       = Qglob(7:n_uncdof,1);
    Qglob_NOKG  = Qglob_NOKG(7:n_uncdof,1);
    Xo_cons     = Xo(7:n_uncdof,1);

  % static solutions for constrained degrees-of-freedom
  %-------------------------------------------------------------------------
    Xo_LKGQ_cons  = Xo_cons + (inv(Kglob_LKGQ) * Qglob);
    Xo_KGQ_cons   = Xo_cons + (inv(Kglob_KGQ)  * Qglob);
    Xo_DKGQ_cons  = Xo_cons + (inv(Kglob_DKGQ) * Qglob);
    Xo_NOKG_cons  = Xo_cons + (inv(Kglob_NOKG) * Qglob_NOKG);
```

```
    Xo_KGQ  = [zeros(1,6), Xo_KGQ_cons']';
    Xo_DKGQ = [zeros(1,6), Xo_DKGQ_cons']';
    Xo_NOKG = [zeros(1,6), Xo_NOKG_cons']';

  % form deflection vector and save pertinent data
  %-----------------------------------------------------------------------
    i = size(Xo_KGQ);
    qnew      = zeros(max(i)/2,1);
    qnew_NOKG = zeros(max(i)/2,1);
    if loop_count == 1
        qprev = 0 * qnew;
        Me_undef=Me;   Ke_undef= Ke;   Kg_undef=Kg;
    end
    if loop_count == 2
        Me_oneiter=Me; Ke_oneiter= Ke; Kg_oneiter=Kg;
    end
    for i = 1:nele+1
        j = (6*i)-5;
        qnew(3*i-2:3*i,1) = Xo_KGQ(j:(j+2),1) - Xo(j:(j+2),1);
        qnew_NOKG(3*i-2:3*i,1) = Xo_NOKG(j:(j+2),1) - Xo(j:(j+2),1);
    end
%   qnew,qnew_NOKG,qprev
    q_track = [q_track, qnew]
    delta = max(abs(qnew - qprev))
    if loop_count ~= 2
      elseif iterate ~= 1, delta = 0          % exit for linear analysis
    end
  %
  % force one update of sys. matrices for static redef. case
    if loop_count == 1
      delta =99;
    end
    qprev = qnew;
end
% echo off
%***********************************************************************
% eigensolution for different cases
%  0) no q, no Kg, linear                                  Kglobal_0
%  1) q only,    non-linear       (static redefinition)  Kglob_NOKG
%  2) Kg only,   non-linear       (no transformations)   Kglob_NOQ
%  3) Kgl and q, non-linear                              Kglob_LKGQ
%  4) Kg and q,  non-linear                              Kglob_KGQ
%  5) dKg and q, non-linear                              Kglob_DKGQ
%%---------------------------------------------------------------------
%
%
% 0)  Kglobal_0:  no stress stiffening or pre-deformation effects
%
 [phi_0,lam_0] = eig((inv(Mglobal_0)*Kglobal_0),'nobalance');
 [phi_0,lam_0] = order(phi_0,lam_0);
 Hzfr_0 = diag(sqrt(lam_0) / (2*pi));
%pause
```

```
%
% 1)  Kglob_NOKG:  static redefinition only (based on (K(q))^-1)
%
 [phi_NOKG,lam_NOKG] = eig((inv(Mglob_NOKG)*Kglob_NOKG),'nobalance');
 [phi_NOKG,lam_NOKG] = order(phi_NOKG,lam_NOKG);
 Hzfr_NOKG = diag(sqrt(lam_NOKG) / (2*pi));
%pause
%
%
% 2)  Kglob_NOQ:  Kg only (no transformation due to static redefinition)
%
 [phi_NOQ,lam_NOQ] = eig((inv(Mglob_NOQ)*Kglob_NOQ),'nobalance');
 [phi_NOQ,lam_NOQ] = order(phi_NOQ,lam_NOQ);
 Hzfr_NOQ = diag(sqrt(lam_NOQ) / (2*pi));
%pause
%
% 3) Kglob_LKGQ: Combined lumped force Kg and static redef. based on (K + Kg)^-1
%
 [phi_LKGQ,lam_LKGQ] = eig((inv(Mglob)*Kglob_LKGQ),'nobalance');
 [phi_LKGQ,lam_LKGQ] = order(phi_LKGQ,lam_LKGQ);
 Hzfr_LKGQ = diag(sqrt(lam_LKGQ) / (2*pi));
%pause
%
% 4) Kglob_KGQ: Combined Kg and static redefinition based on (K + Kg)^-1
%
 [phi_KGQ,lam_KGQ] = eig((inv(Mglob)*Kglob_KGQ),'nobalance');
 [phi_KGQ,lam_KGQ] = order(phi_KGQ,lam_KGQ);
 Hzfr_KGQ = diag(sqrt(lam_KGQ) / (2*pi));
%pause
%
% 5) Kglob_DKGQ: Combined dist'd Kg and static redef. based on (K + Kg)^-1
%
 [phi_DKGQ,lam_DKGQ] = eig((inv(Mglob)*Kglob_DKGQ),'nobalance');
 [phi_DKGQ,lam_DKGQ] = order(phi_DKGQ,lam_DKGQ);
 Hzfr_DKGQ = diag(sqrt(lam_DKGQ) / (2*pi));
%pause
%

% verify mass and stiffness orthogonality
%-----------------------------------------------------------------------
ver_flag = input('Perform routine verification plots (y/n)? (1/0)')
if min(size(ver_flag)) == 0, ver_flag=0; end
if ver_flag == 1, verify_fq; end

% data dump and mode plots for different solutions
%-----------------------------------------------------------------------
disp('type:  diary filename');
keyboard
nele,magn
if loop_count > 1
   Me_undef,Me_oneiter,Me
   Ke_undef,Ke_oneiter,Ke
```

```
   Kg_undef,Kg_oneiter,Kg
else
   Me_undef,Me
   Ke_undef,Ke
   Kg_undef,Kg
end

q_track

Qe_c

interactive_flag = 0;

af = 1;ab=6;
if nele > 1
 af = max(size(Hzfr_KGQ));
 ab = af - 9;
end

[phi_0,lam_0] = order(phi_0,lam_0);
Hzfr_0 = diag(sqrt(lam_0) / (2*pi));

disp('Lowest eigenfrequencies for no reformation case: ');
Hzfr_0(ab:af,1)
columns_shown=sprintf('   %g to %g',ab,af);
columns_shown
col = input('Enter a 3x1 vector of first flap/tors/fore-aft ev col pos: ');
if min(size(col)) == 0, col=[nele*6,nele*6-2,nele*6-4]; end
cas1 = sprintf('%g-g gravity loading',magn);
cas2 = 'NO Kg correction and NO static redefinition.';
phi = phi_0; Hzfreq = Hzfr_0;
plmode; keyboard

disp('Lowest eigenfrequencies for static redef. case: ');
Hzfr_NOKG(ab:af,1)
columns_shown=sprintf('   %g to %g',ab,af);
columns_shown
col = input('Enter a 3x1 vector of first flap/tors/fore-aft ev col pos: ');
if min(size(col)) == 0, col=[nele*6,nele*6-2,nele*6-4]; end
cas1 = sprintf('%g-g gravity loading',magn);
cas2 = 'No Kg correction, only static redefinition';
phi = phi_NOKG; Hzfreq = Hzfr_NOKG;
plmode; keyboard

disp('Lowest eigenfrequencies for Kg only case: ');
Hzfr_NOQ(ab:af,1)
columns_shown=sprintf('   %g to %g',ab,af);
columns_shown
col = input('Enter a 3x1 vector of first flap/tors/fore-aft ev col pos: ');
if min(size(col)) == 0, col=[nele*6,nele*6-2,nele*6-4]; end
cas1 = sprintf('%g-g gravity loading',magn);
cas2 = 'No static redefinition, only consistant Kg';
```

```
phi = phi_NOQ; Hzfreq = Hzfr_NOQ;
plmode; keyboard

disp('Lowest eigenfrequencies for static redef. + lumped KG case: ');
Hzfr_LKGQ(ab:af,1)
columns_shown
col = input('Enter a 3x1 vector of first flap/tors/fore-aft ev col pos: ');
if min(size(col)) == 0, col=[nele*6,nele*6-2,nele*6-4]; end
cas1 = sprintf('%g-g gravity loading',magn);
cas2 = 'with lumped force Kg correction';
phi = phi_LKGQ; Hzfreq = Hzfr_LKGQ;
plmode; keyboard

disp('Lowest eigenfrequencies for static redef. + consistant KG case: ');
Hzfr_KGQ(ab:af,1)
columns_shown
col = input('Enter a 3x1 vector of first flap/tors/fore-aft ev col pos: ');
if min(size(col)) == 0, col=[nele*6,nele*6-2,nele*6-4]; end
cas1 = sprintf('%g-g gravity loading',magn);
cas2 = 'with consistant lumped force Kg correction';
phi = phi_KGQ; Hzfreq = Hzfr_KGQ;
plmode; keyboard

disp('Lowest eigenfrequencies for static redef. + distributed KG case: ');
Hzfr_DKGQ(ab:af,1)
columns_shown
col = input('Enter a 3x1 vector of first flap/tors/fore-aft ev col pos: ');
if min(size(col)) == 0, col=[nele*6,nele*6-2,nele*6-4]; end
cas1 = sprintf('%g-g gravity loading',magn);
cas2 = 'with distributed force Kg correction';
phi = phi_DKGQ; Hzfreq = Hzfr_DKGQ;
plmode
diary off

clear i ii interactive_flag j jj loop_count m n ab af ans cas1 cas2 col
clear columns_shown const delta iterate str ver_flag

disp('')
disp('---------------------------- END OF RUN ------------------------- ')
disp('')
```

B.2 MATLAB Beam M, K, Kg, Kgd Finite Element Function

```
%%%%%%%%%%%%%%%%%%%%%%%%%%%%%%%%%%%%%%%%%%%%%%%%%%%%%%%%%%%%%%%%%%%%%%%%%%%%
% beam_kmkgq.m
%
% MATLAB function called by fembeamq.m to compute the elemental M, K,
% and Kg matrices for a beam element with known nodal positions x1 and x2.
% Automatically performs transformation of M, K, and Kg into global
% coordinates.  Kg matrices are computed for the three cases of plain lumped
% forces, consistent lumped forces, and consistent lumped forces with
% distributed loads.
%
% Uses direct input of homogeneous beam properties in vector 'const'.
%
% author:  E. Balmes and D. A. Rey
% date:    July 1991
%
% revised: Aug. 10, 1992
%%%%%%%%%%%%%%%%%%%%%%%%%%%%%%%%%%%%%%%%%%%%%%%%%%%%%%%%%%%%%%%%%%%%%%%%%%%%

 function [ke,m,kgl,kg,dkg,t_qe]=beam_kmkg(const,x,xref,qelump,qeconc,qedist,g)

% x    is 6x1 column vector of [x1 x2]'
% xref is 3x1 column vector of [uref, vref, wref]'

 EIy=const(1,1); EIz=const(1,2); EA=const(1,3); GIp=const(1,4);
 Ip=const(1,5); ECw=const(1,6); m=const(1,7);  h=const(1,8);
 A=const(1,9); Iy=const(1,10); Iz=const(1,11); Ct=const(1,12);

% determine transformation matrix and deformed element length h
%---------------------------------------------------------------------
w = xref - x(:,1);
w = w /sqrt(w'*w);
u = x(:,2) - x(:,1);
h = sqrt(u'*u);
% note that the above h is probably different from the undeformed h
u=u/h;
w1 = w - u*u'*w;
w1 = w1 / sqrt(w1'*w1);
v = [w1(2)*u(3)-w1(3)*u(2);...
     w1(3)*u(1)-w1(1)*u(3);...
     w1(1)*u(2)-w1(2)*u(1)];
v = v / sqrt(v'*v);
c = [u v w1];
T = [    c'    zeros(3) zeros(3) zeros(3)
     zeros(3)    c'     zeros(3) zeros(3)
     zeros(3)  zeros(3)   c'     zeros(3)
     zeros(3)  zeros(3) zeros(3)   c'    ];
%diag(T)'
```

```
% pause
%T
if max(T) > 1, disp('STOP unless you intended to include deformations')
end

% untransformed elemental matrix definitions for 12 dof beam element
% dof: Ux, Uy, Uz, Ox, Oy, Oz   (where x is neutral axis)
%-------------------------------------------------------------------
 Ke=zeros(12,12); Kg=zeros(12,12); Me=zeros(12,12); Min=zeros(12,12);
 dKg=zeros(12,12); Kgl=zeros(12,12);

 Ke(1,7) = - EA / h;
 Ke(2,6) = 6 * EIz / (h^2);
 Ke(2,8) = -12 * EIz / (h^3);
 Ke(2,12) = 6 * EIz / (h^2);
 Ke(3,5) = -6 * EIy / (h^2);
 Ke(3,9) = -12 * EIy / (h^3);
 Ke(3,11) = -6 * EIy / (h^2);
 Ke(4,10) = -6/5*GIp / h + 12*ECw/ (h^3);
 Ke(5,9) = 6 * EIy / (h^2);
 Ke(5,11) = 2 * EIy / h;
 Ke(6,8) = -6 * EIz / (h^2);
 Ke(6,12) = 2 * EIz / h;
 Ke(8,12) = -6 * EIz / (h^2);
 Ke(9,11) = 6 * EIy / (h^2);
 Ke = Ke + Ke';
 Ke(1,1) = EA / h;
 Ke(2,2) = 12 * EIz / (h^3);
 Ke(3,3) = 12 * EIy/ (h^3);
 Ke(4,4) = 6/5*GIp / h + 12*ECw/ (h^3);
 Ke(5,5) = 4 * EIy / h;
 Ke(6,6) = 4 * EIz / h;
 Ke(7,7) = Ke(1,1);
 Ke(8,8) = Ke(2,2);
 Ke(9,9) = Ke(3,3);
 Ke(10,10) = Ke(4,4);
 Ke(11,11) = Ke(5,5);
 Ke(12,12) = Ke(6,6);
% positive definicy correction
% Ke = Ke + (eye(12)*1e-5*min(min(Ke)));


% Kg with plain lumped forces
%----------------------------
 qe=(T' * qelump)';
 Fxa=qe(1,1);Fya=qe(1,2);Fza=qe(1,3);Mxa=qe(1,4);Mya=qe(1,5);Mza=qe(1,6);
 Fxb=qe(1,7);Fyb=qe(1,8);Fzb=qe(1,9);Mxb=qe(1,10);Myb=qe(1,11);Mzb=qe(1,12);
 gs=g(1,1);gc=g(1,2);

 Kgl(1,2) = (Mza + Mzb) / (h^2);
 Kgl(1,3) = -(Mya + Myb) / (h^2);
 Kgl(1,8) = -(Mza + Mzb) / (h^2);
```

```
 Kgl(1,9) = (Mya + Myb) / (h^2);
% Kgl(2,4) = 1.1*Mya/ h - Myb/ (10*h);
 Kgl(2,4) = Mya/ h;
 Kgl(2,5) = Mxb/ h;
 Kgl(2,6) = Fxb/10;
 Kgl(2,7) = -Kgl(1,2);
 Kgl(2,8) = -6*Fxb/ (5*h);
% Kgl(2,10) = -Mya/ (10*h) + 1.1*Myb/ h;
 Kgl(2,10) =  Myb/ h;
 Kgl(2,11) = -Mxb/ h;
 Kgl(2,12) = Fxb/10;
% Kgl(3,4) = 1.1*Mza/h - Mzb/ (10*h);
 Kgl(3,4) =   Mza/h;
 Kgl(3,5) =  -Fxb/10;
 Kgl(3,6) = Mxb/h;
 Kgl(3,7) = -Kgl(1,3);
 Kgl(3,9) = -6/5*Fxb/h;
% Kgl(3,10) = -Mza/(10*h) + 1.1*Mzb/h;
 Kgl(3,10) =   Mzb/h;
 Kgl(3,11) =  -Fxb/10;
 Kgl(3,12) = -Mxb/h;
% Kgl(4,5) = Mza/10 + Mzb/5;
 Kgl(4,5) = Mza/6 + Mzb/6;
% Kgl(4,6) = -Mya/10 - Myb/5;
 Kgl(4,6) = -Mya/6 - Myb/6;
% Kgl(4,8) = -1.1*Mya/ h + Myb/ (10*h);
 Kgl(4,8) = -Mya/ h;
% Kgl(4,9) = -1.1*Mza/ h + Mzb/ (10*h);
 Kgl(4,9) = -Mza/ h;
 Kgl(4,10) = - 6/5*Fxb*Ip/A / h;
% Kgl(4,11) = - Mza/5 - Mzb/10;
  Kgl(4,11) = - Mza/6 - Mzb/6;
% Kgl(4,12) = Mya/5 + Myb/10;
 Kgl(4,12) = Mya/6 + Myb/6;
 Kgl(5,8) = -Mxb/h;
 Kgl(5,9) = Fxb/10;
% Kgl(5,10) = -Mza/10 - Mzb/5;
 Kgl(5,10) = -Mza/6 - Mzb/6;
 Kgl(5,11) =  -Fxb*h/30;
 Kgl(5,12) = Mxb/2;
 Kgl(6,8) = -Fxb/10;
 Kgl(6,9) = -Mxb/h;
% Kgl(6,10) = Mya/10 + Myb/5;
 Kgl(6,10) = Mya/6 + Myb/6;
 Kgl(6,11) =  -Mxb/2;
 Kgl(6,12) = -Fxb*h/30;
 Kgl(7,8) = (Mza - Mzb) / (h^2);
 Kgl(7,9) = -(Mya + Myb) / (h^2);
% Kgl(8,10) = Mya/(10*h) - 1.1*Myb/h;
 Kgl(8,10) = -Myb/h;
 Kgl(8,11) = Mxb/h;
 Kgl(8,12) = -Fxb/ 10;
```

```
% Kgl(9,10) = Mza/(10*h) - 1.1*Mzb/h;
 Kgl(9,10) = -Mzb/h;
 Kgl(9,11) =  Fxb/10;
 Kgl(9,12) = Mxb/h;
% Kgl(10,11) = Mza/5 + Mzb/10;
 Kgl(10,11) = Mza/6 + Mzb/6;
% Kgl(10,12) = -Mya/5 - Myb/10;
 Kgl(10,12) = -Mya/6 - Myb/6;
 Kgl = Kgl + Kgl';
 Kgl(2,2) = 6/5*Fxb/h;
 Kgl(3,3) = Kgl(2,2);
 Kgl(4,4) = Fxb*Ip/(A*h);
 Kgl(5,5) = 2*Fxb * h/15;
 Kgl(6,6) = Kgl(5,5);
 Kgl(8,8) = Kgl(2,2);
 Kgl(9,9) = Kgl(2,2);
 Kgl(10,10) = Kgl(4,4);
 Kgl(11,11) = Kgl(5,5);
 Kgl(12,12) = Kgl(5,5);

% Kg with consistant lumped forces
%--------------------------------
 qe=(T' * qeconc)'; t_qe=qe';
 Fxa=qe(1,1);Fya=qe(1,2);Fza=qe(1,3);Mxa=qe(1,4);Mya=qe(1,5);Mza=qe(1,6);
 Fxb=qe(1,7);Fyb=qe(1,8);Fzb=qe(1,9);Mxb=qe(1,10);Myb=qe(1,11);Mzb=qe(1,12);
 gs=g(1,1);gc=g(1,2);

 Kg(1,2) = (Mza + Mzb) / (h^2);
 Kg(1,3) = -(Mya + Myb) / (h^2);
 Kg(1,8) = -(Mza + Mzb) / (h^2);
 Kg(1,9) = (Mya + Myb) / (h^2);
% Kg(2,4) = 1.1*Mya/ h - Myb/ (10*h);
  Kg(2,4) = Mya/ h;
 Kg(2,5) = Mxb/ h;
 Kg(2,6) = Fxb/10;
 Kg(2,7) = -Kg(1,2);
 Kg(2,8) = -6*Fxb/ (5*h);
% Kg(2,10) = -Mya/ (10*h) + 1.1*Myb/ h;
  Kg(2,10) =  Myb/ h;
 Kg(2,11) = -Mxb/ h;
 Kg(2,12) = Fxb/10;
% Kg(3,4) = 1.1*Mza/h - Mzb/ (10*h);
  Kg(3,4) =   Mza/h;
 Kg(3,5) =  -Fxb/10;
 Kg(3,6) = Mxb/h;
 Kg(3,7) = -Kg(1,3);
 Kg(3,9) = -6/5*Fxb/h;
% Kg(3,10) = -Mza/(10*h) + 1.1*Mzb/h;
  Kg(3,10) =   Mzb/h;
 Kg(3,11) =  -Fxb/10;
 Kg(3,12) = -Mxb/h;
% Kg(4,5) = Mza/10 + Mzb/5;
```

```
  Kg(4,5) = Mza/6 + Mzb/6;
% Kg(4,6) = -Mya/10 - Myb/5;
  Kg(4,6) = -Mya/6 - Myb/6;
% Kg(4,8) = -1.1*Mya/ h + Myb/ (10*h);
  Kg(4,8) = -Mya/ h;
% Kg(4,9) = -1.1*Mza/ h + Mzb/ (10*h);
  Kg(4,9) = -Mza/ h;
 Kg(4,10) = - 6/5*Fxb*Ip/A / h;
% Kg(4,11) = - Mza/5 - Mzb/10;
  Kg(4,11) = - Mza/6 - Mzb/6;
% Kg(4,12) = Mya/5 + Myb/10;
  Kg(4,12) = Mya/6 + Myb/6;
 Kg(5,8) = -Mxb/h;
 Kg(5,9) = Fxb/10;
% Kg(5,10) = -Mza/10 - Mzb/5;
 Kg(5,10) = -Mza/6 - Mzb/6;
 Kg(5,11) =  -Fxb*h/30;
 Kg(5,12) = Mxb/2;
 Kg(6,8) = -Fxb/10;
 Kg(6,9) = -Mxb/h;
% Kg(6,10) = Mya/10 + Myb/5;
 Kg(6,10) = Mya/6 + Myb/6;
 Kg(6,11) =  -Mxb/2;
 Kg(6,12) = -Fxb*h/30;
 Kg(7,8) = (Mza - Mzb) / (h^2);
 Kg(7,9) = -(Mya + Myb) / (h^2);
% Kg(8,10) = Mya/(10*h) - 1.1*Myb/h;
 Kg(8,10) = -Myb/h;
 Kg(8,11) = Mxb/h;
 Kg(8,12) = -Fxb/ 10;
% Kg(9,10) = Mza/(10*h) - 1.1*Mzb/h;
 Kg(9,10) = -Mzb/h;
 Kg(9,11) =  Fxb/10;
 Kg(9,12) = Mxb/h;
% Kg(10,11) = Mza/5 + Mzb/10;
 Kg(10,11) = Mza/6 + Mzb/6;
% Kg(10,12) = -Mya/5 - Myb/10;
 Kg(10,12) = -Mya/6 - Myb/6;
 Kg = Kg + Kg';
 Kg(2,2) = 6/5*Fxb/h;
 Kg(3,3) = Kg(2,2);
 Kg(4,4) = Fxb*Ip/(A*h);
 Kg(5,5) = 2*Fxb * h/15;
 Kg(6,6) = Kg(5,5);
 Kg(8,8) = Kg(2,2);
 Kg(9,9) = Kg(2,2);
 Kg(10,10) = Kg(4,4);
 Kg(11,11) = Kg(5,5);
 Kg(12,12) = Kg(5,5);


% Kg with distributed loads
```

```
%-------------------------
qe=(T' * qedist)';
 Fxa=qe(1,1);Fya=qe(1,2);Fza=qe(1,3);Mxa=qe(1,4);Mya=qe(1,5);Mza=qe(1,6);
 Fxb=qe(1,7);Fyb=qe(1,8);Fzb=qe(1,9);Mxb=qe(1,10);Myb=qe(1,11);Mzb=qe(1,12);
gs=g(1,1);gc=g(1,2);

 dKg(1,2) =  (Mza + Mzb) / (h^2);
 dKg(1,3) = -(Mya + Myb) / (h^2);
 dKg(1,5) = + m*h*gc/12;
 dKg(1,8) = -dKg(1,2);
 dKg(1,9) = -dKg(1,3);
 dKg(1,11) = -dKg(1,5);
 dKg(2,4) =  Mya/ h - m*h*gc/10;
 dKg(2,5) =  Ct*Mxb/(6*h);
 dKg(2,6) =  Fxb/10;
 dKg(2,7) = -dKg(1,2);
 dKg(2,8) = -6*Fxb/ (5*h) + 3*m*gs/5;
 dKg(2,10) =  Myb/ h - m*h*gc/10;
 dKg(2,11) = -dKg(2,5);
 dKg(2,12) =  Fxb/10;
 dKg(3,4) =   Mza/h;
 dKg(3,5) =  -dKg(2,6);
 dKg(3,6) =   dKg(2,5);
 dKg(3,7) =  -dKg(1,3);
 dKg(3,9) =   dKg(2,8);
 dKg(3,10) =  Mzb/h;
 dKg(3,11) = -dKg(2,12);
 dKg(3,12) = -dKg(2,5);
 dKg(4,5) = (Mza + Mzb)/6;
 dKg(4,6) = -(Mya + Myb)/6 + 7*m*h^2*gc/60;
 dKg(4,8) =  -dKg(2,4);
 dKg(4,9) =  -dKg(3,4);
 dKg(4,10) = -Fxb*Ip/(A*h) + Ip*m*gs/(2*A);
 dKg(4,11) = -dKg(4,5);
 dKg(4,12) = (Mya + Myb)/6 - m*h^2*gc/20;
 dKg(5,7) = -dKg(1,5);
 dKg(5,8) = -dKg(2,5);
 dKg(5,9) =  dKg(2,6);
 dKg(5,10) = -dKg(4,5);
 dKg(5,11) = -Fxb*h/30 + m*h^2*gs/60;
 dKg(5,12) =  dKg(2,5)*h/2;
 dKg(6,8) = -dKg(2,6);
 dKg(6,9) = -dKg(2,5);
 dKg(6,10) = (Mya + Myb)/60 + m*h^2*gc/20;
 dKg(6,11) = -dKg(5,12);
 dKg(6,12) =  dKg(5,11);
 dKg(7,8) = dKg(1,2);
 dKg(7,9) = dKg(1,3);
 dKg(7,11) =  dKg(1,5);
 dKg(8,10) = -Myb/h + m*h*gc/10;
 dKg(8,11) =  dKg(2,5);
 dKg(8,12) = -dKg(9,11);
```

```
dKg(9,10) = -Mzb/h;
dKg(9,11) =  Fxb/10 - m*h*gs/10;
dKg(9,12) =  dKg(2,5);
dKg(10,11) = dKg(4,5);
dKg(10,12) = -(Mya + Myb)/6 - 7*m*h^2*gc/60;
dKg = dKg + dKg';
dKg(2,2) = 6/5*Fxb/h - 3*m*gs/5;
dKg(3,3) = dKg(2,2);
dKg(4,4) = Fxb*Ip/(A*h) - Ip*m*gs/(2*A) ;
dKg(5,5) = 2*Fxb * h/15 - m*h^2*gs/10;
dKg(6,6) = dKg(5,5);
dKg(8,8) = dKg(2,2);
dKg(9,9) = dKg(3,3);
dKg(10,10) = dKg(4,4);
dKg(11,11) = 2*Fxb * h/15 - m*h^2*gs/30;
dKg(12,12) = dKg(11,11);


Me(1,7) = 1/6;
Me(2,6) = 11*h/210;
Me(2,8) = 9/70;
Me(2,12) = -13*h/420;
Me(3,5) = -11*h/210;
Me(3,9) = 9/70;
Me(3,11) = 13*h/420;
Me(4,10) = Ip/(6*A);
Me(5,9) = -13*h/420;
Me(5,11) = -h*h/140; %subs 140 for 420...
Me(6,8) = 13*h/420;
Me(6,12) = -h*h/140;
Me(8,12) = -11*h/210;
Me(9,11) = 11*h/210;
Me = Me + Me';
%
Me(1,1) = 1/3;
Me(2,2) = 13/35;
Me(3,3) = 13/35;
Me(4,4) = Ip/(3*A);
Me(5,5) = h^2/105;
Me(6,6) = h^2/105;
%
Me(7,7) = 1/3;
Me(8,8) = 13/35;
Me(9,9) = 13/35;
Me(10,10) = Ip/(3*A);
Me(11,11) = h^2/105;
Me(12,12) = h^2/105;
Me = m*h * Me;
%
%-------------------------------------------------------------------------
% mass matrix rotational inertia correction terms
%  (omitted for the time being)
```

```
%-------------------------------------------------------------------
%
skip=1;if skip==0,
 Min(2,6) =  Iz/(10*A*h);
 Min(2,8) =  - 6*Iz/(5*A*h^2);
 Min(2,12) =  Iz/(10*A*h);
 Min(3,5) =  -Iy/(10*A*h);
 Min(3,9) =  - 6*Iy/(5*A*h^2);
 Min(3,11) =  - Iy/(10*A*h);
 Min(4,10) = 0;
 Min(5,9) =  Iy/(10*A*h);
 Min(5,11) = - Iy/(30*A);
 Min(6,8) =  - Iz/(10*A*h);
 Min(6,12) =  - Iz/(30*A);
 Min(8,12) =  - Iz/(10*A*h);
 Min(9,11) = Iy/(10*A*h);
 Min = Min + Min';
 Min(2,2) = 6*Iz/(5*A*h*h);
 Min(3,3) = 6*Iy/(5*A*h*h);
 Min(4,4) = 0;
 Min(5,5) = 2*Iy/(15*A);
 Min(6,6) = 2*Iz/(15*A);
 Min(8,8) = 6*Iz/(5*A*h*h);
 Min(9,9) = 6*Iy/(5*A*h*h);
 Min(10,10) = 0;
 Min(11,11) = 2*Iy/(15*A);
 Min(12,12) = 2*Iz/(15*A);
 Min = m*h * Min;
 Me = Me + Min;
end

%  transform elemental matrices
%-------------------------------------------------------------------

ke  = T' * Ke  * T;
m   = T' * Me  * T;
kgl = T' * Kgl * T;
kg  = T' * Kg  * T;
dkg = T' * dKg * T;

%------------------------ eof ---------------------------------------
```

B.3 MATLAB Minguet Beam Initialization Macro

```
%%%%%%%%%%%%%%%%%%%%%%%%%%%%%%%%%%%%%%%%%%%%%%%%%%%%%%%%%%%%%%%%%%%%%%%%%%%%
% minguet.m
%
% MATLAB macro to initialize homogeneous beam properties based on the
% Minguet PhD thesis composite beam.
%
% author:  Daniel A. Rey
% date:    May, 1991
%%%%%%%%%%%%%%%%%%%%%%%%%%%%%%%%%%%%%%%%%%%%%%%%%%%%%%%%%%%%%%%%%%%%%%%%%%%%
echo on

 g = 9.8;                          %m/s^2

 EIz = 276;     %Nm^2
 EIy = 0.707;   %Nm^2

 Iz = 3.353E-9; %m^4
 Iy = 8.27E-12; %m^4

 m = 0.0683;    %kg/m
 l = 0.56;               %m
 A = 0.03 * 1.49E-3;   %m^2

 GIp = 0.183;    %Nm^2
 EA  = EIz / Iz * A;             %N

%Ip = 5.13E-6;  %kg/m given????
%Ip = 3.36E-9; %m^4  calculated
%Ip = 3.0E-9; %m^4  original tuned
 Ip = 4.05E-9; %m^4  second tuned Ip

 ECw = 0;
echo off
```

Appendix C

Guidelines for Designing Simple Spring Suspension Systems

This appendix contains the details of how to select off-the-shelf extensional springs for the purposes of suspending a flexible spacecraft model. Given that the extensional springs are specified by length, pre-tension and unit stiffness, the selection process can be cumbersome if one truly wants to optimize the springs selected. Both sections of this Appendix present simple step-by-step instructions for identifying the optimal spring lengths and types based on criteria of lowest possible bounce mode or maximum possible surge mode.

C.1 Minimizing the Bounce Mode Frequency

C.1.1 Applicability

This appendix is a good introduction to spring selection but is only applicable to those test-beds which are to suspend very low-frequency test articles and for which corruption of higher frequency measurements due to spring surge modes is a lesser concern. If the higher frequency surge mode effects are a greater concern than achieving as low a bounce frequency as possible, see the second section of this Appendix

entitled *"Maximizing Surge Mode Frequencies subject to Bounce Mode and Safety Constraints"*.

C.1.2 Introduction

Given that coil springs, extensional and torsional, are typically pre-tensioned and are specified by the supplier in terms of unit length stiffness, i.e. $in\,lbs/in$ or $N\,m/m$, some care must be exercised in their selection.

The free variables in selecting off-the-shelf springs are the outside coil diameter, wire diameter, and spring length. The first two must typically be selected from a discrete set of available products while the spring length can be cut to measure. Uniquely related to the coil and wire diameter specification pairs are the more convenient initial tension and unit stiffness descriptors.

To reduce the perturbation to the test article dynamics, a frequency separation between the suspension system resonances and the test article resonances of one half to a full order of magnitude is desirable. Further, if the objective of the suspension system is to simulate free-free boundary conditions, it is necessary for this frequency separation to be provided from below, i.e. the suspension resonant frequency must be less than the test article fundamental.

This first section of Appendix A describes the selection of the *optimal* spring where it is assumed that the *optimal* spring is the spring with the lowest allowable stiffness given a known maximum deformed length and load.

C.1.3 Background

Ideally, one would select the softest possible linear or non-linear spring (spring with pre-tension) given a known load range and deformed length range. If the pre-tension in the spring can be arbitrarily selected, the problem is resolved, as this would make it possible to select an arbitrarily small spring stiffness. However, such a simple spring selection procedure is not possible, as one cannot arbitrarily select the pre-tension in

the spring. Physically, the initial tension T_o is subject to an upper-bound which is related to the spring constant. A second problem is that the maximum deformation length, $x_{d_{max}}$, is undetermined since it depends on the undeformed spring length which is not known a priori. The practical pre-tension maximum is roughly equal to the product of the total spring stiffness and the undeformed spring length, i.e.:

$$T_o < k_u/x_s * x_s \tag{C.1}$$

or

$$T_o < K_T * x_s \tag{C.2}$$

C.1.4 Spring Selection

To overcome these problems the selection of the *optimal* spring is best accomplished in terms of the difference between k_u and T_o, and in terms of the total available length, l.

Rewriting the static equilibrium equation,

$$F_o = T_o + K_T x_\delta \tag{C.3}$$

as

$$k_u - T_o = F_o \left(\frac{4\pi^2 f_b^2}{g}(l - \epsilon_w) - 1 \right) \tag{C.4}$$

where

$$l = x_s + x_\delta + \epsilon_w$$

$$K_T = k_u/x_s$$

and where K_T has been written in terms of the desired suspension frequency,

$$K_T = \frac{4\pi^2 f_b^2 F_o}{g} \tag{C.5}$$

The **first step** is thus the determination of the lowest feasible suspension frequency. From Equation C.1 and Equation C.4 it is clear that for $k_u > T_o$

$$f_b > \frac{1}{2\pi}\sqrt{\frac{g}{l}} \tag{C.6}$$

Thus the bounce frequency of a simple spring mass system will always be greater than its pendular frequency.

The **second step**, having selected a feasible suspension bounce frequency based on Equation C.6, is to substitute all known left-hand side values in Equation C.4 to obtain an equation of the following form, where α and β are real numbers:

$$k_u - T_o = \alpha - \beta\epsilon_w \tag{C.7}$$

The **third step** is to scan the spring supplier data sheet to select a spring with $k_u - T_o$ as close to α as possible, but not greater than α, and to solve for the resulting corrector wire length, ϵ_w. This so-called corrector wire is only required in cases such as a multiple suspension point system where the total suspension length at each attach point is critical. The wire is placed in series with the spring and should have a length adjusting mechanism such as a turnbuckle.

The **fourth step** is to verify that the maximum expected load is less than the yield load of the selected spring, and that the initial pre-tension is less than the minimum expected load. If these tests are unsuccessful then attempt to select a heavier spring, even if this means a greater wire length and retry step four. If no spring options are feasible return to step two and select a slightly higher resonant frequency.

The **fifth step** is simply calculating the undeformed spring length,

$$x_s = \frac{k_u}{K_T} \tag{C.8}$$

All information required to place the spring order is now known, i.e. k_u, T_o, and x_s.

The **sixth step** consists of calculating the spring surge eigenfrequencies to evaluate whether or not they will in fact be a concern. Hopefully the first surge eigenfrequency will be sufficiently high such that the undeformed spring length need not be reduced. As detailed in Appendix C.2 the i^{th} surge frequency is given by:

$$(f_s)_i = \frac{i}{2x_s}\sqrt{\frac{3 \cdot k_u}{\mu}} \tag{C.9}$$

C.1.5 Nomenclature

f_b	=	desired suspension bounce frequency	$[Hz]$
$(f_s)_i$	=	i'th surge mode eigenfrequency	$[Hz]$
F_o	=	downward directed point load at spring tip	$[N]$
g	=	gravitational acceleration constant	$[N/kg]$
k_u	=	unit spring stiffness	$[N \cdot m/m]$
K_T	=	total spring stiffness	$[N/m]$
l	=	total suspension length	$[m]$
μ	=	spring mass density	$[kg/m]$
T_o	=	initial pre-tension in spring	$[N]$
x_s	=	undeformed spring length	$[m]$
x_δ	=	change in spring length when loaded	$[m]$
ϵ_w	=	corrector wire length	$[m]$

C.2 Maximizing Surge Mode Frequencies

C.2.1 Approach

The fundamental approach adopted here is to *raise* the first surge resonant frequency as high as possible and to keep the bounce mode at or below a maximum frequency determined by the test article first resonance. This approach of maximimizing the

first surge mode frequency is recommended based on the fact that the surge modes are very lightly damped and linearly spaced in the frequency domain which precludes any attempt to place them below the first test article resonance. The bounce mode frequency on the other hand should be kept one decade to half of a decade below the first test article flexible mode for separation reasons and to approximate the desired free-free boundary condition.

C.2.2 Background

As pointed out by Blackwood [73], the surge mode eigenfrequencies are trivial to predict and are given by the equation for the eigenfrequencies of a pinned-pinned rod:

$$(f_s)_i = \frac{i}{2x_s}\sqrt{\frac{3 \cdot k_u}{\mu}} \tag{C.10}$$

where

$(f_s)_i$	=	i'th surge mode eigenfrequency	$[Hz]$
k_u	=	unit spring stiffness	$[in \cdot lb/in]$
x_s	=	undeformed spring length	$[in]$
μ	=	spring mass density	$[slugs/in]$

For reference purposes the conversion from the manufacturer specified weight per foot, w, to μ is:

$$\mu = \frac{w}{386.4} \tag{C.11}$$

The bounce mode resonance, f_b, is given by,

$$f_b = \frac{1}{2\pi}\sqrt{\frac{k_u \cdot g}{x_s \cdot F_o}} \tag{C.12}$$

where

f_b	=	bounce mode eigenfrequency	$[Hz]$

F_o = nominal load on spring $[lb]$

g = gravitational acceleration $[in/s^2]$

C.2.3 Methodology

Given a desired bounce frequency, f_b, and a known nominal load, F_o, it is possible to solve for the spring length in Equation C.12 and by substitution into Equation C.10 identify $\mu\, k_u$ as the figure of merit for surge spring selection; i.e. the $\mu\, k_u$ product is the only free parameter in the resulting surge mode frequency expression:

$$(f_s)_i = \frac{2\pi^2 F_o f_b^2}{g}\sqrt{\frac{3}{\mu k_u}} \tag{C.13}$$

Step 1

Choose the extensional spring with the smallest possible unit stiffness and unit mass product, (i.e $\mu\ \ k_u$ or $w\ \ k_u$), subject to the requirement that the nominal load be greater than the spring pre-tension and less than the maximum safe load, i.e.

$$\eta T_o < F_o < \frac{T_{max}}{\eta} \tag{C.14}$$

where

T_o = initial pre-tension in spring $[lb]$

F_o = nominal load on spring $[lb]$

η = safety factor $[lb]$

Step 2

Verify that the nominal unit extension does not exceed the safe maximum unit extension,

$$\frac{F_o}{k_u} < s_{max} \tag{C.15}$$

where

s_{max} = safe maximum extension per unit spring length $[in/in]$

If this test is not passed return to step 1 and choose the next best spring.

Step 3

Determine the (as of yet implicit) undeformed spring length, x_s, which was prescribed by the desired bounce frequency, f_b:

$$x_s = \frac{k_u g}{4\pi^2 F_o f_b^2} \tag{C.16}$$

and verify that the undeformed spring length, x_s, represents at least 10 spring coils:

$$\frac{x_s}{d_w} \geq 10 \tag{C.17}$$

where

d_w = spring wire diameter $[in]$

If this final test is passed, the optimal off-the-shelf spring has been selected, (where optimality is as defined in the Approach). If necessary increase the undeformed spring length such that the above test is passed, (which will reduce both the surge mode and bounce mode eigenfrequencies), and proceed thru to step 4 to determine whether the resulting spring performance is satisfactory.

Step 4

Having selected the spring number in steps 1 and 2 and the undeformed spring length in step 3, calculate the resulting surge mode frequencies using Equation C.10.

Step 5

Order spring by specifying spring number and desired length.

References

[1] Crawley, E. F. and Hall, S. R., "The Dynamics of Controlled Structures," Tech. Rep. SERC #10-91-I, M.I.T. Space Engineering Research Center, July 1991.

[2] Balas, M. J., "Trends in Large Space Structure Control Theory: Fondest Hopes, Wildest Dreams," *IEEE Trans. on Automatic Control*, Vol. AC–27, No. 3, June 1982, pp. 522–535.

[3] Skelton, R., "Model Error Concepts in Control Design," *International Journal of Control*, Vol. 49, No. 5, May 1989, pp. 1725–1753.

[4] Ghosh, B. K., "Simultaneous Partial Pole Placement – A New Approach to Multi-mode System Design," *IEEE Trans. on Automatic Control*, Vol. AC–31, May 1986, pp. 440–443.

[5] MacMartin, D. G., Hall, S. R., and Bernstein, D. S., "Fixed Order Multi-Model Estimation and Control," *Proceedings, American Control Conference*, Boston, MA, June 1991, pp. 2113–2118.

[6] Hanks, B. R. and Pinson, L. D., "Large Space Structures Raise Testing Challenges," *Aerospace America*, Oct. 1983, pp. 34–53.

[7] Belvin, W. K., "Experimental and Analytical Generic Space Station Dynamic Models," Tech. Rep. N87-24510, NASA, 1986.

[8] Gronet, M. J., Crawley, E. F., and Allen, B. R., "Design, Analysis, and Testing of a Hybrid Scale Structural Dynamic Model of a Space Station," in *AIAA Structures, Structural Dynamics, and Materials Conference*, Apr. 1989, pp. 1567–1575. AIAA 89-1340-CP.

[9] Barlow, M. S., *Modeling and Ground Modal Identification of Space Structures*, Master's thesis, Massachusetts Institute of Technology, Jan. 1992.

[10] Ashley, H., "Some Considerations on Earthbound Dynamic Testing of Large Space Structures," in *AIAA Structures, Structural Dynamics, and Materials Conference*, June 1986, pp. 362–373. AIAA 86-0908.

[11] Anderson, G. C., Quinn, D. A., Beals, G. A., Nelson, J. D., and Nurre, G. S., "An Overview of the Hubble Space Telescope Pointing Control System Design and Operation," *Proceedings, AIAA Guidance, Navigation, and Control Conference*, Hilton Head Island, SC, Aug. 1992. AIAA 92-4616.

[12] Sharkey, J. P., Nurre, G. S., Beals, G. A., and Nelson, J. D., "A Chronology of the On-Orbit Pointing Control System Changes on the Hubble Space Telescope and associated Pointing Improvements.," *Proceedings, AIAA Guidance, Navigation, and Control Conference*, Hilton Head Island, SC, Aug. 1992. AIAA 92-4618.

[13] Crawley, E. F., deLuis, J., and Miller, D., "Middeck Active Control Experiment (MACE) Phase A Final Report," Tech. Rep. SSL 7-89, Space Systems Laboratory, Dept. of Aeronautics and Astronautics, M.I.T., June 1989.

[14] Wada, B. K., "Extension of Ground-Based Testing for Large Space Structures," in *AIAA Structures, Structural Dynamics, and Materials Conference*, Apr. 1985, pp. 477–483. AIAA 85-0757.

[15] Miller, D., Sepe, R., Rey, D. A., Saarma, E., and Crawley, E. F., "The Middeck Active Control Experiment (MACE)," in 5th *NASA/DOD CSI Technology Conference*, Mar. 1992.

[16] Kienholz, D. A., Crawley, E. F., and Harvey, T. J., "Very Low Frequency Suspension Systems for Dynamic Testing," in *AIAA Structures, Structural Dynamics, and Materials Conference*, Apr. 1989, pp. 327–336. AIAA 89-1194-CP.

[17] Kienholz, D. A., "A Pneumatic/Electric Suspension System for Simulating On-Orbit Conditions," in *ASME Annual Winter Meeting*, (Dallas, TX), Nov. 1990. ASME 90–WA/Aero–8.

[18] Herr, R. W., "Some Cable Suspension Systems and their Effects on the Flexural Frequencies ofSlender Aerospace Structures," Tech. Rep. TN D-7693, NASA LaRC, Sept. 1974.

[19] Gronet, M. J., Brewster, R. G., and Crawley, E. F., "Systems Issues in the Ground Testing of Flexible Structures Supported by Suspension Systems," in *AIAA/AFOSR Workshop on Microgravity Simulation in Ground Validation Testing of Large Space Structures*, (Denver, CO), Nov. 1989.

[20] Crawley, E. F., Barlow, M. S., and van Schoor, M. C., "Variation in the Modal Parameters of Space Structures," in *AIAA Structures, Structural Dynamics, and Materials Conference*, Apr. 1992.

[21] Cooley, V. M., "Laboratory Evaluation of Two Advanced Suspension Devices for Ground Vibration Testing of Large Space Structures," in *AIAA Structures, Structural Dynamics, and Materials Conference*, Apr. 1992, pp. 1700–1710.

[22] Wada, B. K., "Ground Test of Large Flexible Structures," Tech. Rep. N87-24510, NASA, 1987.

[23] Wada, B. K., "Structural Qualification of Large Spacecraft," in *NASA Langley Research Center Report*, 1986.

[24] Shih, C.-F., "Verification of Large Beam-Type Space Structures," *AIAA Journal of Spacecraft*, Vol. 24, No. 5, Sept. 1987, pp. 469–473.

[25] Shih, C.-F., Chen, J. C., and Garba, J. A., "Vibration of a Large Space Beam Under Gravity Effect," *AIAA Journal*, Vol. 24, July 1986, pp. 1213–1216.

[26] Chen, J. C. and Garba, J. A., "Verification for Large Space Structures," in *Large Space Antenna Systems Technology*, Dec. 1984, pp. 393–406.

[27] Norris, M., Thompson, R., and Das, A., "Low-Frequency Response of Accelerometers for Observer Design in a Gravity Environment," *AIAA Journal of Guidance and Control*, Vol. 13, No. 4, July 1990, pp. 732–737.

[28] Yang, Y.-B. and McGuire, W., "Stiffness Matrix for Geometric Nonlinear Analysis," *Journal of Structural Engineering*, Vol. 112, No. 4, Apr. 1986, pp. 853–877.

[29] Yang, Y.-B. and McGuire, W., "Joint Rotation and Geometric Nonlinear Analysis," *Journal of Structural Engineering*, Vol. 112, No. 4, Apr. 1986, pp. 879–905.

[30] Minguet, P. and Dugundji, J., "Experiments and Analysis for Composite Blades under Large Deflections, Part 1: Static Behavior, Part 2: Dynamic Behavior," *AIAA Journal*, Vol. 28, No. 9, Sept. 1990, pp. 1573–1579, 1580–1588.

[31] Adina R&D, *ADINA and ADINA-IN Users Manuals*. 71 Elton Avenue, Watertown, MA 02172, 1987.

[32] Rey, D. A., Alexander, H., and Crawley, E. F., "Direct Gravity Effects on the Control and Output Matrices of Controlled Structure Models," in *AIAA Dynamics Specialist Conference*, Apr. 1992, pp. 128–137. AIAA 92–2094.

[33] Martin, H. C., "On the Derivation of Stiffness Matrices for the Analysis of Large Deflection and Stability Problems," in *Conference on Matrix Methods in Structural Mechanics*, Wright–Patterson Air Force Base, 1965. FI DL–TR–66–80.

[34] Southwell, R. V., "On the General Theory of Elastic Stability," *Philosophical Transactions of the Royal Society*, Vol. 213, 1913, pp. 187–244.

[35] Biot, M. A., *Mechanics of Incremental Deformations*, John Wiley & Sons, Inc., New York, 1965.

[36] Biezeno, C. B. and Hencky, H., "On a General Thory of Elastic Stability," *Proceedings of the Royal Academy, Amsterdam*, Vol. 31, 1928, pp. 569–592.

[37] Biezeno, C. B. and Hencky, H., "On a General Thory of Elastic Stability," *Proceedings of the Royal Academy, Amsterdam*, Vol. 32, 1929, pp. 444–456.

[38] Turner, M. J., Dill, E. H., Martin, H. C., and Melosh, R. J., "Large Deflections of Structures Subjected to Heating and External Loads," *Journal of Aerospace Science*, Vol. 27, 1959, pp. 97–106.

[39] Archer, J. S., "Consistent Matrix Formulations for Structural Analysis using Influence Coefficient Techniques," *AIAA Journal*, Vol. 3, 1965, pp. 1910–1918.

[40] Gallagher, R. H. and Padlog, J., "Discrete Element Approach to Structural Instability Analysis," *AIAA Journal*, Vol. 6, 1963, pp. 1437–1439.

[41] Argryis, J. H., "Recent Advances in Matrix Methods in of Structural Analysis," *Progress in Aeronautical Sciences*, 1964.

[42] Greene, B. C., "Buckling Loads for Columns of Variable Section," Tech. Rep. Structural Analysis Research Memo. No. 12, The Boeing Company, Aerospace Division, Seattle, Washington, June 1960.

[43] Greene, B. C., "Stiffness Matrix for Bending of a Rectangular Plate Element with Initial Membrane Stresses," Tech. Rep. Structural Analysis Research Memo. No. 45, The Boeing Company, Aerospace Division, Seattle, Washington, 1962.

[44] Kapur, K. and Hartz, B., "Stability of Plates using the Finite Element Method," *J. Eng. Mech. Div. Am. Society of Civil Engineers*, Vol. 92, 1966, pp. 177–195.

[45] Bathe, K.-J., *Finite Element Procedures in Engineering Analysis*, Prentice-Hall, Inc., New Jersey, 1982.

[46] Zienkiewicz, O. C. and Taylor, R. L., *The Finite Element Method*, Vol. 2, McGraw-Hill Book Company, London, fourth ed., 1992.

[47] Novozhilov, V. V., *Foundations of the Nonlinear Theory of Elasticity*, Graylock Press, Rochester, N.Y., 1953.

[48] Cook, R. D., *Concepts and Applications of Finite Element Analysis*, John Wiley & Sons, Inc., New York, 1981.

[49] Wood, R. D. and Schrefler, B., "Geometrically Non-Linear Analyssis – A Correlation of Finite Element Notations," *Int. J. for Numerical Methods in Engineering*, Vol. 12, No. 4, 1978, pp. 635–642.

[50] Haisler, W. E., Stricklin, J. A., and Stebbins, F. J., "Development and Evaluation of Solution Procedures for Geometrically Nonlinear Structural Analysis," *AIAA Journal*, Vol. 10, No. 3, Mar. 1972, pp. 264–272.

[51] Przemieniecki, J. S., *Theory of Matrix Structural Analysis*, McGraw-Hill Book Company, London, 1968.

[52] Yang, T. Y., *Finite Element Structural Analysis*, Prentice-Hall, Inc., New Jersey, 1986.

[53] Irretier, H., "Refined Effects in Beam Theories and their Influence on the Natural Frequencies of Beams," in *Lecture Notes in Engineering #28*, pp. 163–179, Springer-Verlag, 1981. Proceedings of the Euromech-Colloquium 219.

[54] Blevins, R. D., *Formulas for Natural Frequencies and Mode Shapes*, Robert E. Krieger Publishing Co., Malabar, Florida, reprint ed., 1984.

[55] Barsoum and Gallager, "Finite Element Analysis of Torsional and Torsional–Flexural Stability Problems," *Int. J. for Numerical Methods in Engineering*, Vol. 2, 1970, pp. 335–352.

[56] Plant, R. H. and Huseyin, K., "Derivatives of Eigenvalues and Eigenvectors in Non-Self-Adjoint Systems," *AIAA Journal*, Vol. 11, No. 2, Feb. 1973.

[57] Hall, K. C., *Optimal Mistuning for Enhanced Aeroelastic Stability of Transonic Fans*, Master's thesis, Massachusetts Institute of Technology, Sept. 1983.

[58] Hou, G. J.-W. and Chuang, C. H., "Eigenvector Sensitivity Analysis of Continuous Beams with Variable Support Locations," in *Structural Dynamics: Recent Advances*, (London), Elsevier Applied Science, 1992, pp. 313–322. Proceedings of the 4th International Conference.

[59] Balmes, E., *Modelling of Flexible Structures for Control*, Master's thesis, Massachusetts Institute of Technology, 1991.

[60] von Flotow, A., "Structural Dynamics." Course Lecture Notes, M.I.T., Spring 1990.

[61] Clough, R. W. and Penzien, J., *Dynamics of Structures*, McGraw-Hill Book Company, New York, 1975.

[62] Meirovitch, L., *Elements of Vibration Analysis*, McGraw-Hill Book Company, New York, 1986.

[63] Blackwood, G. H., Jacques, R. N., and Miller, D. W., "The MIT Multipoint Alignment Testbed: Technology Development for Optical Interferometry," in *SPIE Conference on Active and Adaptive Optical Systems*, July 1991.

[64] Shaw, J. and Jayasuriya, S., "Modal Sensitivities for Repeated Eigenvalues and Eigenvalue Derivatives," *AIAA Journal*, Vol. 30, No. 3, 1991, pp. 850–852.

[65] Eldred, M. S., Lerner, P. B., and Anderson, W. J., "Higher Order Eigenpair Perturbations," *AIAA Journal*, Vol. 30, No. 7, July 1992.

[66] Rey, D. A., "Eigenvalue Convergence in Beam and Truss Modeling." Computer Methods in Dynamics, Term Project, Apr. 1992.

[67] Belvin, W. K. and Edighoffer, H. H., "Dynamic Analysis and Experiment Methods for a Generic Space Station Model," in *AIAA Structures, Structural Dynamics, and Materials Conference*, May 1986, pp. 10–18. AIAA 86-0838.

[68] Boeing Aerospace, E. T., "Assessment and Selection of Zero-G Ground Test Simulation Techniques - Task 3 Final Report," Tech. Rep. NASA-CR-183566, Boeing Aerospace Co., Oct. 1988.

[69] Reaves, M. C., Chew, M.-S., Juang, J.-N., and Chiu, S. H., "Dynamics and Control of a Large Displacement Suspension System for Ground Testing of Flexible Space Structures," in *1992 Aerospace Design Conference*, Feb. 1992. AIAA 92-1178.

[70] Thompson, R., "Predicting Accelerometer Errors in Ground-Based Testing of Large Flexible Structures," in *AIAA/AAS Astrodynamics Conference*, Aug. 1990. AIAA 90–2915.

[71] Mercadel, M., "Middeck Active Control Experiment (MACE) First Sample Problem," Tech. Rep. SERC 6-91-R, M.I.T. Space Engineering Research Center (SERC), June 1991.

[72] Rey, D. A., "Middeck Active Control Experiment (MACE) Scaling Analysis." SERC Tech. Memo. 89-11-22, Nov. 1989.

[73] Blackwood, G. H., "Personal Communication," June 1991. M.I.T. Space Engineering Research Center.